Kinetic Studies of Singlet Molecular Oxygen in a Discharge Flow Shock Tube

by

Patricia M. Borrell

This thesis is submitted to the University of Keele in partial fulfillment of the requirements for the degree of Doctor of Philosophy.

Department of Chemistry
University of Keele

September 1980

This thesis is the author's own account of work carried out under the supervision of Dr. P. Borrell. Experimental results were obtained in collaboration with two other workers; Dr. M.D. Pedley performed and analysed shocks with run numbers beginning with M, and Mr. K.R. Grant those beginning with C; all other shocks were performed and analysed by the author.

Acknowledgements

On submitting this thesis I would like to thank the following people:

Dr. Peter Borrell, my husband, and supervisor in this work, for his patience, help and unceasing encouragement;

Professor I.T. Millar for the facilities in the Department of Chemistry;

The technical staff of the Department, in particular, P.H. Holbrook, R. Dix, C. Cork and T. Bolam;

The computer centre staff and operators;

Mrs. Iris Jones, Mrs. Margaret Furnival and Mrs. Christine Owen who typed this thesis so competently;

Dr. Mike Pedley and Mr. Kevin Grant who worked in the laboratory with me, for their friendly cheerfulness and many helpful discussions;

The Science Research Council for supporting the work; and finally my sons, Paul, Stephen and Michael for their willingness to put up with some erratic housekeeping while I was writing this thesis.

Abstract

The discharge flow shock tube has been used to study the temperature dependences of the reactions of singlet molecular oxygen, by observing their emissions with photomultiplier/filter combinations.

The room temperature deactivation of $O_2(^1\Delta_g)$ has been measured and a value of $9.4 \pm 0.3 \times 10^2$ ℓ mol^{-1} s^{-1} obtained, lower than the previous values, but in accord with some more recent measurements.

The temperature dependence of the collisional quenching of $O_2(^1\Delta_g)$ by oxygen was found to be too slow to measure accurately, and only an upper limit of 3.8×10^4 ℓ mol^{-1} s^{-1} at 1570 K is suggested.

The temperature dependence of the collisional quenching of $O_2(^1\Sigma_g^+)$ by oxygen, nitrogen and argon has been measured in the temperature range 600 to 1500 K, and values of the rate constants are listed in Table 8.8. There is no simple temperature dependence for these reactions, and a combination of two mechanisms is suggested, long range multipolar interactions and short range repulsive interactions which may be dominant at the higher temperatures.

The energy pooling reaction forming $O_2(^1\Sigma_g^+)$ also shows a curved temperature dependence in the region 600 to 1800 K, and may be governed by similar mechanisms. This reaction is independent of added gases.

The dimol emission from two $O_2(^1\Delta_g)$ molecules at 634 nm has been shown to be essentially a simple collisional process between 650 and 1620 K, although there is an increase in emission at temperatures above 1100 K. The relative emission intensities of the dimol emission at 634 nm, 703 nm and 579 nm have been measured, and the rate constants for emission listed at various temperatures in Table 9.2. There is no correlation with Franck Condon factors for the single molecule transitions.

The vibrational relaxation of $O_2(^1\Delta_g)$ has been studied at temperatures up to 1700 K, and the rate is found to be faster than for ground state oxygen. It appears that vibration-vibration exchange is important in the relaxation process.

Contents

Chapter 1.

Introduction

1.1. An Outline of the Thesis

The aim of this work is to study the temperature dependence of reactions of singlet molecular oxygen, ($^1\Delta_g$) and ($^1\Sigma_g^+$), in a discharge flow shock tube.

Much of the earlier work described in this thesis was devoted to a study of the discharge flow shock tube, it s operation and reliability.

The discharge flow system was used to make measurements of the rate of deactivation of $O_2(^1\Delta_g)$ by oxygen at room temperature (Chapter 5). The three dimol emissions from two $O_2(^1\Delta_g)$ molecules were observed both at room temperature and at high temperatures, and their relative emission intensities and emission rate constants evaluated at several temperatures (Chapter 9). The dimol emission at 579 nm, where one $O_2(^1\Delta_g)$ molecule is vibrationally excited, gave a means of studying vibrational relaxation (Chapter 10).

The temperature dependence of collisional quenching of $O_2(^1\Delta_g)$ and $O_2(^1\Sigma_g^+)$, an example of electronic energy transfer, was studied with oxygen, nitrogen and argon as collision partners (Chapter 8).

There is no simple qualitative model for electronic energy transfer, and the overall temperature dependence is not easy to discern. Energy may be transferred in molecular collisions to electronic, vibrational, rotational or translational energy in the collision partner. The temperature dependence may have an exponential form as in the Arrhenius equation, or follow simple collision theory, or possibly have a $T^{-1/3}$ dependence as in the Landau-Teller model for vibrational energy

transfer.

This chapter gives the simple basis for these theories, chapter 2 describes the singlet states of oxygen together with some past experiments, and chapter 3 discusses the discharge flow shock tube and gives the experimental arrangements.

The thesis concludes with an evaluation of the discharge flow shock tube and some suggestions for further work.

1.2. The Temperature Dependence of Reaction Rates

For the majority of reactions, the rate increases with increasing temperature. The change in rate constant with temperature can usually be described by the Arrhenius equation:

$$k = Ae^{-E/RT} \qquad 1.1$$

where E is the activation energy, and A, the preexponential factor, has the same units as the rate constant, k. For a first order reaction, where the rate is dependent on the concentration of one component, A ins^{-1} is called the frequency factor. For a second order reaction, where the rate is dependent on the square of the concentration of the reactant, or the product of the concentrations of two reactants, A can be identified with the collision number.

1.2.1. Simple Collision Theory

For a bi-molecular reaction where two molecules take part, the rate of the reaction can be described by simple collision theory[1] where:

$$\text{Rate of Reaction} = \left[\begin{array}{c}\text{No. of collisions} \\ \text{per second}\end{array}\right]\left[\begin{array}{c}\text{Fraction of collisions with} \\ \text{sufficient energy for reaction}\end{array}\right]$$

The number of collisions per second, or collision frequency, Z, can be calculated for a given gas or mixture of gases.

$$Z_{AB} = \bar{v}_{AB}\, \sigma_{AB}\, c_A\, c_B \qquad 1.2$$

where c_A and c_B are the concentrations of gases A and B, σ_{AB} is the cross sectional area for collision of molecule A with molecule B, and $\bar{v}_{AB}$ is the mean relative velocity,

$$\bar{v}_{AB} = \left(\frac{8kT}{\pi\mu}\right)^{\frac{1}{2}} \qquad 1.3$$

where μ is the reduced mass $\dfrac{m_A m_B}{m_A + m_B}$

If E_{min} is the minimum energy necessary for reaction then:

$$\text{Rate of Reaction} = \sigma_{AB} \left(\frac{8kT}{\pi\mu}\right)^{\frac{1}{2}} e^{-E_{min}/RT} \qquad 1.4$$

or

$$k = a\, T^{\frac{1}{2}}\, e^{-E_{min}/RT} \qquad 1.5$$

which has a similar form to the Arrhenius equation. In this simple theory, E_{min} contains only components of translational energy along the line of centres of the colliding molecules.

For reactions with large activation energies, the $T^{\frac{1}{2}}$ dependence is masked by the exponential dependence, but for many reactions between short lived intermediates or excited molecules where the activation energy is small or zero, the rate will depend simply on the collision frequency and should be proportional to $T^{\frac{1}{2}}$. The dimol emission at 634 nm from $O_2(^1\Delta_g)$ (Chapter 7) has a $T^{\frac{1}{2}}$ temperature dependence.

1.2.2. Activated-Complex Theory

The activated complex theory[1] pictures a bimolecular reaction from reactants A and B to products, as proceeding by the formation of an activated complex. The reaction rate is given by:

$$\text{Rate of Reaction} = \left[\begin{array}{c}\text{Concentration of activated} \\ \text{complex}\end{array}\right]\left[\begin{array}{c}\text{Decomposition frequency} \\ \text{for activated complex}\end{array}\right]$$

This is developed to give the reaction rate constant as:

$$k = \frac{kT}{h} \frac{Q_{\ddagger}}{Q_A Q_B} e^{-E_o^{\ddagger}/RT} \qquad 1.6$$

where $Q_{\ddagger}$ is the molecular partition function per unit volume for the complex, and $E_o^{\ddagger}$ is the energy barrier to reaction.

For most reactions with an appreciable activation energy, the rate constant follows approximately an exponential temperature dependence.

1.3. Vibrational Energy Transfer

When a gas is heated rapidly, as in a shock wave, the energy is taken up in translational and rotational motion within a few collisions. The vibrational degrees of freedom do not adjust so quickly. The rate of vibrational relaxation to equilibrium at the higher temperature is specific for each gas and dependent on it s collision partner.

Landau and Teller developed a theory for vibrational energy transfer dependent on the time of interaction between colliding molecules, where only the repulsive part of the intermolecular potential energy curve is steep enough to influence energy transfer, and the attractive potential is neglected[2]. They used the potential:

$$V(r) = V_o \, e^{(-\alpha r)} \qquad 1.7$$

and a time dependent perturbation theory. This gives a result for the probability of deactivation of a molecule from it s v = 1 to v = 0 state per collision at temperature T as:

$$P_{10} = C \, e^{(-\text{ constant}/T)^{1/3}} \qquad 1.8$$

Most non-polar molecules show a linear Landau-Teller plot of $\log P_{10}$ against $T^{-1/3}$ over a wide temperature range.

The rate of deactivation of a molecule from it s v = 1 to v = 0 state, or the number of vibrational transitions per second, is related to the probability by the collision frequency

$$k_{10} = P_{10} Z \qquad 1.9$$

This assumes that the collision partner is in the v = 0 state, but there is a Boltzmann distribution of molecules between the two levels. The process is reversible so the rate constant for energy transfer k_v, is related to k_{10} as:

$$k_v = k_{10}/[1-e^{-h\nu/kT}] \qquad 1.10$$

and τ_v, the measured relaxation time is:

$$\tau_v = {}^1/_{k_v} \qquad 1.11$$

As the vibrational relaxation time is dependent on Z, it is inversely proportional to the gas pressure; listed relaxation times, or Napier times, are referred to one atmosphere pressure.

The theory most widely used for quantitative comparison with experimental measurements is the Schwartz, Slawsky and Herzfeld (SSH) theory[3]. The intermolecular potential used is:

$$V(r) = U\, e^{(-\alpha r)} - \varepsilon \qquad 1.12$$

This is essentially a repulsive potential, the attractive part, represented by $-\varepsilon$, increases the relative motion to favour a higher transition probability.

There are two alternative methods to determine α by fitting the molecular collision parameters, expressed in terms of the Lennard Jones potential, to the intermolecular potential.

A defect in the SSH theory is that the attractive part of the Lennard Jones intermolecular potential is not taken into account. This is important for all molecules at low temperatures, and polar molecules at all temperatures.

Several other theories of greater complexity give better predictions for some molecules e.g. Shin for non-polar diatomic molecules, and Tanczos for polyatomic molecules[2].

However, the main dependence of relaxation time with temperature is $e^{(C/T)^{1/3}}$ as observed in experimental measurements at moderate to high temperatures.

Chapter 2

Singlet Molecular Oxygen

2.1. Introduction

During the past twenty years there has been much interest in the singlet states of molecular oxygen. They occur in the upper atmosphere, and are thought to take part in oxidation reactions in poluted atmospheres. They have unusually long lifetimes for excited molecules and have been studied extensively.

This chapter gives the electronic configuration of molecular oxygen and reviews the literature relevant to this thesis.

Figure 2.1.

A Molecular Orbital Diagram for Oxygen.

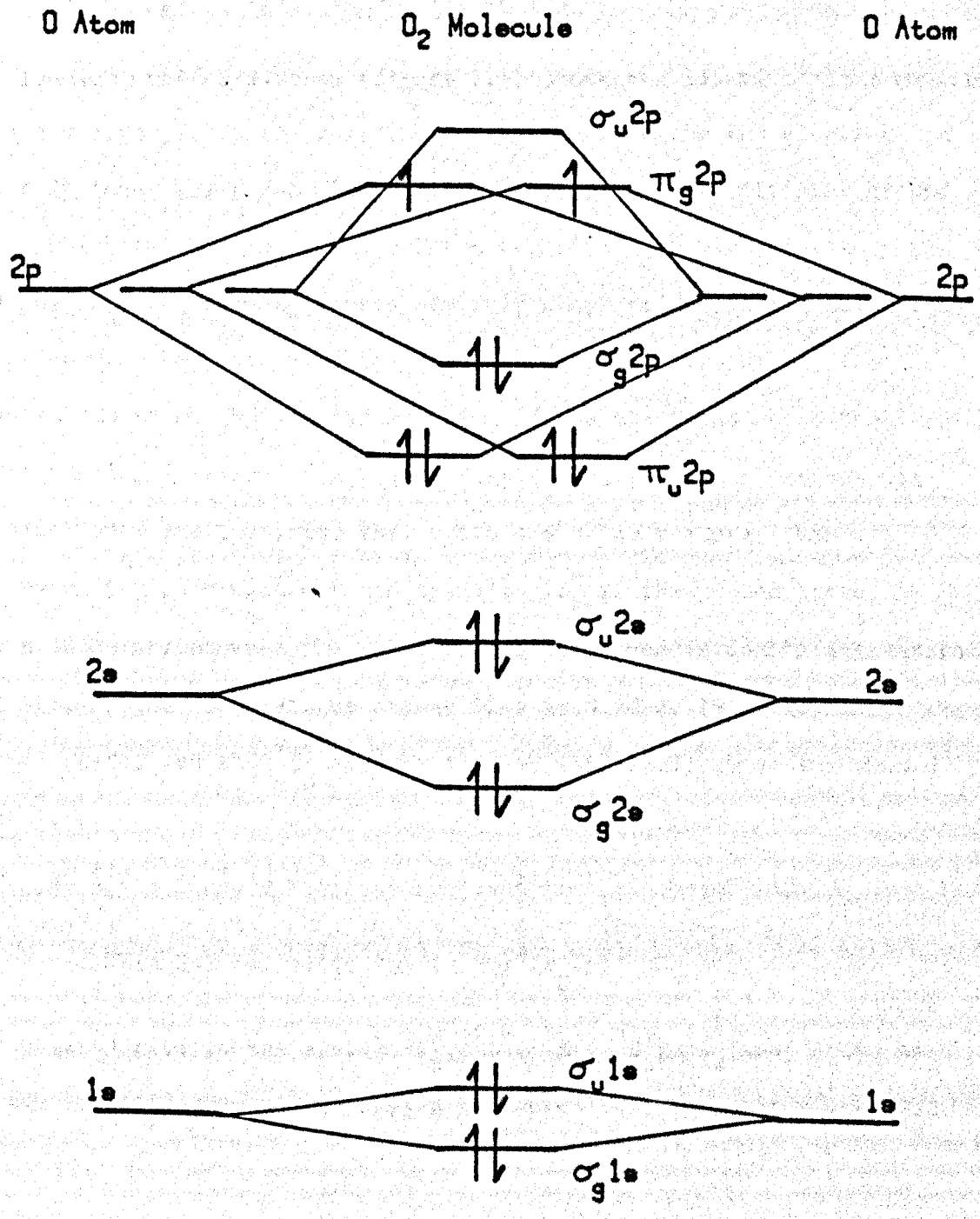

2.2. The Oxygen Molecule

Oxygen is the most widely distributed and by far the most abundant of the elements, it occurs free in the atmosphere, 23% by weight, 21% by volume.

The lowest electron configuration of the oxygen molecule is[4] :

$$KK(\sigma_g 2s)^2(\sigma_u 2s)^2(\sigma_g 2p)^2(\pi_u 2p)^4(\pi_g 2p)^2$$

A molecular orbital diagram (figure 1.1) shows the separate atoms on the left and right, with the molecule in the centre; the two electrons in the $\pi_g 2p$ level are shown with parallel spins, as in the triplet ground state which is paramagnetic[5]. These two electrons give rise to three states, $^3\Sigma_g^-$, $^1\Delta_g$ and $^1\Sigma_g^+$ (there are only three states as the total wave function must be antisymmetric). The Σ states arise when Λ, the quantum number of the angular momentum of the electrons about the inter nuclear axis, is zero. In the triplet state, the two electrons with parallel spin are unpaired, this state has a lower energy than a corresponding pair with opposed spins so $^3\Sigma_g^-$ is the ground state. The Δ state arises when the value of Λ is two, and is doubly degenerate ($M_L = \pm 2$). The $^1\Delta_g$ state of oxygen lies at 0.98 eV (94.3 kJ) above the ground state, and the $^1\Sigma_g^+$ lies at 1.63 eV (157.7 kJ) above the ground state[6].

The first excited electron configuration for oxygen is :

$$KK(\sigma_g 2s)^2(\sigma_u 2s)^2(\sigma_g 2p)^2(\pi_u 2p)^3(\pi_g 2p)^3$$

which gives rise to the states $^1\Sigma_u^+$, $^1\Sigma_u^-$, $^1\Delta_u$, $^3\Sigma_u^+$, $^3\Sigma_u^-$ and $^3\Delta_u$. An energy level diagram of the oxygen molecule[7,8] is shown in figure 2.2.

Figure 2.2

A Potential Energy Level Diagram for Oxygen.

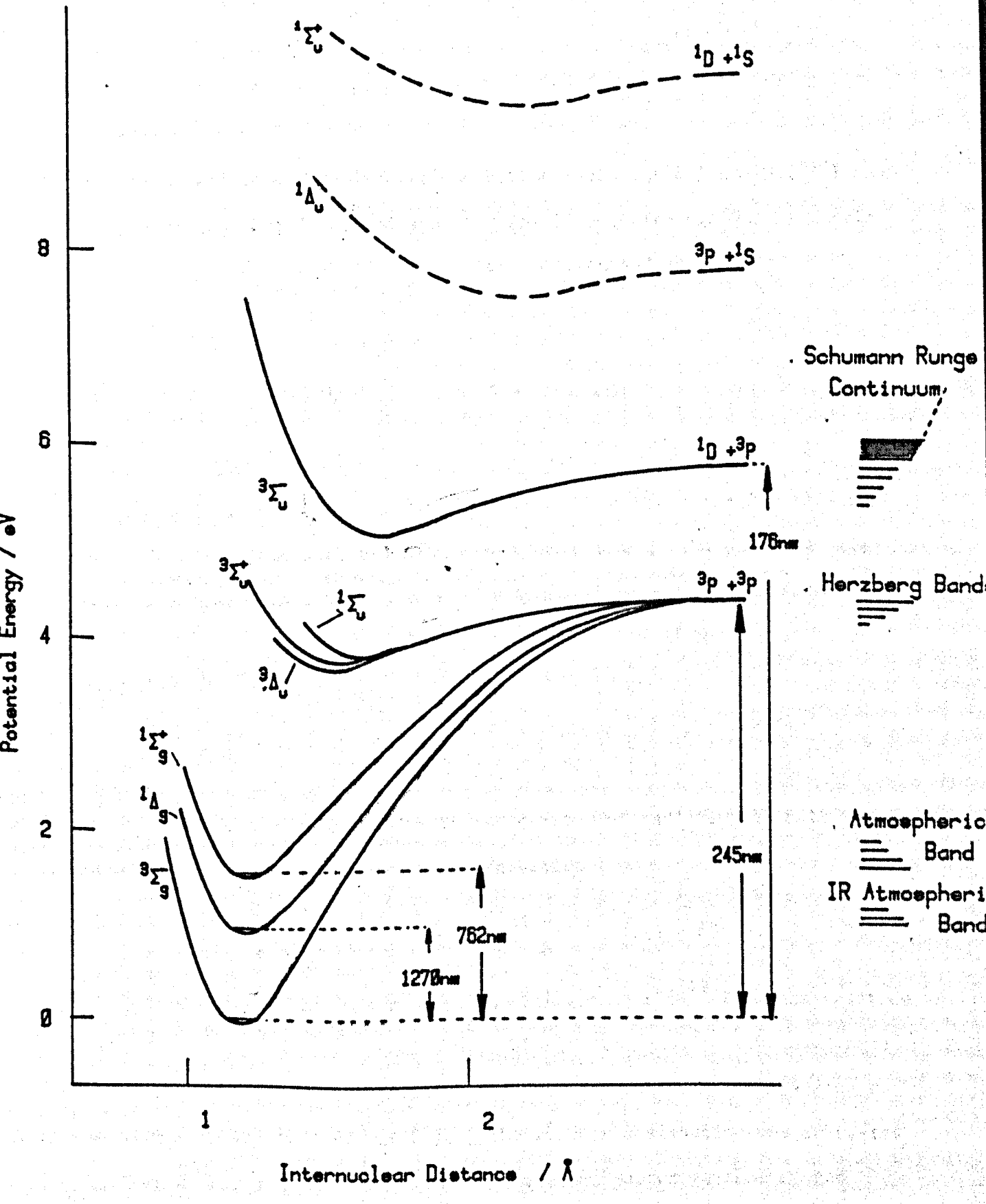

2.3. The Optical Transitions of Singlet Oxygen

The infra-red atmospheric band system at 1270 nm arises from transitions between $O_2(^1\Delta_g)$ and ground state oxygen, $O_2(^3\Sigma_g^-)$. Transitions between $O_2(^1\Sigma_g^+)$ and $O_2(^3\Sigma_g^-)$ give rise to the atmospheric band system at 762 nm. The emissions are seen in the 'airglow' both during the daytime, and at night.

The electric dipole transitions between both $O_2(^1\Delta_g)$ and $O_2(^1\Sigma_g^+)$ and the ground state are spin and symmetry forbidden, although weak magnetic dipole transitions are observed in both emission and absorption

$$O_2(^1\Delta_g) \rightarrow O_2(^3\Sigma_g^-) + h\nu(\lambda = 1270 \text{ nm}) \qquad 2.1$$

$$O_2(^1\Sigma_g^+) \rightarrow O_2(^3\Sigma_g^-) + h\nu(\lambda = 762 \text{ nm}) \qquad 2.2$$

The singlet excited states of oxygen are consequently very long lived compared with most other excited species. The radiative lifetime of $O_2(^1\Delta_g)$ is 45 minutes for the isolated molecule[9]; the observed lifetime of 9.2 seconds at 1 atmosphere pressure of oxygen is considerably shorter due to collisions. The radiative lifetime of the $(^1\Sigma_g^+)$ state is between 7 and 12 seconds[10,11].

These spin forbidden transitions may become spin allowed for simultaneous transitions. The unusual dimol emissions occur when two excited molecules collide and emit one quantum of radiation at half the wavelength for the single molecule transition.

$$O_2(^1\Delta_g) + O_2(^1\Delta_g) \rightarrow 2\,O_2(^3\Sigma_g^-) + h\nu(\lambda = 634 \text{ nm}) \qquad 2.3$$

This red emission was reported by Seliger in 1960[12] from the reaction of hydrogen peroxide with sodium hypochlorite in aqueous solution. Kahn and Kasha[13] studied the reaction and attributed the chemiluminescence to solvent shifted bands of $O_2(^1\Sigma_g^+)$. The correct designation was suggested by Arnold, Ogryzlo and Witzke in 1964[14]; they passed gaseous oxygen

through a microwave discharge and recorded emission bands at 634, 703, 760 and 860 nm. The bands at 760 and 860 nm from the (0,0) and (0,1) transitions of $O_2(^1\Sigma_g^+)$ were rapidly quenched when water was added to the system, so they deduced that the new bands seen at 634 and 703 nm arose from $O_2(^1\Delta_g)$ molecules, and suggested an oxygen dimer, O_4, stabalized by van der Waals forces

$$2\ O_2(^1\Delta_g)_{v=0} \rightarrow O_2(^3\Sigma_g^-)_{v=1} + O_2(^3\Sigma_g^-)_{v=0} + h\nu(\lambda = 703\ nm) \qquad 2.4$$

Further work by Arnold and Ogryzlo[15] suggested that the colliding molecules were not bound. We have studied the dimol reaction and find that the emission at 634 nm is a simple collisional process (Chapter 7).

A further dimol emission band from $O_2(^1\Delta_g)$ was reported by Gray and Ogryzlo[16] at 579 nm arising when one $O_2(^1\Delta_g)$ is vibrationally excited:

$$O_2(^1\Delta_g)_{v=1} + O_2(^1\Delta_g)_{v=0} \rightarrow 2\ O_2(^3\Sigma_g^-)_{v=0} + h\nu(\lambda = 579\ nm) \qquad 2.5$$

We have studied this emission and report results of vibrational relaxation in Chapter 10 .

Cooperative emission bands from $O_2(^1\Sigma_g^+)$ have also been observed[16], but as the concentration of $O_2(^1\Sigma_g^+)$ is usually low, they are weak.

$$2\ O_2(^1\Sigma_g^+)_{v=0} \rightarrow 2\ O_2(^3\Sigma_g^-)_{v=0} + h\nu(\lambda = 380\ nm) \qquad 2.6$$

$$2\ O_2(^1\Sigma_g^+)_{v=0} \rightarrow O_2(^3\Sigma_g^-)_{v=1} + O_2(^3\Sigma^-{}_g)_{v=0} + h\nu(\lambda = 400\ nm) \qquad 2.7$$

Khan and Kasha[17,18] reported the emission from a mixed cooperative band at 478 nm

$$O_2(^1\Delta_g)_{v=0} + O_2(^1\Sigma_g^+)_{v=0} \rightarrow 2\ O_2(^3\Sigma_g^-)_{v=0} + h\nu(\lambda = 478\ nm) \qquad 2.8$$

The collisional enhancement of the (0,0) transition of $O_2(^1\Sigma_g^+)$ noted by Young and Black[19,20], where the optical selection rules are possibly relaxed during the collision of two oxygen molecules, was not observed in our work on the 762 nm emission (Chapter 8).

2.4. Other Optical Transitions of Oxygen

The Schumann-Runge region marks the strong absorption of oxygen in the ultraviolet below 207 nm from the allowed transition $O_2(^3\Sigma_u^-) \leftarrow O_2(^3\Sigma_g^-)$. The Schumann-Runge bands converge to a continuum at 176 nm corresponding to the dissociation of the oxygen molecule into an excited ^1D and a normal ^3P atom[8]. [see figure 2.2]

The Herzberg I bands in the night sky spectrum arise from the transition $O_2(^3\Sigma_u^+) \rightarrow O_2(^3\Sigma_g^-)$ in the wave length region 250-500 nm[21], and the Herzberg II band system from the transition $O_2(^1\Sigma_u^-) \rightarrow O_2(^3\Sigma_g^-)$ at 350-700 nm[22]. Both these band systems arise from forbidden transitions, and are therefore weak.

2.5. The Production of Singlet Oxygen

Singlet oxygen is produced in our system by flowing purified oxygen through a microwave discharge. $O_2(^1\Delta_g)$ is formed in or just after the discharge, $O_2(^1\Sigma_g^+)$ is formed from $O_2(^1\Delta_g)$ by the energy pooling reaction first investigated by Young and Black[19]

$$O_2(^1\Delta_g) + O_2(^1\Delta_g) \rightarrow O_2(^1\Sigma_g^+) + O_2(^3\Sigma_g^-) \qquad 2.9$$

Most workers, studying the reactions of singlet oxygen in the gas phase, use a discharge flow system, and oxygen pressures between 1 and 10 torr (0.13 and 1.33 kPa)[23,24] in the microwave discharge. The less stable radio frequency discharge has also been used[25]. The amount of singlet oxygen produced is enhanced if the flowing oxygen is saturated with mercury vapour before the discharge[26]. Up to 10% of the total flow may be singlet oxygen, but oxygen atoms (up to 3% of the flow[27]) and some ozone are also produced. The oxygen atoms react with the mercury in the gas, depositing mercuric oxide past the discharge, which also serves to remove any remaining atoms[28].

$$Hg + O \rightarrow Hg\,O \qquad 2.10$$

$$Hg\,O + O \rightarrow Hg + {}^1O_2 \qquad 2.11$$

Yaron et al[29,30,31] used a silver cylinder coated with silver oxide placed downstream of the discharge to remove oxygen atoms and ozone.

It is important in kinetic measurements of singlet oxygen that oxygen atoms are removed, as the reactions with atoms are usually fast and would interfere with the system under study. Striking evidence for this is shown in a paper by Furukawa and Ogryzlo[32] when nitrogen dioxide was added to the discharged gas to remove any remaining oxygen atoms; the measured value of the rate constant for quenching of $O_2(^1\Delta_g)$ by 2,3 dimethyl 2 butene dropped dramatically. Measurements in our system

are made at a sufficient distance from the discharge for any oxygen atoms remaining after the mercuric oxide films to have been deactivated on the walls (Chapter 5).

Snelling, Findlay and Fortin[33,34,35] have studied $O_2(^1\Delta_g)$ produced in the gas phase by irradiation of a mixture of benzene and oxygen with a low pressure mercury lamp at 253.7 nm. This method has the advantage that the singlet oxygen is uncontaminated with oxygen atoms or ozone, but benzene in the system makes some measurements impossible. The $O_2(^1\Delta_g)$ is formed when the excited triplet state benzene is quenched by oxygen. These types of reaction have been studied by Kearns[36] where the excited triplet state is formed by intersystem crossing.

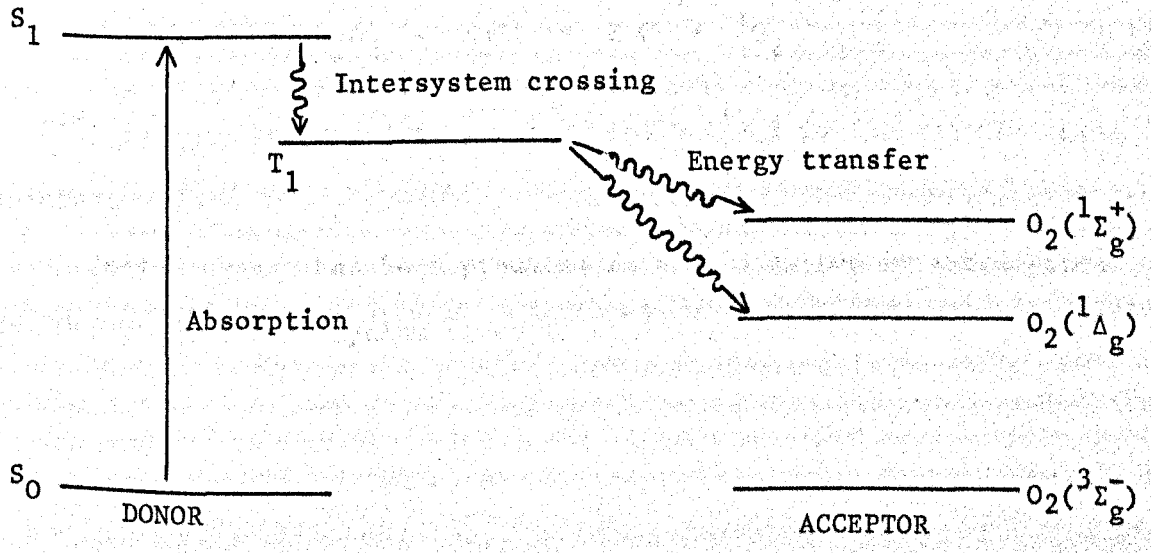

Photosensitized oxygenation reactions, where the singlet oxygen formed reacts with the substrate to form oxygenated products, has been discussed in detail by Gollink[37].

$O_2(^1\Delta_g)$ is formed by electronic energy transfer from excited nitrogen dioxide in mixtures with oxygen, on irradiation between 330 and 700 nm[38,39]. The concentration of $O_2(^1\Delta_g)$ is at a maximum at 390 nm, the first dissociation limit of nitrogen dioxide.

In any system containing $O_2(^1\Delta_g)$, $O_2(^1\Sigma_g^+)$ is always present, but $O_2(^1\Sigma_g^+)$ can be formed alone by vacuum ultraviolet flash photolysis of oxygen at low pressures[40,41,42]. A tuneable dye laser has also been used[43], and more recently $O_2(^1\Sigma_g^+)$ has been formed from the excitation of molecular oxygen by low energy electrons[44].

In solution, singlet oxygen is formed in the reaction of aqueous hydrogen peroxide with sodium hypochlorite[13] or chlorine[45]

$$NaOCl + H_2O_2 \rightarrow NaCl + H_2O + {}^1O_2 \qquad 2.12$$

$O_2(^1\Sigma_g^+)$ is quenched rapidly by water, and $O_2(^1\Delta_g)$ is the only reacting species.

Singlet oxygen has been produced in liquid oxygen by irradiation at 1060 nm from a neodynium glass laser[46].

2.6. Measurement of Singlet Oxygen Concentrations

2.6.1. Physical Methods

Absolute concentrations of $O_2(^1\Delta_g)$ in a flow of molecular oxygen can be determined by isothermal calorimetry[47,48].

Arnold et al[24] measured the heat liberated when $O_2(^1\Delta_g)$ is deactivated on a cobalt wire, the efficiency of deactivation was 95%. Later workers[49,50] used a platinum wire electroplated with cobalt and partially oxidised. The method is not wholly satisfactory, as other excited species in the flow, perhaps $O_2(^1\Sigma_g^+)$, will also be deactivated but with a different efficiency.

A photomultiplier, viewing the emissions from $O_2(^1\Delta_g)$ and $O_2(^1\Sigma_g^+)$ can be calibrated absolutely using the NO + O reaction[23,51] :

$$NO + O \rightarrow NO_2 + h\nu \qquad 2.13$$

This emission has an almost continuous spectrum between 388 nm and 1400 nm, and the light intensity is independent of pressure over a wide range, depending only on the product of the concentrations, [O][NO][52].

A specific method measures the photoionization current produced using an argon resonance lamp at 11.72 eV. This is able to ionize $O_2(^1\Delta_g)$ but not ground state oxygen, ozone or oxygen atoms[53]. A krypton resonance lamp at 10.64 eV is able to ionize both singlet states of oxygen[54]. These methods cannot be used if organic molecules or oxides of nitrogen are present.

Electron paramagnetic resonance spectroscopy has been used to study $O_2(^1\Delta_g)$ concentrations[55,56,57]. Falick et al found that their discharged oxygen contained about 10% $O_2(^1\Delta_g)$[58].

The photolysis of ozone and oxygen mixtures at 253.7 nm forms $O_2(^1\Delta_g)$ as the primary step, $O_2(^1\Sigma_g^+)$ is probably formed by energy trsnsfer from excited oxygen atoms[51,59,60,61,62].

$$O_3 + h\nu(\lambda < 316\ nm) \rightarrow O_2(^1\Delta_g) + O(^1D) \qquad 2.14$$

$$O(^1D) + O_2 \rightarrow O_2(^1\Sigma_g^+) + O(^3P) \qquad 2.15$$

The known quantum efficiency of these two reactions has been used as an internal standard by Gauthier and Snelling in a study of the reaction of nitric oxide with ozone.

2.6.2. Chemical Methods

Any chemical method must be reasonably rapid, specific for singlet oxygen, free from complicating side reactions and have easily analysed products. These criteria are not easily satisfied; for example, the reaction of tetramethylethylene, TME, with singlet oxygen gives a rearranged allylic hydroperoxide which can be detected by gas chromatography[63]:

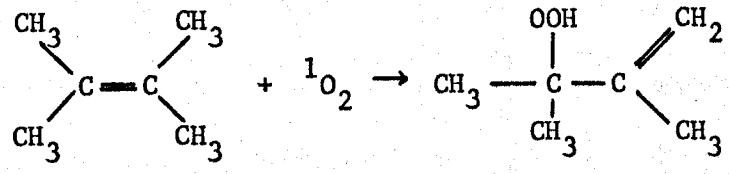

2.16

However, the same product may be formed from ground state oxygen in a chain reaction involving free radicals[64].

Probably best is the 1-4 cyclo addition of singlet oxygen to conjugated dienes[65]:

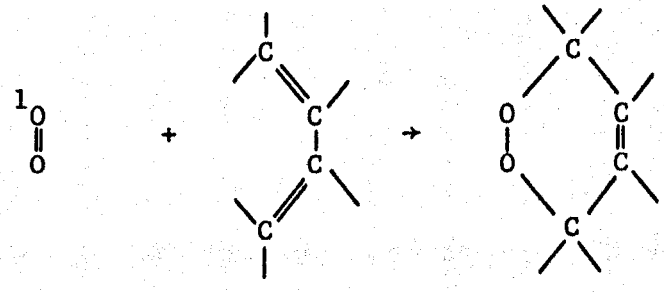

2.17

Most of these methods detect singlet oxygen in the gas phase and cannot be used in solution, though emission spectroscopy may be useful. A novel solution method follows the reaction of singlet oxygen with a

coloured acceptor, 1,3-diphenyl iso benzofuran, to a colourless product[66].

In our system, the absolute concentrations of singlet molecular oxygen generated by the microwave discharge have not been measured, as the results reported in this thesis require only comparative measurements.

2.7. Gas Phase Quenching of Singlet Oxygen

The quenching of singlet oxygen to the ground state without chemical reaction, has been studied with a large number of gases and organic molecules as collision partners at room temperature.

The temperature dependence of collisional quenching has only been studied in a limited temperature range for a few gases. The discharge flow shock tube is an ideal tool to look at collisional quenching over a wide temperature range, and several collision partners have been studied. (Chapter 8)

In an early paper, Ogryzlo[67] suggested that the rapid deactivation of $O_2(^1\Sigma_g^+)$ by most gases forms $O_2(^1\Delta_g)$ which is a spin allowed process; the deactivation of $O_2(^1\Delta_g)$ is much slower.

$$O_2(^1\Sigma_g^+) + M \rightarrow O_2(^1\Delta_g) + M \qquad 2.18$$

He plotted the logarithm of the quenching rate constant against boiling point of the quencher, and although there was only an approximate correlation, no other molecular property yielded a better one.

In a review in Chemiluminescence and Bioluminescence in 1973, Davidson and Ogryzlo[68] plotted the logarithm of the quenching rate constant against the highest fundamental vibrational frequency of the quencher, and found a good correlation for the quenching of both $O_2(^1\Delta_g)$ and $O_2(^1\Sigma_g^+)$ by homonuclear diatomic molecules. For polyatomic quenchers, most rate constants were an order of magnitude higher than predicted, possibly due to the availability of additional vibrational modes in the quencher. (Figure 2.3)

Oxygen, which in this context has a low vibrational frequency is a poor quenching agent. Molecules containing hydrogen tend to be effective quenchers. Water must be excluded from any reaction to be studied as even a few ppm can increase significantly the deactivation rate constant.

Figure 2.3.

Variation of log(Quenching Rate Constant) wit
Highest Fundamental Vibrational Frequency of the Quencher
(from Reference 68

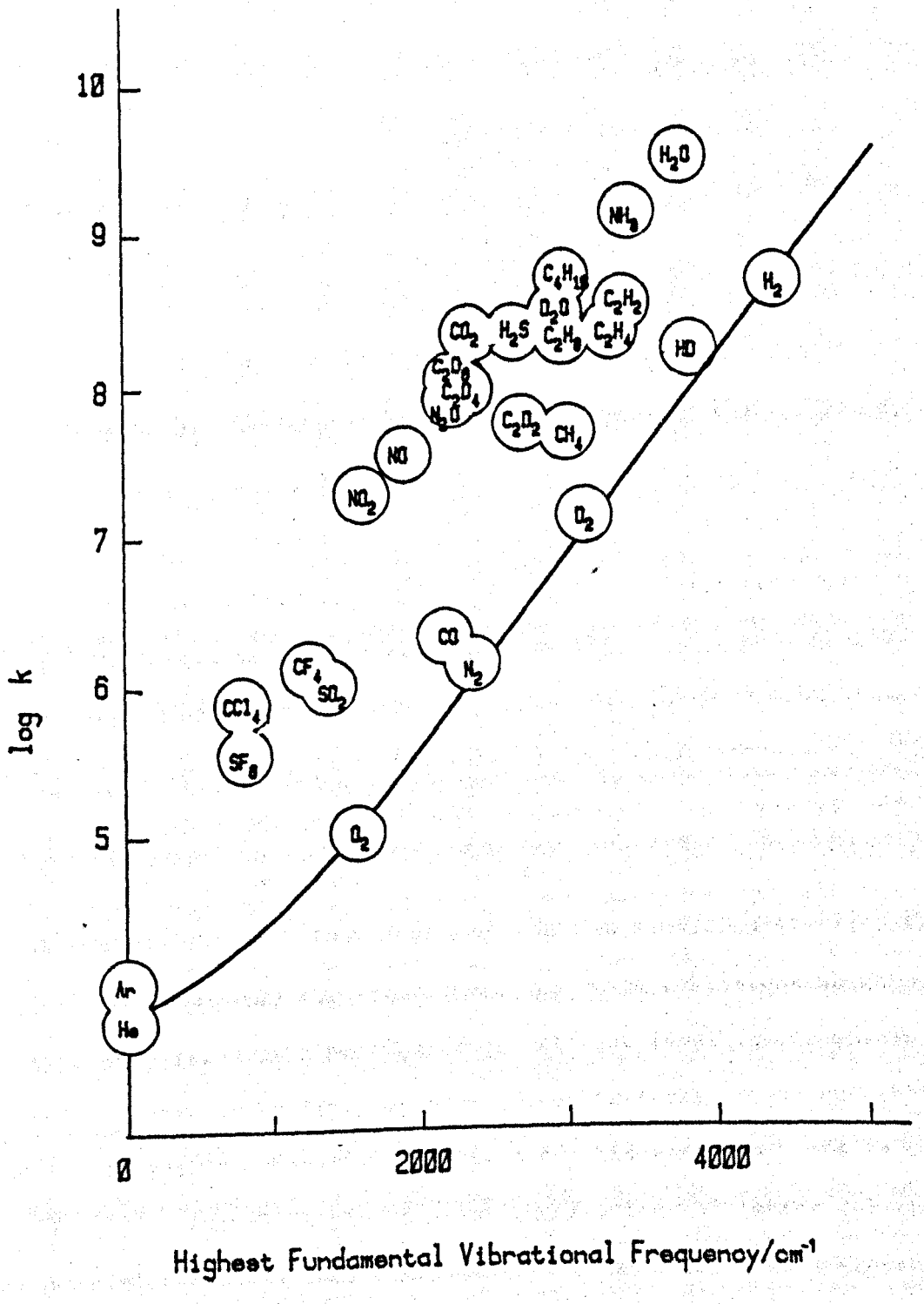

Kear and Abrahamson[69], in a theoretical approach to electronic energy transfer from $O_2(^1\Sigma_g^+)$, calculated quenching cross sections for a variety of diatomic molecules. Their method assumed that energy is transferred under the influence of short range repulsive forces. The calculated values for the quenching constants were roughly an order of magnitude too low for most gases, but for oxygen itself, the theory gave a very much smaller quenching constant than experiment.

Braithwaite, Davidson and Ogryzlo[70] considered the influence of long range forces in the quenching of $O_2(^1\Sigma_g^+)$ by diatomic molecules. Their calculated values agree quite well with experiment, but they too were unsuccessful with oxygen.

On looking at the temperature dependence between 173 and 393 K, of the quenching of $O_2(^1\Sigma_g^+)$ by hydrogen[71] and hydrogen bromide[72], they came to the conclusion that although long range multipolar interactions make a major contribution to the quenching, short range repulsive interactions also contribute. A sum of the two theoretical rate constants best fit the experimental results. These calculations show that the main contribution to the quenching rate is from those processes which convert the maximum amount of energy into vibration, and the minimum amount into translation and rotation of the product.

Thomas and Thrush[73] looked at quenching rates with a statistical theory. They compared the fraction of quenching collisions which result in population of a particular vibrational level in the quencher[74], with a calculated probability of the particular level of the quencher being populated; the negative logarithm of this ratio is known as the surprisal. A surprisal plot against the fraction of energy released going into vibration, showed a linear relationship for a wide variety of simple gases for the quenching of both $O_2(^1\Sigma_g^+)$ and $O_2(^1\Delta_g)$.

They suggested, on this evidence, that although energy goes preferentially into vibration of the products, resonant transfer is not important, and they favoured a common non specific mechanism where quenching occurs on the repulsive part of the inter-molecular potential.

The temperature dependence for collisonal quenching of $O_2(^1\Delta_g)$ and $O_2(^1\Sigma_g^+)$ is needed to help to distinguish between the roles of long range attractive interactions, and the short range repulsive interactions.

2.8. Decay of Singlet Oxygen in Solution

Merkel and Kearns[75] proposed that the major pathway for radiationless decay of the $^1\Delta_g$ state in solution is by conversion of electronic energy from the oxygen directly into vibrational excitation of the solvent. The quenching efficiency of the solvent can be related to its infrared overtones and absorption bands in the energy regions of the $O_2(^1\Delta_g) \leftarrow O_2(^3\Sigma_g^-)$ transitions. They list the lifetimes of the $O_2(^1\Delta_g)$ molecule in various solvents[66], and discuss temperature dependence and solvent effects[76].

2.9. Some Reactions of Singlet Oxygen with Organic Molecules

The reactions reported in the literature concern $O_2(^1\Delta_g)$.

$O_2(^1\Delta_g)$ adds to unsaturated hydrocarbons forming endoperoxides:

e.g. 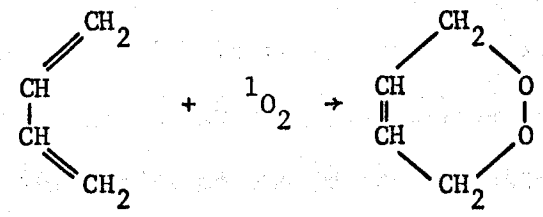 2.19

This is similar to the Diels Alder reaction, but the reaction is much faster[77].

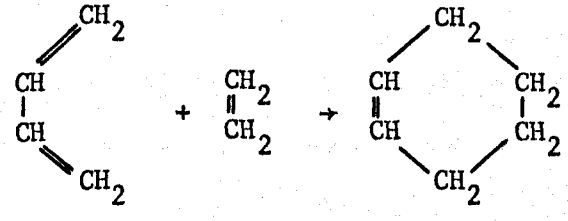 2.20

The rate constants for some of these reactions have been measured; they increase with the number of alkyl groups on the olefin, but decrease as the alkyl groups get larger[78].

A study of the reaction of $O_2(^1\Delta_g)$ with tetramethylethylene by electron paramagnetic resonance spectroscopy shows that the rate of chemical reactions is much faster than any deactivation process[79].

Two books have recently been published on the reactions of singlet oxygen with a wide variety of organic compounds[80,81]. They are both largely devoted to reactions of $O_2(^1\Delta_g)$ in solution. A recent review by Bellus considers quenching of $O_2(^1\Delta_g)$ in solution[82]. These reactions will not be considered here.

2.10. Singlet Oxygen in the Atmosphere

Singlet oxygen is known to exist in both the upper and lower atmosphere, and most of the earlier work on gas phase kinetics of singlet oxygen was performed in order to elucidate the mechanisms by which it is formed, in which it takes part, and also to assess the concentrations necessary to produce the observed bands in the air glow[23,83]. The infrared atmospheric and atmospheric bands have been observed at high altitudes[84], and Vlasov[85] shows plots of the height distribution of excited species present in the atmosphere. The intensities of the two band systems differ from daytime to nighttime, suggesting that the excitation of molecular oxygen may well be photochemical, though the concentration of singlet oxygen present is too large to have been formed by the absorption of solar radiation by oxygen alone[86].

The role of singlet oxygen in poluted atmospheres[87] is not completely understood, but it is certainly important in many oxydation reactions forming unwanted and unpleasant intermediates. The vast literature in this field will not be discussed further here.

Chapter 3

The Discharge Flow Shock Tube

3.1. Introduction

Shock tubes have been used for many years to study vibrational relaxation, and reactions of excited intermediates formed in the shock wave. In the discharge flow shock tube, excited molecules and atoms are formed in the gas before the shock.

In 1966, Hartunian, Thompson and Hewitt[88] developed a glow discharge shock tube to study the chemiluminescence of the reactions of oxygen atoms with carbon monoxide and nitric oxide; and although the system gave encouraging results, not much interest was shown in the technique. In 1968 a discharge flow shock tube was built here at the University of Keele to look at the reactions of nitrogen atoms at high temperatures[89]. Gross and Cohen looked at the temperature dependence of the afterglow from nitrogen[90], nitric oxide[91] and sulphur dioxide[92], and recently Breen, Quy and Glass have studied the vibrational relaxation of oxygen in the presence of oxygen atoms[93], and hydrogen in the presence of hydrogen atoms[94].

The combination offers a large temperature range for reactions studied in a discharge flow system, but the method has certain limitations.

The reactions of the excited intermediates have to be slow at room temperature, so that they exist for long enough in the pre-shock flowing gas to be present in the shock tube. The rate of the reactions at the high shock temperature must be fast enough for them to be measured within the hot flow time behind the shock front; the total uniform heating time is less than 1 ms. Signal averaging techniques available for small but

repetitive signals cannot, of course, be used. The results show the scatter inherent in shock tube measurements.

In this chapter, the apparatus is described together with the tests carried out on it. These tests are necessary to assure ourselves that each part is working satisfactorily, and that meaningful kinetic results can be obtained from such a system. The chapter concludes with the procedure to obtain a result from a shock experiment.

A general view of the apparatus can be seen in plates 1 and 2, and a schematic diagram is shown in figure 3.1.

Plate 1

The Discharge Flow Shock Tube, looking towards the driver section

1. Delivery system for driver gases
2. Driver section of shock tube
3. Oil diffusion pump
4. Diethylphthalate filled manometer
5. Pressure controller
6. Flowmeter
7. Needle valve
8. Cleaning column filled with molecular sieve
9. Cooled trap
10. Transient recorders
11. Low pressure section of shock tube.

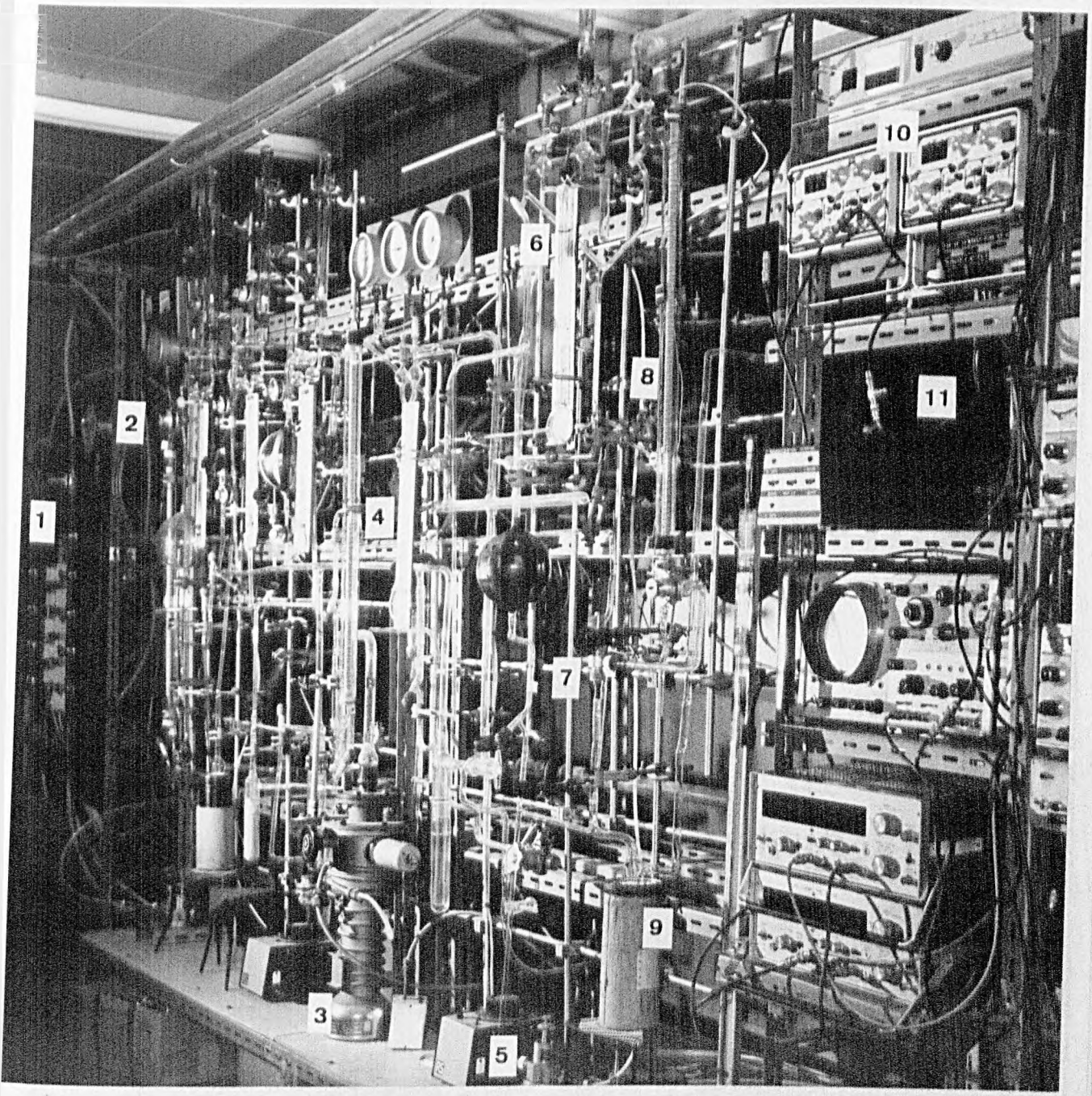

Plate 2

The Discharge Flow Shock Tube, looking towards the Discharge Section

1. Power supply for photomultipliers
2. Transient Recorders
3. Low Pressure Section of Shock Tube
4. Time Interval Meters
5. Discharge Cavity inside black box
6. Photomultiplier Housing
7. Paper Tape Punch
8. Microtron Unit
9. Digital Voltmeter
10. Light screen photomultipliers

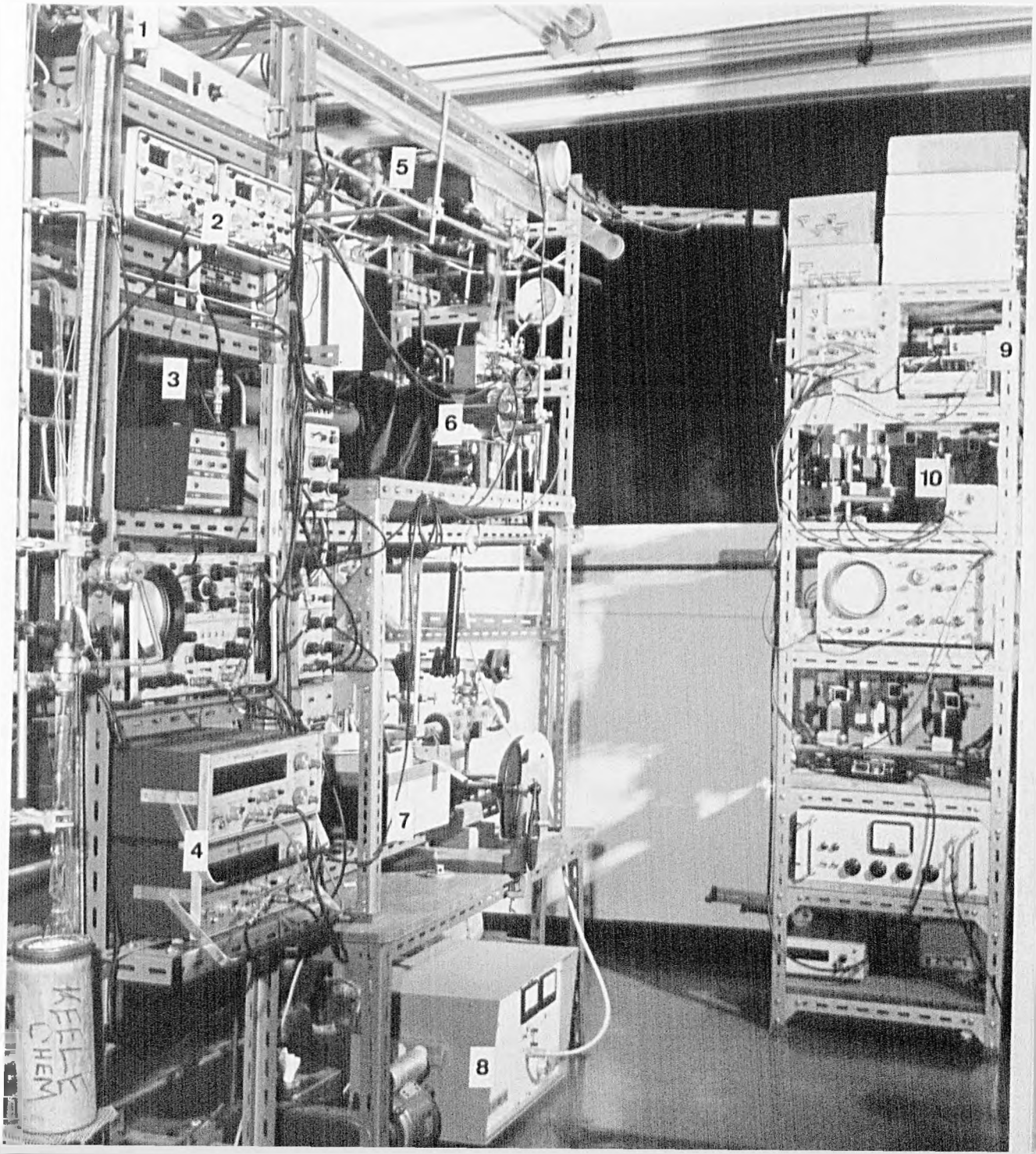

Figure 3.1. A Schematic Diagram of the Apparatus.

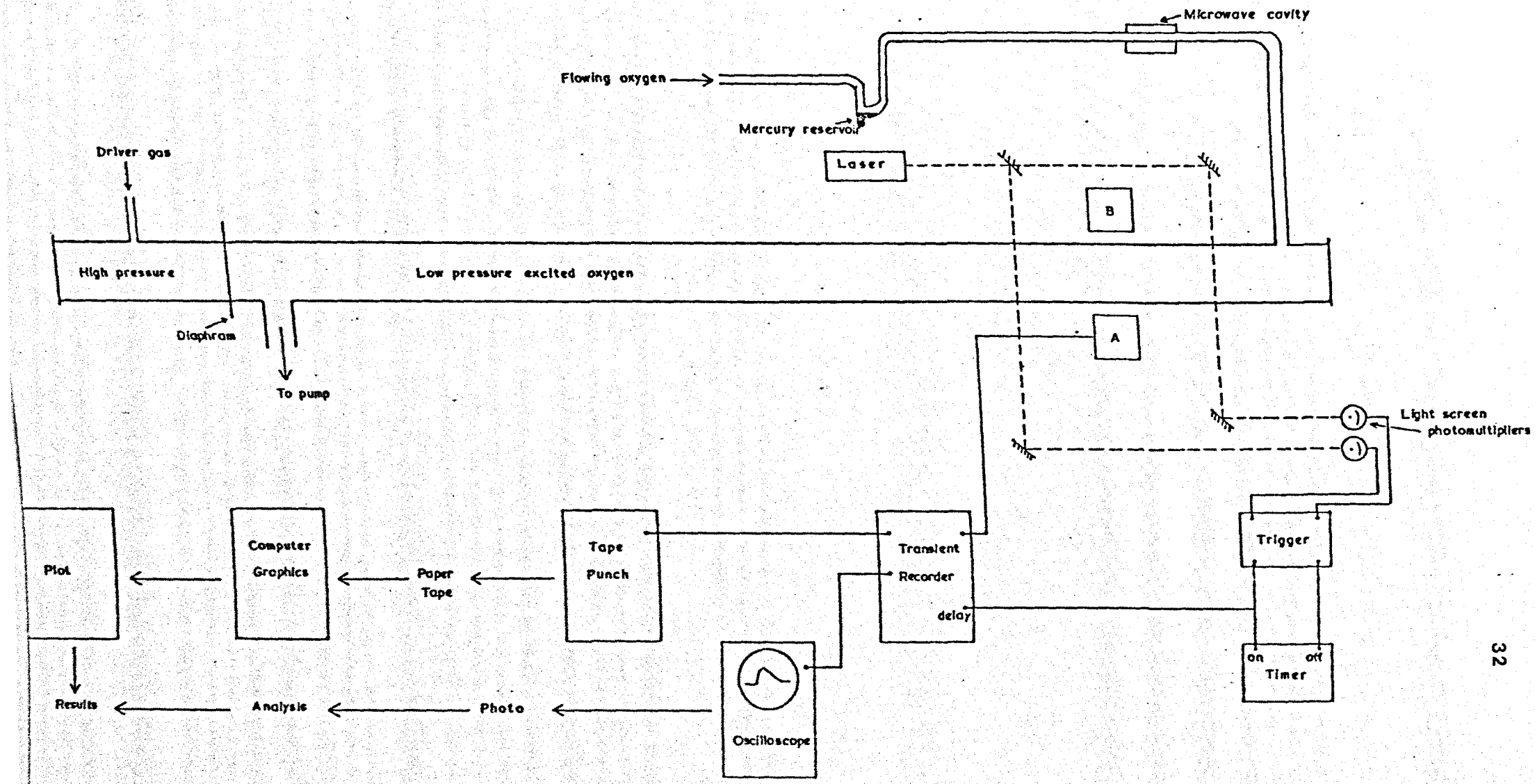

3.2. The Discharge Flow Apparatus

The test gases, after purification, flow through a microwave discharge and then into the shock tube. The flow of gas along the shock tube is maintained by a water cooled pump (Edwards ISC 3000) situated in the basement of the building, and connected to the apparatus by 35 mm o.d. copper tubing.

The gas handling apparatus is built on a frame (2.5 m x 1.75 m) attached to the shock tube framework, and can be evacuated with an oil diffusion pump (N.G.N.) backed by a rotary pump (Edwards ED 35).

Figure 3.2 shows the glassware system for introducing the purified gas into the shock tube at a measured flow rate. All the taps used are of a greaseless rotaflow type (Corning-Quickfit).

The gas is delivered from a cylinder through a pressure controller (Edwards VPC 1) which maintains the pressure in the glass sytem at 720 mm Hg (96 kPa). The flow rate into the discharge section and shock tube is regulated with a stainless steel needle valve (Edwards) and measured with a calibrated capillary flowmeter. The gas is dried, and any hydrocarbon impurities are removed, by flowing it through a column filled with molecular sieve (type 4A). The sieve is regularly regenerated and dried by heating it to 473 K with an 'in situ' heating coil, and flowing gas through it to sweep out the moisture, which is collected outside the apparatus.

On the low pressure side of the needle valve, the gas flows through a packed trap (molecular sieve, type 4A) at 77 K.

Three identical flow systems are built into the framework to handle the different test gases (nitrogen and argon). Only oxygen flows through the discharge, nitrogen and argon combine with the oxygen flow past the discharge.

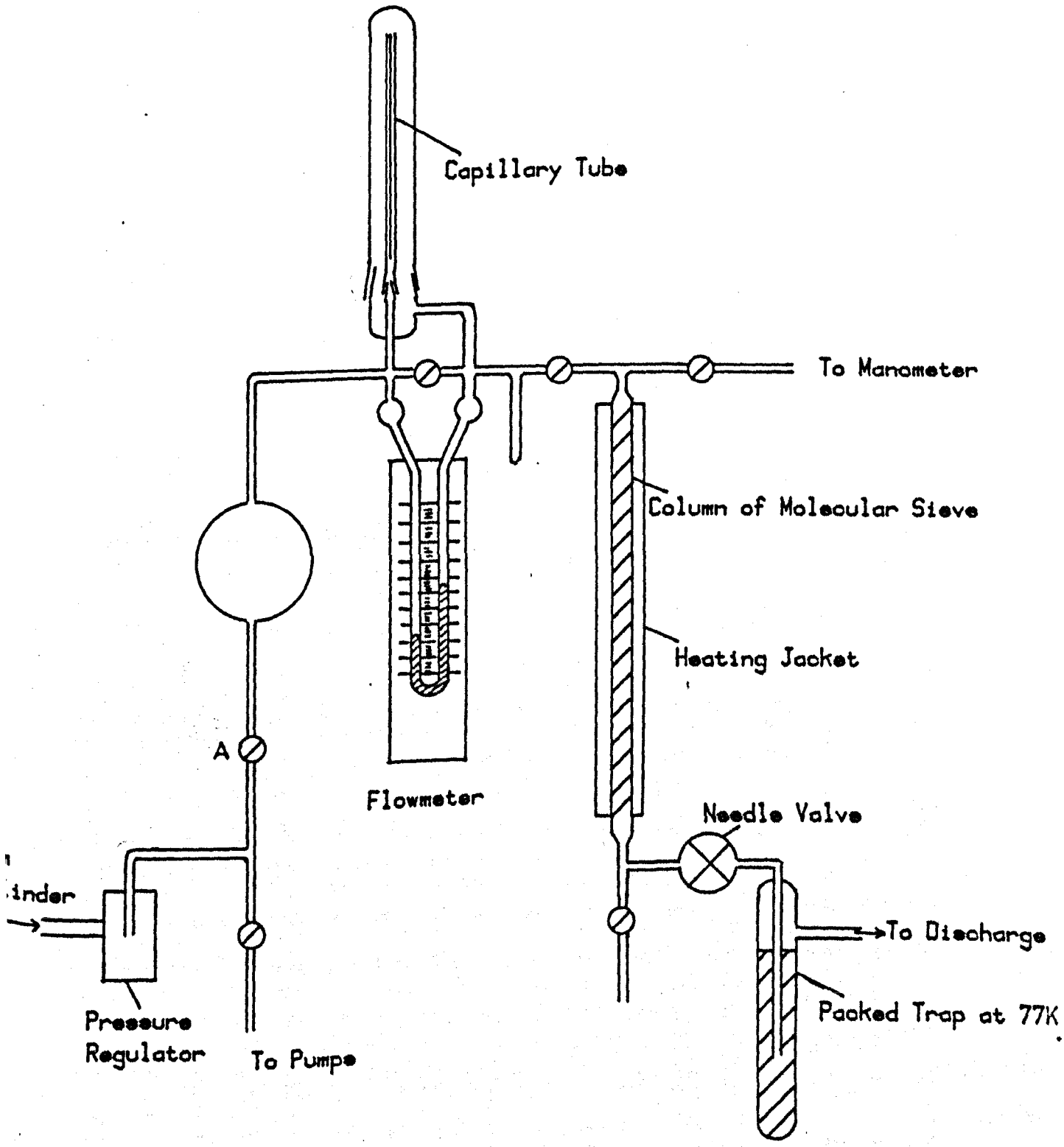

Figure 3.2.

A Flow System for Purifying and Regulating the Gases

The oxygen used in this work is obtained from B.O.C. and is normal industrial grade, being at least 99.5% oxygen; the main impurities are argon and nitrogen, any other impurities are less than 0.01%. Nitrogen (white spot) and argon are also obtained from B.O.C.

The oxygen is saturated with mercury before it enters the discharge section. The mercury bubbler arrangement can be seen in figure 3.8. The end of the inlet tube is just clear of the mercury surface, and the flow of oxygen clears away the surface film of mercuric oxide which is unavoidably blown back after each shock. The bubbler can be cleaned and refilled with fresh mercury when necessary.

3.2.1. The Microwave Discharge

Microwave energy is generated in a magnetron, which is basically a vacuum tube operating in a magnetic field. The magnetron is run from a Microtron 200 unit (Electro Medical Supplies), and the microwave energy is conveyed to a gas discharge cavity (type 214L, E.M.S.) shown in figure 3.3. The discharge cavity is fitted on to the discharge section, which is a 300 mm length of quartz tubing (10 mm i.d.) between the mercury bubbler and the shock tube.

When a microwave field is applied across a gas, electrons in the gas are accelerated, and as the field direction changes, the direction of force on the electron changes, so the electron is made to oscillate within the cavity. The energy gained by the electron in the field can be transferred to molecules in the gas on collision. If the energy of the electron is above the excitation energy of the molecules, energy transfer can yield excited molecules[95]. The use of microwave frequencies to excite a discharge in a gas was first used by Meggers[96].

Most of our experiments were performed with a microtron power of 100 watts but some runs were performed at 40, 60 and 80 watts to test the system. Lower powers were used for the room temperature measurements at low pressures (Chapter 5).

Figure 3.3. The Discharge Cavity. (E.M.S. type 214L)

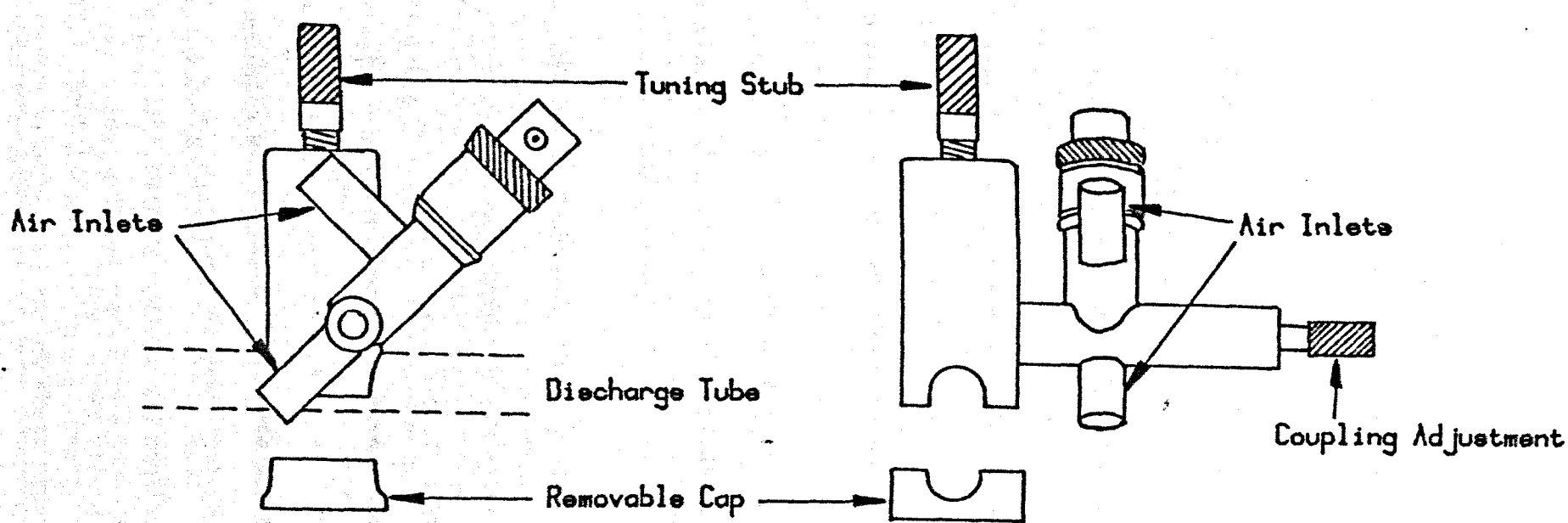

When the generator power was set at 100 watts, the power reflected back to the magnetron was 7 watts, and taking into account losses along the cable this gives the actual power discharged at the cavity as between 75 and 80 watts.

A graph of dimol emission intensity at 634 nm from $O_2(^1\Delta_g)$ against microtron power is shown in figure 3.4. The range of our experiments is within the linear section; above 130 watts, the emission intensity begins to fall, and below 25 watts, the reflected power rises rapidly until the discharge becomes unstable and finally dies.

A microwave discharge in oxygen produces oxygen atoms, as well as the singlet excited states. The oxygen atoms react with mercury in the oxygen flow and mercuric oxide is deposited on the walls of the discharge tube downstream of the discharge cavity.

The effectiveness of the mercury for removing all the oxygen atoms was tested by adding nitric oxide to the discharged gas (section 2.5. and 2.6.1.).

$$NO + O \rightarrow NO_2 + h\nu \qquad 3.1$$

The eye is very sensitive to the yellow green emission produced by the nitric oxide titration, but no glow was observed where the flowing gas enters the shock tube. A small glow was observed when the microtron power was raised above 120 watts.

No increase in emission was observed by a photo-multiplier with a 547 nm filter, above the background emission from excited oxygen, for microtron powers of 100 watts and less, and it was concluded that the mercury was effective in removing all oxygen atoms before the region of measurement, for the conditions used during shock experiments.

Figure 3.4. Variation of Emission Intensity with Microtron Power.

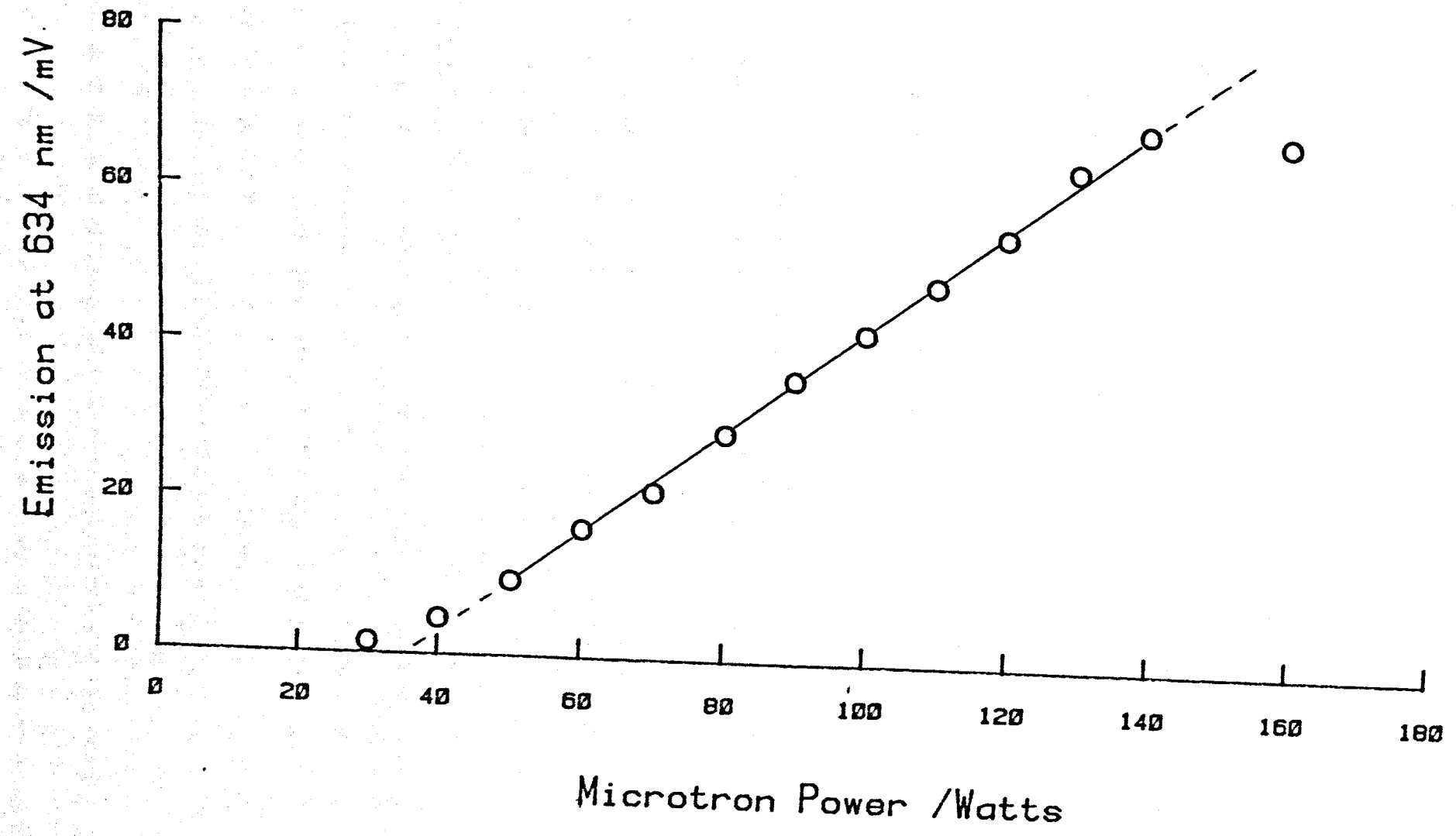

3.2.2. The Capillary Flowmeters

Capillary flowmeters, filled with diethylphthalate, are used to measure the flow of the gases. They are calibrated with oxygen, and the rate of flow of nitrogen and argon is calculated from the flowmeter readings and relative viscosities.

The rate of flow of a gas through a cylind-rical tube is inversely proportional to its viscosity (Poiseuille's Law).

$$\phi_{N_2} = \phi_{O_2} \frac{\eta_{O_2}}{\eta_{N_2}} \qquad 3.2$$

where ϕ_{O_2} is the flow rate of oxygen and η_{O_2} is its viscosity. Values of viscosities at 295 K are used in the calculations and are interpolated from the values below.

	Viscosity/10^{-5} kg m^{-1} s^{-1}		
T/K	273	293	298
Oxygen	1.91	2.03	2.08
Nitrogen	1.67	1.76	1.78
Argon	2.08	2.23	2.27
References	97	97	98

3.2.3. Calibration Procedure

The volume of the shock tube test section, together with the oxygen flow system up to tap A (figure 3.2) was measured by expanding a known volume of air at atmospheric pressure into the evacuated system, and noting the final pressure.

The calibration was made by measuring the pressure rise in the system after a given time, at various flowmeter readings. The time was chosen so that the increase in pressure in the system was too small to affect the flow rate appreciably. The stop watch was started as

the regulating valve at the end of the shock tube (figure 3.8) was shut, and stopped when the oxygen flow was switched off at tap A (figure 3.2). The needle valve was fully opened to allow the pressure to adjust quickly, and a final pressure reading taken. A zero pressure reading was subtracted from each result, as the pressure in the oxygen flow system is maintained at 720 mm Hg throughout the experiments. The flow rate can be calculated from the measured pressure difference and the length, ℓ, and bore, radius r, of the capillaries used in the flow-meters using Poiseuille's formula[99] :

$$\phi = \frac{\pi}{16\eta} (P_1^2 - P_2^2) \frac{r^4}{\ell} \qquad 3.3$$

where P_1 and P_2 are the pressures at the beginning and end of the capillary. The actual measured flow rates were only in approximate agreement with the calculated flow rates, possibly due to end effects and irregularities in the bore, and the calibration curves were always used.

3.3. The Shock Tube

The shock tube is a device to generate a shock wave. In our system, high pressure driver gas in a stainless steel tube, is separated from the low pressure test gas in a pyrex tube, by an aluminium diaphragm. When the diaphragam bursts, a shock wave is propagated into the test gas, heating and compressing it.

3.3.1. Formation of a Shock Wave

The build up of a shock wave can best be visualized by considering a piston travelling into a gas, accelerating from rest to a constant velocity, v, which is greater than the speed of sound in the gas, a. For a small increment, dv, in the velocity of the piston, a weak compression is propagated into the gas, travelling at velocity, a, a second increment in piston velocity will propagate a second compression at a slightly faster velocity, $a + da$, into the gas heated by the first compression. A third increment will propagate a faster compression and so on. The compression waves coalesce to form a shock wave travelling at velocity w_s, which will be greater than the piston velocity v. Between the shock front and the piston, there is a column of gas of increasing length which has been heated by the shock wave, it is in this region that measurements are made[100].

A distance-time diagram for a shock tube is shown in figure 3.5. In a gas driven shock tube, the contact surface is between the heated test gas and the cold expanding driver gas which acts as the piston. As the driver gas expands into the test section, a rarefaction wave travels in the opposite direction; increasing rarefactions travel into increasingly colder gas and fan out into the driver section.

When the shock wave meets the end of the shock tube, it is reflected back into the shock heated gas, heating it further. The rarefaction head is also reflected by the end of the driver section, and accelerates

Figure 3.5. A Distance versus Time Diagram for a Shock Tube.

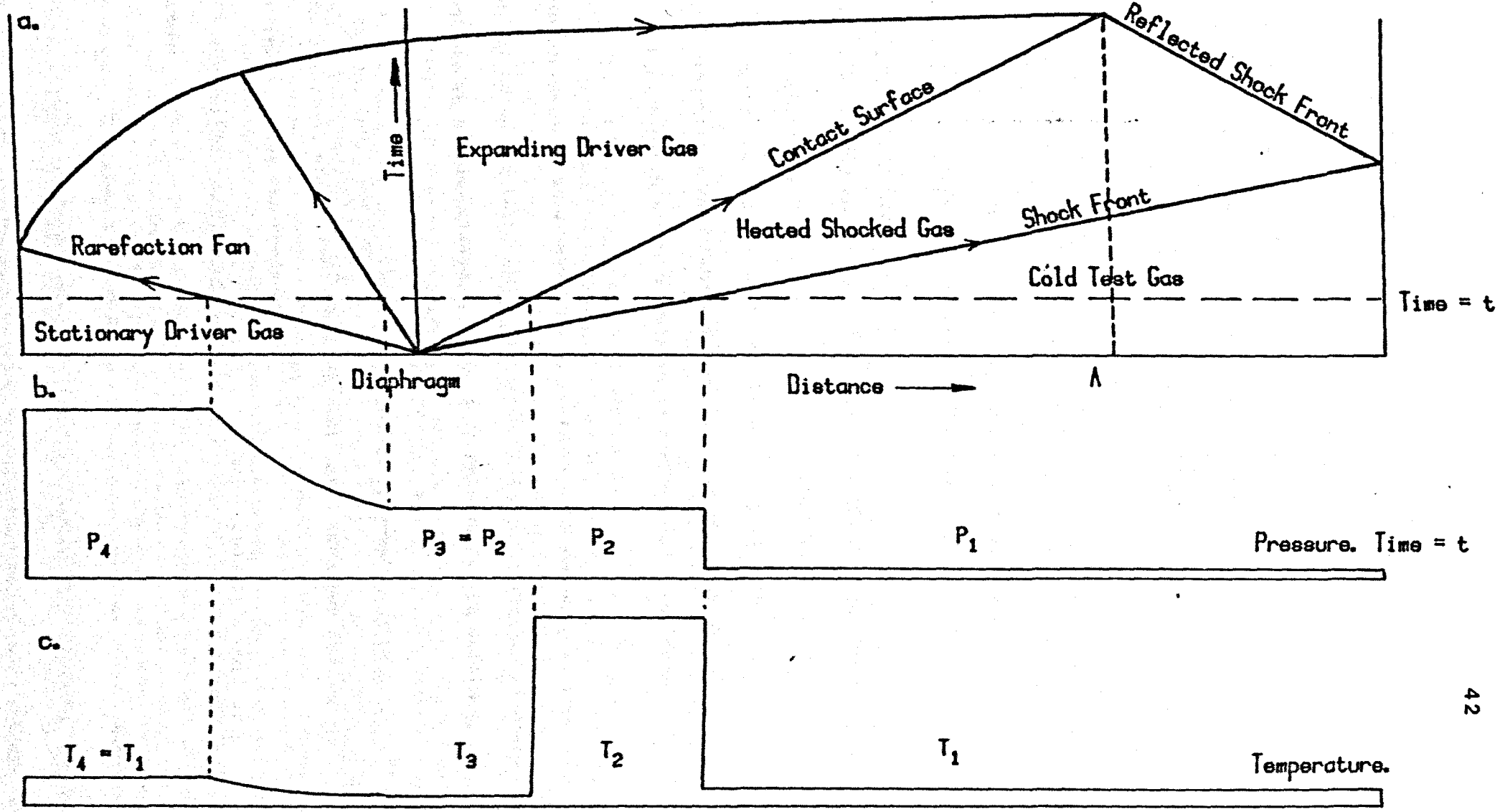

as it passes through the fan, eventually travelling faster than the shock front. Whether the reflected rarefaction overtakes the contact surface before it meets the reflected shock depends on the length of the shock tube for a given shock speed. Measurements are made in the shock heated gas between the shock front and the contact surface; the time in which measurements can be made is the hot flow time and is at a maximum at point A along the tube (figure 3.5); this is the ideal position for the observation station.

The variation of pressure and temperature with distance at time, t, after bursting the diaphragm is shown in figures 3.5b and 3.5c.

3.3.2. The Shock Equations

The pressure and temperature changes in the shocked gas behind the shock front can be measured with pressure transducers and temperature gauges[101], but it is usually more convenient to measure the speed of the shock front, then calculate the conditions in the test gas.

The shock equations are formulated in shock fixed coordinates, where the shock front is assumed to be stationary, and the test gas to be moving towards it at a velocity, u, equal to $-w_s$, where w_s is the measured speed of the shock front. (Figure 3.6) The density, pressure and temperature are designated ρ, P and T respectively, the suffixes, 1 for the unshocked test gas, 2 for the shocked gas, 3 for the driver gas in motion, and 4 for the stationary driver gas, are used throughout.

The equations are derived assuming that mass, momentum and energy are conserved across the shock front[102].

For concentration of mass, consider the mass crossing a unit area per second:

$$m = \rho_1 u_1 = \rho_2 u_2 \qquad 3.4$$

Figure 3.6.

Change of Laboratory Coordinates to Shock Coordinates

to formulate Shock Equations

(a) Laboratory Coordinates

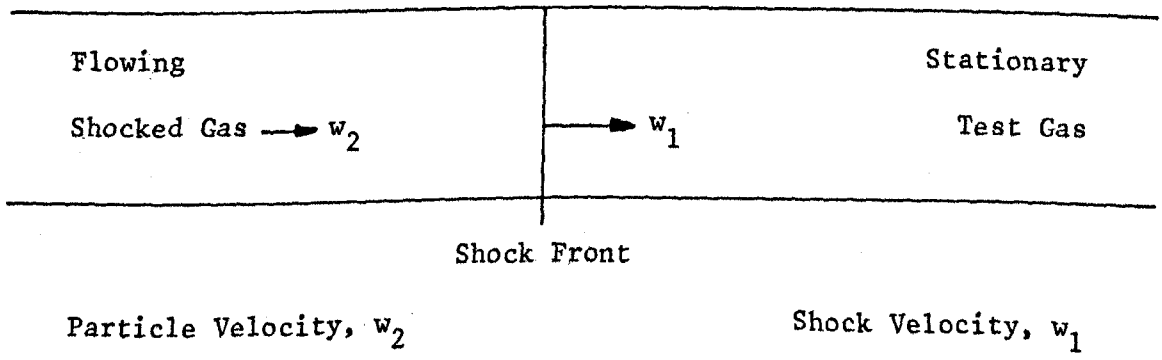

(b) Shock Coordinates

Consider movement of gas across planes A and B

either side of stationary shock front

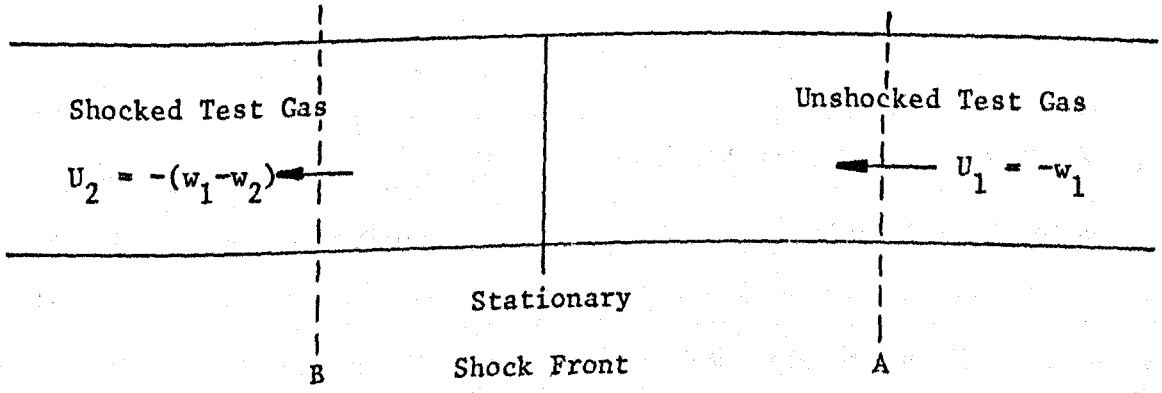

For conservation, the decrease in momentum per unit area per second is equal to the increase in pressure:

$$m u_1 - m u_2 = P_2 - P_1 \qquad 3.5$$

and from equations 3.4 and 3.5

$$\rho_1 u_1^2 - \rho_2 u_2^2 = P_2 - P_1 \qquad 3.6$$

For conservation of energy, the decrease in kinetic energy per unit area per second equals the increase in enthalpy of the gas:

$$\tfrac{1}{2} m u_1^2 - \tfrac{1}{2} m u_2^2 = H_2 - H_1 \qquad 3.7$$

and for unit mass:

$$\tfrac{1}{2} u_1^2 - \tfrac{1}{2} u_2^2 = h_2 - h_1 \qquad 3.8$$

where h is the enthalpy per gram of substance.

Equations 3.4, 3.6 and 3.8 are known as the Rankine-Hugoniot relationships.

For an ideal gas, c_p and c_v, the gram specific heats of the gas at constant pressure and constant volume, are independent of temperature and:

$$h = c_p T = \left[\frac{\gamma}{\gamma-1}\right] RT \qquad 3.9$$

where $\gamma = c_p/c_v$

Assuming the equation for an ideal gas:

$$p = \rho RT, \qquad 3.10$$

the density ratio across the shock front can be found by rearrangement:

$$\frac{\rho_2}{\rho_1} = \left\{ \frac{(\gamma+1)}{(\gamma-1)} \frac{P_2}{P_1} + 1 \right\} \Big/ \left\{ \frac{\gamma+1}{\gamma-1} + \frac{P_2}{P_1} \right\} \qquad 3.11$$

and similarly the ratios P_2/P_1 and T_2/T_1.

These equations can be solved for the post shock conditions by using the shock speed usually expressed as a mach number M :

$$M = \frac{u_1}{a_1} \qquad 3.12$$

where a_1 is the speed of sound in the test gas,
or for shocks into a stationary test gas

$$M = \frac{w_s}{a_1} \qquad 3.13$$

where w_s is the measured speed of the shock front.

Substituting M in the equations for the ratios gives :

$$\frac{\rho_2}{\rho_1} = \frac{(\gamma+1)M^2}{(\gamma-1)M^2+2} \qquad 3.14$$

$$\frac{P_2}{P_1} = \frac{2\gamma M^2 - (\gamma-1)}{\gamma+1} \qquad 3.15$$

and

$$\frac{T_2}{T_1} = \frac{[\gamma M^2 - (\gamma-1)/2]\,[(\gamma-1/2)M^2 + 1]}{[(\gamma+1)/2]^2 M^2} \qquad 3.16$$

3.3.3. Real Gases

The shock equations calculate conditions behind the shock front for ideal gases. For a real gas, when the temperature rises, the translational and rotational degrees of freedom attain equilibrium within about 10^{-8} s., but the attainment of equilibrium within the vibrational levels is much slower. The enthalpy of the gas is changing as the

vibrational degrees of freedom relax, and h is no longer a linear function of temperature. The shock equations cannot now be solved explicitly, and an iterative procedure is used.

The conditions behind the shock front are calculated by computer for our system in a program called DISHOCK, adapted from Millikan[103]. The frozen conditions are listed from equations 3.14, 3.15 and 3.16, and used as initial values in the calculation of the relaxed conditions by an iterative procedure at each shock speed. A polynomial equation is formed for the enthalpy variation with temperature, from values taken from the JANAF tables[104] and the coefficients of this equation are used in the iteration.

The temperature, pressure and density ratios for oxygen are plotted in figure 3.7 against Mach number; both the frozen and relaxed conditions are shown.

3.3.4. Shock Tube Design

In a normal laboratory, without special buildings for a shock tube, the maximum length of the tube will be governed by the size of the room, and must be at least 1 m. less than the length of the room to facilitate changing the diaphragm and cleaning the tube.

The driver section needs to be strong enough to withstand the high driver gas pressures, long enough for the rarefaction fan not to catch the shock front too early, but not too long to give too high a residual pressure in the test section likely to damage it or the instrumentation.

The inside of the test section must be smooth and, as far as possible, free from entry ports. These should be placed as near as possible to the ends of the test section where they will interfere least with the passage of the shock front, and the flow of the test gas.

The position of the observation station is very important for the best use of a shock tube in studying reactions behind the shock front.

Figure 3.7. Temperature, Pressure and Density Ratios for Oxygen against Mach Number.

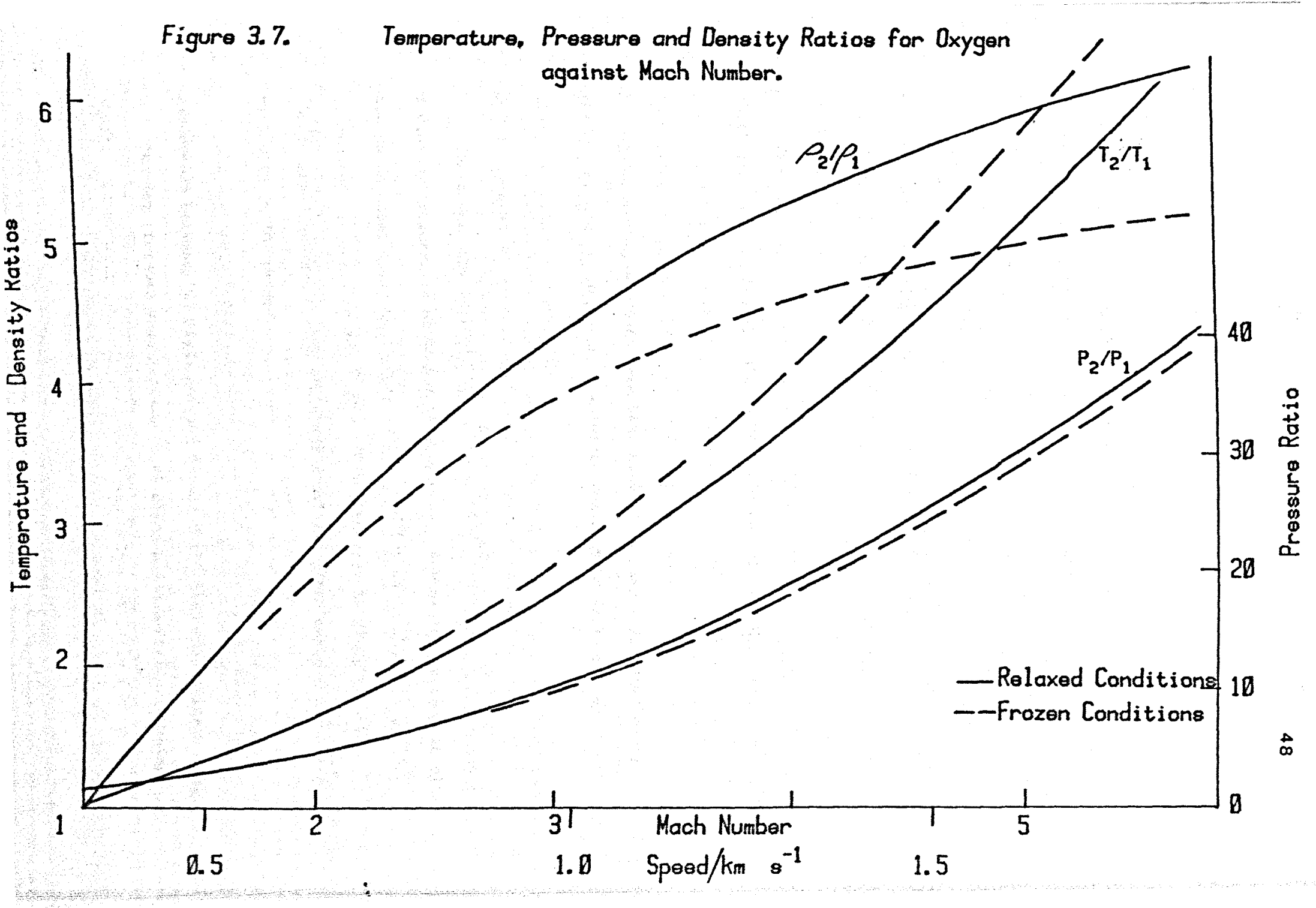

The ideal position is where the hot flow time is at a maximum (position A in figure 3.5); normally the observation station is between 50 and 100 tube diameters from the diaphragm.

It is possible to calculate the length of the test section from the diaphragm to the observation station for a given Mach number and the required observation or hot flow time, from equations in Gaydon and Hurle[105]. (Appendix I) For a shock of Mach 5, using a helium driver into oxygen, the minimum length calculated for the test section is 3.27 m for an observation time of 500 μs. The minimum driver section length is 1.12 m.

The build up of a boundary layer between the cold walls of the shock tube and the heated shocked gas affects the flow duration, and real gas effects shorten the hot flow time, so the actual observation time is cut to about a half for this length of tube.

Boundary layer effects are less serious in larger diameter tubes, but the larger the diameter, the longer the tube needs to be, so the design is always a compromise.

3.3.5. Apparatus

The shock tube is built on a "Handy Angle" framework (6.4 m x 2.1 m x 0.42 m), figure 3.8 shows the arrangement. The driver section is of stainless steel (3.75 mm thick), constructed for us in the University Workshops; it rests on vee shaped rollers and can be drawn back to change the diaphragm. The stainless steel end plate makes a gas tight seal with an 'O' ring.

The diaphragm section is also of stainless steel, the diaphragm is sandwiched between 'O' rings and the hinged bolts tightened (figure 3.9).

The low pressure test section is of pyrex glass pipeline (Corning--QVF); the main section (15 feet long) was made especially for us to maintain a smooth surface. The sections are bolted together with PTFE

Figure 3.8. The Discharge Flow Shock Tube Apparatus.

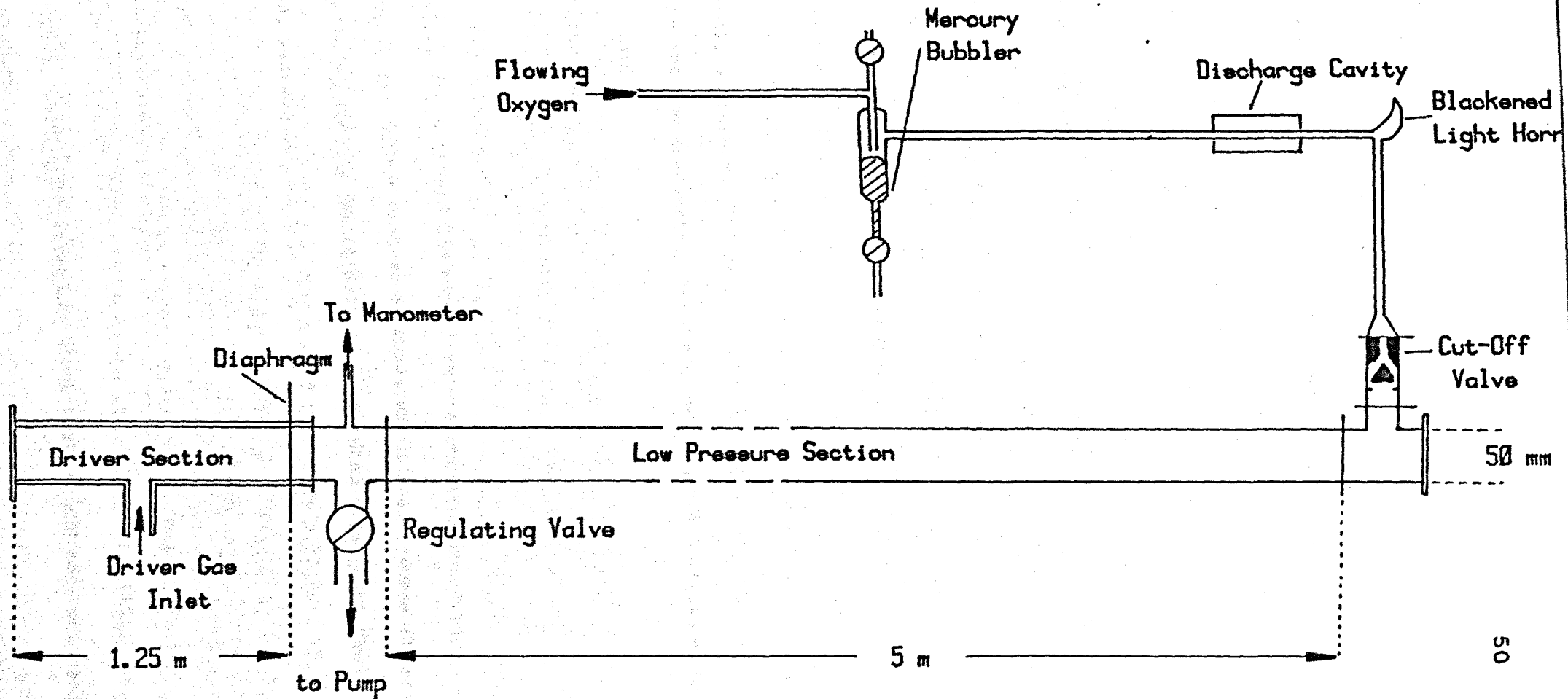

inserts to provide leak tight joints, but, care was necessary in tightening the bolts to avoid cracking the glass.

The discharge section is protected from the shock wave by a cut-off valve (figure 3.8) which closes as the shock front lifts the moveable plug. The valve is effective in preventing the mercury from being blown back into the trap and needle valve, and stopping pieces of diaphragm material from reaching the discharge cavity. However, mercuric oxide is blown back into the mercury bubbler as the pressure equilibrates.

The pressure in the test section is adjusted with a PTFE regulating valve (Corning-QVF) at the outlet to the main pump. The pressure is measured with a pumped di-ethylphthalate manometer; the specific gravity of the di-ethylphthalate was measured as 1.1136×10^3 kg m^{-3}.

The pressure gradient along the tube was measured with two dial gauges, one at each end, and except for very fast flow rates (> 30 ml s^{-1} at atmosphere), or at pressures greater than 10 torr, there was no difference in the two readings. All shock experiments were performed within these limits.

The driver gases, either helium (Gas and Equipment Ltd.) or nitrogen (B.O.C. - white spot), are delivered from their cylinders by high pressure regulators (B.O.C. type OR 14), and cleaned and dried by passage over molecular sieve (type 4A and 13X mixed) before entering the driver section. The pressure in the driver section is measured on a dial guage (Budenburg).

Aluminium diaphragms (Multifoil Ltd.) are used throughout these experiments, various thicknesses being used to obtain different shock speeds. The aluminium bursts cleanly, sending some fragments into the shock stream, but most petalling back out of the way. The shock speeds for a given thickness were reproducible for the same downstream pressure.

Melanex diaphragms (I.C.I. Ltd.) were also tried, but these stretched before bursting, leading to irregular shock speeds, and were not used in these experiments.

Figure 3.9. The Position of the Diaphragm.

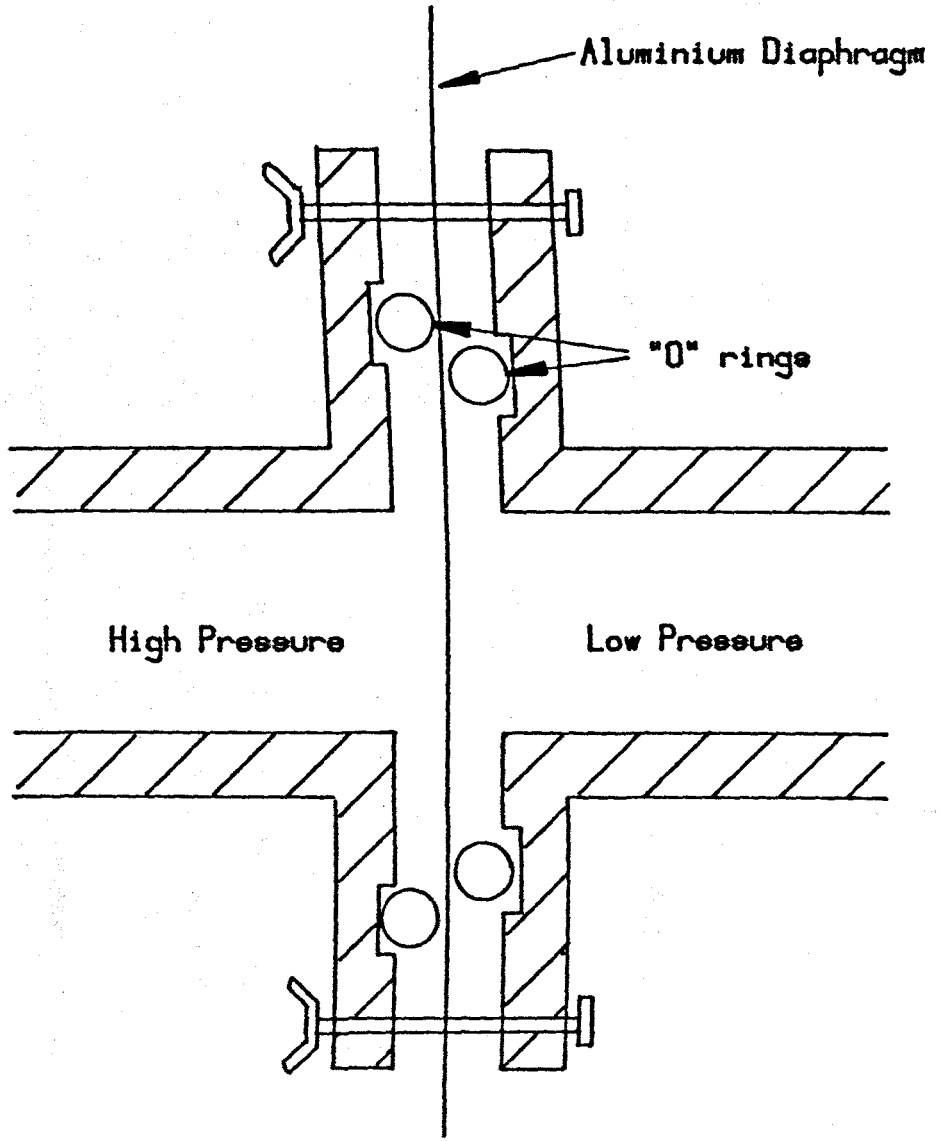

The ratio of bursting pressure, P_4, to test gas pressure, P_1, determines the speed of the shock. The dotted lines in figure 3.10 are the measured pressure ratios using either helium or nitrogen as driver gas, for the range of thicknesses of aluminium diaphragm used. A theoretical equation[105] gives the pressure ratio from the shock speed for a "perfect" shock where the diaphragm bursts instantaneously.

$$\frac{P_4}{P_1} = \frac{2\gamma_1 M^2 - (\gamma_1 - 1)}{\gamma_1 + 1} \left\{ 1 - \frac{\gamma_4 - 1}{\gamma_1 + 1} \frac{a_1}{a_4} \left(M - \frac{1}{M} \right) \right\}^{-2\gamma_4/\gamma_4 - 1} \qquad 3.17$$

The full lines in figure 3.10 are calculated from this equation for helium and nitrogen drivers into oxygen. The experimental shock speed is always less than the calculated value for a given diaphragm bursting pressure.

A speed between Mach 3 and 4 is difficult to obtain in our system, as helium shocks in this range need very thin diaphragms which often burst prematurely, so a mixture of driver gases was used. The nitrogen entered the driver section first, usually less than 30% of the pressure required for bursting, then helium was added slowly until the diaphragm burst. The resultant shocks had similar shock speeds if the same procedure was used each time.

The shock tube was cleaned periodically by pulling through it a piece of cloth soaked in diethylether, and then thoroughly outgassed for several hours.

3.3.6. Shock Tube Tests

(a) The effect of flowing gas in the test section

The results of experiments into undischarged flowing oxygen were compared with shocks into static oxygen at the normal test pressure. The flowing gas was found to have no effect on the shock speed, and no emission was recorded from the photo multipliers at the shock front.

Figure 3.10. Variation of Mach Number with Bursting Pressure, P_4.

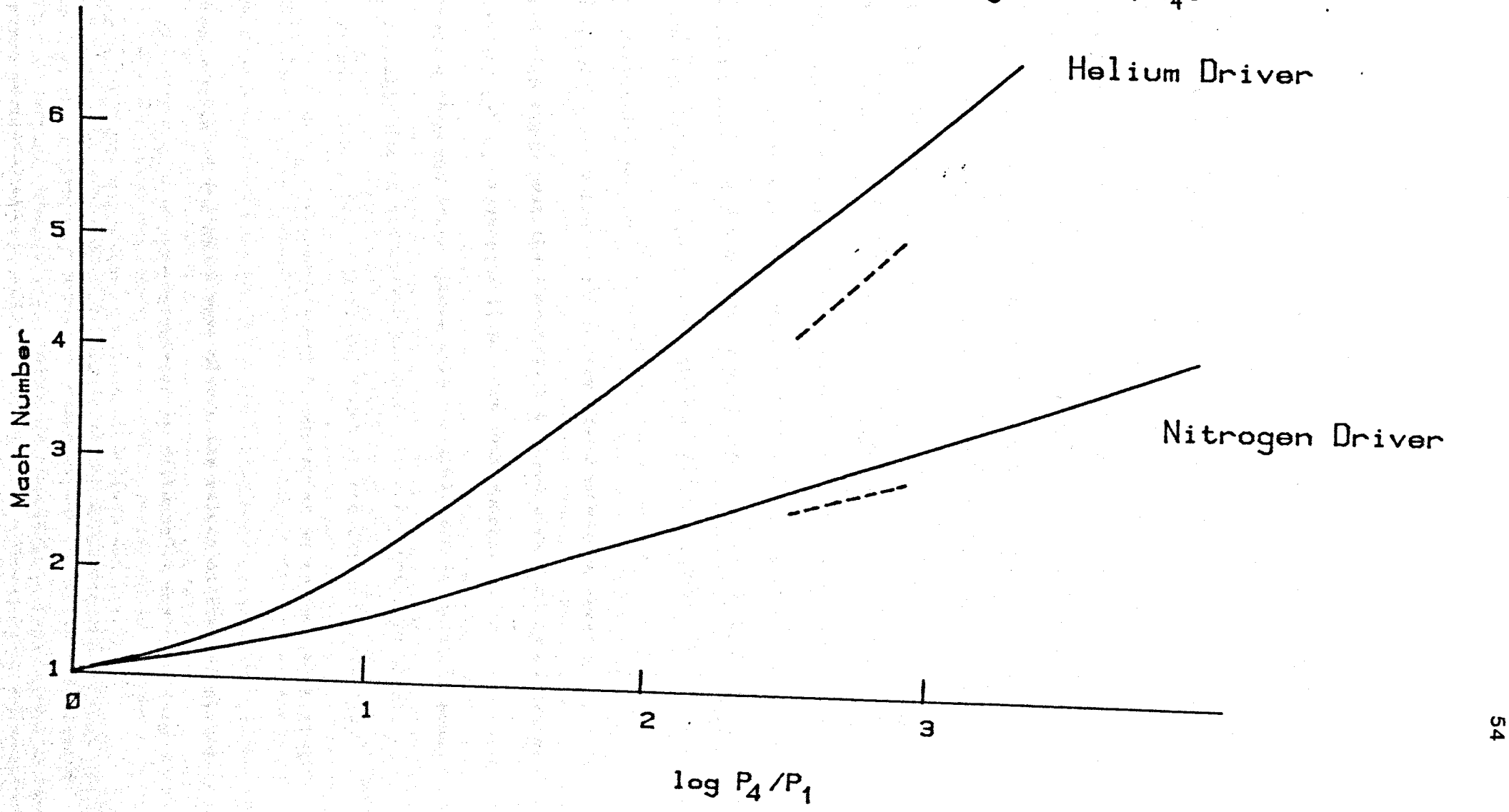

Breen, Quy and Glass[94] looked at the thickness of the shock front in their discharge flow shock tube with a laser schlieren technique[106]. They found a similar shock structure in both flowing and static systems. We conclude that accurate kinetic measurements at high temperatures can be made by propagating shock waves into flowing systems.

Our earliest experiments with a discharge flow shock tube had the discharged gases flowing into the test section at the diaphragm end which is the configuration used by other workers.[88,90-94] The system was reversed to increase the concentration of excited species at the observation station. All the experiments reported here have this configuration - flow against shock.

(b) Measurement of Attenuation in the Shock Tube

The speed of the shock front was measured with laser light screens (section 3.4.1.) at several positions along the test section to measure any deceleration. When comparisons were made with measurements near the diaphragm to measurements near the observation station, the deceleration was found to be appreciable (up to 3% m^{-1}). A second set of measurements taken at 1.5 m from the observation station and compared with those near the observation station showed no deceleration for fast shocks, and less than 1% m^{-1} for slow shocks.

Tests with mixed driver gases showed a small acceleration in some cases, probably due to incomplete mixing. We were unable to obtain mixed cylinder gases, and long mixing times in the driver section are inadvisable. The acceleration could be minimised by adding the helium slowly.

Deceleration of the shock wave alters the values of the calculated parameters. A computer program written by Millward[107] for his 25 mm diameter shock tube, using the equations of Belford and Strelow[108] derived from the analysis of Mirels[109] computes the corrections necessary for a given deceleration.

Boundary layer effects in shock tubes are, in part, responsible for shock attenuation, and also affect flow conditions behind the shock front. Pedley[110] investigated the buildup of a boundary layer in our tube, and suggested that the effect of boundary layer formation has been overestimated. Bowman[111] observed that non-ideal flow effects vary for different shock tubes in a manner not accounted for by the usual boundary layer theories, and suggested that "flow corrections based on existing theories should not be made arbitrarily since this may introduce errors larger than present originally".

In this work, no corrections are made for either shock attenuation or boundary layer effects in the temperature and density ratios behind the shock front.

That corrections are unnecessary in our tube is well demonstrated as the computed ratios for temperature and density used in the calculations give results which agree with the physical properties we are measuring. In chapter 7 the correlation between the measured pre-shock decay of excited species and the computed post shock decay is good, and in chapter 9 the graph of the relative K values for the 634 and 579 nm emission fit the theoretical population distribution function over the temperature range 960 to 1500 K. (figure 9.3)

3.4. Recording Apparatus

3.4.1. Laser Light Screens

The shock speed is calculated from the time taken for the shock front to travel a measured distance. The change in density at the shock front deflects a laser beam onto the sensitive area of a photomultiplier, and the resultant pulse is used as a trigger for a timing system.

The beam from a helium/neon laser (Ferranti - type GP2), is split into three and reflected through the shock tube, across the laboratory and onto three photo multipliers (EMI - 9660B) sensitive in the visible region. The laser, front silvered mirrors, and photomultipliers are firmly mounted independently of the shock tube, so that any vibration transmitted to the framework on bursting the diaphragm, does not affect their stability. The laser beam traverses the tube at an angle of $\sim 87^{o}$ to the tube; the optical path is 5 m long.

When the shock front passes, the laser beam is deflected from the back of the shock front, where reflection and refraction reinforce each other (figure 3.11). The photomultipliers are positioned so that the beam is to one side of the sensitive area, the deflection then causes a sharp rise in output which is used, via an emitter follower (Venner) and trigger unit (Hewlett Packard 5263A) to start or stop a time interval meter (Venner TSA 5536). The adjustment of the photomultipliers is checked before each shock by monitoring their output on an oscilloscope (Hewlett Packard 140A).

The pulse from the first light screen is also used to trigger the transient recorders.

The shock speed is measured over two distances, both in the region of the observation station, the two results were always the same, within $\pm$ 0.5%.

Figure 3.11. The Deflection of the Laser Beam as the Shock Front passes.

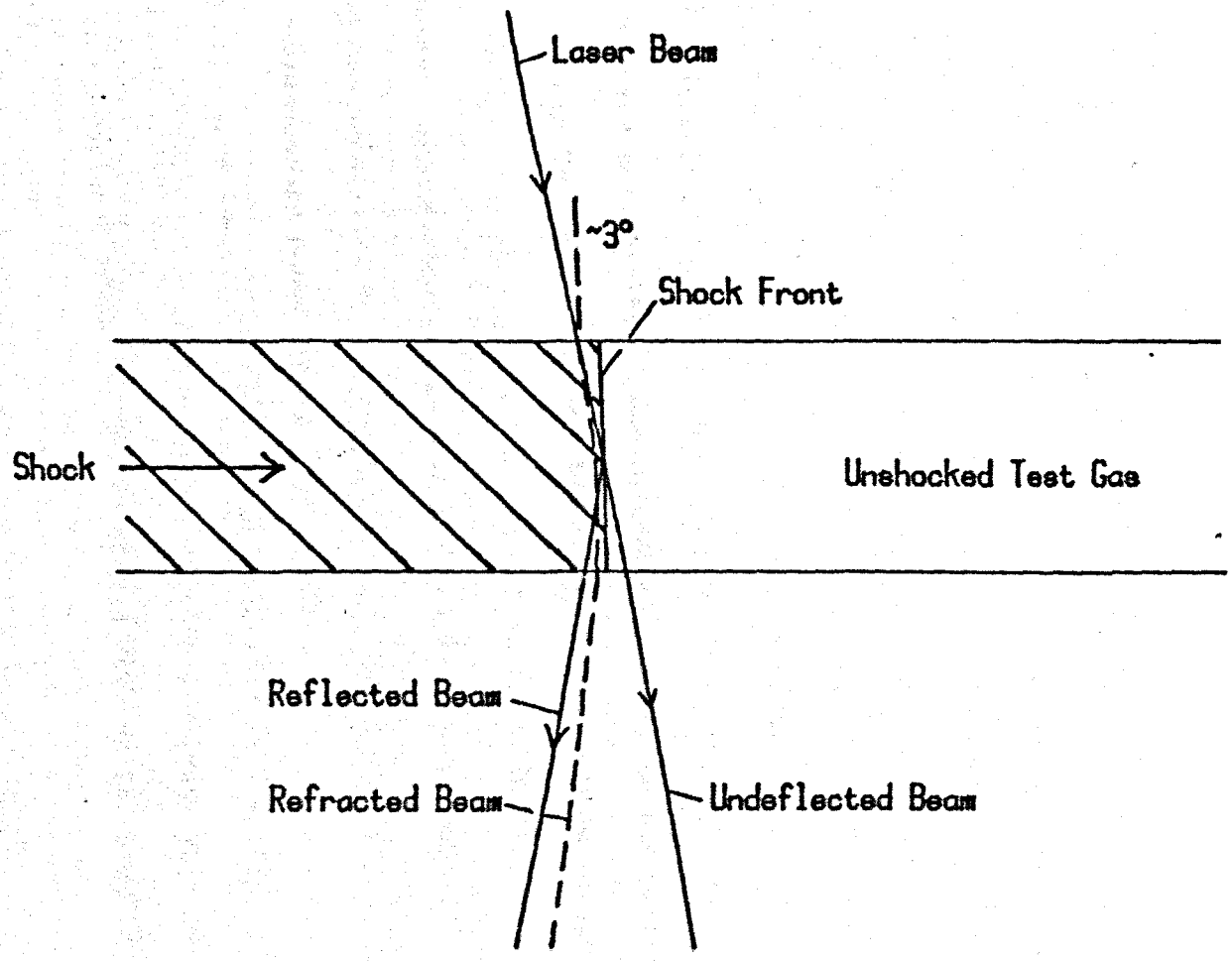

For weak shocks, the shock front is broader and the light screens are less reliable. As long as the first light screen fires to trigger the transient recorder, the shock result can be used, and then the speed of the shock is calculated from the time to the shock front measured from a photo of the emission output. The speed so measured is within ± 2% of the value calculated from the timers.

3.4.2. The Photomultiplier Detectors

A photomultiplier tube consists of a photocathode, a dynode chain to multiply the secondary emission, (the potential gradient is maintained between successive stages by suitable resistors), and an anode. The output is a current which is usually measured as a voltage across a load resistor.

The experiments in this thesis used a 9658B photomultiplier (E.M.I.) which has a trialkali S 20 cathode and an internally corrugated end window to enhance the red sensitivity. The quantum efficiency in the wavelength range 400 - 800 nm is plotted out in figure 3.12 from the manufacturers' published curves. The photomultiplier circuit is shown in figure 3.13; it is a standard high current, high gain circuit for pulsed applications. The cathode was maintained at the recommended potential for each individual tube with a Brandenburg power supply (type 472R).

The output from the photomultipler was generated as a voltage across a 51 K ohm load resistor, and was measured through a voltage follower made from an operational amplifier (Radio Spares 741) as is shown in figure 3.13.

Some early experiments used a 9684B photomultiplier (E.M.I.) which has an S1 cathode of AgOCs to look at the (0,0) transition of $O_2(^1\Delta_g)$ at 1270 nm. This is the only cathode to provide any response between 900 and 1200 nm, and although the manufacturers' curves suggest that the response would be negligible at 1270 nm, a weak emission was

Figure 3.12. Variation in Quantum Efficiency with Wavelength for the 9658B Photomultiplier.

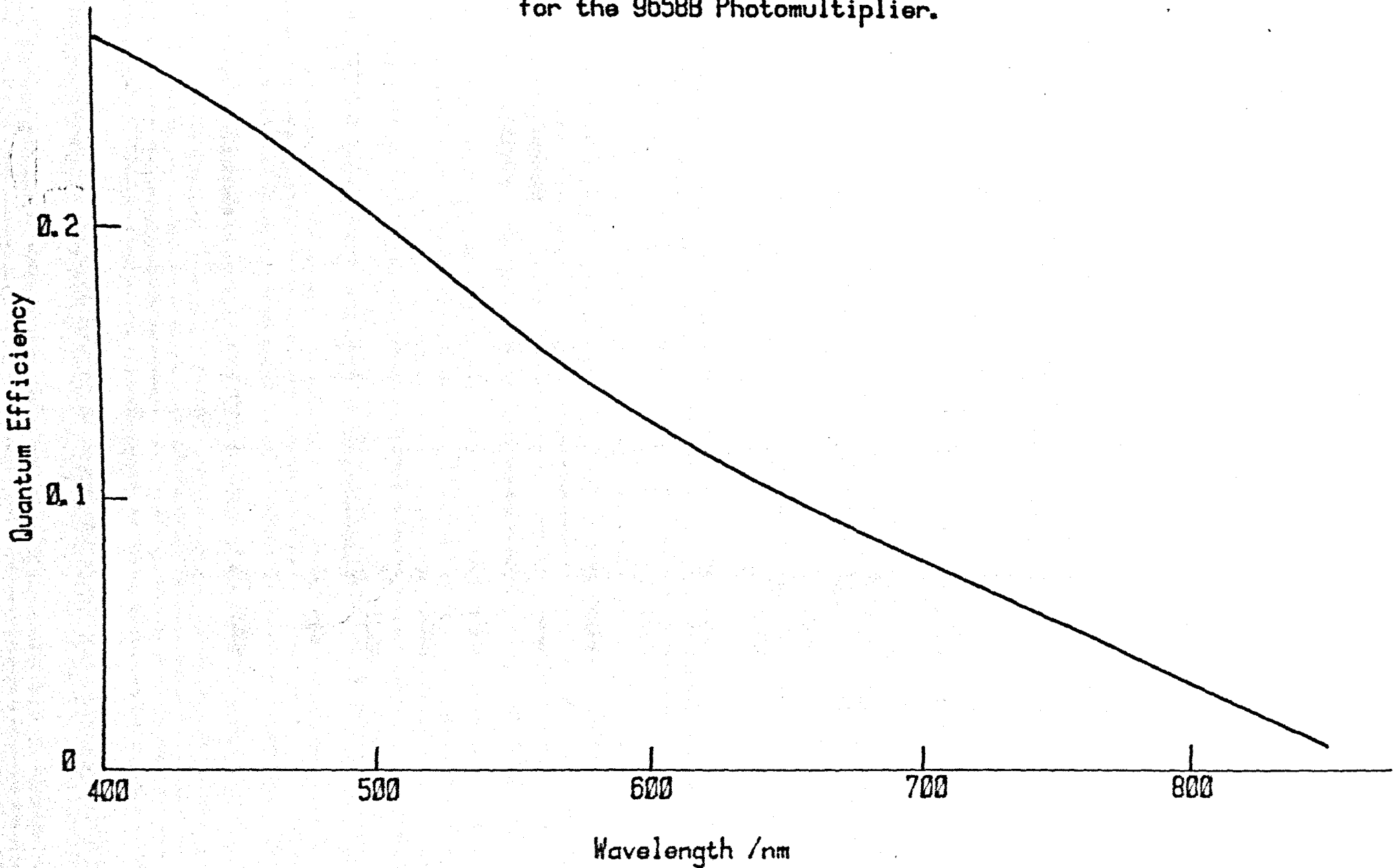

Figure 3.13.

The Electronic Circuit for the 9658B Photomultiplier.

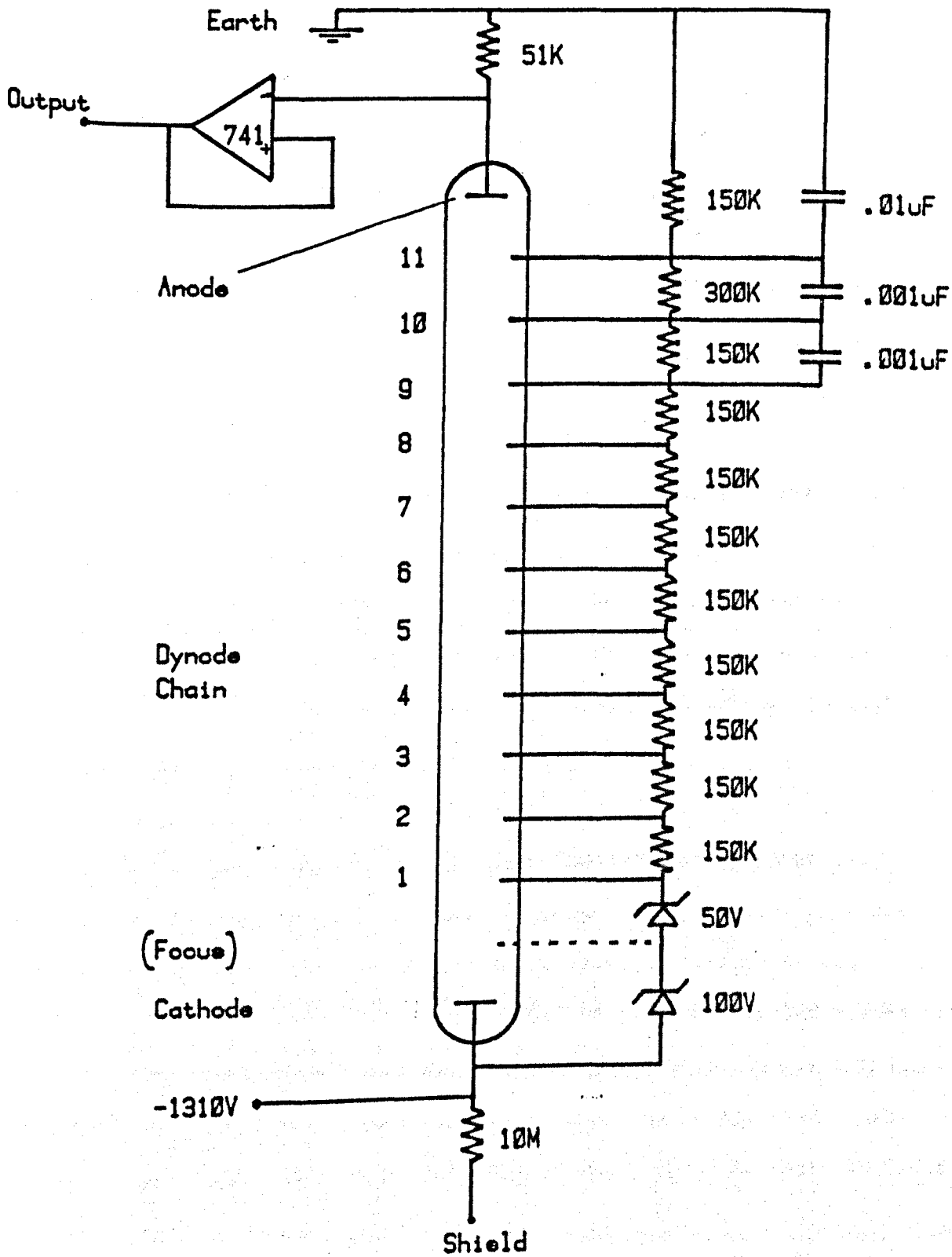

observed (chapter 4). This photomultiplier was cooled to 77 K in an Oxford Instruments housing which was kept under vacuum to avoid condensation on the window or the electronic components within the casing. At this temperature the thermal component of the dark current is at a minimum and the signal to noise ratio is improved. The circuit is similar to that shown in figure 3.13 but with the focus electrode.

3.4.3. Digital Voltmeter

The room temperature readings of the voltage signal from the photomultipliers are measured with a digital voltmeter (Solatron 7040). A reading of the voltage output when there is no emission, is subtracted from all the values, being the voltage output from stray background light and the null reading of the voltage follower. This zero correction is checked with each reading.

3.4.4. Transient Recorders

During the early part of this work, the post-shock output from the photomultiplier was fed into a storage oscilloscope (Hewlett Packard 141A with time base and delay generator, 1421A, and dual beam trace amplifier, 1408A) and a photograph taken of the single sweep. The photographic record of the post shock emission was difficult to analyse by hand, and was time consuming and imprecise.

Worthwhile results were obtained when a transient recorder was purchased, (Data Lab DL905) and the post shock emission output was digitised and punched out onto paper tape for later computer analysis. The emission recorded in the transient recorder is relayed to the oscilloscope and a photograph of the trace is taken for record purposes.

The first laser light screen activates the trigger in the transient recorder, and after a set delay time, the emission is recorded. The delay time is calculated from the expected shock speed so that the first

part of the trace shows the preshock emission, then the shock front arrives, seen as a sharp increase in emission, followed by the emission from the shock heated gas as it is swept past the observation station. (Plate 3)

Recently a second transient recorder was purchased, and so for each shock two results are obtained, from the two photomultipliers (Plate 3b). The sensitivity of the transient recorders was checked periodically using the one volt calibrating signal from the oscilloscope, and this checked against the voltage reading of the digital voltmeter, to make sure that all three instruments gave identical readings for the same voltage input. The time scale was also checked using the crystal oscillator in the timer.

At the end of the work recorded in this thesis, the University computer was changed, and the interactive graphics program (Chapter 6) which was written especially for the I.C.L.4130 was no longer workable. A new program has now been written and the transient recorders are interfaced directly to an Intelligent Graphics Terminal (Hewlett Packard 2647A). The output is stored on magnetic tape in the terminal, and later partially processed before being transferred to the University's new computer (G.E.C.4082) for disc storage. Complete analysis on the terminal follows a similar pattern to that described in chapter 6.

3.4.5. The Experimental Arrangements

The two photomultipliers are set opposite each other at the observation station, 4.4 m from the diaphragm. One photomultiplier rests on slides which run parallel to the tube, and it is moved along the tube to take emission readings of the concentration of excited species. The slide is marked out at 100 mm intervals for 2.5 m.

The photomultiplier cathodes are situated 80 mm from the surface of the shock tube, which is the minimum distance and is governed by the

geometry of their housings. A filter is positioned between the photomultiplier housing and the shock tube. Its casing has a parallel set of slits which can be adjusted to suit the level of the emission being studied. (figure 3.14)

The shock tube is wrapped in black paper and the photomultiplier assemblies are covered in black cloth; all experiments are performed in a darkened room.

3.4.6. Photomultiplier Tests

The response of the photomultipliers to a single pulse of light was tested with a red light emitting diode (L.E.D.) coupled to a square wave generator (Marconi Instruments Ltd. TF 2010). The L.E.D. was positioned inside the shock tube, so that its emission level at the observation station was of the same order of magnitude to that expected from the excited states. The response of the detectors was measured when the L.E.D. emitted a single square wave pulse, by measuring the area under the pulse on the output from the detectors via the transient recorder. This was checked with the value found for one pulse when the L.E.D. emitted a string of square wave pulses of the same height and duration as the single one. For both the 9658B photomultipliers used in this work, their response to a single pulse was found to be better than 98% of the value for one pulse in a string.

The rise times of the photomultipliers in these experiments were less than 5 μs with a load resistor of 51 k ohms, but up to 10 μs with a load resistor of 100 k ohms.

In shock experiments the rise times are also affected by the volume of emitting gas which can be viewed by the photomultiplier cathode, which is illustrated in figure 3.14. A narrower cone could have been achieved with a slit nearer the cathode, but this was not possible without modification of the photomultiplier housings. A lens system to focus

Figure 3.14. The Cone of Gas viewed by the Photomultiplier.

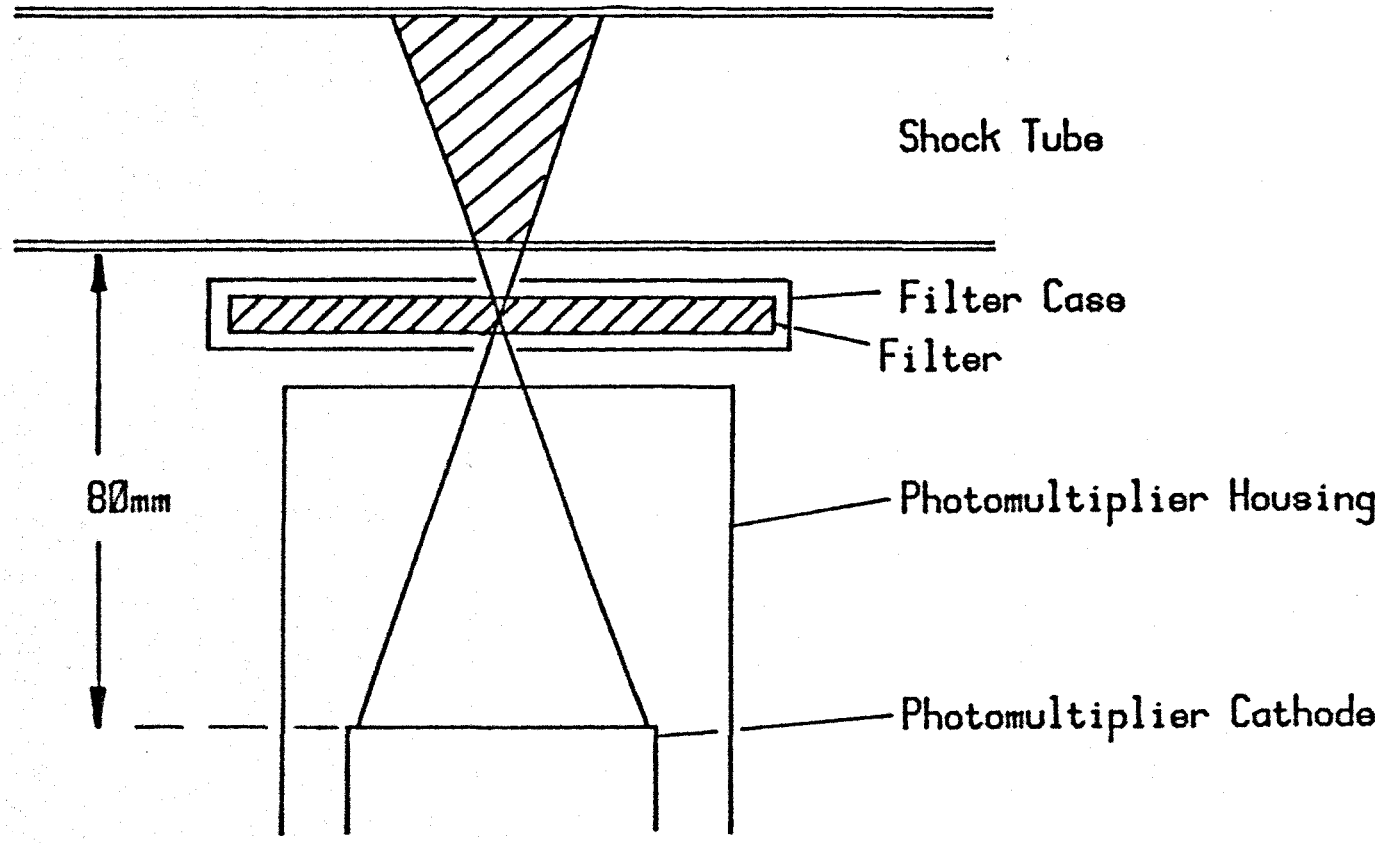

the emission onto the cathode was tried, but it was difficult to set up, and any improvement in the signal was more than off-set by the loss because of the increased distance of the cathode from the tube.

The rise times in shock experiments were normally 10 μs or longer, depending on the size of the slit necessary to get a measurable emission. Shocks looking at the 634 nm, where the sharp emission rise at the shock front is dependent on the square of the density ratio, were used to measure the rise times for narrow slits (< 1 mm). The rise time was found to be in the region of 4 to 5 μs.

3.5. Procedure for a Typical Experiment

The pumps are switched on, and the discharge tube, test and driver sections of the shock tube are all thoroughly evacuated. The flow of oxygen is established in the discharge tube and shock tube test section and adjusted with the needle valve. The downstream pressure is adjusted with the PTFE regulating valve, and the discharge is initiated with a teslacoil. The discharge is left to equilibrate for at least 30 minutes before a shock.

The change in concentration of the excited species along the tube is measured at room temperature before each shock by taking readings of the emission level at stations along the test section with the travelling detector. The detector is replaced at the observation station, the filter checked, and readings of the emission noted from both photomultipliers - this is the pre-shock glow, and is an important quantity in the analysis of the results.

The light screen photomultipliers are now adjusted so that the laser beam falls just to the side of the active area. The detector outputs are plugged into the transient recorders, and the sweep speed, sensitivity and delay adjusted for the expected shock speed; the trigger levels are set on the trigger units, time interval meters and transient recorders, and all are put in the "ready" mode. Finally the flow rate and downstream pressure are checked and the tap to the monometer closed.

The shock is set off by raising the pressure of driver gas in the driver section until the diaphragm bursts; reproducible shocks are obtained when the pressure rises slowly and evenly.

After the shock, the discharge is switched off and the photomultiplier voltage zero corrections are checked; the times are noted for calculation of the shock speed, and photographs of the emission trace are taken from the oscilloscope screen. The emission trace from the transient recorder

is output to paper tape for later analysis.

The flow of oxygen is switched off and the whole shock tube and discharge section raised to atmospheric pressure. A new diaphragm is inserted and the shock tube evacuated ready for the next experiment.

Chapter 4

The (0,0) Transition of $O_2(^1\Delta_g)$.

4.1. Introduction

The (0,0) transition of $O_2(^1\Delta_g)$ occurs in the infrared at 1270 nm. In our system, measurement of the concentration of $O_2(^1\Delta_g)$ by observing this emission is not very satisfactory, as the sensitivity of the 9684B photomultiplier is extremely small beyond 1200 nm. (section 3.4.2.) However, the dimol emission at 634 nm is easily observed, and the experiments described in this chapter justify the use of the 634 nm emission as a measure for the $O_2(^1\Delta_g)$ concentration.

4.2. Experimental and Results.

The intensity of the 1270 nm emission is directly related to the $O_2(^1\Delta_g)$ concentration:

$$O_2(^1\Delta_g) \rightarrow O_2(^3\Sigma_g^-) + h\nu(\lambda = 1270\ nm) \qquad 4.1$$

The intensity of the 634 nm emission, if the dimol attribution is correct[14], should be related to the square of the $O_2(^1\Delta_g)$ concentration:

$$O_2(^1\Delta_g) + O_2(^1\Delta_g) \rightarrow O_2(^3\Sigma_g^-) + O_2(^3\Sigma_g^-) + h\nu(\lambda = 634\ nm) \qquad 4.2$$

Our experiments at 1270 nm used a 9684B photomultiplier cooled to liquid nitrogen temperatures; the cooling minimised the dark current and enabled the weak signal to be seen above the noise.

Comparative measurements were made between the intensity of emission at 634 nm and 1270 nm at room temperature with this photomultiplier for different downstream pressures between 3 and 8 torr (400 - 1100 Pa). The measurements are shown as a log plot in figure 4.1. The points are on a straight line of slope 2, and the squared relationship is verified

$$^{634}I \ \alpha \ (^{1270}I)^2 \qquad 4.3$$

The signal to noise ratio for shock experiments at 1270 nm was too small for analysis, and no further experiments at this wavelength were attempted.

Figure 4.1.

A Plot of the Relative Intensity of Emissions from $O_2(^1\Delta_g)$

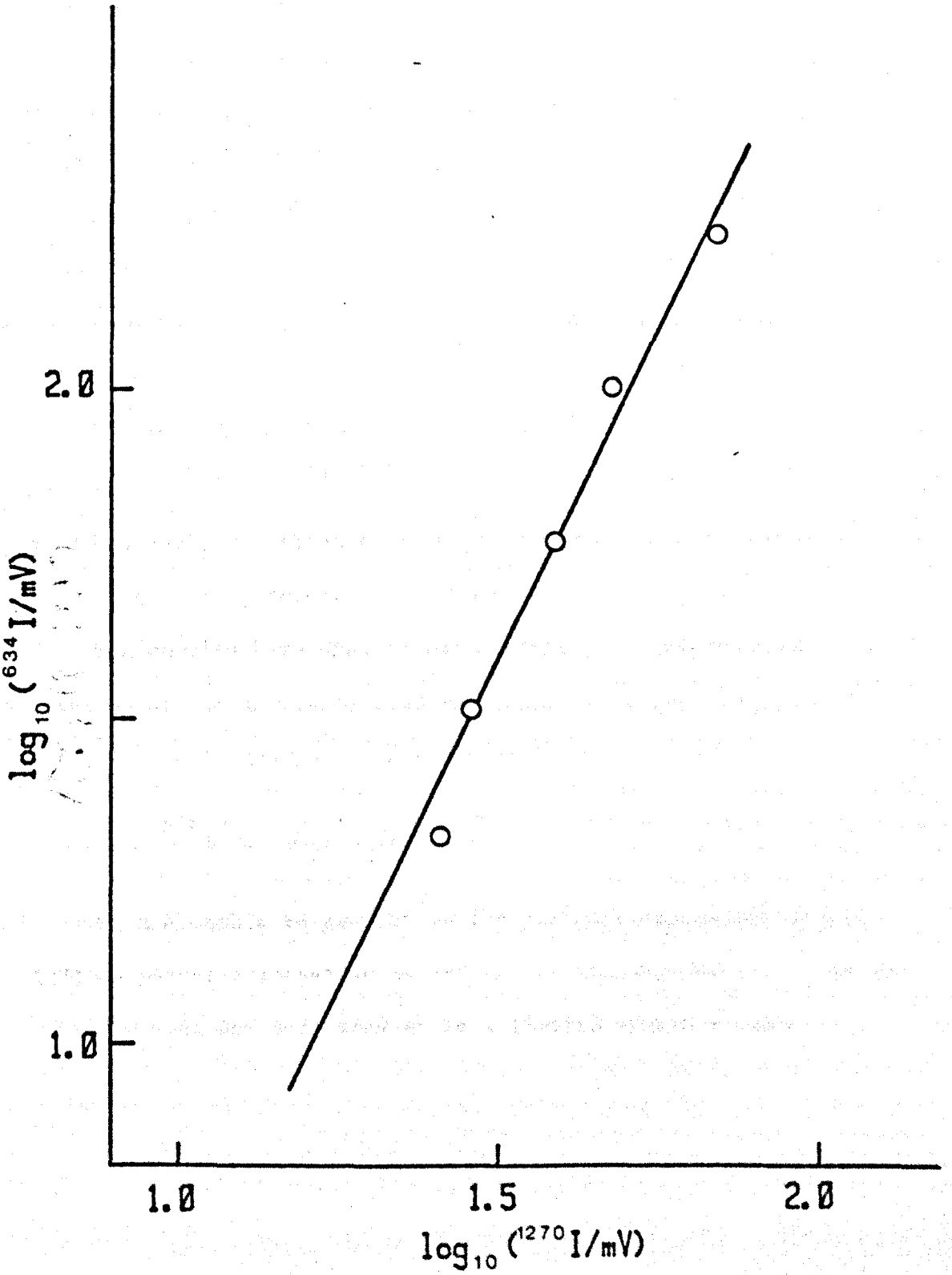

4.3. Discussion.

We have found that the intensity of the emission at 634 nm is related to the square of the emission intensity at 1270 nm (equation 4.3) as would be expected from the origin of the emissions (reactions 4.1 and 4.2). March, Furnival and Schiff[26], in an early paper, found a linear relationship between the two emissions, but this was later discounted and the expected squared relationship found by Whitlow and Findlay[112].

The wavelength region in the near infrared is a difficult region to study with a photomultiplier, though Izod and Wayne[113] had some success with an R.C.A. 7102 photomultiplier cooled to solid carbon dioxide temperatures.

The emission at 1270 nm can be monitored with a cooled germanium detector[34, 35, 59, 114, 115] but Findlay and Snelling[34, 35] found only a weak signal, and obtained results only after signal averaging over a large number of repetative outputs.

The results here show in our system, as in others, that the dimol emission at 634 nm can be used as a measure of the concentration of $O_2(^1\Delta_g)$, and is dependent on the square

$$^{634}I \quad \alpha \quad [O_2(^1\Delta_g)]^2 \qquad 4.4.$$

We are unable to comment on the pressure dependence of the 1270 nm emission suggested by Badger, Wright and Whitlock[9], as the emission here was only studied in a limited pressure range.

Chapter 5

The Room Temperature Deactivation of $O_2(^1\Delta_g)$ by Oxygen.

5.1. Introduction

In our experiments, the room temperature decay of the excited species as the gas flows along the shock tube, is measured before each shock with a travelling photomultiplier. (section 3.5)

Within the limited pressure range used for the shock experiments, we found a lower value for the collisional quenching of $O_2(^1\Delta_g)$ than expected. This lead to a study of the decay rate at the normal laboratory temperature of 295 K for oxygen pressures between 2 torr and 14 torr (260 - 1900 Pa) at various flow rates.

5.2. Treatment of Results.

$O_2(^1\Delta_g)$ is generated in or just after the microwave discharge, and is deactivated as the gas flows along the tube. The deactivation occurs through collisional quenching by oxygen molecules;

$$O_2(^1\Delta_g) + O_2(^3\Sigma_g^-) \overset{k_q}{\rightarrow} 2O_2(^3\Sigma_g^-) \qquad 5.1$$

diffusion to and deactivation at the wall;

$$O_2(^1\Delta_g) + \text{wall} \overset{k_w}{\rightarrow} O_2(^3\Sigma_g^-) \qquad 5.2$$

and by the optical transitions.

$$O_2(^1\Delta_g) \rightarrow O_2(^3\Sigma_g^-) + h\nu(\lambda = 1270\ \text{nm}) \qquad 5.3$$

$$O_2(^1\Delta_g) + O_2(^1\Delta_g) \rightarrow O_2(^3\Sigma_g^-) + O_2(^3\Sigma_g^-) + h\nu(\lambda = 634\ \text{nm}) \qquad 5.4$$

$O_2(^1\Delta_g)$ molecules are also lost in the energy pooling reaction forming $O_2(^1\Sigma_g^+)$ molecules.

$$O_2(^1\Delta_g) + O_2(^1\Delta_g) \overset{k_p}{\rightarrow} O_2(^1\Sigma_g^+) + O_2(^3\Sigma_g^-) \qquad 5.5$$

Of these reactions, only 5.1 and 5.2 are rate controlling. The forbidden optical transitions are very slow in comparison with reactions 5.1 and 5.2 and although the energy pooling reaction 5.5 is 10^6 times faster than the dimol emission[116], this reaction only becomes significant in comparison with reactions 5.1 and 5.2 at high concentrations of $O_2(^1\Delta_g)$.

So the rate of decay of $O_2(^1\Delta_g)$ can be expressed as:

$$\frac{-d[O_2(^1\Delta_g)]}{dt} = k_q[O_2][O_2(^1\Delta_g)] + k_w[O_2(^1\Delta_g)] \qquad 5.6$$

$$= k_{obs}[O_2(^1\Delta_g)] \qquad 5.7$$

where k_{obs} is the pseudo first order rate constant for the decay of $O_2(^1\Delta_g)$.

$$\frac{-d[O_2(^1\Delta_g)]}{[O_2(^1\Delta_g)]} = k_{obs}\, dt \qquad 5.8$$

Integrating equation 5.8 between zero time and t = t gives:

$$\ln \frac{[O_2(^1\Delta_g)]_t}{[O_2(^1\Delta_g)]_o} = -k_{obs}\, t \qquad 5.9$$

where $[O_2(^1\Delta_g)]_o$ is the concentration of $O_2(^1\Delta_g)$ at zero time.

The concentration of $O_2(^1\Delta_g)$ is monitored along the tube by observing the intensity of the dimol emission at 634 nm (Chapter 4) where:

$$^{634}I \;\alpha\; [O_2(^1\Delta_g)]^2 \qquad 4.4$$

The slope of a log plot of the intensity against time should then give $k_{obs/2}$.

The change in emission intensity along the tube is measured as a function of length, and k_{obs} is found by multiplying the slope of a log plot of intensity against length, by the linear flow velocity of the gas along the tube. The linear velocity is calculated from the measured flow rate at 1 atmosphere pressure at 295 K by:

$$\text{Linear Velocity} = \frac{\text{Flow Rate}}{\pi r^2} \cdot \frac{760}{p_{O_2}} \qquad 5.10$$

where p_{O_2} is the downstream pressure of oxygen in torr.

It is also possible to monitor the concentration of $O_2(^1\Delta_g)$ by looking at the emission at 762 nm from $O_2(^1\Sigma_g^+)$.

$$O_2(^1\Sigma_g^+) \rightarrow O_2(^3\Sigma_g^-) + h\nu(\lambda = 762 \text{ nm}) \qquad 5.11$$

$O_2(^1\Sigma_g^+)$ is formed entirely from $O_2(^1\Delta_g)$ in the energy pooling reaction 5.5, and is deactivated by oxygen quenching, and at the walls

$$O_2(^1\Sigma_g^+) + O_2(^3\Sigma_g^-) \xrightarrow{k_q^*} 2O_2(^3\Sigma_g^-) \qquad 5.12$$

$$O_2(^1\Sigma_g^+) + \text{wall} \xrightarrow{k_w^*} O_2(^3\Sigma_g^-) \qquad 5.13$$

The forbidden radiative decay at 762 nm (reaction 5.11) is again very slow in comparison with reactions 5.12 and 5.13 and is omitted from the rate equation. At any point in the tube, the concentration of $O_2(^1\Sigma_g^+)$ is at a steady state, where its rate of formation equals its rate of deactivation:

$$k_p[O_2(^1\Delta_g)]^2 = k_q^*[O_2][O_2(^1\Sigma_g^+)] + k_w^*[O_2(^1\Sigma_g^+)] \qquad 5.14$$

and

$$[O_2(^1\Sigma_g^+)] = \frac{k_p[O_2(^1\Delta_g)]^2}{k_q^*[O_2] + k_w^*} \qquad 5.15$$

So the concentration of $O_2(^1\Sigma_g^+)$ is proportional to the square of the $O_2(^1\Delta_g)$ concentration when the oxygen pressure remains constant, and the intensity of emission at 762 nm can be used to monitor the

$O_2(^1\Delta_g)$ concentration.

$$^{762}I \quad \alpha \quad [O_2(^1\Sigma_g^+)] \quad \alpha \quad [O_2(^1\Delta_g)]^2 \qquad 5.16$$

5.3 Results.

The decay of $O_2(^1\Delta_g)$ along the tube was measured by observing both the dimol emission at 634 nm, and the 762 nm emission from $O_2(^1\Sigma_g^+)$. The series of runs are listed in table 5.1. For the 762 nm emission the photomultiplier slit width was about 0.5 mm, and the signal to noise ratio varied along the tube in the measurement region from 600 to 200. For the dimol emission at 634 nm, the photomultiplier slit was widened to about 1 mm, and the signal to noise ratio varied from 10 down to 2.

Results for the two emissions as first order plots are shown in figure 5.1. The slopes are identical and the equivalence of the two emissions is demonstrated. Most of the runs listed in table 5.1 used the 762 nm emission which has the better signal to noise ratio for a narrower slit.

A plot of k_{obs} against oxygen concentration is shown in figure 5.2. A good straight line is obtained, the slope of which gives the collisional deactivation rate constant of $O_2(^1\Delta_g)$ by oxygen, k_q, as $(9.4 \pm 0.3) \times 10^2$ ℓ mol^{-1} s^{-1} at 295 K.

The intercept in figure 5.2 is a measure of the wall deactivation rate constant, k_w, and is 0.106 ± 0.013 s^{-1} in our system. The wall deactivation efficiency, γ, is $(1.23 \pm 0.14) \times 10^{-5}$ where

$$\gamma = \frac{2 k_w r}{\bar{c}} \qquad 5.17$$

and $\bar{c}$ is the mean velocity of an oxygen molecule, and r is the radius of the tube.[30]

Initially runs at pressures below 5 torr and with fast flow rates, gave higher values of k_{obs} than expected. Reducing the microtron

Table 5.1.

Results of the Room Temperature Deactivation of $O_2(^1\Delta_g)$

Oxygen Pressure /torr	Oxygen Conc. /10^{-4} mol l^{-1}	Microtron Power /watts	Flow Rate /ml s^{-1}	Flow Rate /m s^{-1}	Decay Rate /m^{-1}	k_{Obs} /s^{-1}
3.0	1.64	60	11.3	2.02	0.431	0.312
4.2	2.30	100	30.0 *	3.21	0.265	0.355
5.6	3.06	100	23.05 *	1.73	0.480	0.371
8.6	4.70	100	23.05 *	1.07	1.020	0.511
3.7	2.02	60	6.9	0.86	0.875	0.306
4.7	2.57	60	6.9	0.65	1.19	0.321
4.7	2.57	60	10.1	0.95	0.847	0.349
5.3	2.90	60	8.7	0.69	1.22	0.372
5.8	3.17	60	10.1	0.73	1.08	0.373
12.2	6.67	80	20.2	0.65	2.30	0.715
11.1	6.07	80	20.0	0.72	1.98	0.677
7.6	4.16	80	20.2	1.07	0.958	0.477
7.0	3.83	100	30.0 *	1.73	0.601	0.483

Table 5.1.(continued)

Results of the Room Temperature Deactivation of $O_2(^1\Delta_g)$

Oxygen Pressure /torr	Oxygen Conc. /10^{-4} mol l^{-1}	Microtron Power /watts	Flow Rate /ml s^{-1}	Flow Rate /m s^{-1}	Decay Rate /m^{-1}	k_{Obs} /s^{-1}
8.4	4.59	100	30.0	1.42	0.833	0.536
6.5	3.56	60	9.3	0.54	1.65	0.443
7.3	3.99	60	9.3	0.48	2.07	0.495
4.7	2.57	60	30.4	2.42	0.288	0.349
11.9	6.51	60	9.3	0.29	4.84	0.709
8.55	4.68	60	30.4	1.32	0.863	0.575
6.4	3.50	60	30.4	1.18	0.498	0.443
2.5	1.37	40	9.3	1.40	0.304	0.212
2.0	1.09	35	9.3	1.75	0.181	0.150
9.8	5.36	100	9.3	0.36	3.40	0.604
10.7	5.83	100	17.5	0.61	2.17	0.665
14.0	7.66	100	17.5	0.47	3.58	0.838

Figure 5.1. First Order Plots of the Decay of Emission Intensity against Distance.

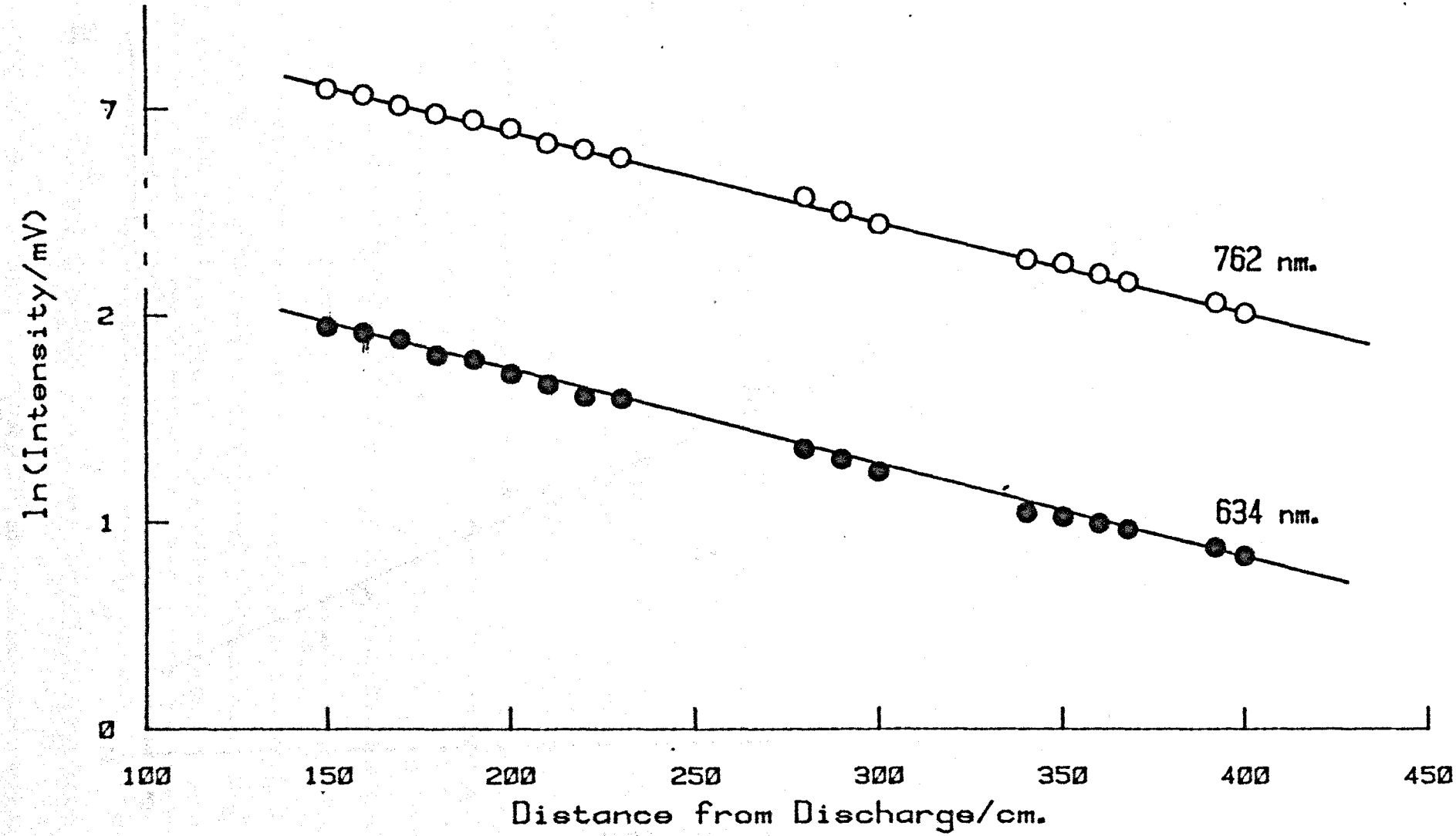

Figure 5.2. First Order Rate Constants for the Deactivation of $O_2(^1\Delta_g)$ plotted against Concentration of Oxygen.

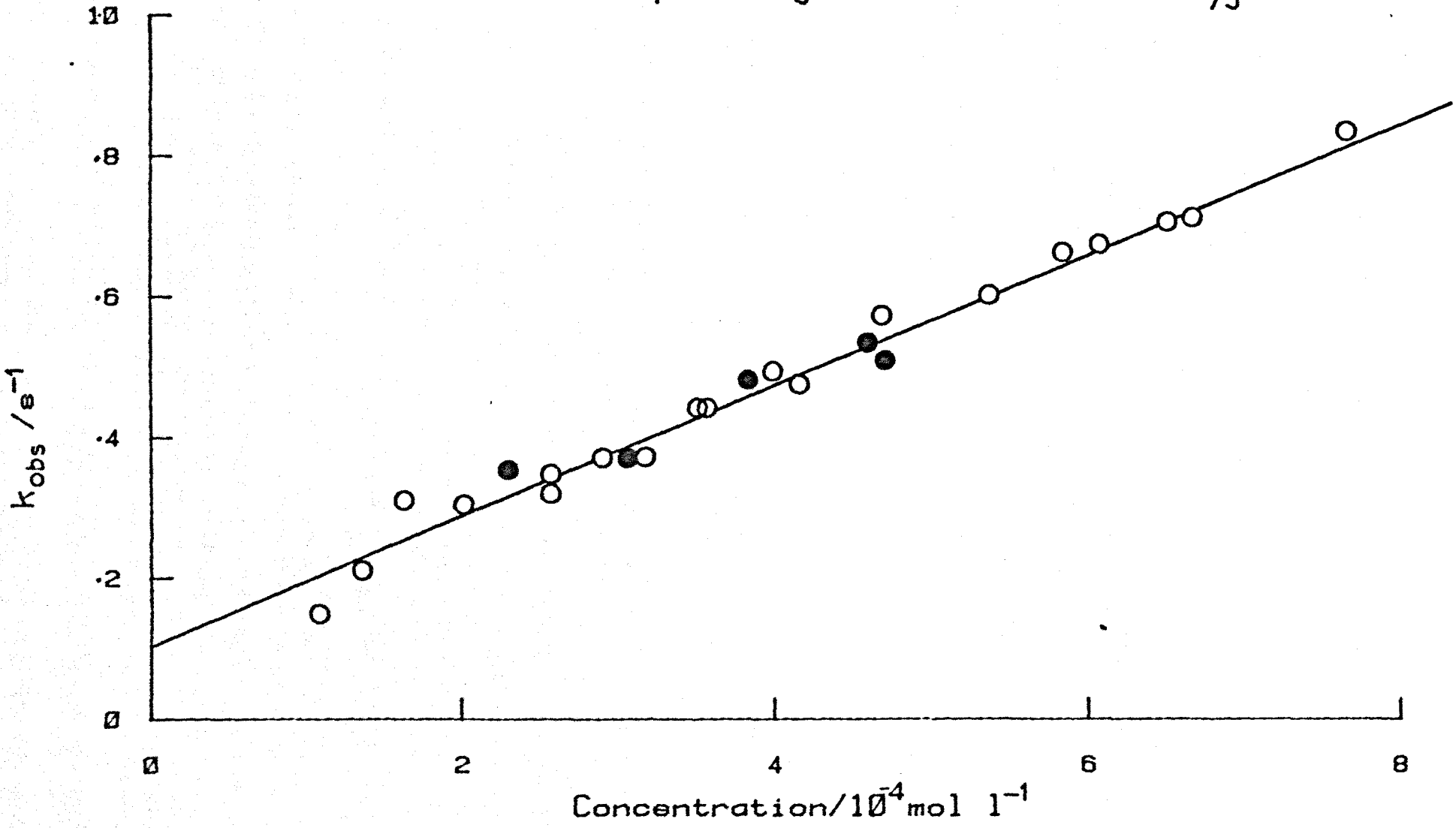

power for these runs gave satisfactory values of k_{obs}. Reducing the microtron power not only lowers the concentration of $O_2(^1\Delta_g)$, but also reduces the number of oxygen atoms formed. At the low pressures and fast flow rates, the mercury in the oxygen flow is probably not so effective in removing oxygen atoms, and any remaining would increase the rate of deactivation of $O_2(^1\Delta_g)$.

Several runs were performed with only 10% of the total oxygen flowing through the discharge as in Wayne's technique[117]. Here the concentration of $O_2(^1\Delta_g)$ is appreciably lower, but the values of k_{obs} fit well with the other results; these runs are indicated with an asterisk in table 5.1 and as 'filled in' points in figure 5.2.

5.4. Discussion.

A plot of the pseudo first order rate constant, k_{obs}, against concentration (figure 5.2) is a good straight line, giving a value of $(9.4 \pm 0.3) \times 10^2$ ℓ mol^{-1} s^{-1} for the collisional quenching of $O_2(^1\Delta_g)$ by oxygen, which is lower than the previous published values. We believe that measurements made at a long distance from the discharge over a long length of flow tube of wide bore, as in our system, give more accurate results.

The straight line in figure 5.2 confirms the suggestion that the second order energy pooling reaction 5.5 does not conbribute significantly to the removal of $O_2(^1\Delta_g)$. The results with only 10% of the oxygen flowing through the discharge fit well with the other results; so even when the total oxygen flow is through the discharge the concentration of $O_2(^1\Delta_g)$ is too low for the energy pooling reaction to have a significant effect.

Table 5.2 lists the published values of the rate constant for deactivation of $O_2(^1\Delta_g)$ by oxygen. The last value in the table by Leiss, Schurath, Becker and Fink[115] of $(8.8 \pm 0.3) \times 10^2$ ℓ mol^{-1} s^{-1} was published after this work was completed, and confirms the lower value. Of course, any impurity in the system would serve to increase the rate of deactivation of $O_2(^1\Delta_g)$, and this could be the reason for the previous higher values.

The wall deactivation efficiency measured here is lower than that of other workers, but similar to that obtained by Clark and Wayne[117] using a tube rinsed with HF.

Table 5.2.

Rate Constants for the Deactivation of $O_2(^1\Delta_g)$ at Room Temperature.

k /10^3 l $mol^{-1}s^{-1}$	k /s^{-1}	γ /10^5	Wavelength /nm	References
0.94±0.03	0.11±0.02	1.2±0.2	762/634	118 (This work)
1.32±0.30	0.17±0.03	2.1	1270	117
1.31±0.07	0.3±0.1	4.0	1270	34
1.23±0.14	0.13±0.06	1.3	1270	119
1	0.2	1	634	120
1.02±0.6	6.1×10^{-4} to 1.1×10^{-3}	0.7 to 1.3 (Stainless Steel)	1270	121
1.65±0.12	-	4.0	(Calorimetry)	29
0.91±0.03	3×10^{-3}	-	1270	115

Chapter 6.

Analysis of Post-Shock Results by Interactive Computer Graphics

6.1. Introduction

The emission from the excited species is monitored by photomultipliers/filter combinations at the observation station, both pre-shock, across the shock front and in the shock heated gas. The emission has the form shown in plate 3, trace (a) is at 634 nm, the dimol emission from $O_2(^1\Delta_g)$, and trace (b) is the emission from $O_2(^1\Sigma_g^+)$ at 762 nm. The compression at the shock front is easily seen on both photos, the fall-off in intensity past the shock front reflects the change in concentration of excited species as the gas flows along the tube before the shock, and is seen at the observation station as the gas downstream from the discharge is swept past the photomultiplier in the wake of the shock front. In trace (b) at 762 nm, there is a curved region after the initial shock compression to an enhanced level of emission before the fall-off described above takes over, this is the relaxation zone where the concentration of $O_2(^1\Sigma_g^+)$ adjusts to a new steady state at the higher shock temperature. The relaxation zone is not observed in the 634 nm dimol emission, trace (a).

The analysis proceeds by fitting the trace to the equations derived in chapters 7 and 8 . For analysis of shocks at 634 nm the equation used is:

$$^{634}I_2 = \frac{^{634}I_1 \, K}{A\Delta t} \left(\frac{\rho_2}{\rho_1}\right)^2 \left(\frac{T_2}{T_1}\right)^{\frac{1}{2}} e^{At} (1 - e^{-A\Delta t}) \qquad 7.6$$

Plate 3

Photographs of the Emission Trace from a Shock Experiment

(a) At 634 nm. Run No. 6.

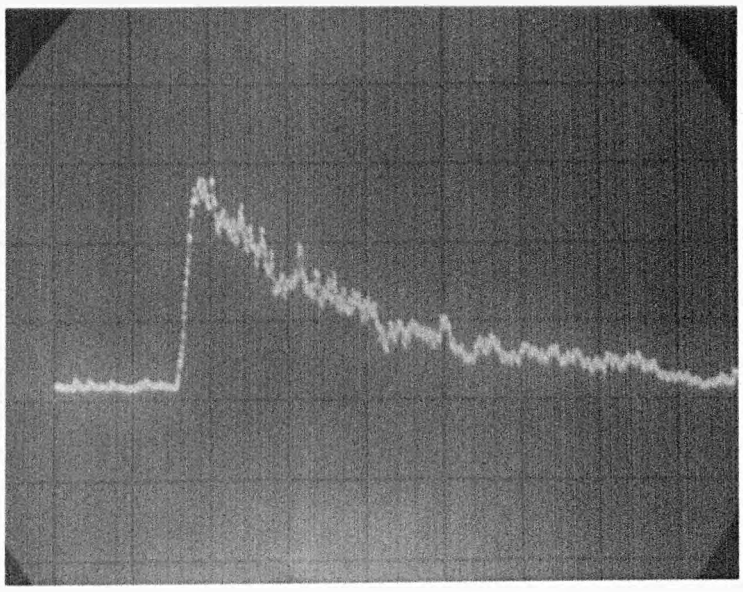

(b) At 762 nm. Run No. 914.

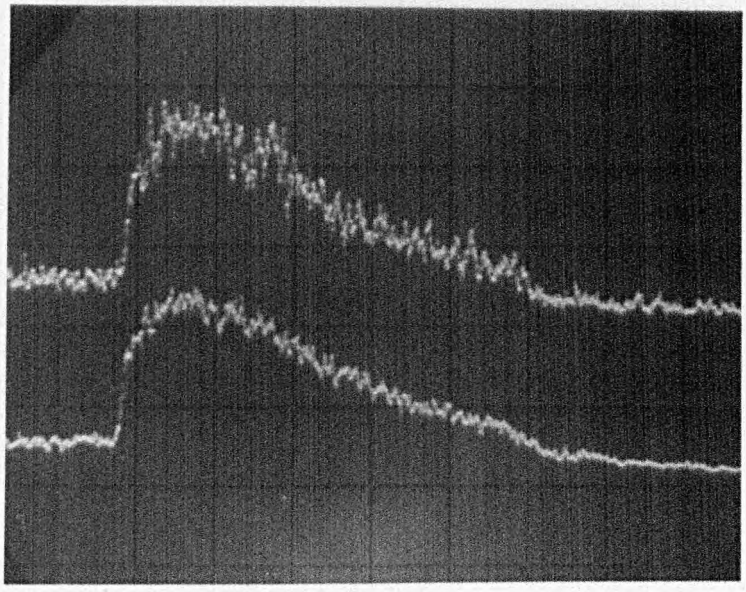

For analysis of shocks at 762 nm, the equation used is:

$$^{762}I_2 = \frac{^{762}I_1}{\Delta t}\left(\frac{\rho_2}{\rho_1}\right)\left\{\frac{Ke^{At}}{A}(1-e^{-A\Delta t}) + \frac{1-K}{A-k_q'}\cdot(1-e^{-(A-k_q')\Delta t})\, e^{(A-k_q')t}\right\} \qquad 8.14$$

where (I_2,t) are the coordinates of the points on the trace, I_1 is the measured preshock glow, and (ρ_{2/ρ_1}) and (T_{2/T_1}) are calculated from the shock speed and shock equations (chapter 3).

The parameters in these equations, K, an enhancement factor; A, to describe the decay of excited species along the tube; k_q' a pseudo first order rate constant to describe the relaxation zone; and Δt, the integration time necessary to correct for the finite rise time of the system, are first found approximately by analysing the trace in parts using an interactive graphics routine. Better values of the parameters are obtained by an iterative non linear least squares routine, and a final line is calculated and displayed across the trace. A flow diagram of the programme is shown in figure 6.1. The values of the parameters, together with their errors are printed out, and the graphical display is stored for later "off line" plotting. At any stage in the analysis, the operator may intervene, but, more importantly, he can assess the fit of the parameters generated as the programme progresses.

The photomultiplier output is not only displayed on an oscilloscope, but digitized by the transient recorder into 1024 points across the time scale, and output to paper tape. The paper tape is fed into the 4130 computer (I.C.L.) using a programme called TRANS where the coordinates of all the points in millivolts and microseconds are calculated from the sweep speed and sensitivity valves of the

Figure 6.1.

A Flow Diagram for the Interactive Computer Graphics Program.

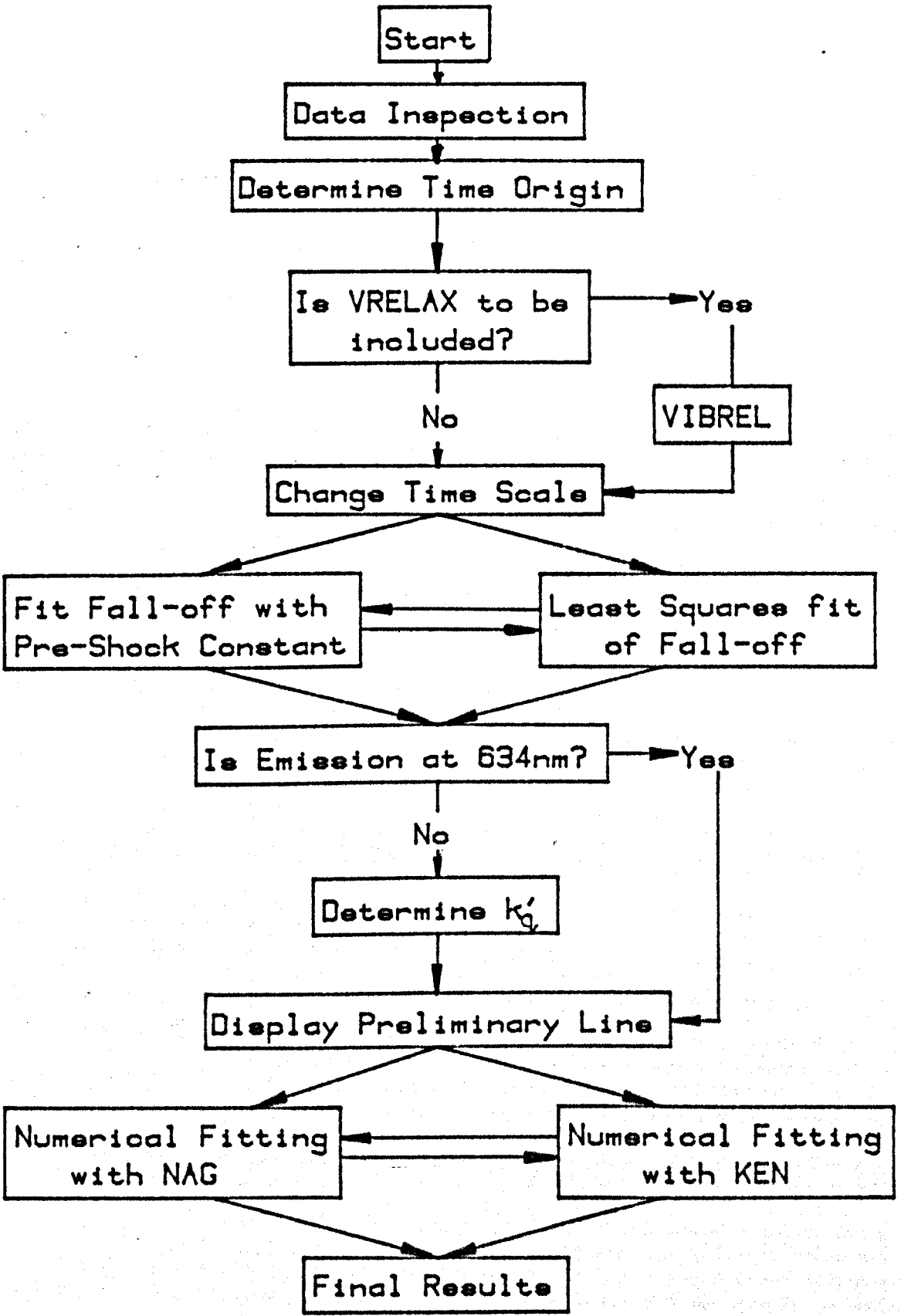

transient recorder which head the paper tape. The coordinates are stored in a disc file and can be called up as required for analysis by the main programme GRAPH2.

The steps in the initial analysis are shown in figure 6.2 and the programme is described in sections labelled with the names of the major subroutines.

Figure 6.2. Initial Steps in the Analysis of the Shock Emission.

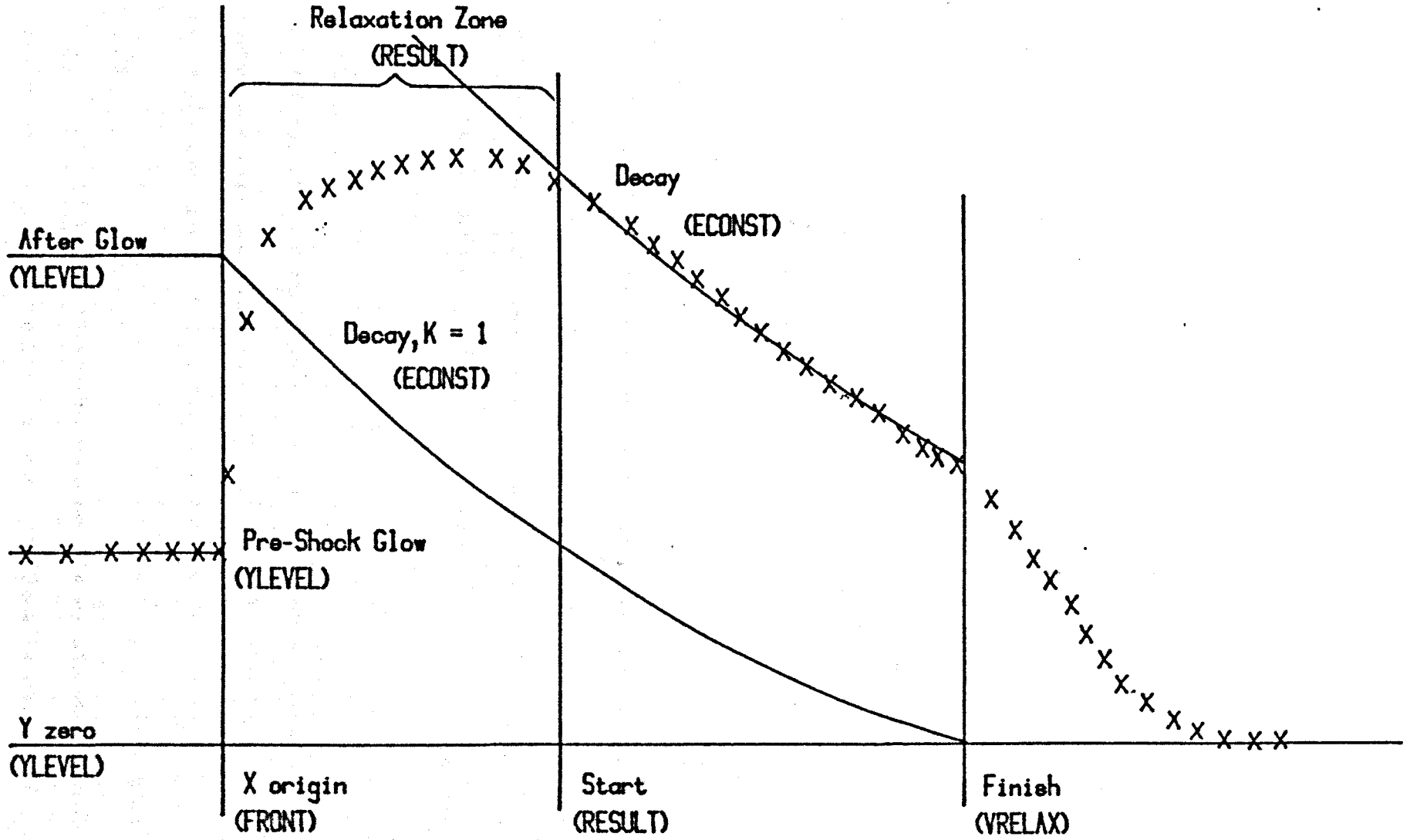

6.2. BEGIN

BEGIN calls up the run number specified on an input data card from the disc storage, and the points are displayed in graphical form on a graphical display unit (G.D.U.).

The points are inspected, and any unwanted ones can be rejected. Normally points are only rejected at the end of the trace if there is a long tail beyond the end of the shock, though some fast shocks show odd spurious peaks towards the end of the hot flow time. These can be removed by the operator using a light pen to mark the region where the points are to be rejected. The peaks may be due to conbustion in the tube from dirt on the walls, or small pieces of diaphragm material being swept past the detector. These traces yield reasonable results, but the peaks are often an indication that the tube needs to be cleaned.

6.3. FRONT

The time origin is set with the light pen as the beginning of the sharp initial rise at the shock front. An area round the light pen is enlarged in the top right hand area of the screen so it is possible to set X origin to within one data point (figure 6.3) or better than ± 1 μs.

6.4. DIVIDE

DIVIDE selects alternate points for analysis as the programme is lengthy and time consuming with 1024 points. The loss of accuracy is very small compared to the overall accuracy of the analysis.

6.5. VRELAX

The subroutine VRELAX gives the operator the option of studying the effects of vibrational relaxation where the density ratio and shock temperature are changing across the time scale behind the

Figure 6.3.

Setting the Time Origin.

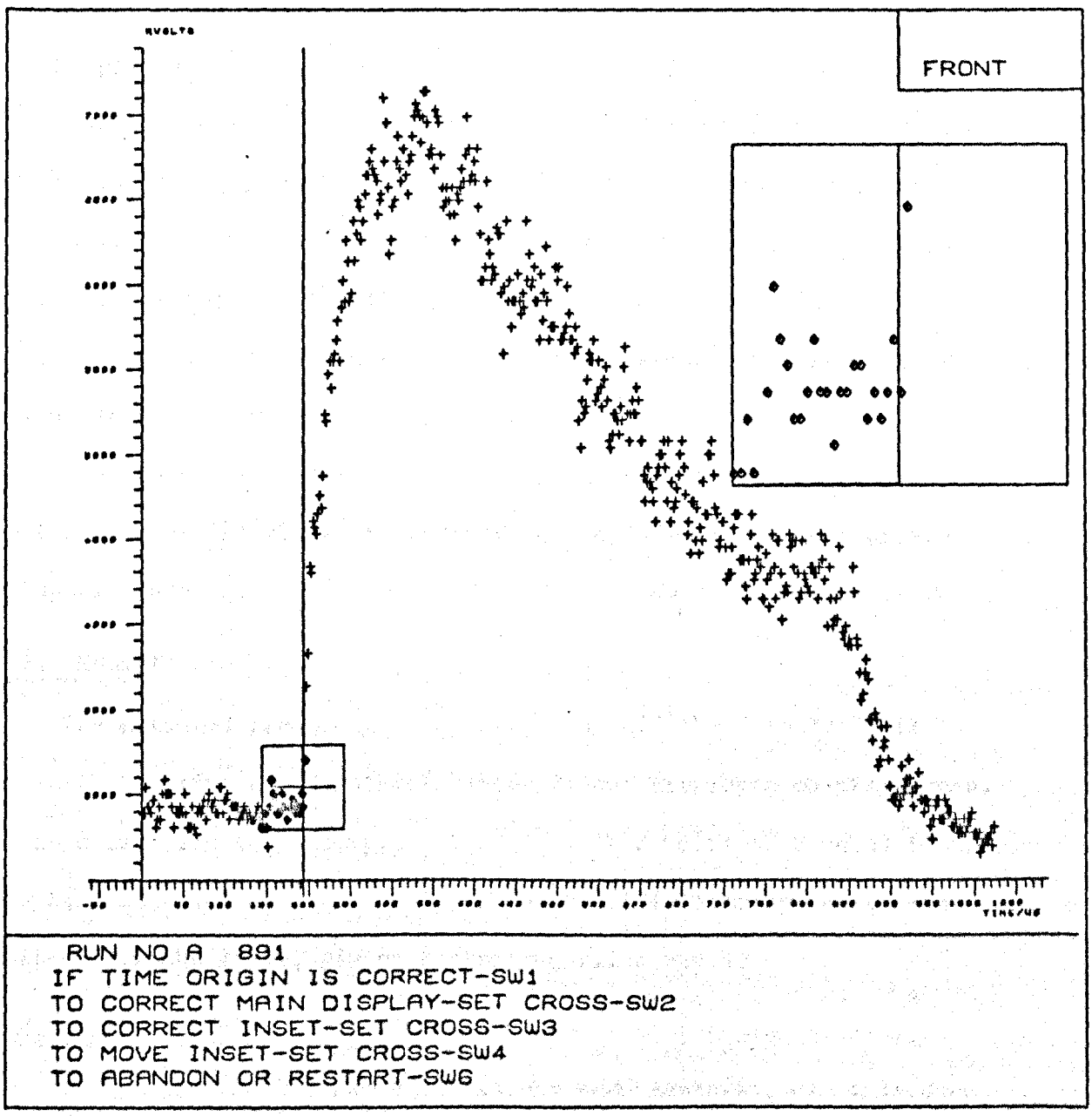

shock front (chapter 8). The laboratory time scale is changed to the particle time scale for the rest of the analysis, and the end of the analysis region (Finish) is set with the light pen.

6.6. YLEVEL

An average Y value for all the points before X origin is found and a line drawn through the points. The level of this line corresponds to the pre-shock glow, and from the measured value read in from the data card for the run, a Y zero line is calculated and drawn. If the end of the shock is on the trace, the Y zero line should go through the points, and is a good check on the measured value of the pre-shock glow. It is possible for the operator to change the position of the Y zero line, but in all shocks where the end was on the trace, this was unnecessary and this option was not used.

A value for the after glow, the emission at the shock front due to the compression alone, is calculated and indicated on the screen (chapters 7 and 8).

6.7. ECONST

The measured pre-shock decay rate read off the data card, is converted to time coordinates (chapter 7) and displayed on the points. It is drawn from the afterglow, that is with a value of K equal to one. The line is moved up with the light pen until it corresponds to the fall-off on the trace, giving a starting value for K.

6.8. ECALC

If the pre-shock decay rate has not been measured, or if it does not fit the points well, a calculated value can be found by fitting an exponential curve to the experimental points in the fall-off region chosen by the operator.

Normally the measured decay rate is a good fit, and is used without alteration.

6.9. RESULT

The quenching rate constant at the shock temperature is derived from the shape of the relaxation zone for traces at 762 nm, the region between X origin and a start specified with the light pen by the operator, beyond which the decay line fits the fall-off on the trace (figure 6.2).

If the overall decay of excited species down the tube is removed from the trace by division the points will follow a normal relaxation curve, where the relaxation time is the time for the intensity to reach (1-1/e) of the maximum value.

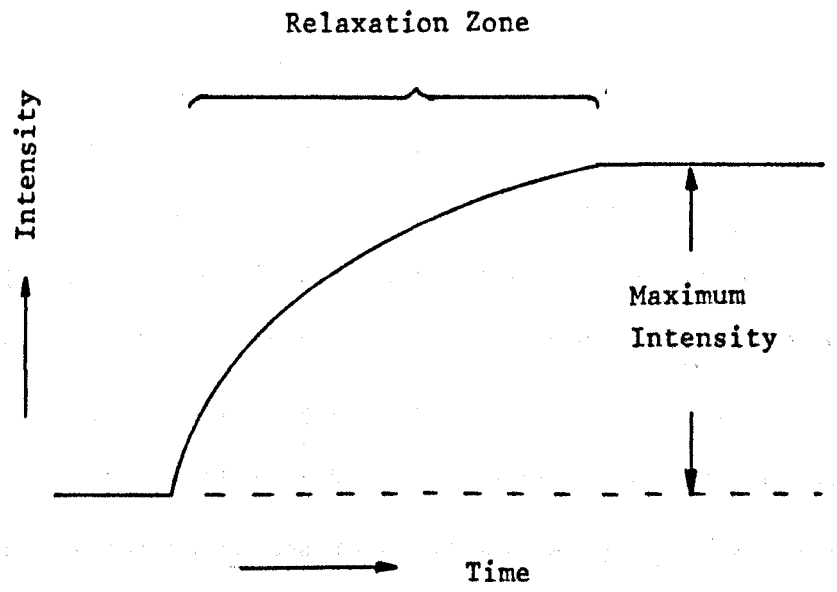

In RESULT the relaxation time is found from the relaxation zone by first order analysis; it is the reciprocal of k_q'. The points are displayed as a normal relaxation curve and the calculated line drawn on them so the operator can assess the fit.

If K is nearly one, the relaxation zone is poorly defined, and the programme can proceed into FINALD. RESULT is bypassed for the analysis of traces at 634 nm.

The programme will not run if the relaxation is to a smaller intensity, that is when K is less than one, but values of K, Δt and A can still be found.

6.10. FINALD

The complete integrated equation (equation 7.6 . or 8.14.) is calculated from the approximate values found and an integration time of of 16 μs (laboratory time scale), and drawn on the screen together with the experimental points. The line is usually a reasonable fit, but at this stage the operator can change the value of any parameter if necessary.

The values of the parameters are improved by an iterative non-linear least squares routine. Two fitting programmes are available, KENFIT developed by Dr. K. Newman using Newton's method[122], and NAGFIT from the Nottingham University Algorithms Library[123]. Both fitting routines minimise the sum of the squares of the residuals when the calculated emission is subtracted from the experimental value at each point. They require the differentials with respect to each parameter. The differentiation is complicated by the integration time in the region of the shock front, and different equations are necessary when t > X origin >t + Δt, where t=0 at X origin and Δt is negative. A later modification to this part of the programme calculated the differentials numerically.

The values of the parameters found with KENFIT were generally a good fit to the experimented points, and this method was preferred. However, it could be unstable, and sometimes the values diverged and the iteration had to be stopped by the operator. NAGFIT iterated quickly to self consistent values of the parameters, but in some cases the values were not a good fit to the experimental points. NAGFIT was found to be a useful routine to get better starting values for

inclusion into KENFIT.

Normally self consistent values were obtained after 3 to 10 iterations. After each iteration the new values were displayed on the screen together with the previous values for comparison. The iteration could be stopped at any time, and the calculated line displayed or not as the operator wished.

6.11 PRPLOT

When the operator is satisfied with the values of the parameters and the fit of the calculated curve to the experimental prints, the values of the parameters are printed out and the graphical display stored for off-line plotting later. A sample print-out is shown in figure 6.4 and plot in figure 6.5.

The programme was written for this work by Dr. P. Borrell[124], and the subroutine VRELAX to include vibrational relaxation by Dr. M.D. Pedley[110], and modified by the author.

Figure 6.4. Sample Printout of the Results from a Shock.

```
        ANALYSIS FROM GRAPHICAL DISPLAY                          25 05 78

        RUN NUMBER A  910    SIGMA RUN                           FITTED BY KEN

  RESULTS                                                        VIBRATIONAL RELAXATION INCLUDED

FITTED      QUENCHING CONST     :    0,008601  ERROR    0,000679 USEC-1  116,26410  ERROR   9,17961   USEC
FITTED      RATIO(K)            :    2,183641  ERROR    0,026663
PROVIDED    DECAY CONSTANT      :   -0,001400   USEC-1                          -0,01050  CM-1
FITTED      INTEGRATION TIME    :   52,669579  ERROR    3,708118 USEC

  RATE CONSTANTS

FITTED      ENERGY POOLING(K1)  :  0,6987E+06  ERROR 0,8531E+04 L MOLE-1 S-1      LOG(K1) = 5,844
FITTED      COLL. QUENCHING(K2) :  0,4398E+07  ERROR 0,3473E+06 L MOLE-1 S-1      LOG(K2) = 6,643

  DATA PROVIDED

        PRE-SHOCK GLOW-GIVEN :    458,00    USED   458,00
        AFTER GLOW     GIVEN :   2683,83    USED  2683,83

        ROAVG =  5,820   TAVG = 1472,   SPEED =     0,1608 CM/US   PERCENT OXYGEN = 100,00
        X ORIGIN =   646,73 US
        Y ORIGIN =  1391,46 MVOLTS

        NO OF ITERATIONS =  5                                NO OF DATA POINTS =  350

        SUM OF THE SQUARES OF THE RESIDUALS = 0,29074E+08

        FITTING COMPLETED
```

Figure 6.5.

A Computer Plot of the Analysis of a Shock.

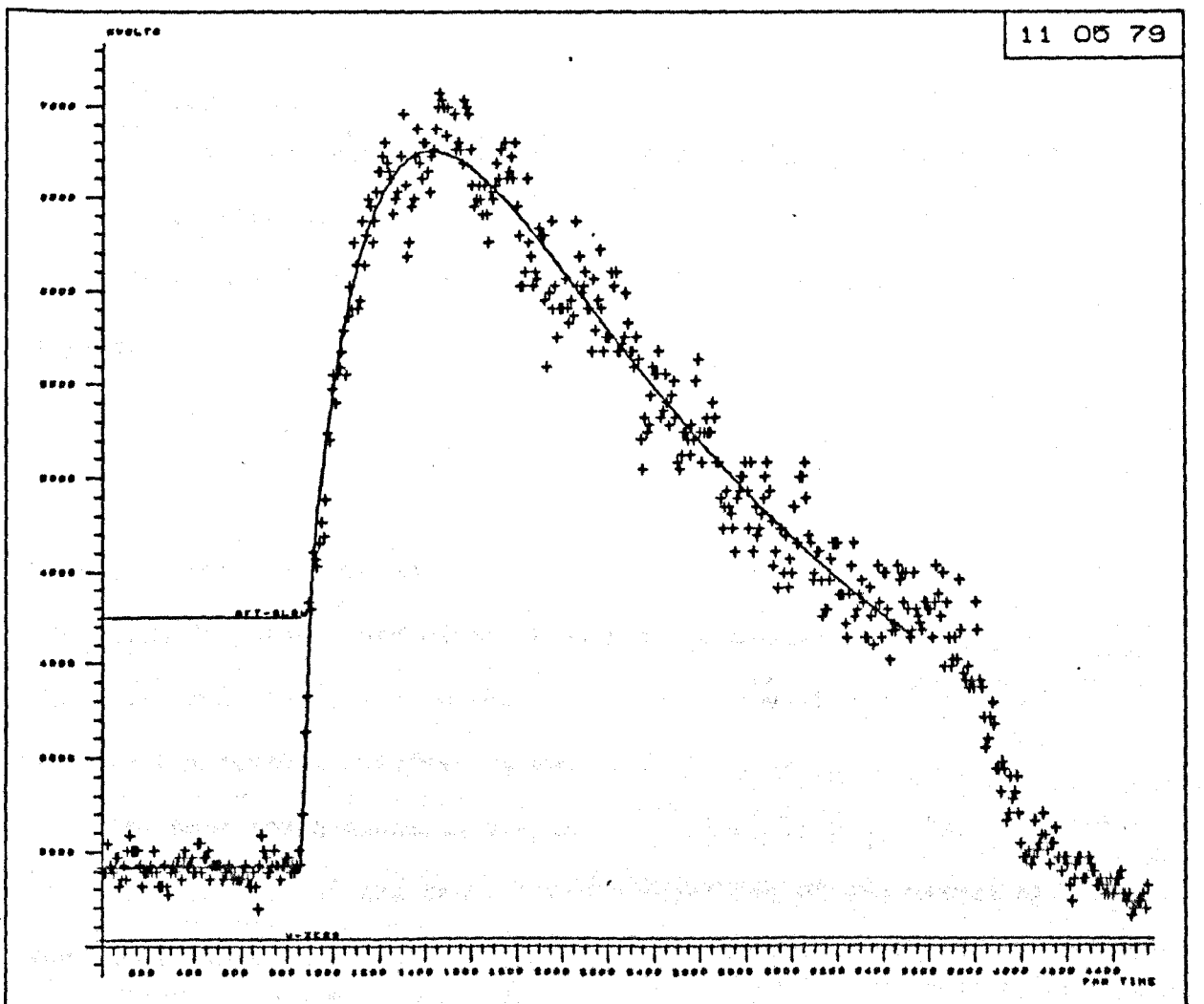

RUN NO A 891 SIGMA FITTED BY KEN RELAXATION NOT INCLUDED

QUENCHING CONST	: .0028279	ERR .0001366	FITTED
RATIO (K)	: 3.903393	ERR .0853645	FITTED
DECAY CONSTANT	: -.000536	ERR .0000121	FITTED
INTEGRATION TIME	: 49.34058	ERR 3.972732	FITTED

Chapter 7

High Temperature Studies of the dimol emission at 634 nm from $O_2(^1\Delta_g)$

7.1. Introduction

The dimol emission, at 634 nm between two $O_2(^1\Delta_g)$ molecules is followed by photomultiplier/filter combinations at the high temperature attained when a shock is run into flowing discharged oxygen.

$$O_2(^1\Delta_g) + O_2(^1\Delta_g) \rightarrow 2O_2(^3\Sigma_g^-) + h\nu(\lambda = 634\ nm) \qquad 7.1$$

Shocks of different speeds are run with different thicknesses of aluminium diaphragms and either helium or nitrogen as driver gas. The test pressure is kept within a limited range (6.5 ± 0.5 torr) and the temperature attained is 600 to 1620 K.

The post shock emission has the form shown in plate 3a, detailed analysis of the trace reveals something of the nature of the dimol emission, and the temperature dependence of the deactivation of $O_2(^1\Delta_g)$.

7.2. Treatment of Results.

7.2.1. The Emission Trace at the Shock Temperature.

$O_2(^1\Delta_g)$ is formed in or just after the discharge, the concentration of $O_2(^1\Delta_g)$ decreases as the gas flows along the tube due to collisional quenching with oxygen, and deactivation on the walls (Chapter 5). The dimol emission intensity at 634 nm during a shock has the form shown below.

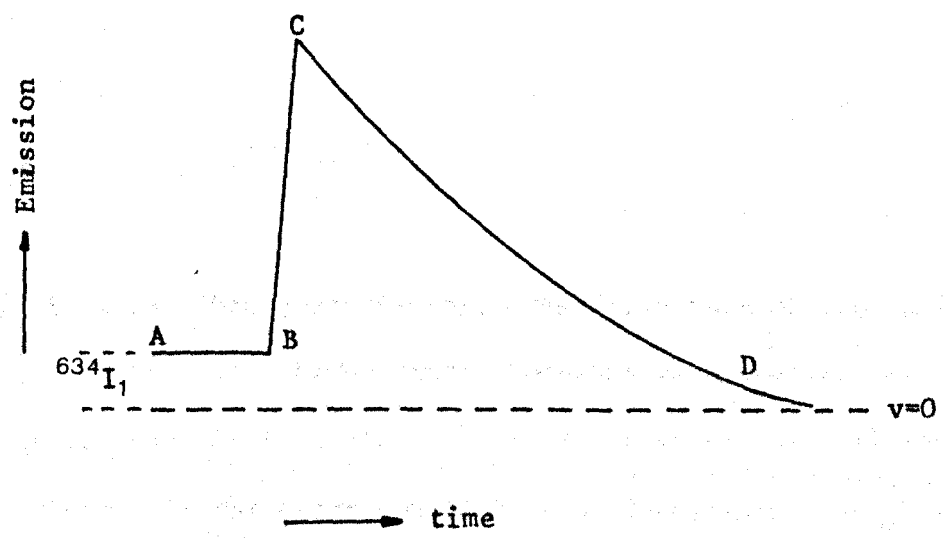

At the shock front, the initial compression and rise in temperature is shown as an increase in emission, BC, followed by a fall-off, CD, seen as the gas downstream of the observation station, with its decrease in concentration of $O_2(^1\Delta_g)$, is swept past the detector behind the shock front. Any deactivation of $O_2(^1\Delta_g)$ at the high temperature is superimposed on this fall-off. The trace is analysed using the following model.

At the shock front, the initial rise in emission $^{634}I_2^0$ is related to the pre-shock glow, $^{634}I_1$, by:

$$^{634}I_2^0 = {}^{634}I_1 \left\{\frac{\rho_2}{\rho_1}\right\}^2 \left\{\frac{T_2}{T_1}\right\}^{\frac{1}{2}} \qquad 7.2$$

as expected for a simple collisional process involving two emitting molecules where, (ρ_2/ρ_1) is the density ratio, and (T_2/T_1) is the temperature ratio. Any enhancement in emission at the high temperature can be taken into account and the experimental rise fitted to:

$$^{634}I_2^0 = {}^{634}I_1 \; K\left\{\frac{\rho_2}{\rho_1}\right\}^2 \left\{\frac{T_2}{T_1}\right\}^{\frac{1}{2}} \qquad 7.3$$

where K is an enhancement factor. The decay rate of the excited species at the shock temperature, together with the initial preshock change in concentration along the tube has an exponential form, e^{At}, where A is the decay constant, and is negative. The whole shock trace can then be fitted to:

$$^{634}I_2 = {}^{634}I_1 \; K\left\{\frac{\rho_2}{\rho_1}\right\}^2 \left\{\frac{T_2}{T_1}\right\}^{\frac{1}{2}} e^{At} \qquad 7.4$$

Experimentally, the initial rise at the shock front is not instantaneous, due to the finite slit width and the rise time of the photomultiplier. The equation is integrated to take this into account:

$$\frac{1}{\Delta t}\int_{t-\Delta t}^{t}\frac{^{634}I_2}{^{634}I_2^0}\,dt = \frac{1}{\Delta t}\int_{t-\Delta t}^{t} K\,e^{At}\,dt \qquad 7.5$$

where Δt is the integration time. This gives:

$$^{634}I_2 = \frac{^{634}I_1\,K}{A\,\Delta t}\left\{\frac{\rho_2}{\rho_1}\right\}^2\left\{\frac{T_2}{T_1}\right\}^{\frac{1}{2}} e^{At}\left\{1 - e^{-A\,\Delta t}\right\} \qquad 7.6$$

and the experimental points, ($^{634}I_2$, t), are fitted to this equation (Chapter 6).

For each shock at the high temperature T_2, the results are values of K and A. The value of the integration time, Δt, is constant for shocks of the same speed and same photomultiplier slit width.

7.2.2. Comparison of Pre and Post Shock Decay Rates.

Before the shock, the decay rate of excited species along the tube is measured as a function of length, $\frac{d\ \ln I}{d\ell}_1$. The shock decay rate, A, is calculated as a function of time at temperature T_2;

$$A = \frac{d\ \ln I_2}{dt_p} \qquad 7.7$$

where the time is particle time, that is the time elapsed from when the gas is shocked, to when it passes the observation station. The experimental measurements are made in laboratory time, t_ℓ, that is the time elapsed between the passing of the shock front to the arrival of the gas.

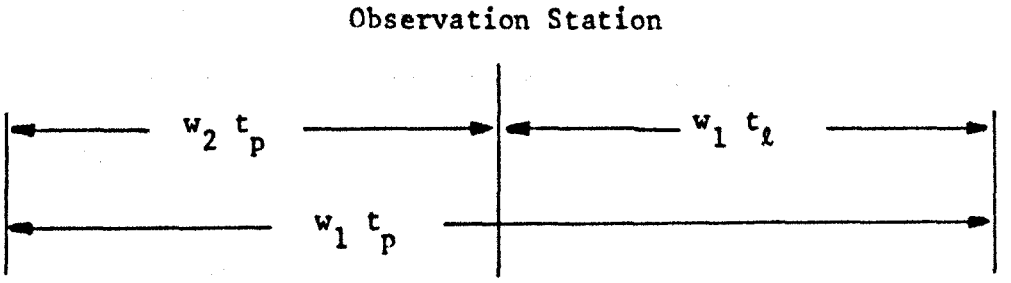

point at which gas was shocked

point where shocked gas is now

position of shock front now

The distances apart of the shock front and the shocked gas at the observation station are shown above, where w_1 is the speed of the shock front, and w_2 is the speed of the shocked gas (see figure 3.6). Then:

$$w_1\ t_p = w_2\ t_p + w_1\ t_\ell \qquad 7.8$$

In shock coordinates, the measured shock speed u_1 is:

$$u_1 = -w_1 \quad \text{and} \quad u_2 = -(w_1 - w_2)$$

and from equation 3.4:

$$\frac{t_p}{t_\ell} = \frac{u_1}{u_2} = \frac{\rho_2}{\rho_1} \tag{7.9}$$

The distance travelled by the shocked gas is $w_2\, t_p$ and:

$$w_2\, t_p = w_1(t_p - t_\ell) = w_1\, t_p(1 - \rho_1/\rho_2) \tag{7.10}$$

$$\ell = u_1\, t_p(1 - \rho_1/\rho_2) \tag{7.11}$$

The calculated decay rate, A, can now be changed to the same coordinates as the measured pre-shock decay rate, so that the two can be compared directly; these values are listed in the tables of results.

$$\frac{d \ln I_2}{d\ell} = \frac{d \ln I_2}{dt_p} \Big/ \left[1 - \frac{\rho_1}{\rho_2}\right] u_1 \tag{7.12}$$

$$= A \Big/ \left[1 - \frac{\rho_1}{\rho_2}\right] u_1 \tag{7.13}$$

7.2.3. Calculation of the High Temperature Decay Rate of $O_2(^1\Delta_g)$ from the Shock Decay Rate.

At room temperature, the change in concentration of $O_2(^1\Delta_g)$ along the tube can be discribed at time t by (Chapter 5):

$$\frac{^1[O_2(^1\Delta_g)]}{^1[O_2(^1\Delta_g)]_0} = e^{-(k_q[O_2] + k_w)t} \qquad 7.14$$

$$= e^{-k_{obs}\, t} \qquad 7.15$$

and at length ℓ by:

$$\frac{^1[O_2(^1\Delta_g)]}{^1[O_2(^1\Delta_g)]_0} = e^{-\alpha\ell} \qquad 7.16$$

where $\alpha = d\ \ln I_1/d\ell$.

At the shock temperature, the change in concentration of $O_2(^1\Delta_g)$ along the tube at any given particle time, t_p, is:

$$\frac{[O_2(^1\Delta_g)]}{[O_2(^1\Delta_g)]_0} = e^{-\alpha\, w_2\, t_p} \qquad 7.17$$

$$= e^{-\alpha\, u_1(1 - \rho_1/\rho_2)t_p} \qquad 7.18$$

At any point in the tube however, the concentration of $O_2(^1\Delta_g)$ pre-shock is constant.

If there is any change in the quenching rate of $O_2(^1\Delta_g)$ at the higher shock temperature, T_2, then at time, t_p;

$$\frac{[O_2(^1\Delta_g)]_{T_2}}{[O_2(^1\Delta_g)]} = e^{-k_{T_2}[O_2]t_p} \qquad 7.19$$

Where k_{T_2} is the quenching rate constant for $O_2(^1\Delta_g)$ by oxygen at temperature T_2. The wall deactivation is omitted from equation 7.19 as it becomes an insignificant mode of deactivation of $O_2(^1\Delta_g)$ at the high shock density where the wall temperature remains at T_1.

The overall deactivation of $O_2(^1\Delta_g)$ at the shock temperature is the measured shock decay rate, A:

$$\frac{[O_2(^1\Delta_g)]_{T_2}}{[O_2(^1\Delta_g)]_0} = e^{At} \qquad 7.20$$

So:

$$-A = k_{T_2}[O_2] + \alpha u_1(1 - \rho_1/\rho_2) \qquad 7.21$$

From this equation, the pseudo first order rate constant for the collisional quenching of $O_2(^1\Delta_g)$ by oxygen at the shock temperature, $k_{T_2}[O_2]$, can be calculated from the difference in decay rates measured pre-shock, α, and at the shock temperature, A. The second order rate constant is obtained by dividing by the concentration of oxygen, in torr, at the higher pressure behind the shock front.

$$[O_2] = \frac{P_2}{760}\ \frac{273}{T_2}\ \frac{1}{22.4}\ \text{mol}\ \ell^{-1} \qquad 7.22$$

7.3. Results.

An oscillograph of a typical shock experiment is shown in figure 7.1. The shape fits the model postulated at the beginning of this chapter. A computer plot of the result is shown in figure 7.2. The experimental points are displayed, and the calculated line from equation 7.6 using the computed parameters fits well.

The results are listed in tables 7.1 and 7.2. The flow rate for experiments listed in table 7.1 was 17.5 ml s^{-1} at 1 atmosphere pressure, the pre-shock decay rate was measured using the 762 nm emission (Chapter 5). The experiments listed in table 7.2 are the controls for the vibrational relaxation studies at 579 nm (Chapter 10). In these shocks, it was important that the relative photomultiplier positions were fixed, and pre-shock decay measurements were not made. The control 634 nm results of Mr. Kevin Grant for the vibrational relaxation studies are not listed here, but they are included in figure 7.3. In all these shock the flow rate was maintained at 28 ml s^{-1} at 1 atmosphere pressure.

The initial experiments in the discharge flow shock tube observed the 634 nm dimol emission, and although accurate analysis was not possible before the transient recorder was bought, hand analysis suggested that K was approximately equal to one in the temperature range 1150 to 1450 K.

The enhancement factor, K, is plotted against shock temperature for all analysed runs at 634 nm, in figure 7.3. For a simple collisional process, K (equation 7.3) would be equal to one. Figure 7.3 shows that K is approximately equal to one at low temperatures (600 to 1100 K) as expected if the dimol emission is a simple collisional process. Then there is a systematic increase

Figure 7.1.

The Shock Emission at 634 nm.

Run No. 6.

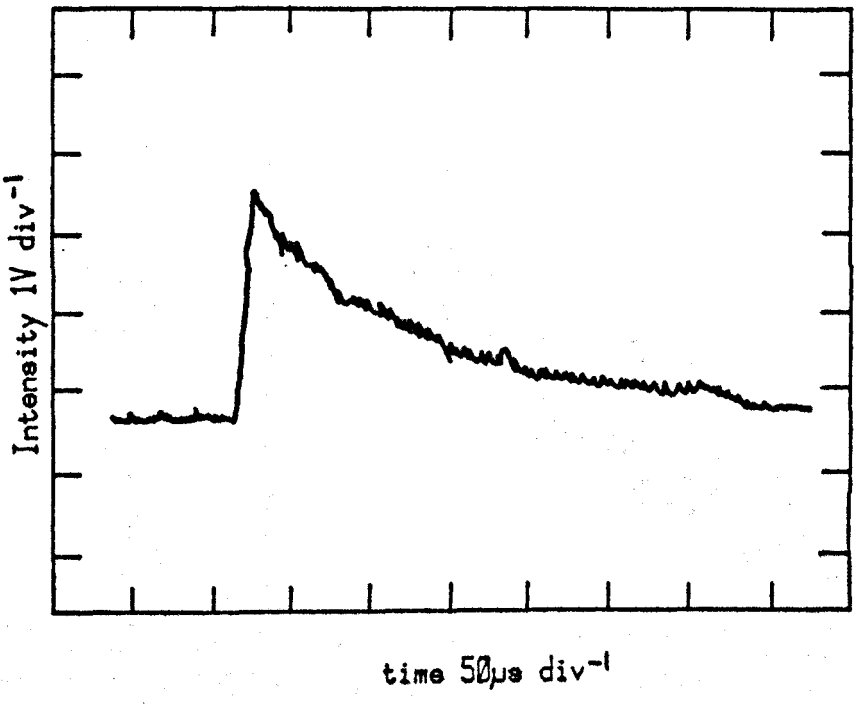

Figure 7.2.

A Computer Plot of an Emission Trace at 634 nm.

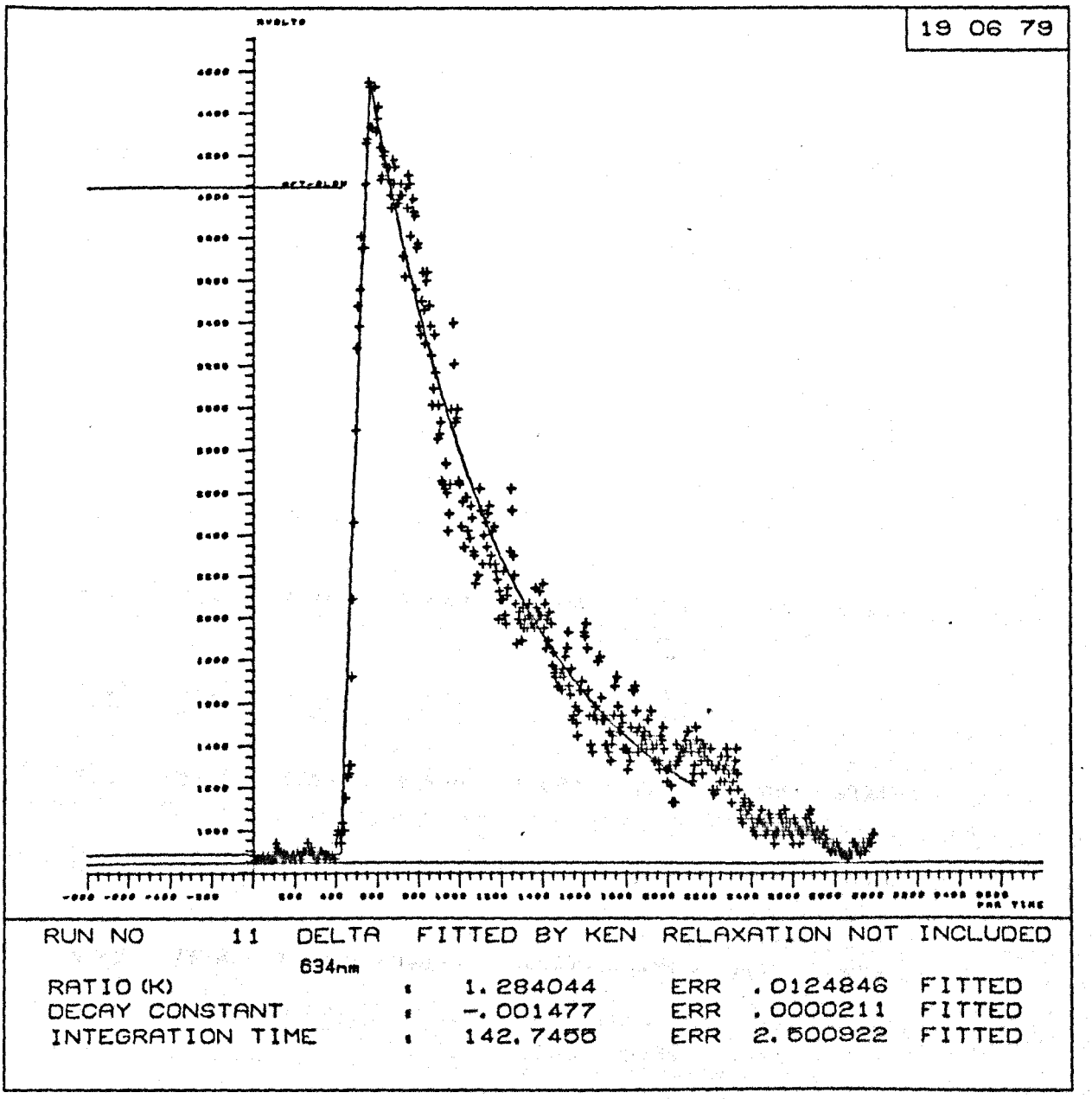

Table 7.1.

Results of the Analysis of Shocks at 634 nm into 100% Oxygen.

	Pre Shock Measurements						Post-Shock	
Run No.	P_1 /torr	Glow /mV	Decay /m^{-1}	Speed /km s^{-1}	ρ_2/ρ_1	K	Decay /m^{-1}	T_2/K
758	6.30	15.6	-	1.609	5.862	1.19	1.31	1458
771	6.2	13.6	1.04	1.586	5.821	1.30	1.04	1426
791	6.5	5.3	1.13	1.586	5.833	1.24	1.13	1426
793	6.4	6.4	1.03	1.593	5.833	1.39	1.08	1435
795	6.5	6.0	1.11	0.947	3.763	0.83	1.31	751
805	6.3	4.5	1.01	0.874	3.537	0.89	1.09	638
807	6.6	5.3	1.08	1.687	5.999	1.54	1.16	1569
821	5.95	28.7	0.90	1.438	5.527	1.16	1.20	1230
823	6.6	21.2	1.01	1.520	5.691	1.06	1.09	1333
825	6.0	25.1	1.05	0.875	3.537	0.80	1.14	680
827	5.82	25.4	1.01	0.875	3.537	0.96	1.16	680
828	5.76	45.7	1.00	0.866	3.505	0.90	1.17	671

Table 7.1.(continued)

Results of the Analysis of Shocks at 634 nm into 100% Oxygen.

Run No.	Pre Shock Measurements P_1 /torr	Glow /mV	Decay /m^{-1}	Speed /km s^{-1}	ρ_2/ρ_1	K	Post-Shock Decay /m^{-1}	T_2/K
M126	6.5	7.8	1.00	1.403	5.455	0.92	1.18	1187
M130	6.5	1.44	0.91	1.404	5.455	1.01	1.25	1187
M131	6.5	1.36	0.88	1.724	6.058	2.19	0.74	1621
M137	6.4	30.2	1.33	0.885	3.570	0.74	1.16	698
M139	6.8	20.4	1.29	0.870	3.522	0.83	1.12	676
M140	6.6	21.1	1.29	0.864	3.505	0.91	1.11	671
M145	6.45	22.4	1.09	1.416	5.483	1.11	1.12	1203

Table 7.2.

Results of the Analysis of Shocks at 634 nm.
(Controls for Shocks at 579 nm.)

	Pre Shock Measurements						Post-Shock	
Run No.	P_1 /torr	Glow /mV	Decay /m^{-1}	Speed /km s^{-1}	ρ_2/ρ_1	K	Decay /m^{-1}	T_2/K
930	6.68	28.3	-	1.371	5.029	1.24	1.12	1147
931	6.51	35.0	-	1.586	5.821	1.29	1.08	1426
932	6.18	36.0	-	1.209	4.490	1.09	0.97	1008
933	6.35	37.9	-	1.500	5.67	1.29	1.04	1311
934	6.31	34.0	-	1.371	5.031	1.11	1.09	1148
935	6.39	28.8	-	1.372	5.031	1.19	1.01	1148
936	6.68	29.1	-	1.610	5.864	1.28	1.12	1460
938	6.84	36.8	-	1.350	4.989	1.26	1.21	1122
939	6.76	40.1	-	1.287	4.861	1.15	1.09	1047
940	6.64	45.0	-	1.226	4.729	1.08	1.09	978
941	6.59	44.4	-	1.383	5.051	1.15	1.12	1162
942	6.43	20.6	-	1.586	5.821	1.26	0.83	1426
943	6.84	21.1	-	1.571	5.793	1.24	1.10	1405
944	6.31	21.1	-	1.488	5.368	1.33	1.34	1295

Table 7.2.(continued)

Results of the Analysis of Shocks at 634 nm.
(Controls for Shocks at 579 nm.)

	Pre Shock Measurements						Post-Shock	
Run No.	P_1 /torr	Glow /mV	Decay /m^{-1}	Speed /km s^{-1}	ρ_2/ρ_1	K	Decay /m^{-1}	T_2/K
945	6.35	16.6	-	1.465	5.197	1.14	1.24	1343
946	6.39	4.0	-	1.588	5.824	1.27	0.80	1429
956	6.23	43.1	-	1.386	5.057	1.19	0.98	1165
957	6.39	43.6	-	1.597	5.841	1.24	0.93	1441
958	6.39	44.5	-	1.597	5.841	1.27	0.97	1441
959	6.96	41.0	-	1.573	5.797	1.18	0.96	1408
980	6.55	24.3	-	1.569	5.789	1.35	1.20	1403
981	6.02	26.9	-	1.584	5.817	1.41	1.21	1423
982	6.31	26.7	-	1.310	4.910	1.15	1.10	1074
983	6.14	25.7	-	1.337	4.964	1.15	1.11	1106
985	6.51	48.2	-	1.614	5.871	1.19	0.90	1465
986	6.59	46.5	-	1.597	5.841	1.25	0.97	1441
990	6.84	41.3	-	1.386	5.051	1.05	1.10	1162
998	6.47	24.2	-	1.589	5.824	1.22	1.12	1429

in K at temperatures above 1100 K, to K = 1.39 at 1600 K.

The decay rates of the initial experiments analysed by hand suggested that there was no change between the measured pre-shock decay rate and the shock decay rate. The differences in decay rates for the analysed shocks (table 7.1) are small, and no systematic variation can be discerned. The decay rates are converted to length co-ordinates.

The change in decay rate at the high shock temperature is too small to be measured within the limited hot flow time available for shock-tube measurements, and so the temperature dependence of the collisional quenching rate constant of $O_2(^1\Delta_g)$ by oxygen must be small. The decay rates are shown in figure 7.4. The graph against initial pressure, figure 7.4a, shows a systematic increase in pre-shock decay rate with pressure for the same flow rate as expected, and as found in the room temperature studies (Chapter 3). A similar graph against shock temperature, figure 7.4b, shows no pattern.

Additional evidence for the small temperature dependence can be seen in a comparison of the pre- and post-shock decay rates for shocks at 762 nm, as the decay at 762 nm from $O_2(^1\Sigma_g^+)$ can be used to study the change in concentration of $O_2(^1\Delta_g)$ (Chapter 5). These shocks are listed in table 7.3 with the pre- and post-shock decay rates together with the differences. There is no systematic change in decay rate with temperature, and the quenching rate constant for $O_2(^1\Delta_g)$ is little changed with increasing temperature.

If we assume that a 15% increase in decay rate could be detected in our analysis, then an upper limit of 3.8×10^4 $\ell\ mol^{-1}\ s^{-1}$ at 1570 K for the collisional quenching of $O_2(^1\Delta_g)$ by oxygen can be calculated from equation 7.21 using the pre-shock decay rate of $1.08\ m^{-1}$ from shock No. 807.

Figure 7.3. Variation of K Value with Temperature for the Dimol Emission at 634 nm.

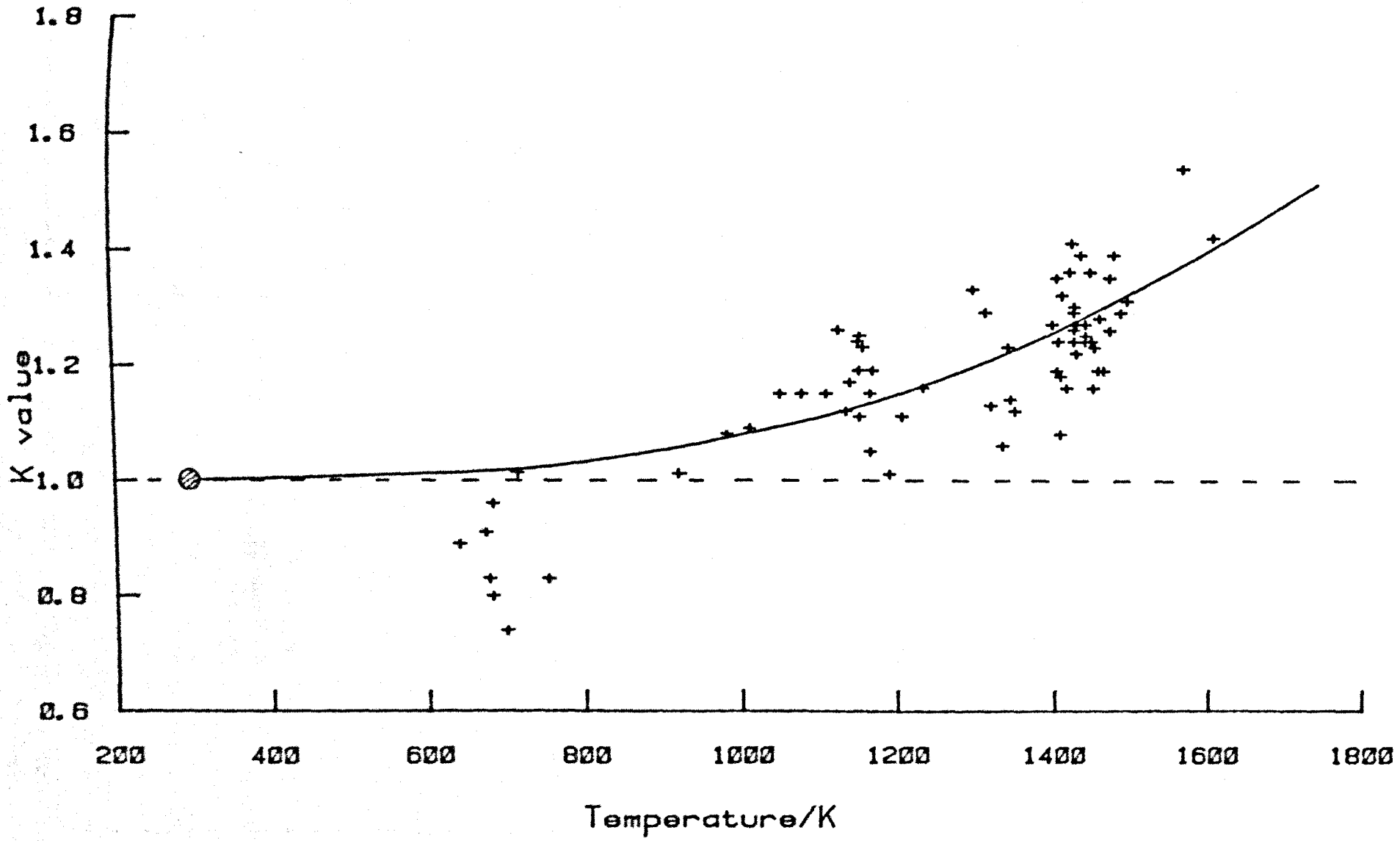

Figure 7.4. Variation of Decay Rates with Pressure and Temperature.

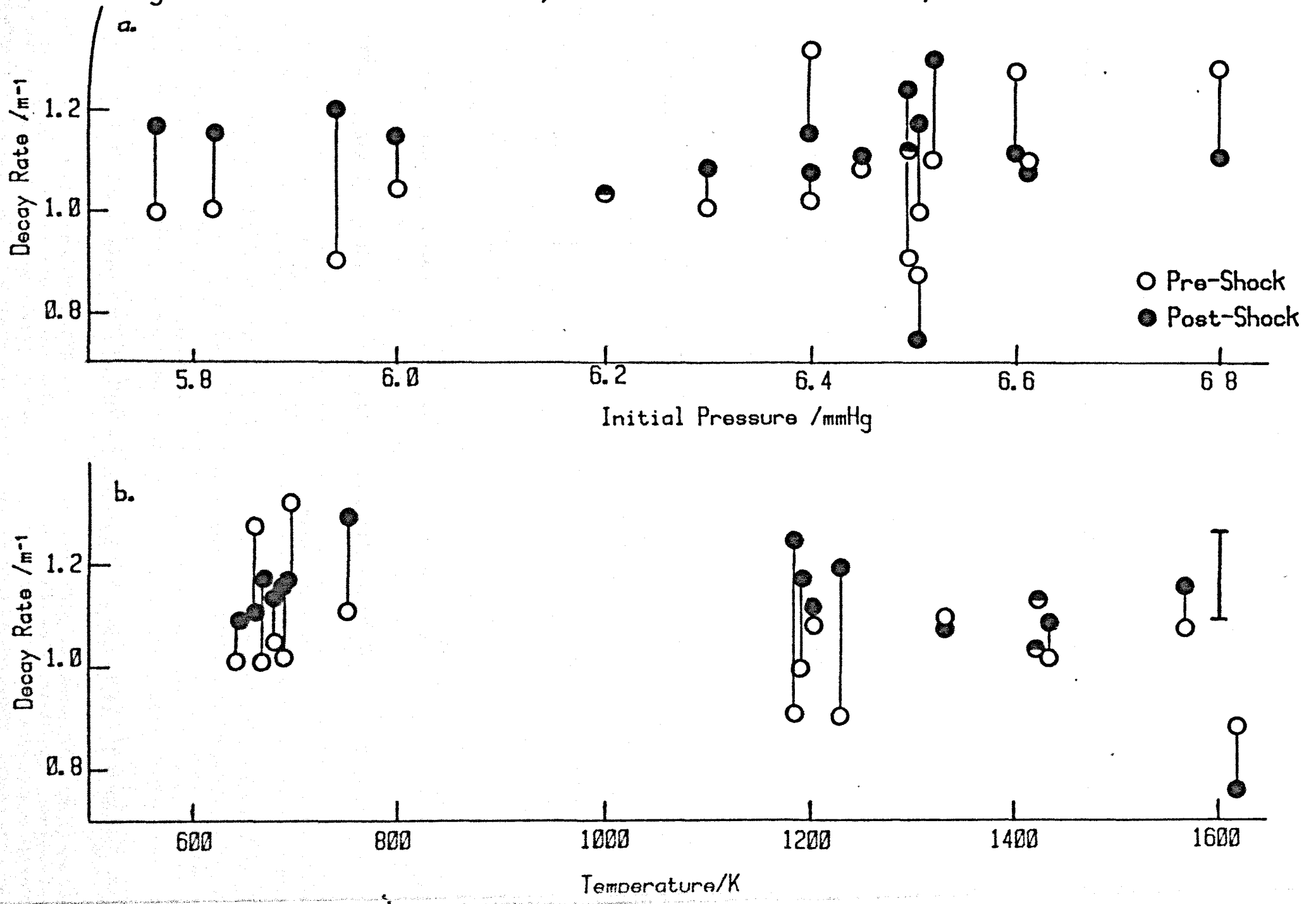

Table 7.3.

Results of the Analysis of Shocks at 762 nm into 100% Oxygen.

Run No.	P_1 /torr	Pre-Shock Decay /m^{-1}	Post-Shock Decay /m^{-1}	T_2/K	Difference in Decay
777	6.5	1.01	1.04	1460	+0.03
797	6.4	1.10	1.15	1480	+0.05
801	6.5	1.09	1.11	1185	+0.02
803	6.4	1.09	0.98	650	-0.11
835	5.8	0.96	1.25	738	+0.29
839	5.65	0.94	1.07	1238	+0.14
853	6.2	1.31	1.35	961	+0.04
854	6.2	1.31	1.61	935	+0.30
855	6.47	1.16	1.08	937	-0.08
856	6.84	1.21	1.38	943	+0.17
870	6.6	1.48	1.39	1054	-0.09
A881	6.2	1.13	1.13	1197	0.0
882	6.5	1.19	1.19	1181	0.0
A884	6.3	1.14	1.18	1449	+0.04

Table 7.3.(continued)

Results of the Analysis of Shocks at 762 nm into 100% Oxygen.

Run No.	P_1 /torr	Pre-Shock Decay /m^{-1}	Post-Shock Decay /m^{-1}	T_2/K	Difference in Decay
M110	6.47	1.07	1.07	1140	0.0
M124	6.47	1.05	1.05	1495	0.0
M125	6.50	1.05	1.08	673	+0.03
M127	6.7	1.09	1.07	681	-0.02
M129	6.5	1.04	1.10	611	+0.06
M146	6.56	1.02	1.05	1220	+0.03
M147	6.41	1.01	1.03	1647	+0.02
M150	6.5	1.09	1.12	1650	+0.03
M151	6.56	1.30	1.30	1608	0.0

7.4. Discussion

7.4.1. The Temperature Dependence of the Dimol Emission at 634 nm.

If the dimol emission at 634 nm (reaction 7.1) is a simple collisional process with a zero activation energy the rate constant will have a (temperature)$^{\frac{1}{2}}$ dependence and the shock emission will fit equation 7.4 with the enhancement factor, K, equal to one. Over the temperature range 600 to 1620 K, this is approximately true, but there is a systematic increase in K at temperatures above 1100 K (figure 7.3).

Arnold, Browne and Ogryzlo[15] studied the dimol emission in the temperature range 323 to 473 K, and they too found only the $T^{\frac{1}{2}}$ temperature dependence of a simple collisional process. They concluded that there was no evidence for the formation of a bound O_4 complex (Chapter 9).

The increase in emission observed at temperatures greater than 1100 K has not a simple temperature dependence. An Arrhenius plot of log K against T^{-1} does not give a straight line (figure 7.5), and a Landau-Teller plot is also strongly curved. One possibility to account for these results would be a variation in transition probability with collisional energy. The more energetic collisions higher up the steep repulsive wall of the potential energy curve for the dimol emission might lead to an increased probability of emission.

There is a second possibility, where an additional route for emission is available at the higher temperatures, and indeed a plot of $\ln(K - 1)$ against T^{-1} does give a straight line (figure 7.6) with an activation energy of 36 kJ mol^{-1}. The nature of any such second mechanism between the two $O_2(^1\Delta_g)$ molecules is, however, uncertain.

Figure 7.5. An Arrhenius Plot of ln K against (Temperature)$^{-1}$

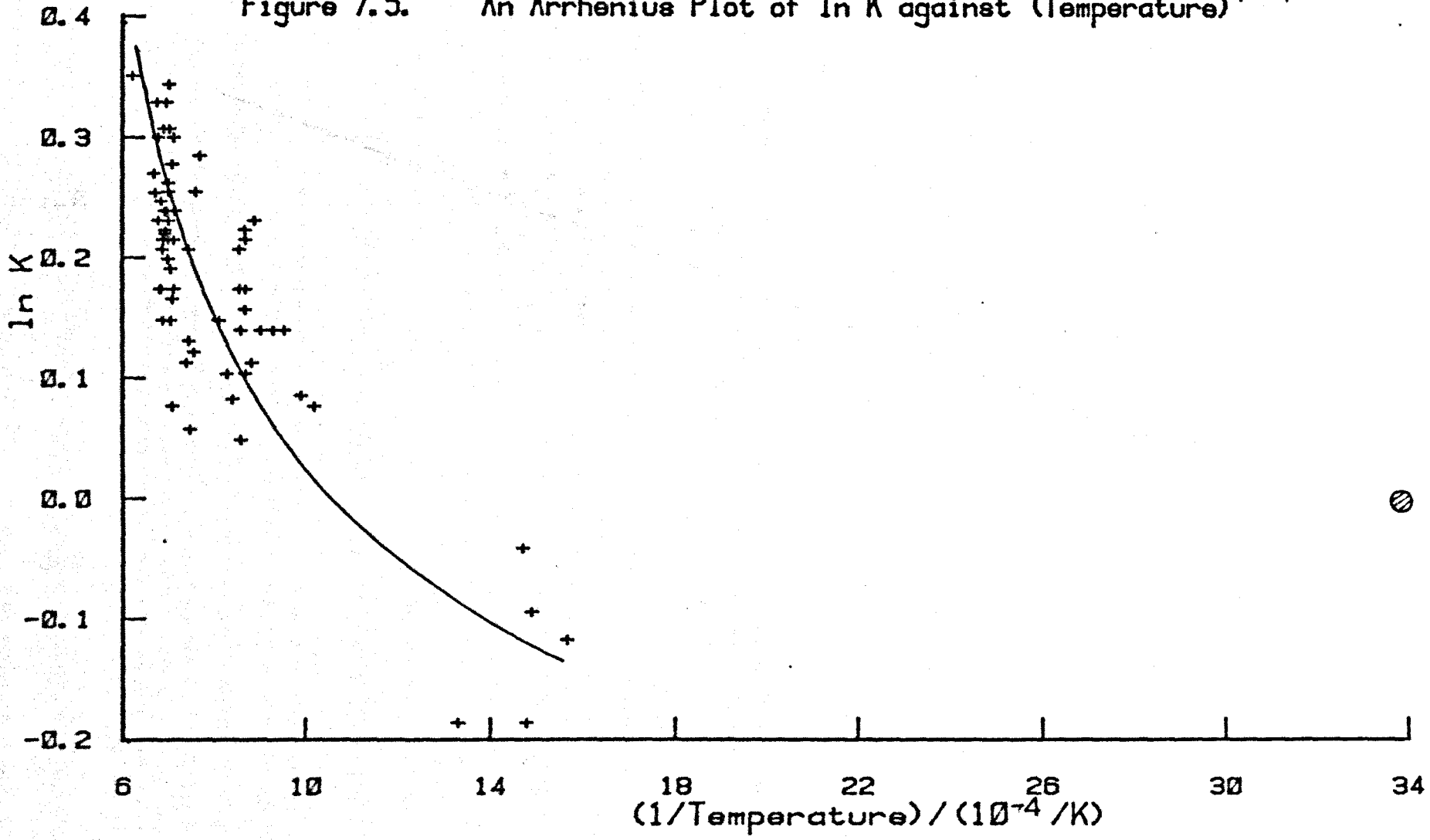

Figure 7.6. Variation of ln(K-1) with (Temperature)$^{-1}$

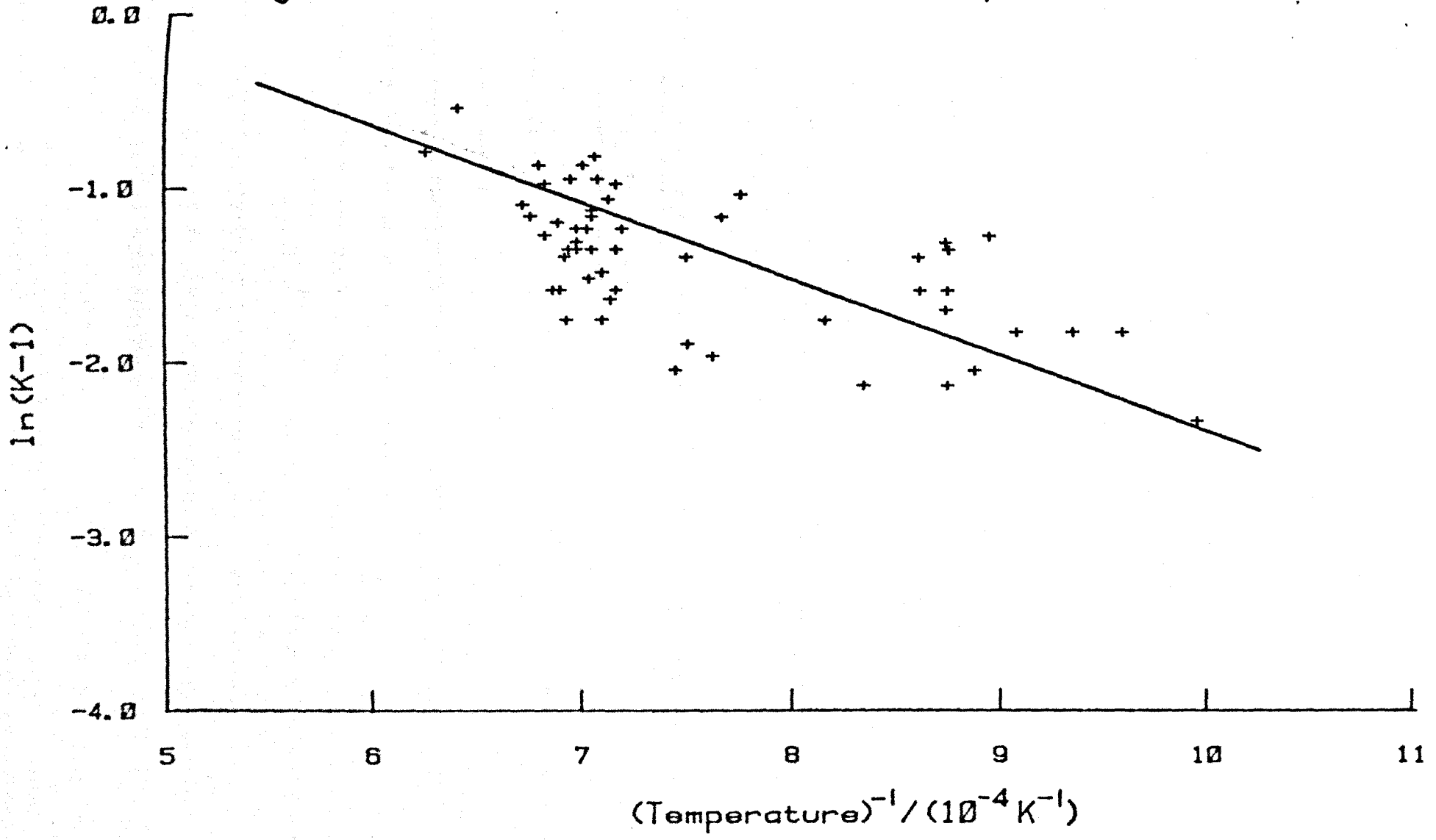

7.4.2. Temperature Broadening of the 634 nm Dimol Band.

Arnold, Browne and Ogryzlo[15] suggested that the 634 nm dimol band broadened with increasing temperature. The band is a wide diffuse band with a half height peak width of 15 to 17 nm.[83,112], and no fine structure. It is viewed in our system with a narrow band filter with a half height peak width of 10 nm and maximum transmittance of 44% at 630 nm. The overlap of the filter with the emission band was assessed by plotting out the band from Bader and Ogryzlo[83] together with the transmittance of our filter (figure 7.7). The filter will transmit 26% of the band (see Section 9.2).

An overall broadening of the 634 nm band could affect the value of K. Some shocks using a broad band filter (625 to 675 nm) gave K values in the same range as with the narrow band filter usually used, and so it appears that temperature broadening of the dimol band at 634 nm does not occur to any significant extent.

7.4.3. The Temperature Dependence of Collisional Quenching of $O_2(^1\Delta_g)$ by Oxygen.

The rate of collisional quenching of $O_2(^1\Delta_g)$ by oxygen does not change very much with increase in temperature, and so it now appears to have been an unsuitable reaction to study in the limited hot flow time available for shock tube measurements. We can, however, give an upper limit to the rate constant of 3.8×10^4 ℓ mol^{-1} s^{-1} at 1570 K.

Findlay and Snelling[35], in the only other study of the temperature dependence of collisional quenching of $O_2(^1\Delta_g)$ by oxygen, worked between 285 and 322 K, and for this small temperature range derived an equation for the rate constant;

Figure 7.7. The 634 nm Dimol Emission Band and the 634 nm Filter.

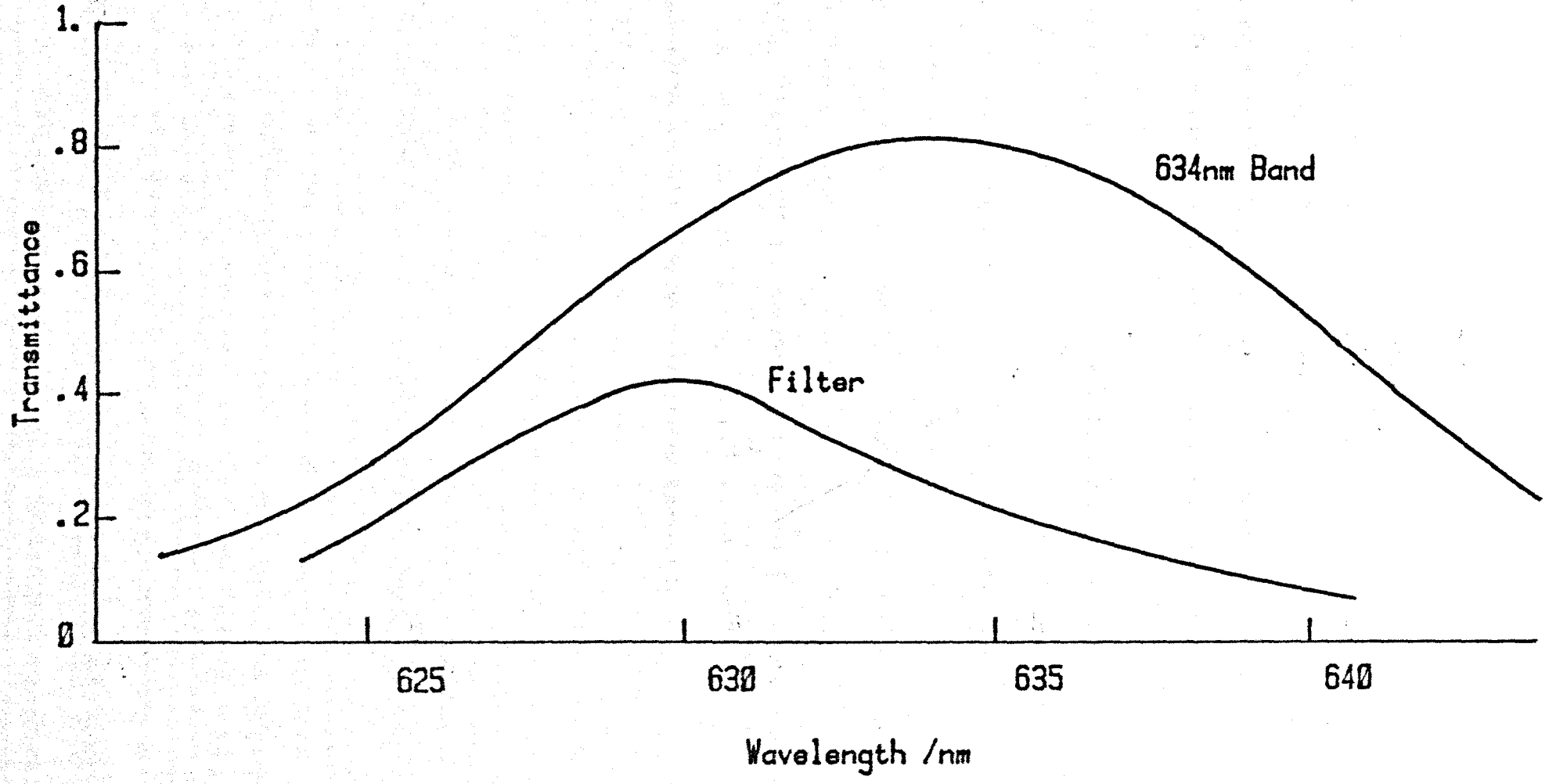

$$k_q = (1.32 \pm 0.54) \times 10^3 \, (T/300)^{0.78 \pm 0.32}$$

Extrapolation of their equation to 1570 K gives values between 2×10^3 and 1×10^4 ℓ mol^{-1} s^{-1}.

The upper limit suggested here is within an order of magnitude of this result, but it would be unreasonable to place any emphasis on such an extrapolation.

The small temperature dependence of the collisional quenching of $O_2(^1\Delta_g)$ by oxygen found in the work is used as a result in some further studies with the discharge flow shock tube. The post-shock decay rate is assumed to be identical with the measured pre-shock decay rate in the analysis of shocks at 762 nm where vibrational relaxation is included (Chapter 8). In the studies of the dimol emission at 579 nm, (Chapter 10) the post-shock decay rate is calculated from the shock trace at 634 nm, and is used as a check on the system where the pre-shock decay rate is not measured.

Chapter 8

The Collisional Quenching of $O_2(^1\Sigma_g^+)$ at High Temperatures

8.1. Introduction

The collisonal quenching of $O_2(^1\Sigma_g^+)$ is studied by following the emission at 762 nm at the high temperatures obtained when a shock wave is propagated into flowing discharged oyxgen.

$$O_2(^1\Sigma_g^+) \rightarrow O_2(^3\Sigma_g^-) + h\nu(\lambda = 762\ nm) \qquad 8.1$$

Oxygen, nitrogen and argon have been studied as collision partners, and the temperature dependence for the quenching rate constants and for the energy pooling reaction found, in the range 600 to 1650 K.

$O_2(^1\Sigma_g^+)$ is formed in the discharged gas by the energy pooling reaction[19] from two $O_2(^1\Delta_g)$ molecules.

$$O_2(^1\Delta_g) + O_2(^1\Delta_g) \xrightarrow{k_p} O_2(^1\Sigma_g^+) + O_2(^3\Sigma_g^-) \qquad 8.2$$

Schurath[116], studying this reaction, found that $O_2(^1\Sigma_g^+)$ was preferentially produced in the second excited vibrational level. $O_2(^1\Sigma_g^+)$ is deactivated on collision with another molecule and at the walls:

$$O_2(^1\Sigma_g^+) + M \xrightarrow{k_q^M} O_2(^1\Delta_g) + M \qquad 8.3$$

$$O_2(^1\Sigma_g^+) + \text{wall} \xrightarrow{k_w} O_2(^1\Delta_g \text{ or } ^3\Sigma_g^-) \qquad 8.4$$

where M is O_2, N_2 or Ar.

$O_2(^1\Sigma_g^+)$ is quenched to $O_2(^1\Delta_g)$ as suggested by Ogryzlo[68] and confirmed by Thomas and Thrush[74] by measuring the vibrational excitation of the quenching molecule.

The rate of collisional quenching of $O_2(^1\Sigma_g^+)$ by oxygen[49], nitrogen[121] and argon[121] has been measured previously at room temperature. These three gases are not efficient quenchers of $O_2(^1\Sigma_g^+)$ (see figure 2.3). For oxygen, where the vibrational level is at 1556 cm^{-1} and nitrogen at 2331 cm^{-1}, there is only a poor match with the excitation energy from the $O_2(^1\Sigma_g^+)$ to $O_2(^1\Delta_g)$ transition at 5240 cm^{-1}. These gases are also inefficient quenchers of $O_2(^1\Delta_g)$, although here oxygen is more efficient than nitrogen[125]. The temperature dependence of the quenching rate constants have not been measured previously.

The emission from $O_2(^1\Sigma_g^+)$ at 762 nm has an Einstein A factor[126] of 0.077 s^{-1} and can be easily studied in our system. The post-shock emission has the form shown in plate 3b. Detailed analysis of the trace is described in the next section.

The results for shocks into pure oxygen, oxygen/nitrogen mixtures and oxygen/nitrogen/argon mixtures are listed in section 8.4, and the chapter concludes with a discussion of the temperature dependence of the rate constants for energy pooling and for collisional quenching of $O_2(^1\Sigma_g^+)$ by the three gases.

8.2. Treatment of Results

8.2.1. The Emission Trace at the Shock Temperature

The emission intensity from shock heated $O_2(^1\Sigma_g^+)$ at 762 nm has the form shown below:

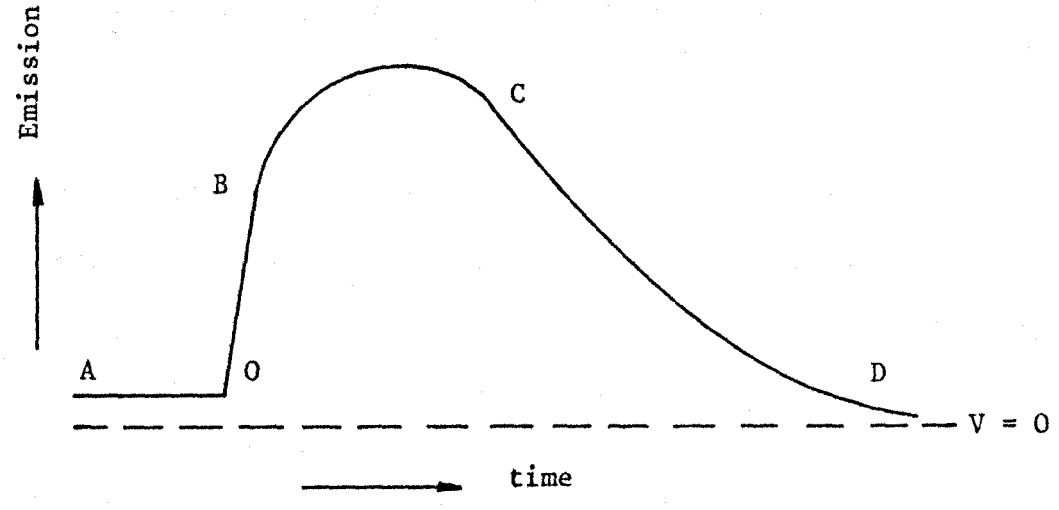

AO shows the emission before the shock arrives, the height of AO above the zero line is a measure of the pre-shock glow, $^{762}I_1$, OB is the initial rise at the shock front, $^{762}I_2^0$, due to the shock compression, and is related to the pre-shock glow by the density ratio across the shock front :

$$^{762}I_2^0 = {}^{762}I_1 \quad (\rho_2/\rho_1) \qquad 8.5$$

as postulated for the optical transition (reaction 8.1). The fall-off in emission intensity CD is observed as gas downstream from the discharge, with a lower concentration of $O_2(^1\Sigma_g^+)$ pre-shock, is swept past the photomultiplier. The curved zone, BC, to an enhanced level of emission is where the rate of formation and deactivation of $O_2(^1\Sigma_g^+)$ is adjusting to the high temperature values. An enhancement is seen in shocks for all

mixtures of gases, and the analysis is developed for this situation (see Plate 3b).

Before the shock, at any point in the tube, there is a steady state concentration of $O_2(^1\Sigma_g^+)$ where the rate of formation equals the rate of deactivation :

$$[O_2(^1\Sigma_g^+)]_1 = \frac{k_p(\text{at } T_1)\,[O_2(^1\Delta_g)]_1^2}{k_q^M(\text{at } T_1)\,[M] + k_w} \qquad 8.6$$

The curved relaxation zone corresponds to the adjustment to the new steady state equilibrium at the shock temperature, T_2, where :

$$[O_2(^1\Sigma_g^+)]_2^{Eq} = \frac{k_p(\text{at } T_2)\,[O_2(^1\Delta_g)]_2^2}{k_q^M(\text{at } T_2)\,[M]} \qquad 8.7$$

At the high density behind the shock front, diffusion of $O_2(^1\Sigma_g^+)$ to the wall will be slow, and as the walls remain at room temperature :

$$k_w(\text{at } T_1) \ll k_q^M(\text{at } T_2)\,[M] \qquad 8.8$$

and the wall deactivation can be omitted from equation 8.7.

During the curved relaxation zone the steady state is reached :

$$\frac{d[O_2(^1\Sigma_g^+)]_2}{dt} = k_p(\text{at } T_2)\,[O_2(^1\Delta_g)]_2^2 - k_q^M(\text{at } T_2)\,[M]\,[O_2(^1\Sigma_g^+)]_2 \qquad 8.9$$

where the subscript, 2, denotes the concentrations at T_2. Integrating this equation between time = 0, where $[O_2(^1\Sigma_g^+)]_2^0$ is the concentration of $O_2(^1\Sigma_g^+)$, and time = t :

$$\frac{[O_2(^1\Sigma_g^+)]_2}{[O_2(^1\Sigma_g^+)]_2^0} = \frac{k_p(\text{at } T_2)[O_2(^1\Delta_g)]_2^2}{k_q^M(\text{at } T_2)[M][O_2(^1\Sigma_g^+)]_2^0}$$

$$+ \left[1 - \frac{k_p(\text{at } T_2)[O_2(^1\Delta_g)]_2^2}{k_q^M(\text{at } T_2)[M][O_2(^1\Sigma_g^+)]_2^0}\right] e^{-k_q^M(\text{at } T_2)[M]t} \qquad 8.10$$

This equation would fit a relaxation process as shown below.

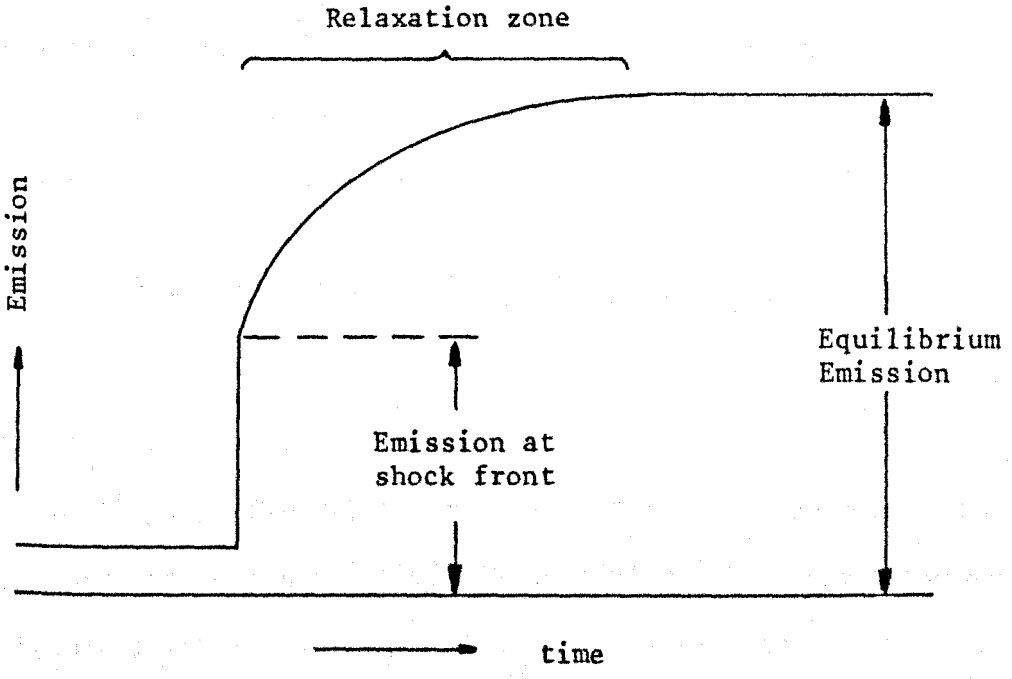

With the discharge flow shock tube, there is a concentration gradient of the excited species along the tube before the shock. This decay is superimposed on the relaxation and has an exponential form, e^{At}, where A is the decay constant, and is negative in our configuration. So equation 8.10 will fit the concentration of $O_2(^1\Sigma_g^+)$ at any one point in the tube, but at any other point $[O_2(^1\Sigma_g^+)]$ will differ by e^{At}.

The enhancement of emission at equilibrium over that expected from the compression at the shock front, K, can be described from equations 8.6 and 8.7 as the ratio of rate constant ratios at the pre and post shock temperatures :

$$K = \left[\frac{k_p(\text{at } T_2)}{k_q^M(\text{at } T_2)}\right] \Bigg/ \left[\frac{k_p(\text{at } T_1)}{k_q^M(\text{at } T_1) + k_w/[M]}\right] \qquad 8.11$$

The overall equation for the concentration of $O_2(^1\Sigma_g^+)$ from equation 8.10, then becomes :

$$\frac{[O_2(^1\Sigma_g^+)]_2}{[O_2(^1\Sigma_g^+)]_2^0} = \left\{ K + (1-K)\, e^{-k_q^M(\text{at } T_2)[M]t} \right\} e^{At} \qquad 8.12$$

The intensity of emission at 762 nm is proportional to the concentration of $O_2(^1\Sigma_g^+)$, and the intensity of emission at the shock front, $^{762}I_2^0$, is a measure of $O_2(^1\Sigma_g^+)_2^0$.
So equation 8.12 with equation 8.5 is now :

$$^{762}I_2 = {}^{762}I_1 \frac{\rho_2}{\rho_1} e^{At} \left\{ K + (1-K) e^{-k_q' t} \right\} \qquad 8.13$$

where k_q' is the pseudo first order rate constant $k_q^M(\text{at } T_2)[M]$.

In the experiments, the rise in emission at the shock front is not instantaneous, but has a finite rise time due to the rise times of the photomultiplier and voltage follower, and the slit width. This is taken into account in the integration time, Δt, and equation 8.13 is integrated with respect to time from $t-\Delta t$ to t, giving :

$$^{762}I_2 = \frac{^{762}I_1}{\Delta t} \frac{\rho_2}{\rho_1} \left\{ \frac{K}{A} e^{At} (1 - e^{-A\Delta t}) \right.$$

$$\left. + \frac{1-K}{A-k_q'} (1 - e^{-(A-k_q')\Delta t}) e^{(A-k_q')t} \right\} \qquad 8.14$$

The experimental points are fitted to this equation using the interactive computer graphics programme described in chapter 6.

The results of each shock are values of the parameters, K, k_q', A and Δt in equation 8.14 at the shock temperature, T_2.

From the value of the pseudo first order rate constant, k_q', the rate constant for collisional quenching can be obtained at the shock temperature, T_2.

For shocks into 100% oxygen :

$$k_q^{O_2} = k_q'/[O_2] \qquad 8.15$$

where $[O_2]$ is the concentration of oxygen at the shock density.

For shocks into mixtures of oxygen and nitrogen :

$$k_q^{M} = k_q'/([O_2] + [N_2]) \qquad 8.16$$

where k_q^{M} is a composite rate constant for collisonal quenching by both species :

$$k_q^{M} = k_q^{O_2} x_{O_2} + k_q^{N_2} x_{N_2} \qquad 8.17$$

x is the mole fraction, and $k_q^{N_2}$ is the rate constant for collisional quenching of $O_2(^1\Sigma_g^+)$ by nitrogen.

Similarly for shocks into oxygen/nitrogen/argon mixtures :

$$k_q^{M} = k_q^{O_2} x_{O_2} + k_q^{N_2} x_{N_2} + k_q^{Ar} x_{Ar} \qquad 8.18$$

From the values of K obtained for each shock, the energy pooling rate constant, k_p (at T_2), can be calculated from equation 8.11 using the value obtained for k_q^{M} (at T_2) and room temperature values from the literature (see section 8.4). The rate constant for deactivation at the wall at room temperature is calculated at the initial pre-shock pressure, P_1 in torr, from the equation by Derwent and Thrush[49] :

$$k_w = \left\{ \frac{a^2}{8Do\ P_1/760} + \frac{2a}{\gamma\bar{u}} \right\}^{-1} \qquad 8.19$$

where a is the radius of the tube, D_o is the diffusion coefficient of $O_2(^1\Sigma_g^+)$ at one atmosphere pressure, γ is the wall deactivation efficiency, and $\bar{u}$ is the mean velocity of $O_2(^1\Sigma_g^+)$. The value of D_o is taken as 0.201 $cm^2\ s^{-1}$ the diffusion coefficient for $O_2(^1\Delta_g)$ at atmospheric pressure measured by Vidaud, Wayne and Yaron[31].

A, the decay constant is the same as the measured pre-shock decay rate (Table 7.3).

8.2.2. The Effect of Vibrational Relaxation on the Analysis of the Shock Emission

During the time of the shock, vibrational relaxation is occurring. At the shock front the frozen conditions apply where the translational and rotational degrees of freedom have attained equilibrium at the frozen temperature, but the vibrational degrees of freedom have not. The fully relaxed conditions apply when the gas is at equilibrium at the shock temperature T_2. (see Figure 3.7).

(a) 100% Oxygen Shocks

During vibrational relaxation, the density ratio increases from ρ_A/ρ_1 to ρ_2/ρ_1. At time, t, the density ratio will be :

$$\frac{\rho_t}{\rho_1} = \frac{\rho_2}{\rho_1} - \left[\frac{\rho_2}{\rho_1} - \frac{\rho_A}{\rho_1}\right] e^{-t/\tau_v} \qquad 8.20$$

where τ_v is the vibrational relaxation time for the gas.

If τ_v is long compared to the measurement period for the shock, the gas can be assumed to be in its frozen state throughout, but if τ_v is comparable with the period of measurement then the density ratio will be changing during the time of the experiment. The changes in density due to vibrational relaxation affect the values of the quenching rate constant, k_q', and the equilibrium ratio of levels, K.

For oxygen, the temperature dependence of the vibrational relaxation time is given by[102] :

$$\ln(\tau_v / \text{ s atm}) = 126.0 + T^{-1/3} - 21.95 \qquad 8.21$$

The table below compares the vibrational relaxation times at the post shock pressure with the period of measurement for that shock, (the times are in particle time) where it can be seen that except for the slowest shock, vibrational relaxation will affect the density ratio in the analysis region, and thus should be included in the analysis.

Run Number	P_2 /torr	$\frac{\rho_A}{\rho_1}$	$\frac{\rho_2}{\rho_1}$	T_2 /K	Calculated τ_v/μs	Measurement period/μs
803	50.77	3.168	3.427	650	8970	2606
889	109.5	4.193	4.704	1000	993.6	2587
A915	145.1	4.617	5.295	1213	206.6	1906
797	193.5	4.993	5.891	1480	71.8	1649

In the computer analysis described in chatper 6, VIBREL calculates ρ_t/ρ_1, P_t/P_1 and T_t for each point between X origin and the end of the trace. The time scale is changed to particle time for these points, where :

$$t_p = t_\ell \rho_t / \rho_1 \qquad 8.22$$

and for points before x origin :

$$t_p = t_\ell \rho_A / \rho_1 \qquad 8.23$$

Values of the expected emission at each point past X origin are calculated using the measured pre-shock decay rate, and these are fitted to a polynomial, the coefficients of which are used later to display the calculated line. Equation 8.14 to which the points are fitted is modified by substituting ρ_t for ρ_2.

(b) Oxygen/Nitrogen Mixtures

For experiments with mixed gases, the vibrational relaxation can be considered in two parts, the vibrational relaxation of oxygen while nitrogen remains frozen (to the B state), followed by complete relaxation to the fully relaxed (2) state.

$$\frac{\rho_t}{\rho_1} = \frac{\rho_2}{\rho_1} - \left[\frac{\rho_B}{\rho_1} - \frac{\rho_A}{\rho_1}\right] e^{-t/\tau_{O_2}} - \left[\frac{\rho_2}{\rho_1} - \frac{\rho_B}{\rho_1}\right] e^{-t/\tau_M} \qquad 8.24$$

τ_{O_2} can be calculated from equation 8.21 as the addition of nitrogen does not affect the vibrational relaxation time of oxygen, but τ_M, the vibrational relaxation time for the two gases is not the vibrational relaxation time of nitrogen, as the presence of oxygen increases the vibrational relaxation rate of nitrogen. τ_M has been calculated by Pedley[110] from results of White[127] on vibrational relaxation of oxygen/nitrogen mixtures; and the following values are used in the computer programme.

$$\ln(\tau_M / \text{ s atm.}) = CT^{-1/3} - D \qquad 8.25$$

where C = 86.5 and D = 16.9 for mixtures containing more than 80% oxygen, and

$$C = 130.49 - 128.3\, x_{O_2} + 102.7\, x_{O_2}^2 \qquad 8.26$$

$$D = 4.159 + 2.118\, x_{O_2} - 0.792\, x_{O_2}^2 \qquad 8.27$$

for mixtures containing less than 80% oxygen.

When ρ_t/ρ_1 has been calculated for each point past X origin, then the analysis proceeds as before.

(c) Oxygen/Nitrogen/Argon Mixtures

Vibrational relaxation was not included in the analysis of mixtures containing argon (see section 8.4.7.)

8.3. Experimental

The discharge flow shock tube system was tested with shocks into 100% oxygen by observing the 762 nm emission. The initial parameters were changed and their effects investigated.

The initial pressure was varied between 3 torr and 10 torr (400 to 1330 Pa). At the lower pressures, oxygen atoms may be present in the flow (chapter 5) and distort the results, at higher pressures the light screens tended to be unreliable and often the shocks were missed. Results were obtained at pressures around 6 torr.

For the pure oxygen runs, the flow rate was maintained at 17.5 ml s^{-1} at one atmosphere pressure; for mixed gases the total flow rate was increased to 28 ml s^{-1} at one atmosphere pressure.

All the shocks recorded in this chapter had the microtron power at 100 watts, within the linear region in figure 3.4. Lower microtron powers were tried, but the smaller emission lead to difficulties in the analysis.

The photomultiplier slit width was chosen to give a measurable pre-shock glow, and a post-shock emission level not exceeding 5 V. The slit widths were generally kept constant for a series of shocks.

8.4. Results

The results for each mixture of gases are treated separately in this section. The overall temperature dependences are discussed in the following section 8.5.

8.4.1. Accuracy of the Results

Shock tube measurements generally show a wide scatter, inevitable for a procedure where the results are not only dependent on the accuracy of any measurements, but vary with the bursting of the diaphragm and the establishment of the shock front.

The errors in measurement of the pre-shock glow, pre-shock decay, initial temperature and pressure and shock speed, are estimated to total less than ± 5%. Irregularities in the flow have largely been eliminated by the use of the pressure regulator (figure 3.2), but a low signal to noise ratio for the weaker emissions does add to the errors.

The computer analysis gives statistical error values for the parameters for each shock, evaluated mainly from the scatter of the transient recorder data. These errors are not a true guide to the accuracy of the calculated rate constants which could be better described by the overall scatter of the results. For shocks into pure oxygen at lower temperatures, the value of K was found to be near one, and so the relaxation zone is poorly defined. In these cases the statistical error value for the quenching constant, k_q', could be as high as ± 10%, although the actual value could be in error by as much as ± 50% between shocks with the same speed.

For lower temperature runs, the maximum error comes from the quenching constant. The scatter is higher at the higher temperatures due to shock irregularities.

Shocks where the enhancement in emission is high, that is where K is high, are easier to analyse. These shocks showed a clearly defined relaxation zone, and the increased emission gave a better signal to noise ratio. The subsequent results show a smaller scatter then usual (see figures 8.14 and 8.15). The pure oxygen results are the least precise of the series.

Overall, the rate constants measured in the discharge flow shock tube are considered to be within ± 15% of the true value. As this is only an estimate, error limits are not included in the results.

8.4.2. 100% Oxygen

A trace of the shock emission at 762 nm from $O_2(^1\Sigma_g^+)$ in pure oxygen is shown in figure 8.1. A computer plot of the analysis is shown in figure 8.2; vibrational relaxation is included in the analysis. The postulated model has the same shape as the experimental trace, and the calculated line using the parameters found in the analysis fits the experimental points well. An enhancement in emission from that expected from the shock compression alone is observed, and the value of K is greater than one. At the higher shock temperatures, then, the quenching rate constant has increased more than the energy pooling rate constant.

Results of shocks into 100% oxygen are listed in table 8.1, in all cases vibrational relaxation is included in the analysis.

The quenching rate constant, k_q, in this case $k_q{}^{O_2}$, comes from the value of k_q' using equation 8.15. The energy pooling rate constant, k_p, is calculated from k_q and K using equation 8.11. The following room temperature values are used[49] :

$$k_p(\text{at } T_1) = 1.22 \times 10^4 \text{ ℓ mol}^{-1} \text{ s}^{-1}$$

$$k_q(\text{at } T_1) = 1.0 \times 10^5 \text{ ℓ mol}^{-1} \text{ s}^{-1}$$

The best value of k_q(at T_1) for dry oxygen by Thomas and Thrush[128] is $(2.8 \pm 0.8) \times 10^4$ ℓ mol^{-1} s^{-1}, but the value of 1×10^5 ℓ mol^{-1} s^{-1} is more realistic in our system. Although the flowing gases are themselves dried, water cannot be excluded completely from a system which is opened to the atmosphere between shocks. Our value assumes a maximum water content of 30 p.p.m. where the rate constant for quenching of $O_2(^1\Sigma_g^+)$ by water is Thomas and Thrush's value[128] of 2.8×10^9 ℓ mol^{-1} s^{-1}. This amount of water will have only a small effect on the value of the quenching rate constant at the high shock temperature. The wall deactivation rate constant at T_1 is calculated from equation 8.19 using a value of 10^{-2} for γ[49] and 4.39×10^4 cm s^{-1} for $\bar{u}$ at the initial pressure, P_1, for each shock.

Plots of the quenching rate constant and the energy pooling rate constant against shock temperature are shown in figures 8.3 and 8.4. The room temperature values are in good agreement with the extrapolated experimental curves. The "filled in" points in figure 8.3 are from shocks where K was found to be very close to one. In these cases the relaxation zone cannot be defined. A value of k_p from the overall energy pooling graph (figure 8.30) and K = 1 gives a calculated value of k_q which is plotted on the graph.

Figure 8.1.

A Trace of the Shock Emission at 762 nm.

Run No. 881. 100% Oxygen.

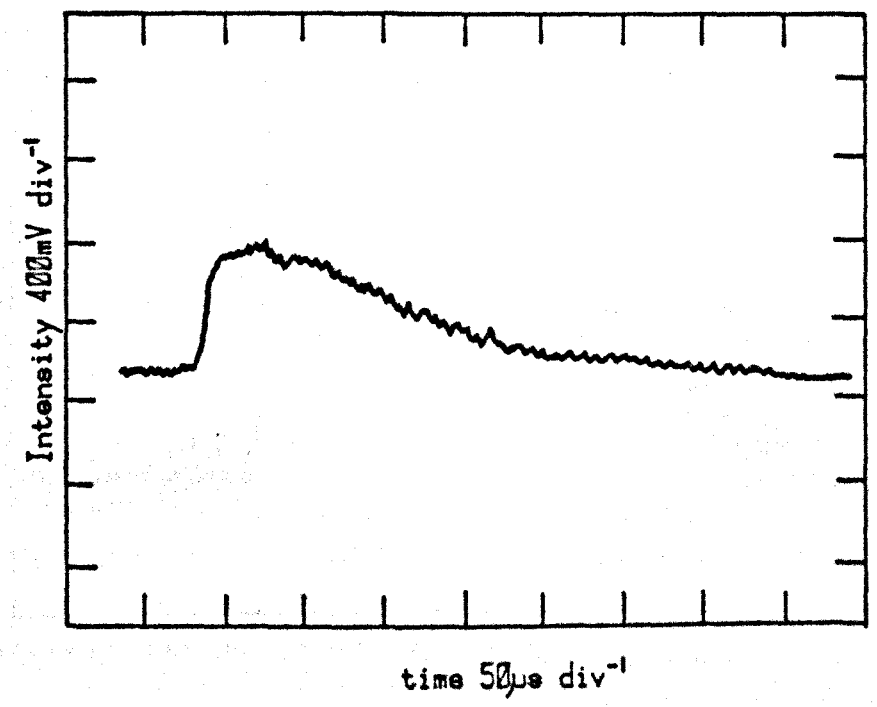

Figure 8.2.

A Computer Plot of the Analysis. 100% Oxygen.

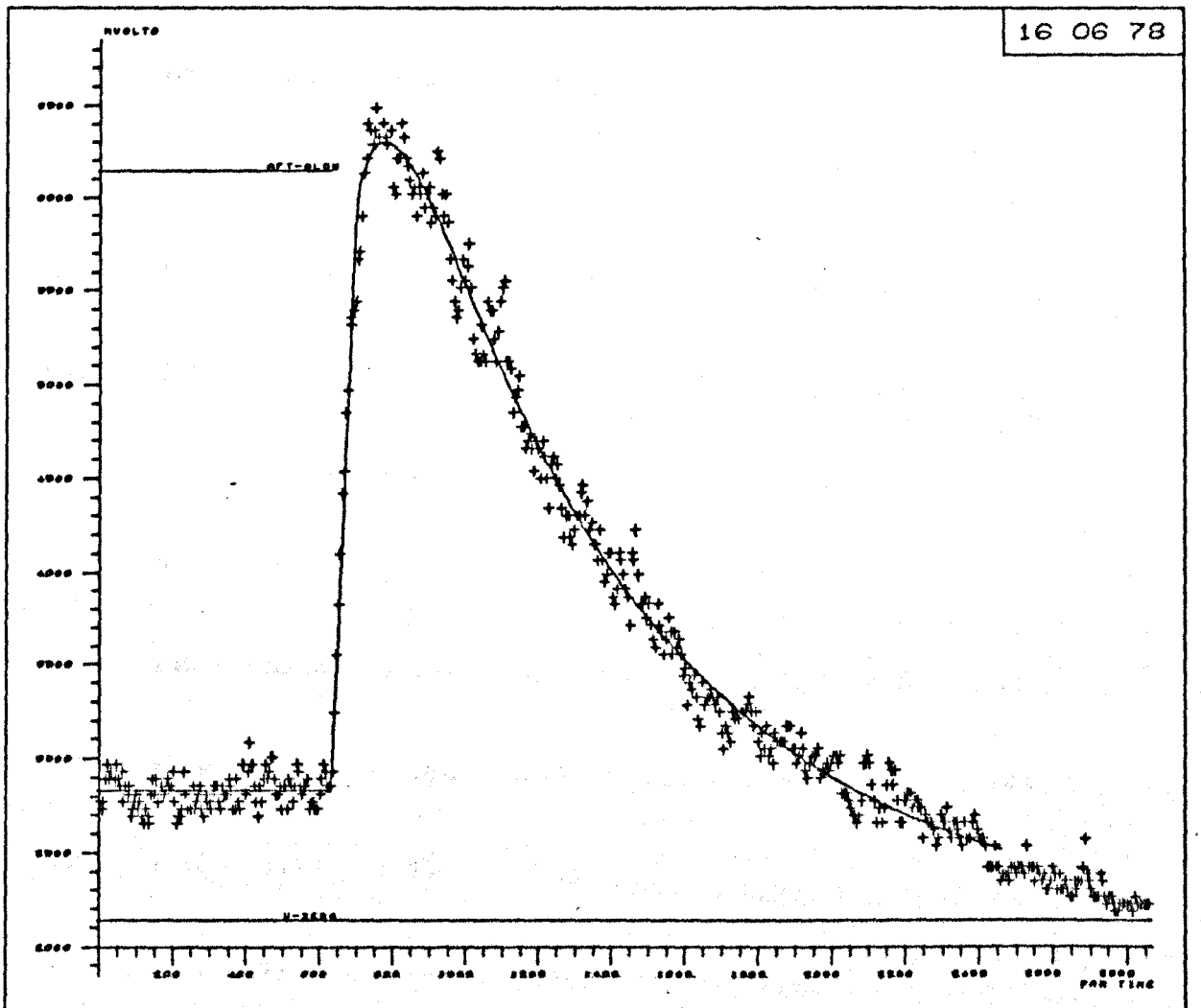

Table 8.1.

Results of the Analysis of Shocks at 762 nm into 100% Oxygen.

Run No.	Pre Shock Measurements P_1 /torr	Glow /mV	Decay /m^{-1}	Speed /km s^{-1}	ρ_2/ρ_1	K	Rate Constants /l mol^{-1} s^{-1} $k_q/10^6$	$k_p/10^5$	T_2/K
770	6.4	977	1.00	1.616	5.874	1.65	3.48	4.32	1475
777	6.5	973	1.01	1.604	5.851	1.31	4.25	4.18	1460
797	6.4	353	1.10	1.618	5.880	1.45	4.13	4.49	1480
801	6.5	340	1.09	1.383	5.586	1.13	3.13	2.68	1185
803	6.4	778	1.09	0.864	3.831	1.0	(0.83)	-	650
835	5.8	972	0.96	0.948	3.883	1.0	(1.12)	-	738
839	5.65	249	0.94	1.431	5.511	1.10	3.38	2.54	1238
853	6.2	1280	1.31	1.162	4.543	0.94	(2.57)	-	961
854	6.2	1180	1.31	1.142	4.268	1.08	2.38	1.67	935
855	6.47	1145	1.16	1.152	4.282	1.17	2.24	1.82	937
856	6.84	294	1.21	1.077	4.261	1.03	2.19	1.62	943
870	6.6	1134	1.48	1.269	4.510	1.04	(2.81)	-	1054
881	6.2	860	1.13	1.385	4.694	1.10	3.67	2.95	1197

Table 8.1.(continued)

Results of the Analysis of Shocks at 762 nm into 100% Oxygen.

Run No.	Pre Shock Measurements P_1 /torr	Glow /mV	Decay /m^{-1}	Speed /km s^{-1}	ρ_2/ρ_1	K	Rate Constants /l mol^{-1} s^{-1} $k_q/10^6$	$k_\rho/10^5$	T_2/K
882	6.5	621	1.19	1.375	4.597	1.08	2.72	2.21	1181
884	6.3	688	1.14	1.596	5.821	1.41	4.79	5.13	1449
910	6.14	461	1.05	1.607	5.860	2.21	3.91	6.30	1473
A910	6.14	458	1.05	1.607	5.860	2.18	4.39	6.98	1473
M110	6.47	1238	1.07	1.352	5.256	1.30	2.73	2.56	1140
M124	6.47	940	1.05	1.629	5.847	1.38	6.84	6.67	1497
M125	6.5	915	1.05	0.872	3.567	1.0	(0.91)	-	673
M127	6.7	863	1.05	0.882	3.613	1.03	1.05	0.82	681
M129	6.5	886	1.04	0.864	3.540	1.0	(0.89)	-	611
M146	6.56	317	1.02	1.411	5.353	1.0	(4.90)	-	1220
M147	6.41	263	1.01	1.738	6.035	1.97	5.37	7.76	1647
M150	6.5	204	1.09	1.734	6.049	2.32	8.13	13.90	1650
M151	6.56	163	1.30	1.705	5.975	2.89	3.37	7.80	1680

Figure 8.3. Temperature Dependence of Quenching Rate Constant of $O_2(^1\Sigma_g^+)$ by Oxygen.

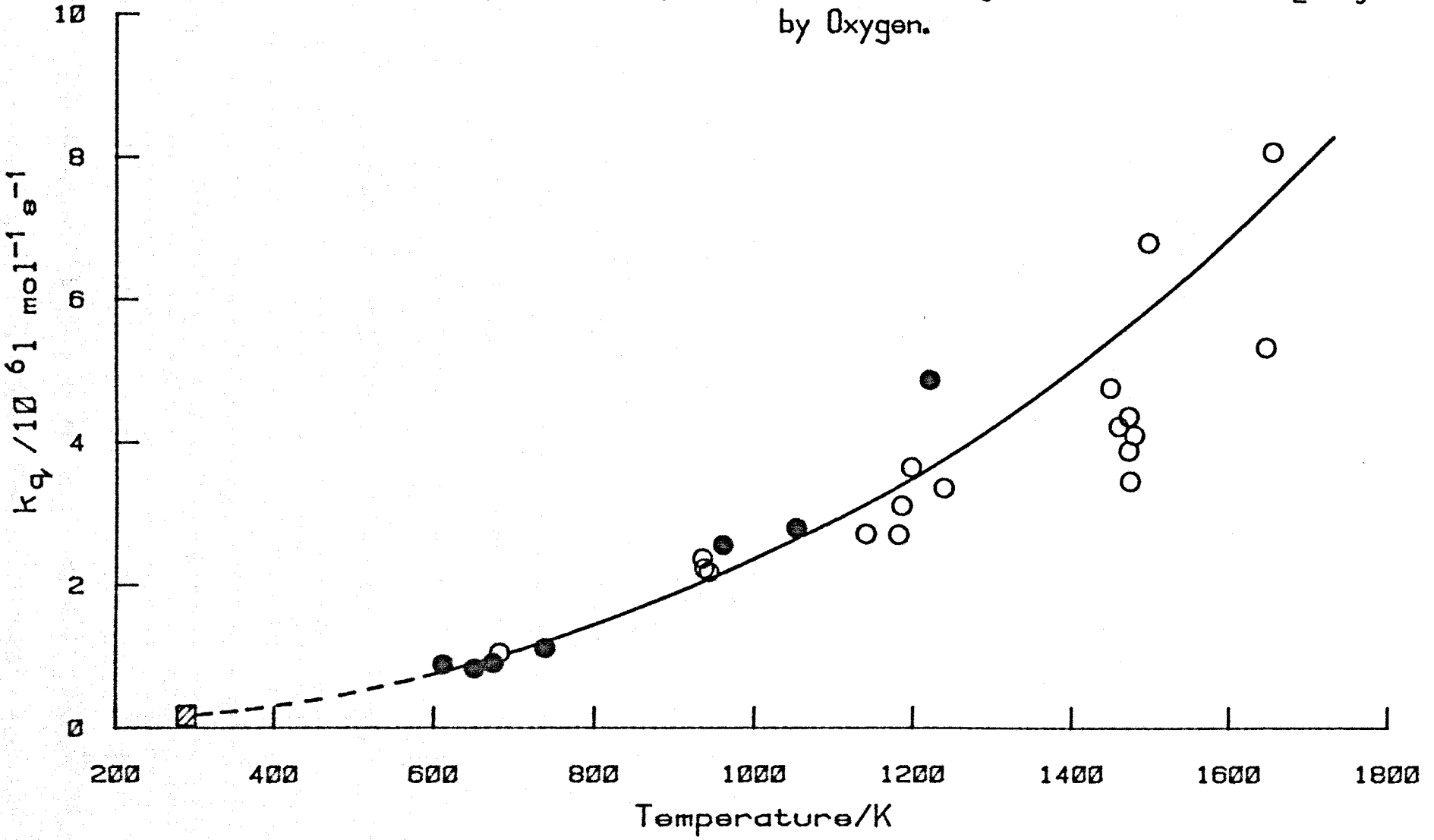

Figure 8.4. Temperature Dependence of Energy Pooling Rate Constant.
100% Oxygen.

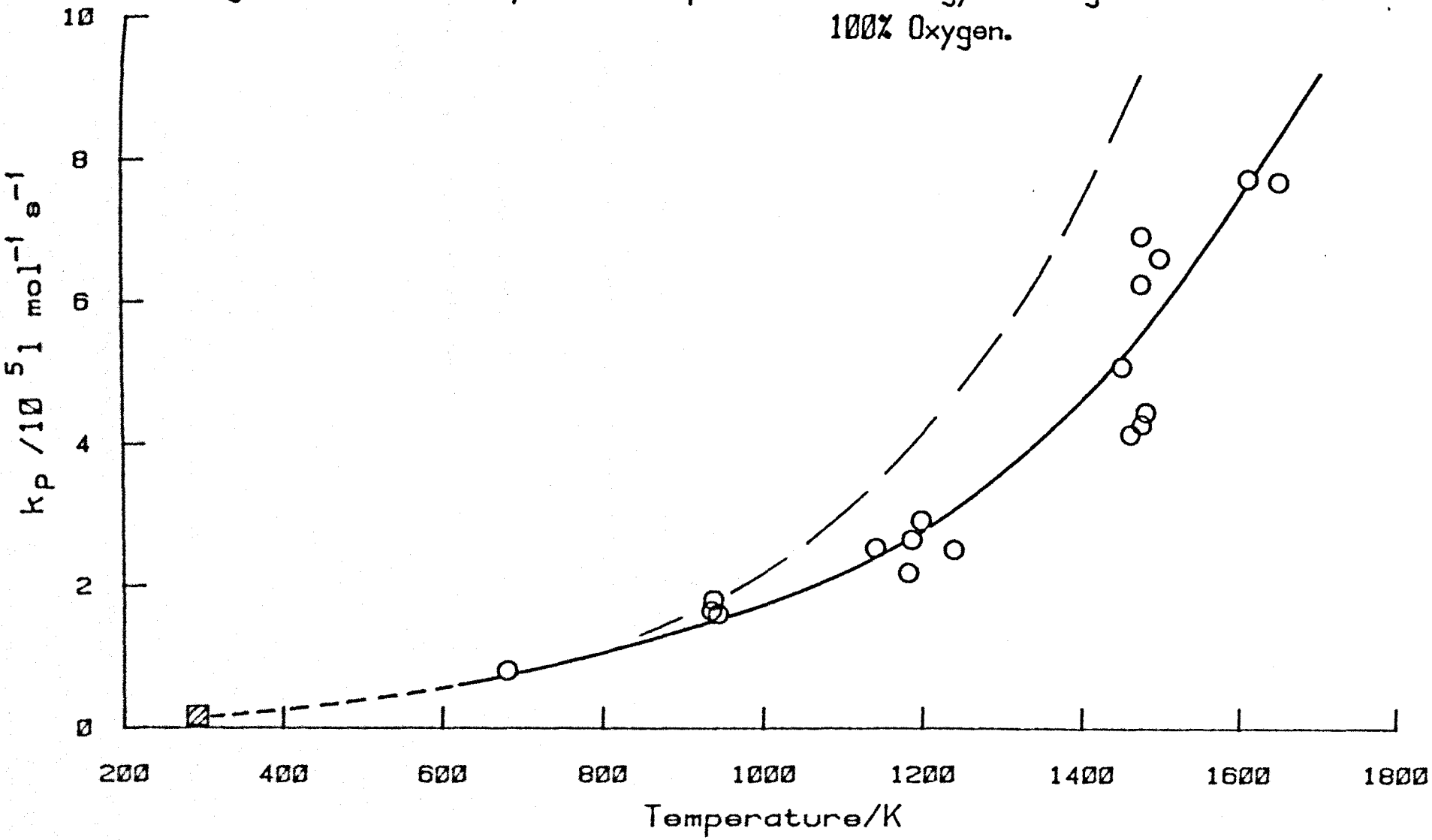

8.4.3. 90% Oxygen/10% Nitrogen

A typical shock trace for 90% oxygen/10% nitrogen is shown in figure 8.5a. The general shape is the same as the postulated model. The addition of nitrogen to the oxygen flow after the discharge decreases the intensity of the pre-shock glow as $k_q^{N_2} > k_q^{O_2}$ at room temperature, but the shock emission increases more than for the pure oxygen shocks due to the change in rate constants at the higher temperature. A computer plot of the analysis of this run is shown in figure 8.6, the calculated line fits the experimental points well.

Table 8.2. lists the results of shocks into 90% oxygen/10% nitrogen, vibrational relaxation is included. The value of k_q listed is the second order rate constant for the quenching of $O_2(^1\Sigma_g^+)$ by the mixture, k_q^M. k_p is calculated from K and k_q using equation 8.11 as before, but here k_q (at T_1) is for the mixture where :

$$k_q(\text{at } T_1) = k_q^{O_2}(\text{at } T_1)x_{O_2} + k_q^{N_2}(\text{at } T_1)x_{N_2}$$

the value of $k_q^{N_2}$ (at T_1) is taken from Becker, Groth and Schurath[121] as 1.3×10^6 ℓ mol^{-1} s^{-1}.

Plots of the quenching rate constant for the mixture, and the energy pooling rate constant, against temperature are shown in figures 8.7 and 8.8.

Figure 8.5.

Traces of the Shock Emission at 762 nm.

a. Run No. 914. 90% Oxygen/10% Nitrogen.

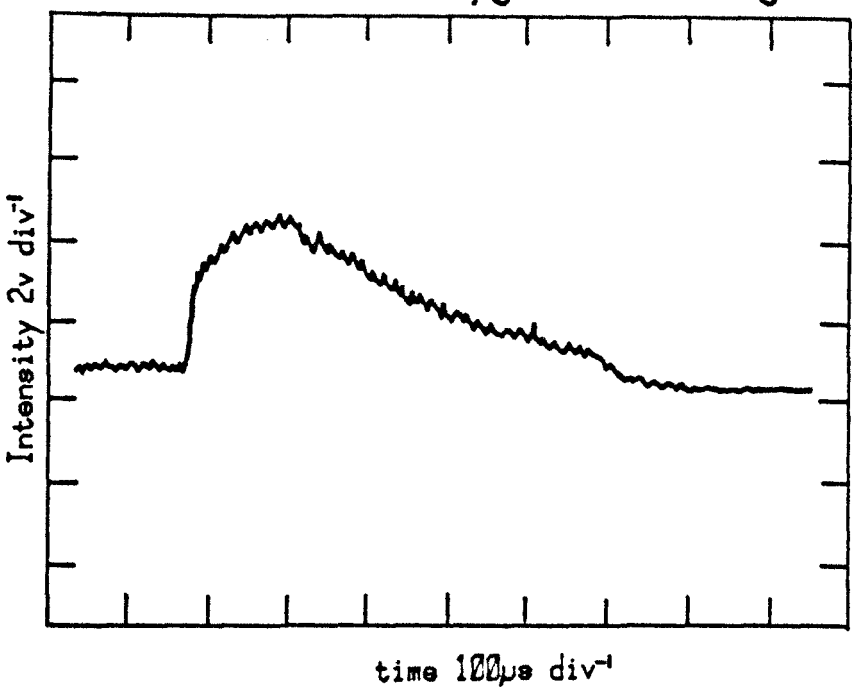

b. Run No. 890. 72.1%Oxygen/27.9%Nitrogen.

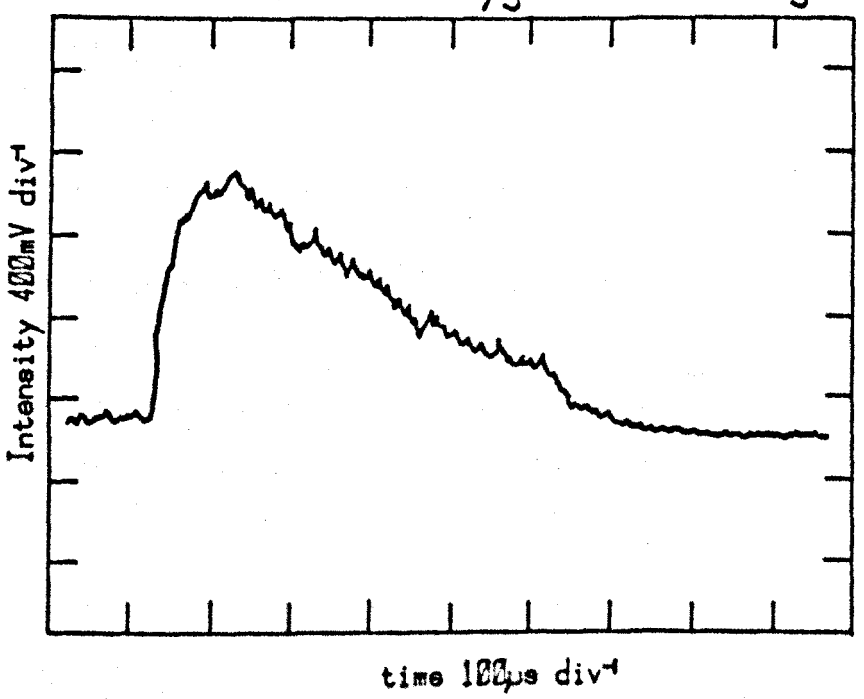

Figure 8.6.

A Computer Plot of the Analysis. 90% Oxygen/10% Nitrogen.

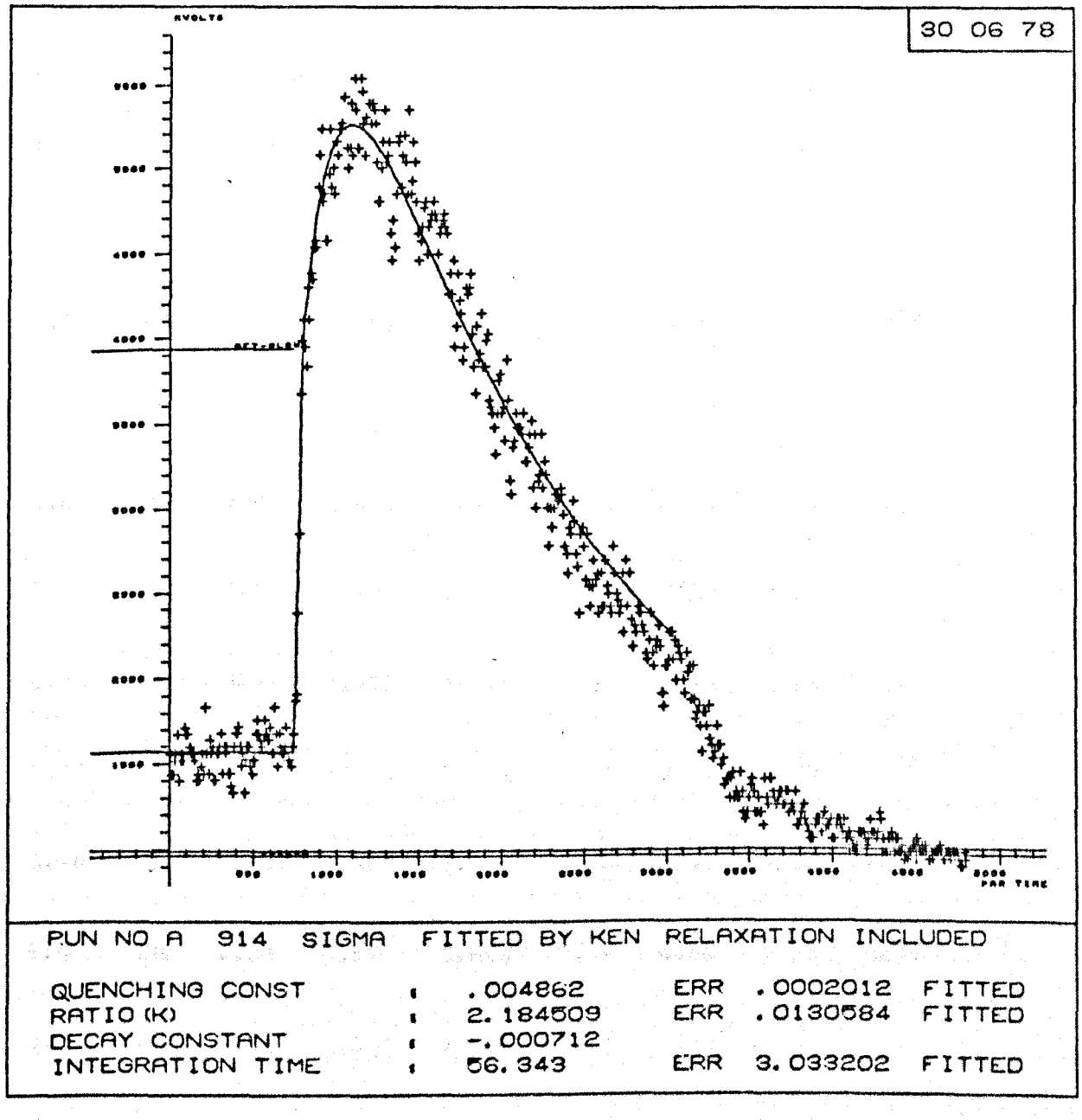

Table 8.2.

Results of the Analysis of Shocks at 762 nm into 90% Oxygen/10% Nitrogen.

Run No.	Pre Shock Measurements P_1 /torr	Glow /mV	Decay $/m^{-1}$	Speed $/km\ s^{-1}$	ρ_2/ρ_1	K	Rate Constants /l mol^{-1} s^{-1} $k_q/10^6$	$k_\rho/10^5$	T_2/K
A912	6.51	800	0.74	1.204	4.767	1.92	3.13	2.60	975
912	6.51	791	0.74	1.204	4.767	1.51	4.36	2.88	975
A913	6.35	787	0.74	0.966	3.900	1.54	2.14	1.42	852
A914	6.23	610	0.75	1.192	4.692	2.19	3.05	2.84	969
914	6.23	854	0.75	1.192	4.692	1.79	3.07	2.34	969
A915	6.80	768	0.92	1.410	5.295	2.64	3.09	3.59	1213
915	6.80	788	0.92	1.410	5.295	2.31	3.85	3.92	1213
M201	6.75	259	0.73	1.392	5.279	2.02	3.33	2.96	1186
M202	6.70	534	0.85	1.381	5.254	1.99	3.52	3.07	1172
M203	6.70	397	0.84	1.381	5.245	2.00	3.97	3.48	1174
M204	6.6	380	0.84	1.571	5.648	2.74	6.08	7.26	1419
M204A	6.6	379	0.84	1.571	5.648	2.81	8.73	10.69	1416
M206	6.64	349	0.84	1.574	5.652	2.80	6.55	8.00	1424
M206A	6.64	389	0.84	1.574	5.652	3.00	5.62	7.36	1424

Table 8.2.(continued)

Results of the Analysis of Shocks at 762 nm into 90% Oxygen/10% Nitrogen.

Run No.	Pre Shock Measurements P_1 /torr	Glow /mV	Decay /m^{-1}	Speed /km s^{-1}	ρ_2/ρ_1	K	Rate Constants /1 mol^{-1} s^{-1} $k_q/10^6$	$k_p/10^5$	T_2/K
M205	6.80	333	0.879	1.539	5.565	2.50	6.15	6.76	1380
M207	6.5	471	0.824	0.844	3.443	1.43	1.15	0.71	644
M207A	6.5	527	0.824	0.844	3.443	1.61	1.12	0.78	644
C4A	6.56	578	0.726	0.867	3.541	1.59	1.17	0.81	661
C5	6.4	543	0.698	0.845	3.458	1.37	1.29	0.77	642
C5A	6.4	554	0.698	0.845	3.458	1.48	1.02	0.66	642
C6	6.5	575	0.752	0.932	3.781	1.41	1.71	1.05	720
C6A	6.5	578	0.752	0.932	3.781	1.58	1.72	1.18	720
C7	6.3	563	0.706	0.930	3.773	1.43	1.87	1.15	718
C8	6.3	568	0.719	0.925	3.756	1.44	1.79	1.11	714
C8A	6.3	550	0.719	0.925	3.756	1.52	1.65	1.08	714
C9	6.65	115	0.800	1.520	5.574	2.93	5.56	7.12	1345
C9A	6.65	100	0.800	1.520	5.574	3.10	3.48	4.72	1342
C10	6.56	133	0.745	1.620	5.781	3.33	8.52	12.33	1477

Figure 8.7. Temperature Dependence of Quenching Rate Constant for Mixture 90% Oxygen/10% Nitrogen.

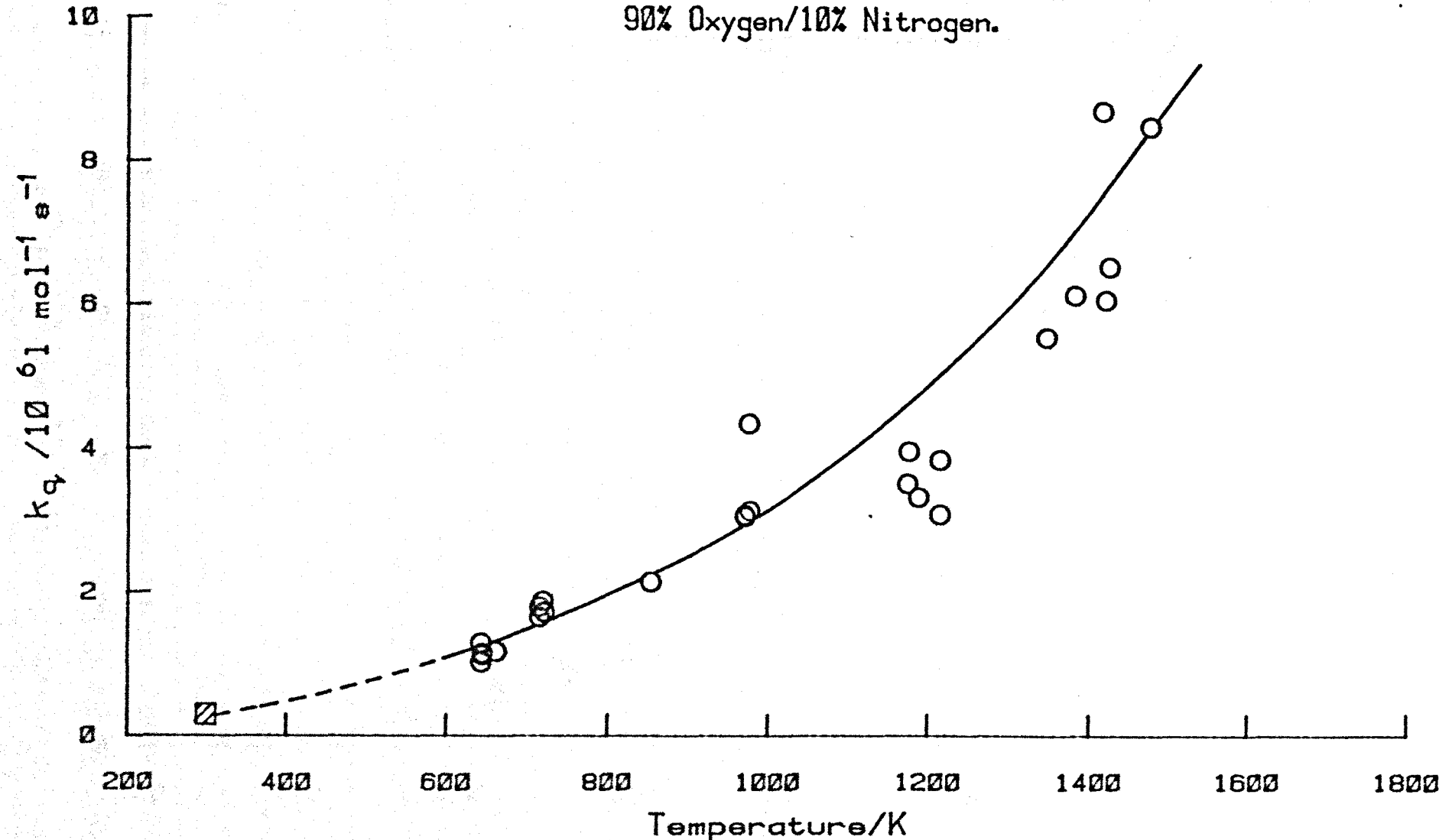

Figure 8.8. Temperature Dependence of Energy Pooling Rate Constant.
90% Oxygen/10% Nitrogen

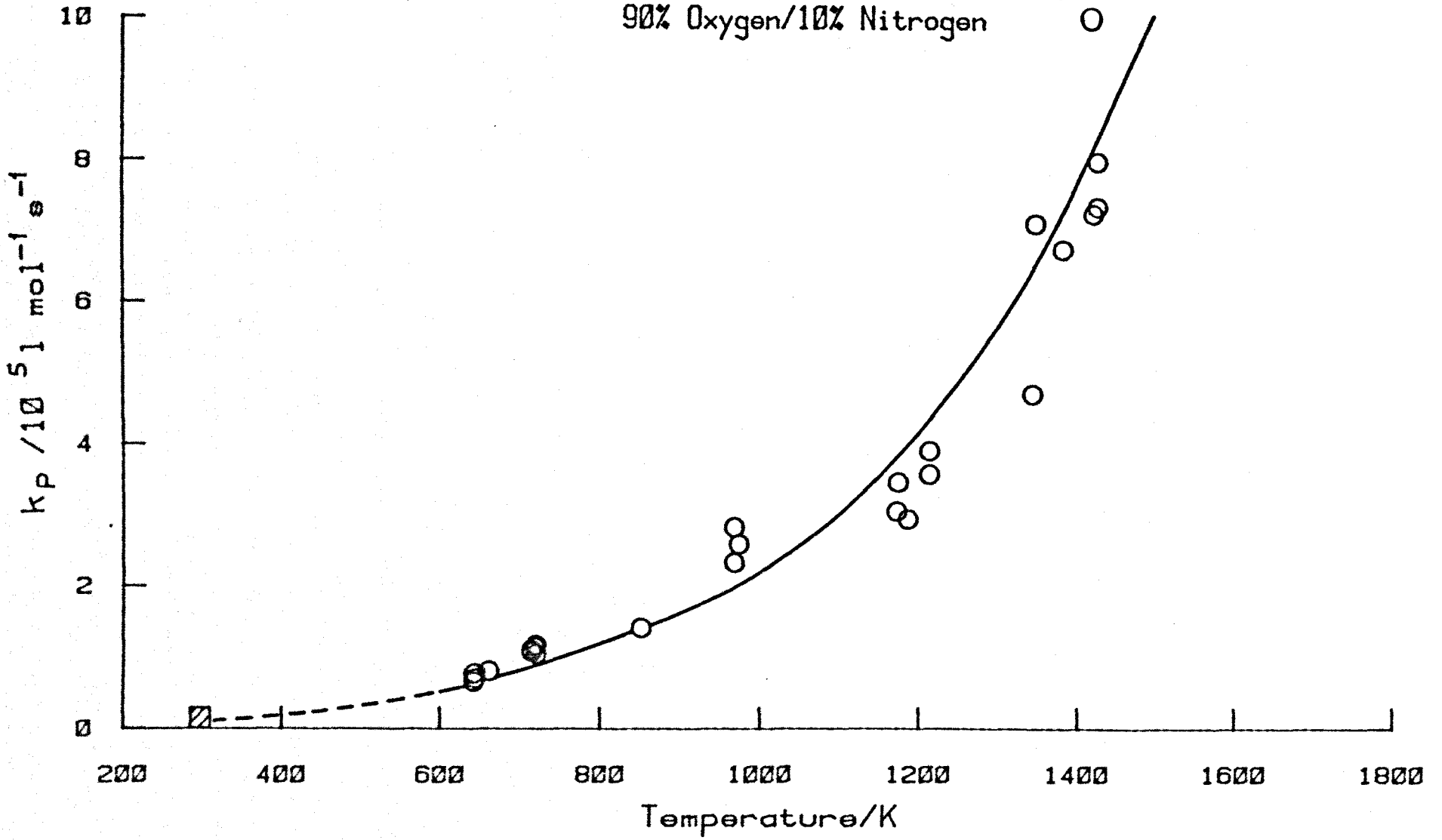

8.4.4. 72.1% Oxygen/27.9% Nitrogen

A trace of the shock emission from this mixture is shown in figure 8.5b, and a computer plot of the analysis in figure 8.9. The calculated line fits well the experimental points. The end of the hot flow time can be seen clearly on this trace.

The results of shocks into 72.1% oxygen/27.9% nitrogen are listed in table 8.3. Runs 886, 888, 889 and 890 give two sets of results for the same shock. The two photomultipliers had the same wavelength filters and two transient recorders are now used. The correlation between the pairs of results is good.

The temperature dependence of the quenching rate constant for the mixture is shown in figure 8.10 and that for the energy pooling rate constant in figure 8.11.

Figure 8.9.

A Computer Plot of the Analysis. 72.1%Oxygen/27.9%Nitrogen.

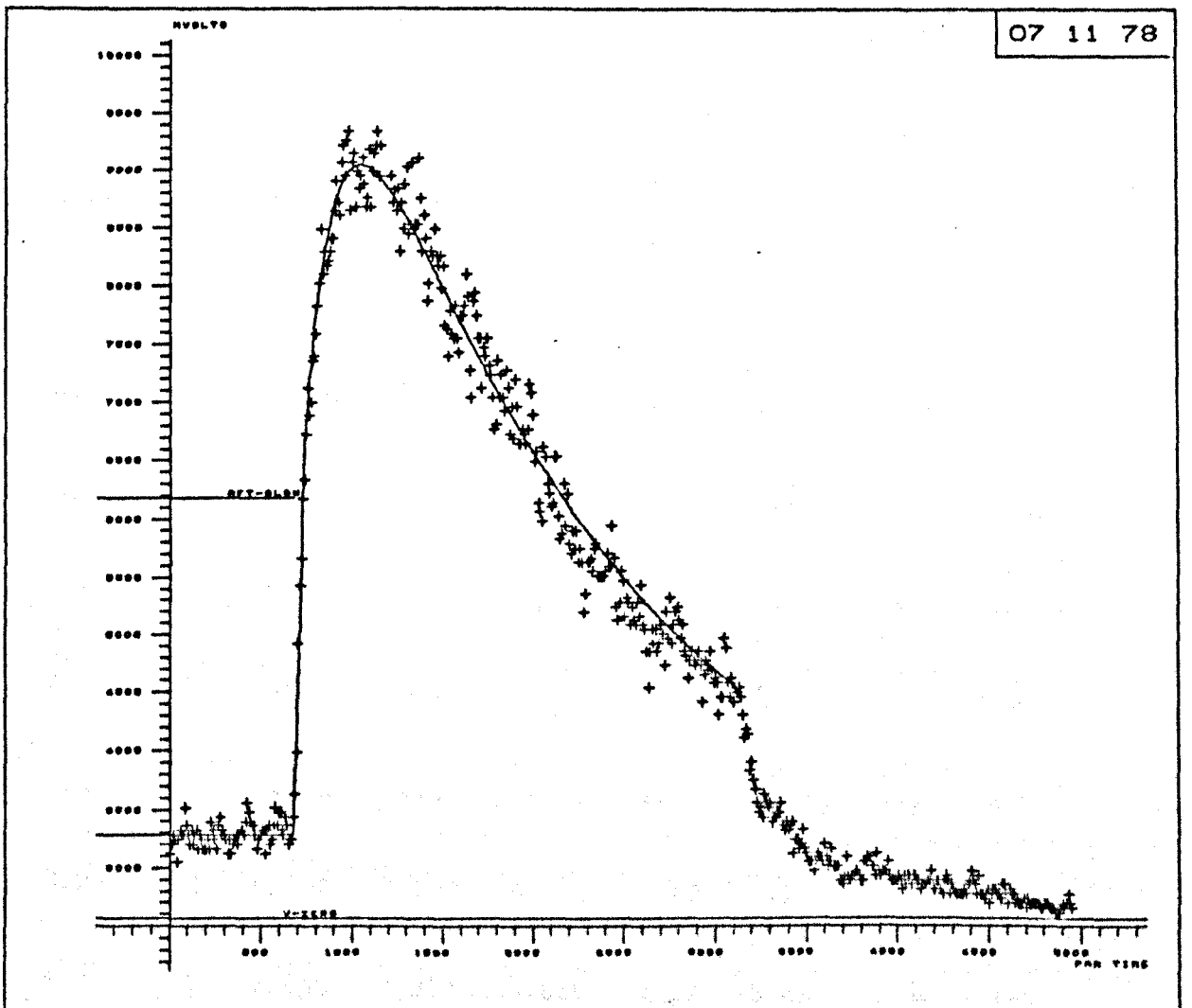

RUN NO A 890 SIGMA FITTED BY KEN RELAXATION INCLUDED

QUENCHING CONST	: .0057999	ERR	.000197	FITTED
RATIO (K)	: 2.561314	ERR	.0119329	FITTED
DECAY CONSTANT	: -.000643			
INTEGRATION TIME	: 59.59705	ERR	3.126974	FITTED

Table 8.3.

Results of the Analysis of Shocks at 762 nm into 72.1% Oxygen/27.9% Nitrogen.

Run No.	Pre Shock Measurements P_1 /torr	Glow /mV	Decay $/m^{-1}$	Speed /km s^{-1}	ρ_2/ρ_1	K	Rate Constants /l mol^{-1} s^{-1} $k_q/10^6$	$k_p/10^5$	T_2/K
A885	6.23	181	0.741	1.367	5.169	3.47	3.44	2.88	1175
886	6.84	294	0.717	1.077	4.261	2.20	2.22	1.26	847
A886	6.84	312	0.717	1.077	4.261	2.13	2.28	1.19	850
887	6.40	441	0.656	1.180	4.408	2.45	3.76	2.24	949
888	6.60	374	0.691	1.040	4.126	2.31	1.41	0.78	814
A888	6.60	685	0.691	1.040	4.126	2.23	1.85	1.00	813
889	6.23	375	0.652	1.229	4.546	2.68	2.99	1.90	1000
A889	6.23	707	0.652	1.229	4.546	2.59	3.11	1.93	1000
890	6.23	323	0.633	1.271	4.868	2.43	3.73	2.37	1047
A890	6.23	727	0.633	1.271	4.868	2.37	3.48	2.18	1047

Table 8.3.(continued)

Results of the Analysis of Shocks at 762 nm into 72.1% Oxygen/27.9% Nitrogen.

Run No.	Pre Shock Measurements P_1 /torr	Glow /mV	Decay /m^{-1}	Speed /km s^{-1}	ρ_2/ρ_1	K	Rate Constants /l $mol^{-1} s^{-1}$ $k_q/10^6$	$k_p/10^5$	T_2/K
M175	6.90	197	0.898	1.353	5.050	2.97	3.84	2.84	1139
M176	7.0	262	0.900	1.361	5.068	3.05	4.00	3.04	1120
M177	6.86	217	0.905	1.338	5.018	2.93	4.93	3.59	1120
M178	6.9	344	0.890	0.853	3.425	1.74	1.37	0.59	645
M179	6.8	329	0.920	0.831	3.339	1.75	1.21	0.53	627
M180	6.9	323	0.930	0.836	3.354	1.69	1.45	0.61	632
M182	6.85	165	0.897	1.481	5.308	3.66	6.32	5.74	1302
M183	6.85	160	0.946	1.479	5.356	4.10	4.54	4.61	1289
M184	6.7	165	0.935	1.483	5.352	3.70	6.65	6.07	1297
M185	6.75	165	0.980	1.519	5.431	4.27	7.41	7.83	1347
M186	6.7	96.7	0.975	1.627	5.658	4.04	11.07	11.12	1488
M188	6.7	159	0.717	1.384	5.133	2.84	4.39	3.08	1177

Figure 8.10. Temperature Dependence of Quenching Rate Constant for Mixture 72.1%Oxygen/27.9%Nitrogen.

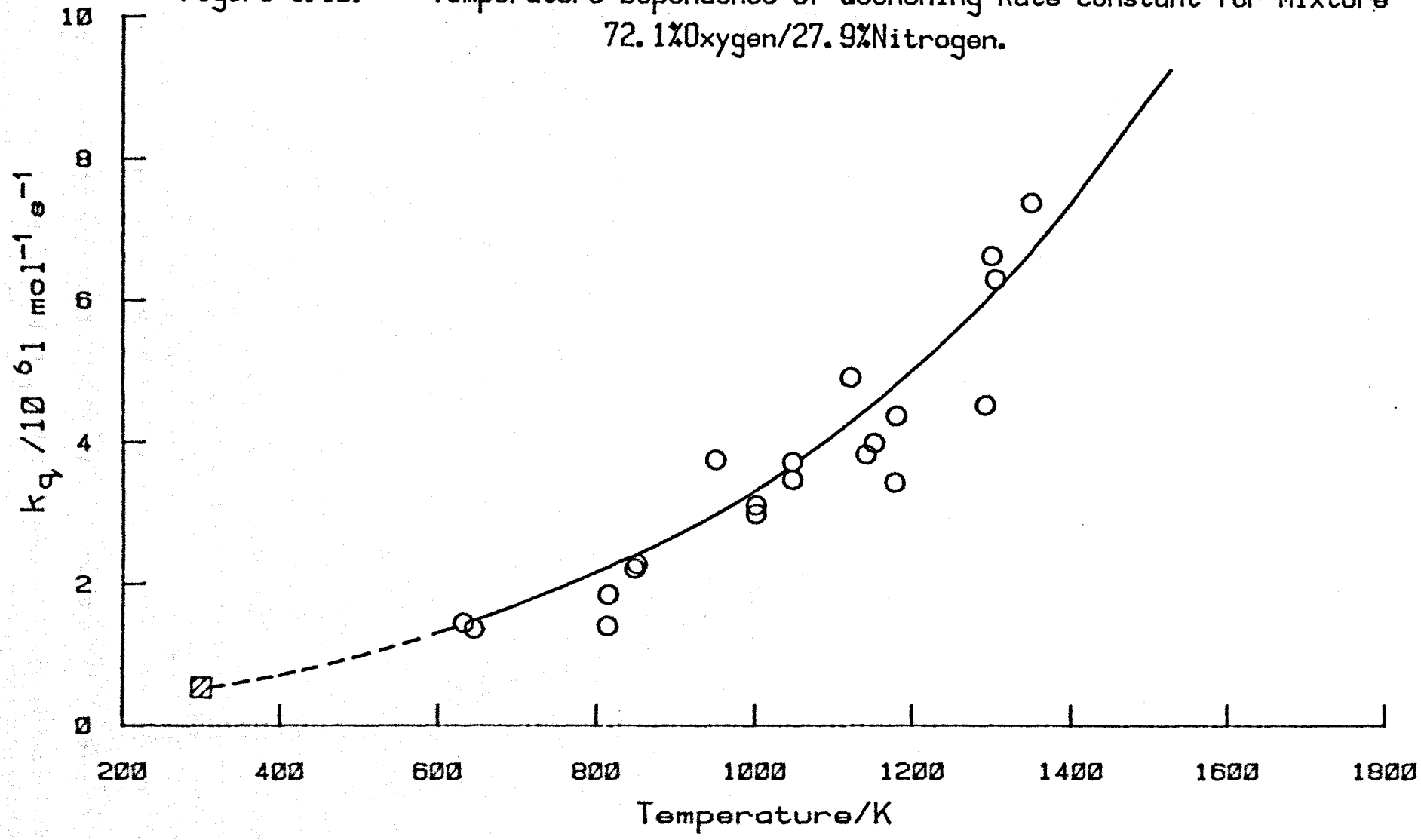

Figure 8.11. Temperature Dependence of Energy Pooling Rate Constant.
72.1%Oxygen/27.9%Nitrogen

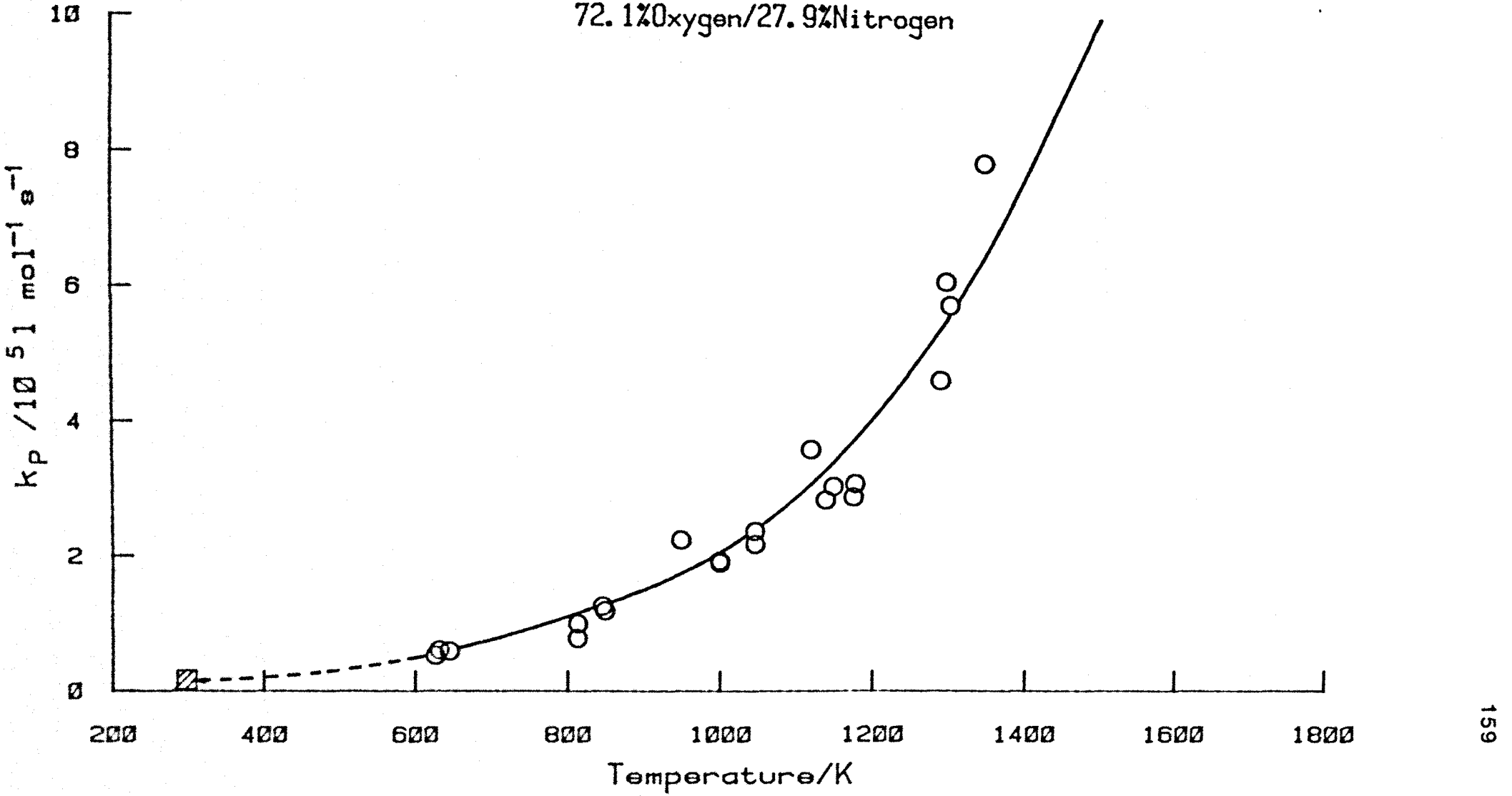

8.4.5. 46.3% Oxygen/53.7% Nitrogen

A trace of the shock emission at 762 nm from this mixture is shown in figure 8.12a. A computer plot of the analysis of this run is shown in figure 8.13. Although the pre-shock glow is considerably smaller than in 100% oxygen, the increase in emission at the shock temperature has increased by up to four times the pure oxygen value.

Table 8.4. lists the results of shocks into 46.3% oxygen/53.7% nitrogen. The temperature dependence of the quenching rate constant for the mixture, and the energy pooling rate constant are shown in figures 8.14 and 8.15. The scatter on these points is small, the high signal to noise ratio of the traces and the high K values mean that the analysis is more accurate.

Figure 8.12.

Traces of the Shock Emission at 762 nm.

a. Run No. 891. 46.3%Oxygen/53.7%Nitrogen.

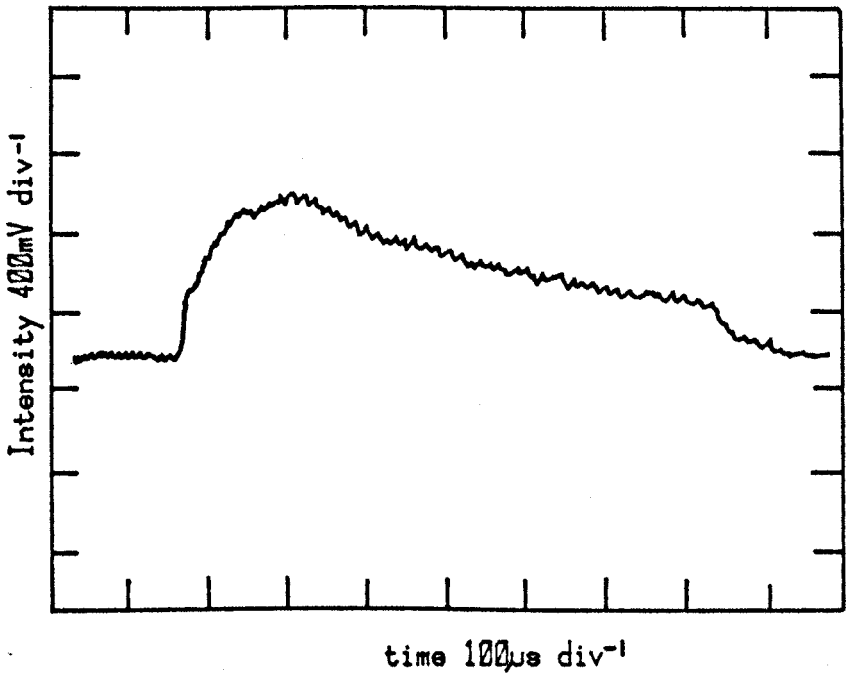

b. Run No. 898. 25% Oxygen/75% Nitrogen.

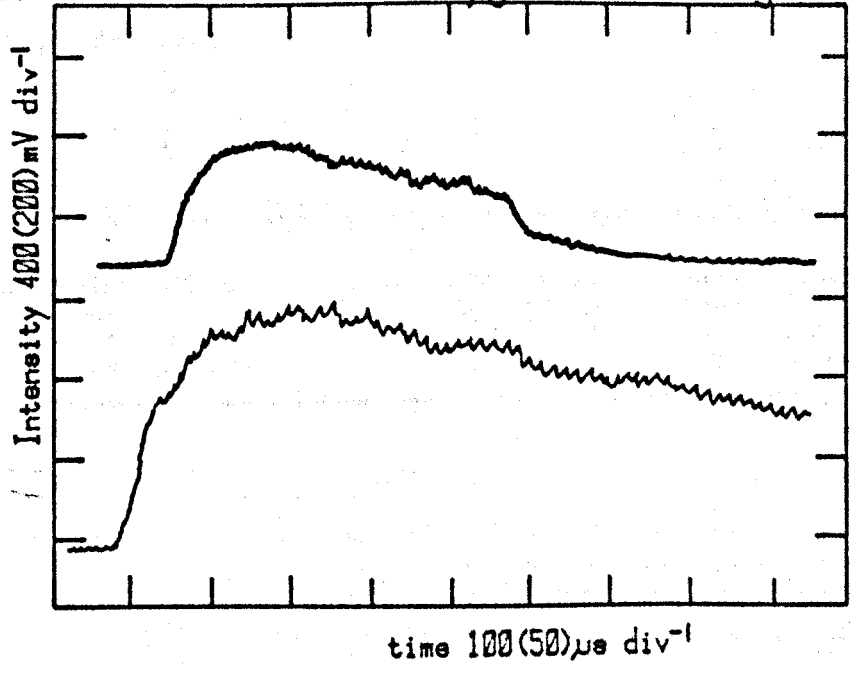

Figure 8.13.

A Computer Plot of the Analysis. 46.3%Oxygen/53.7%Nitrogen.

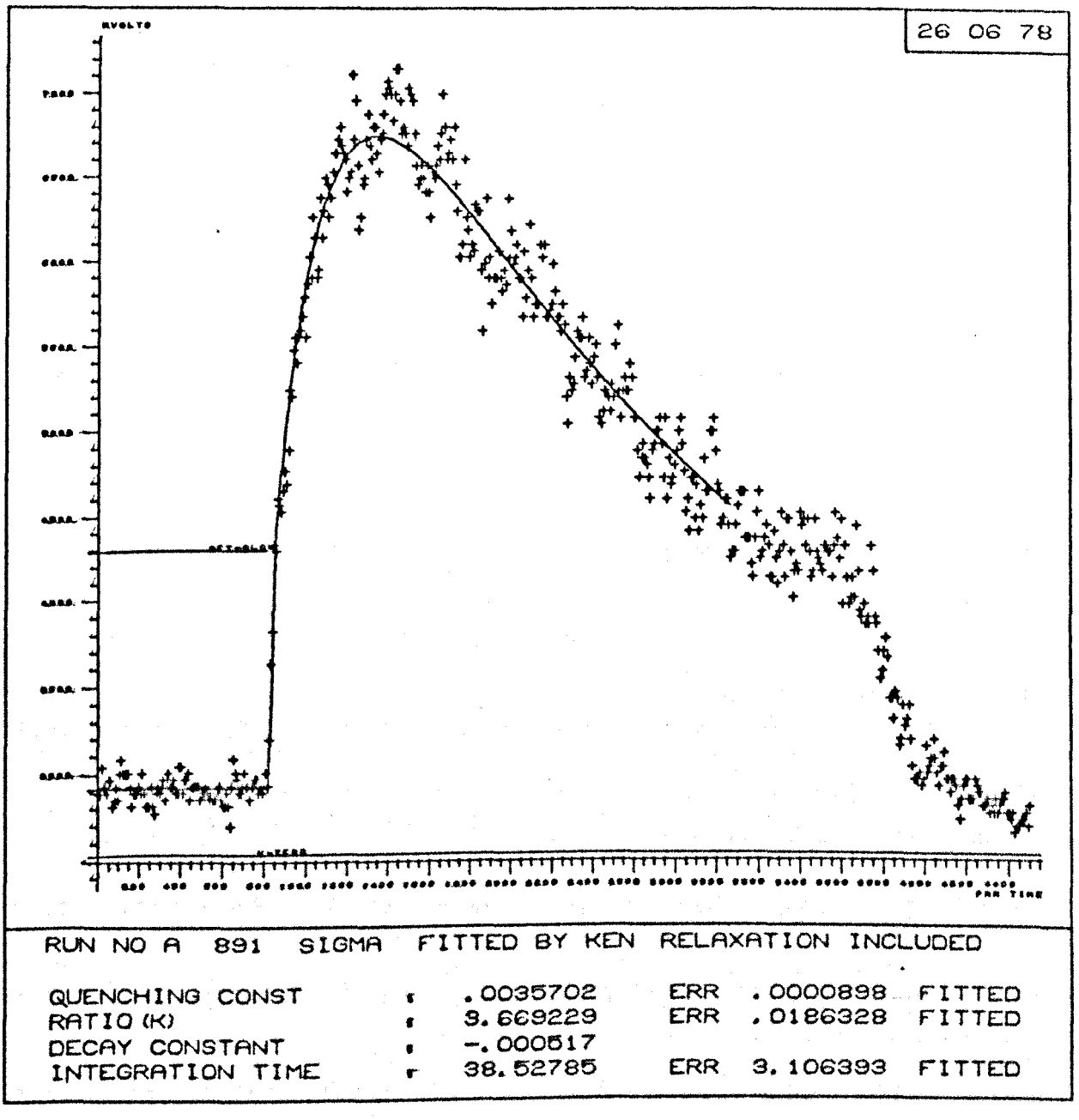

Table 8.4.

Results of the Analysis of Shocks at 762 nm into 46.3% Oxygen/53.7% Nitrogen.

Run No.	Pre Shock Measurements P_1 /torr	Glow /mV	Decay /m^{-1}	Speed /km s^{-1}	ρ_2/ρ_1	K	Rate Constants /l mol^{-1} s^{-1} $k_q/10^6$	$k_\rho/10^5$	T_2/K
A891	6.47	388	0.566	1.170	4.446	3.37	3.00	1.60	929
891	6.47	191	0.566	1.170	4.446	3.53	2.29	1.27	930
A892	6.35	386	0.515	1.097	4.149	3.28	2.52	2.03	868
892	6.35	176	0.515	1.097	4.149	3.39	2.66	2.21	867
A893	6.59	398	0.546	1.110	4.163	3.71	2.13	1.20	865
893	6.59	165	0.546	1.110	4.163	3.81	2.47	1.43	865
A894	6.70	417	0.544	1.070	4.069	3.12	4.22	1.16	829
894	6.70	152	0.544	1.070	4.069	2.98	2.82	1.28	829
A895	6.70	415	0.585	1.168	4.327	3.60	2.70	1.43	927
895	6.70	151	0.585	1.168	4.327	3.48	2.48	1.36	930
A896	6.8	356	0.587	1.012	3.950	2.99	2.03	0.93	773
896	6.8	139	0.587	1.012	3.950	2.86	2.02	0.88	774
A897	6.2	401	0.509	1.026	4.000	2.93	2.55	1.13	788
897	6.2	149	0.509	1.026	4.000	2.81	2.46	1.04	788

Table 8.4.(continued)

Results of the Analysis of Shocks at 762 nm into 46.3% Oxygen/53.7% Nitrogen.

Run No.	Pre Shock Measurements P_1 /torr	Glow /mV	Decay /m^{-1}	Speed /km s^{-1}	ρ_2/ρ_1	K	Rate Constants /l mol^{-1} s^{-1} $k_q/10^6$	$k_\rho/10^5$	T_2/K
M160	6.75	100	0.507	1.417	5.028	4.51	5.26	3.60	1208
M161	6.56	117	0.532	1.389	4.961	4.57	4.91	3.39	1175
M162	6.81	97	0.531	1.407	5.012	4.93	3.61	2.70	1195
M163	6.7	137	0.528	0.883	3.468	1.89	1.89	0.54	661
M164	6.7	266	0.533	0.877	3.446	2.27	1.34	0.46	655
M165	6.7	239	0.551	0.868	3.423	2.32	1.91	0.67	646
M166	6.7	94	0.530	1.629	5.480	6.99	5.59	5.93	1475
M167	6.75	41	0.562	1.701	5.613	5.68	9.59	8.28	1574
M168	6.86	89	0.555	1.590	5.387	6.25	6.47	6.15	1434
M169	6.9	82	0.559	1.540	5.306	6.09	6.75	6.27	1363
M170	6.64	86	0.559	1.582	5.355	6.09	6.19	5.73	1420
M171	6.64	110	0.548	1.730	5.652	8.37	7.24	9.18	1617
M172	6.9	121	0.577	1.398	5.000	4.58	5.36	3.74	1182
M173	6.75	130	0.553	1.396	4.981	4.87	4.74	3.51	1183
M174	6.7	69	0.530	1.718	5.640	7.63	7.13	8.26	1599

Figure 8.14. Temperature Dependence of Quenching Rate Constant for Mixture 46.3%Oxygen/53.7%Nitrogen.

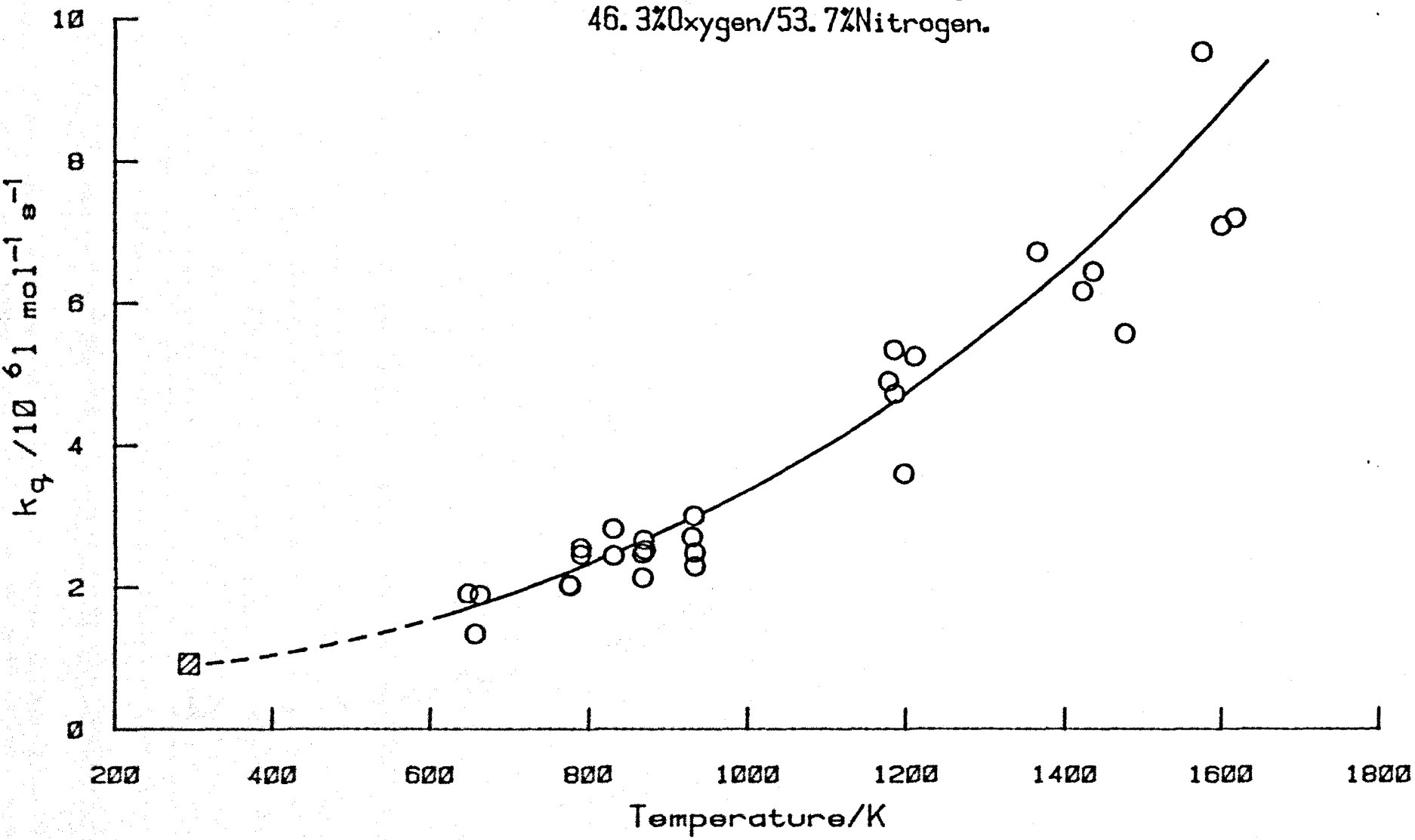

Figure 8.15. Temperature Dependence of Energy Pooling Rate Constant.
46.3%Oxygen/53.7%Nitrogen

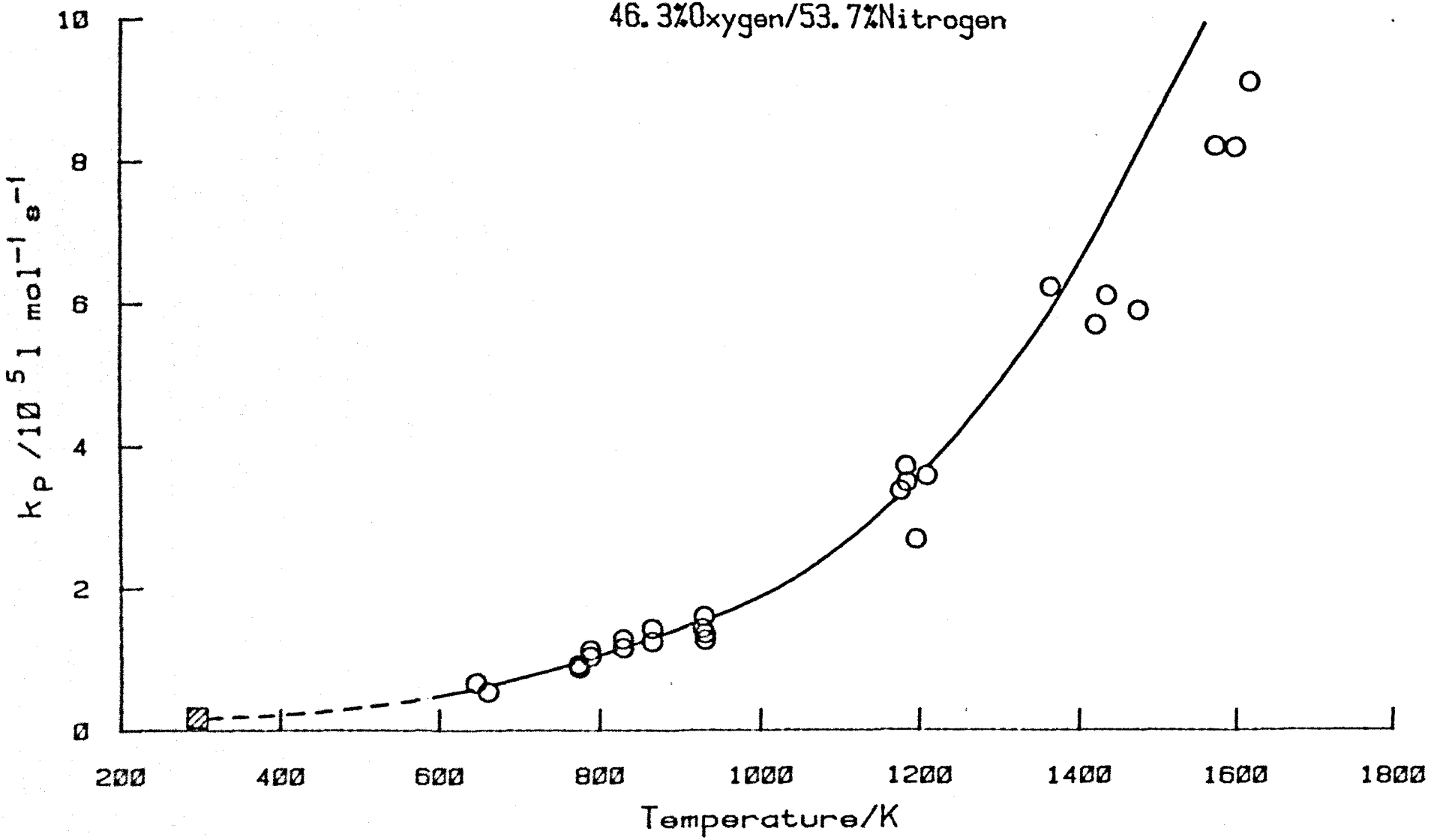

8.4.6. 25% Oxygen/75% Nitrogen

A typical shock trace for 25% oxygen/75% nitrogen is shown in figure 8.12b, and a computer plot of the analysis is shown in figure 8.16. This run was analysed with the new computer programme written for the HP 2647A intelligent graphics terminal and the University's new GEC 4082 computer. The postulated model fits the experimental trace, and the computed line fits the experimental points.

Table 8.5 lists the results of shocks into this mixture. The temperature dependence of the rate constants are plotted in figures 8.17 and 8.18. Despite the enhancement in emission at the shock temperature, these results show more scatter than for the 46.3% oxygen results, probably because of the lower pre-shock glow for this mixture weak in oxygen.

RUN NUMBER P898 07 JUL 1980
762.nm SIGMA

RESULTS

fitted	Quenching Const.	:	2.5589E-02	us-1
		:	3.9079E+01	us
	err.	:	7.1024E-01	
fitted	Ratio (K)	:	7.4824E+00	
	err.	:	2.6240E-02	
fitted	Decay Constant	:	-1.8203E-03	us-1
		:	-3.1897E-03	cm-1
	err.	:	2.7874E-05	
fitted	Integration Time	:	7.4482E+00	us
	err.	:	8.1153E-01	

RATE CONSTANTS (in l mol-1 s-1)

fitted	Quenching : kq	:	2.7296E+06	
	err.	:	4.9609E+04	
	log kq	:	6.4361	
fitted	Pooling : kp	:	2.3171E+05	
	err :		8.1257E+02	
	log kp	:	5.3649	

RUN DATA

Oxygen	:	25.000	%
N2	:	75.000	%
Shock Speed	:	1.414	mm us-1
Initial Pressure	:	6.800	torr
P21	:	20.060	
Initial Temperature	:	295.000	K
T2	:	1164.000	K
Density Ratio, RO21	:	5.036	
Xzero	:	113.600	us
Yzero	:	2488.034	mV
Pre-shock glow, PSG	:	104.800	mV
Afterglow	:	527.772	mV

FITTING

Fitted by NAG	:	complete fit.
No. of iterations	:	7
No. of points	:	286
Sum of the Squares	:	1.2764E+07

* * *

Figure 8.16. A Computer Plot of the Analysis.

25% Oxygen/75% Nitrogen

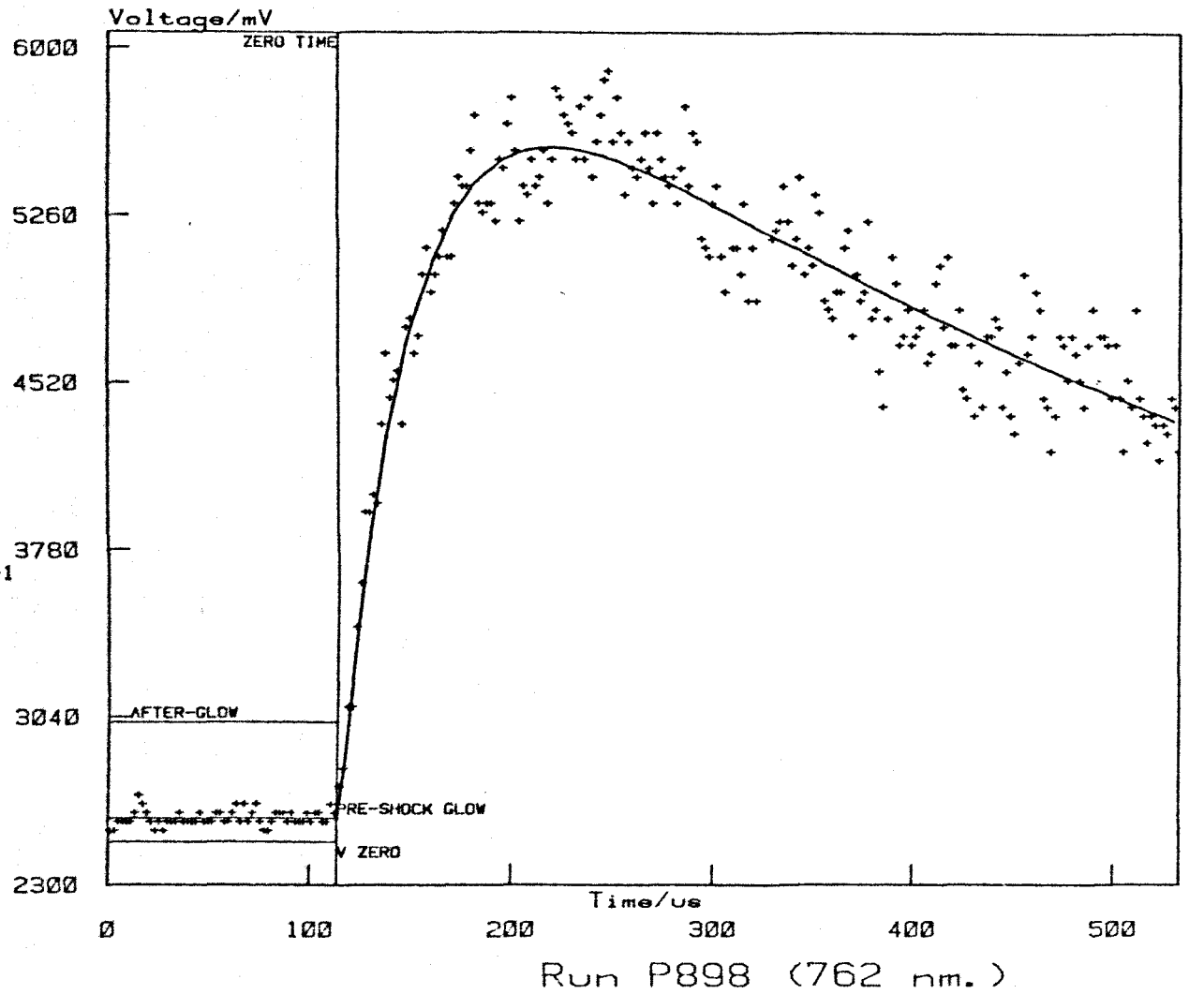

Table 8.5.

Results of the Analysis of Shocks at 762 nm into 25% Oxygen/75% Nitrogen.

Run No.	Pre Shock Measurements P_1 /torr	Glow /mV	Decay $/m^{-1}$	Speed /km s^{-1}	ρ_2/ρ_1	K	Rate Constants /l $mol^{-1}s^{-1}$ $k_q/10^6$	$k_\rho/10^5$	T_2/K
898	6.80	105	0.319	1.414	5.036	7.48	2.73	2.32	1164
899	6.23	44.9	0.392	1.387	4.776	7.02	5.26	4.23	1173
A899	6.23	134	0.392	1.387	4.776	7.13	3.60	2.93	1173
900	6.27	40.7	0.421	1.105	4.107	3.97	3.13	1.42	856
A900	6.27	119	0.421	1.105	4.107	4.09	2.93	1.37	856
A901	6.72	87.0	0.450	1.007	3.830	3.42	2.38	0.94	759
M192	6.50	126	0.380	1.406	4.808	7.55	3.91	3.80	1190
M192A	6.50	26.8	0.380	1.406	4.808	7.06	4.99	4.04	1191
M193	6.41	141	0.381	1.420	4.831	7.66	3.40	3.07	1207
M193A	6.41	29.7	0.381	1.420	4.831	8.10	4.86	4.54	1207
M194	6.40	143	0.368	1.592	5.089	11.74	4.74	6.38	1432
M194A	6.40	27.0	0.368	1.592	5.089	11.05	4.83	6.12	1432

Table 8.5.(continued)

Results of the Analysis of Shocks at 762 nm into 25% Oxygen/75% Nitrogen.

Run No.	Pre Shock Measurements P_1 /torr	Glow /mV	Decay /m^{-1}	Speed /km s^{-1}	ρ_2/ρ_1	K	Rate Constants /l mol^{-1} s^{-1} $k_q/10^6$	$k_p/10^5$	T_2/K
M196	6.70	110	0.404	1.598	5.232	11.52	6.38	8.61	1439
M196A	6.70	22.5	0.404	1.698	5.232	13.02	4.41	6.61	1437
M197	6.70	125	0.418	0.874	3.411	3.04	1.62	0.57	638
M197A	6.70	20.7	0.418	0.874	3.411	2.12	2.01	0.49	638
M198	6.64	131	0.404	0.867	3.391	2.90	1.67	0.56	634
M198A	6.64	124	0.404	0.867	3.391	2.91	1.54	0.51	634
M199	6.75	125	0.403	0.874	3.406	2.95	1.63	0.55	639
M199A	6.75	123	0.403	0.874	3.406	3.34	1.55	0.60	639
M200	6.56	104	0.383	1.419	4.854	8.70	3.43	3.43	1210

Figure 8.17. Temperature Dependence of Quenching Rate Constant for Mixture 25% Oxygen/75% Nitrogen.

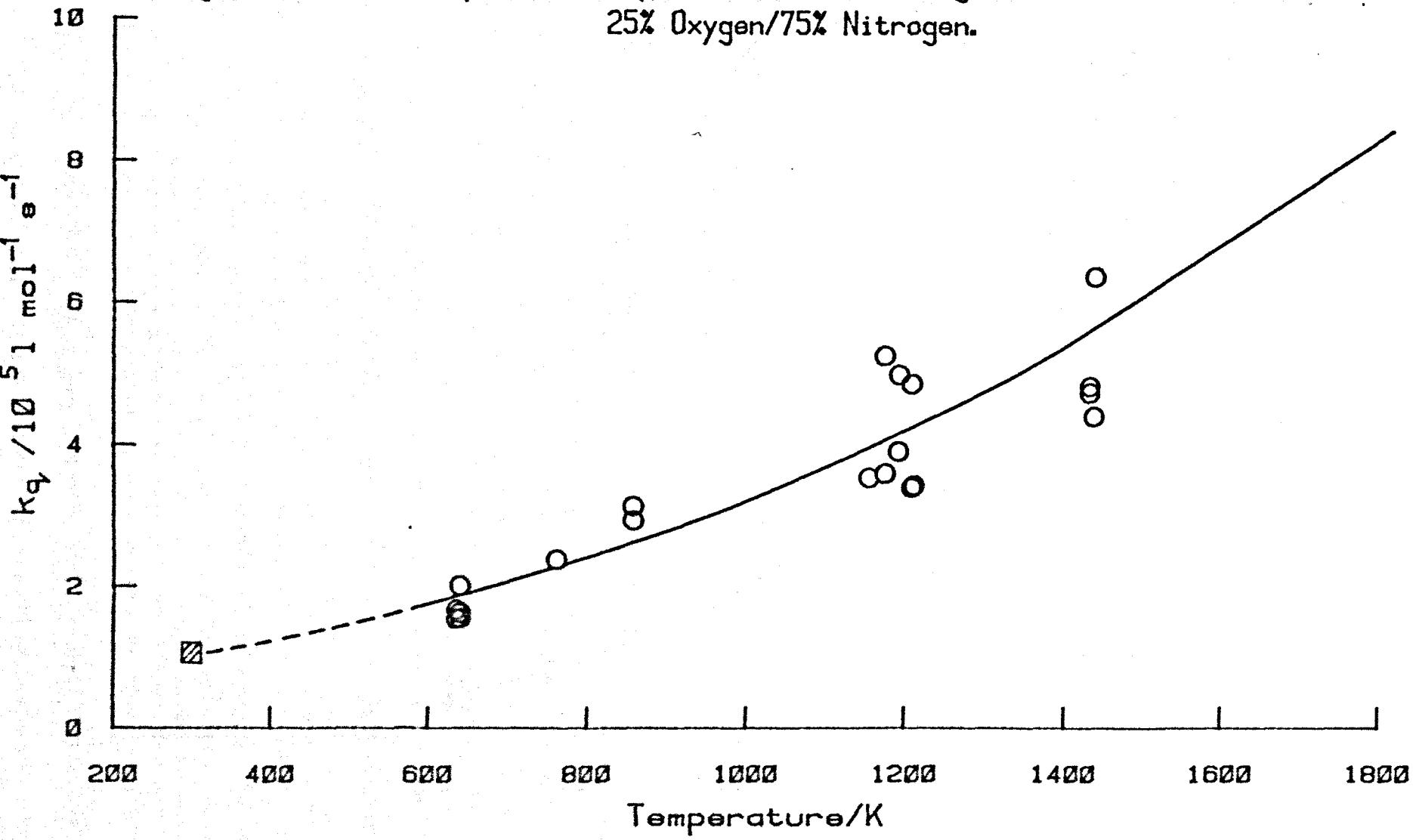

Figure 8.18. Temperature Dependence of Energy Pooling Rate Constant.
25% Oxygen/75% Nitrogen

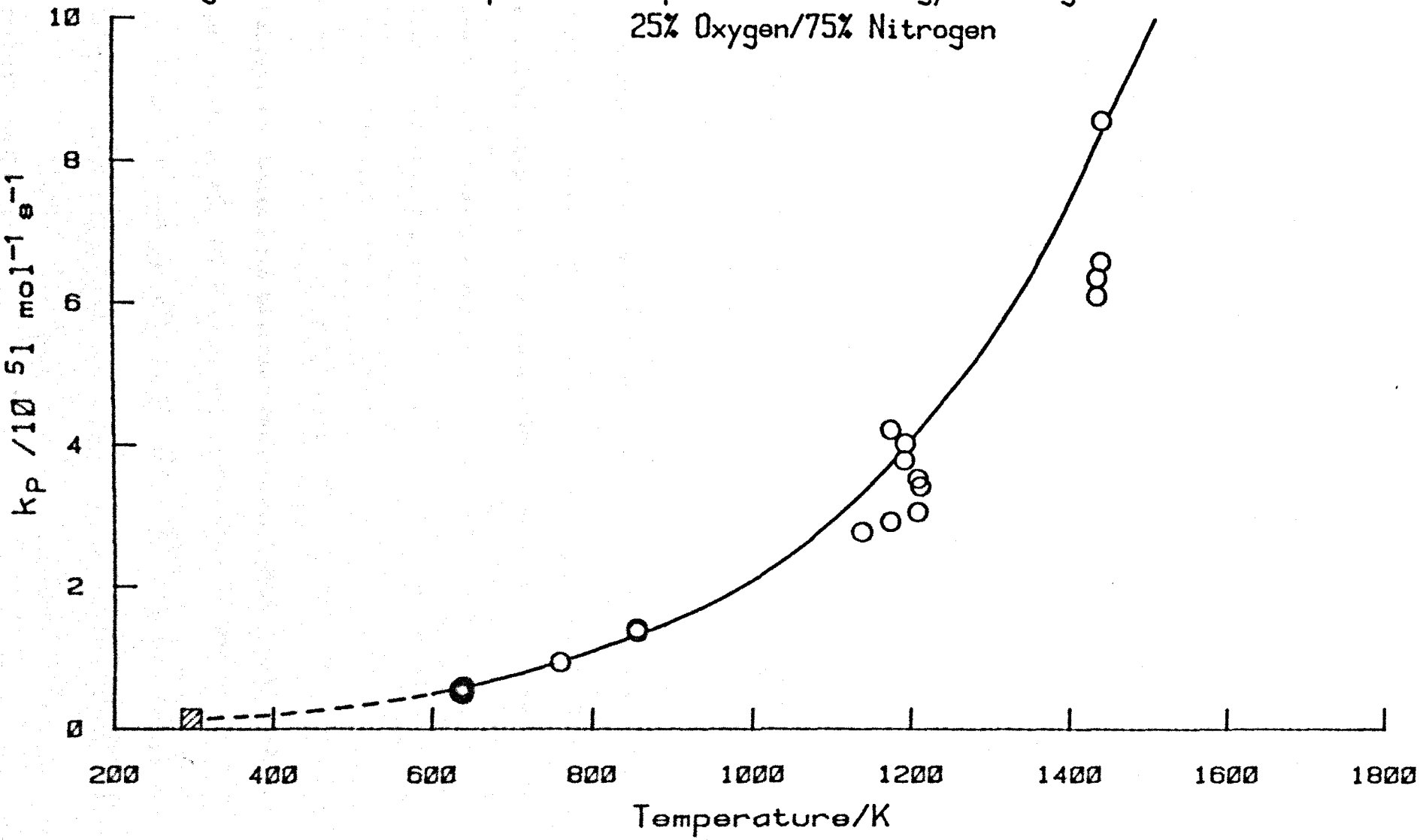

8.4.7. 45% Oxygen/45% Nitrogen/10% Argon

The collisional quenching of $O_2(^1\Sigma_g^+)$ by argon at room temperature is very slow,[121] (9×10^3 ℓ mol^{-1} s^{-1}), but the rate constant might be expected to increase with temperature where, for a monatomic gas, short range interactions would predominate.

Figure 8.19a shows a shock trace of the 762 nm emission for the mixture 45% oxygen, 45% nitrogen and 10% argon. The features of the shock emission are the same as for the oxygen and nitrogen mixtures. Figure 8.20 shows the computer analysis of the same run, the line calculated from the parameters found in the analysis fits the experimented points well.

The results of shocks into this mixture are listed in table 8.6. The rate constant for quenching of $O_2(^1\Sigma_g^+)$ by the mixture at the shock temperature, k_q, is calculated from the parameter k_q' by :

$$k_q = k_q'/([O_2] + [N_2] + [Ar]) \qquad 8.28$$

where the concentrations of the gases are at the shock density. The energy pooling rate constant is calculated from the value of K and k_q from equation 8.11; the room temperature value of k_q^M is calculated from equation 8.18 using a value of 9×10^3 ℓ mol^{-1} s^{-1} for k_q^{Ar}.

The temperature dependence of the quenching rate constant for the mixture, and the energy pooling rate constant are shown in figures 8.21 and 8.22. The effects of vibrational relaxation are not included in the analysis of shocks into mixtures containing argon. The addition of argon increases the vibrational relaxation time of oxygen, and so with the large K values the effects of vibrational relaxation on the analysis become less important. The addition of nitrogen to these mixtures ensures large K values, well defined relaxation zones and more accurate analysis.

Figure 8.19.

Traces of the Shock Emission at 762 nm.

a. Run No 993 45% O_2/45% N_2/10% Ar

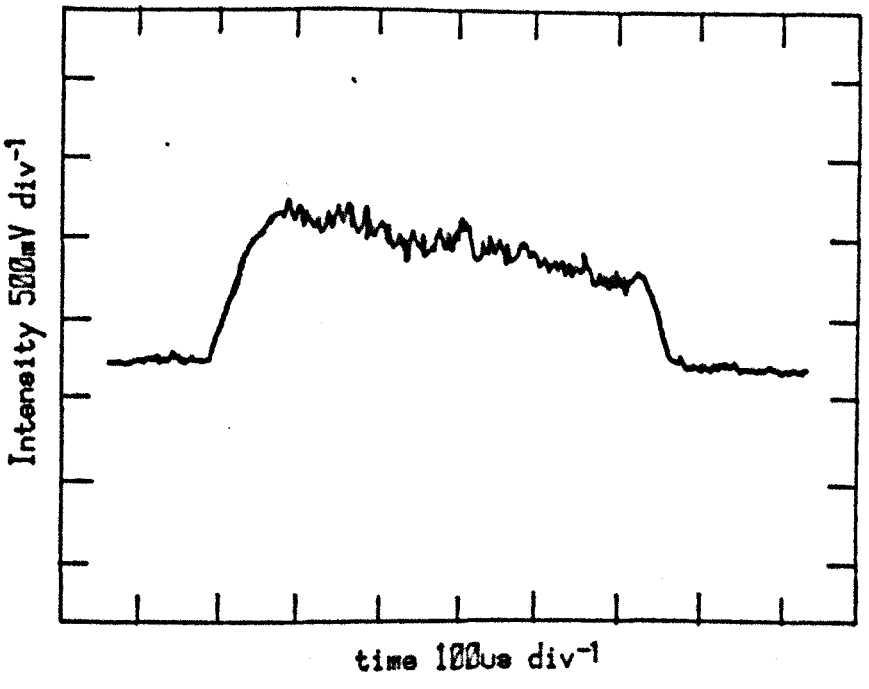

b. Run No C139 30% O_2/30% N_2/40% Ar

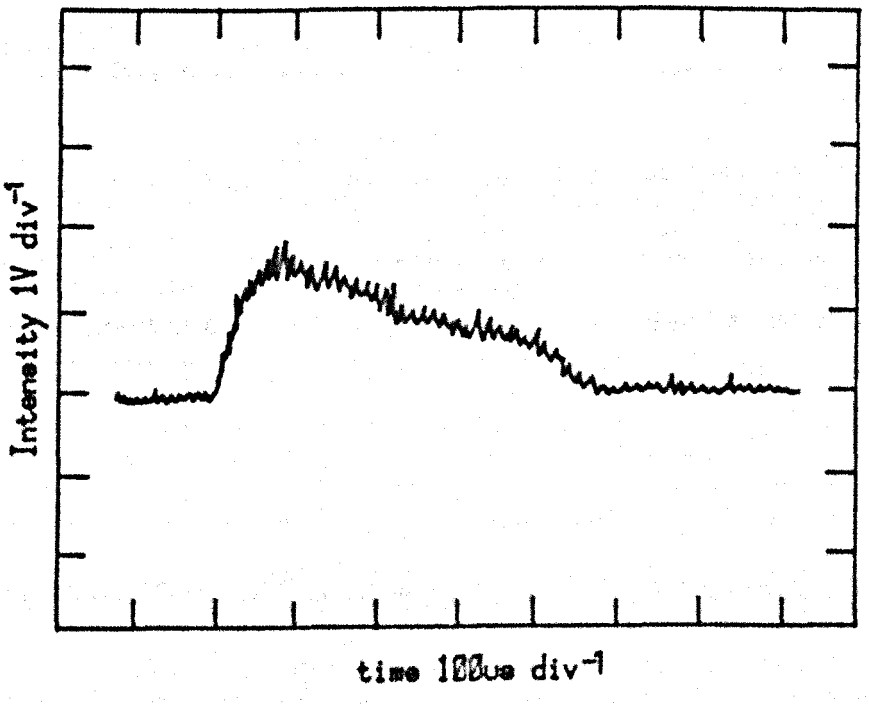

Figure 8.20

A Computer Plot of the Analysis.

45% Oxygen/45% Nitrogen/10% Argon

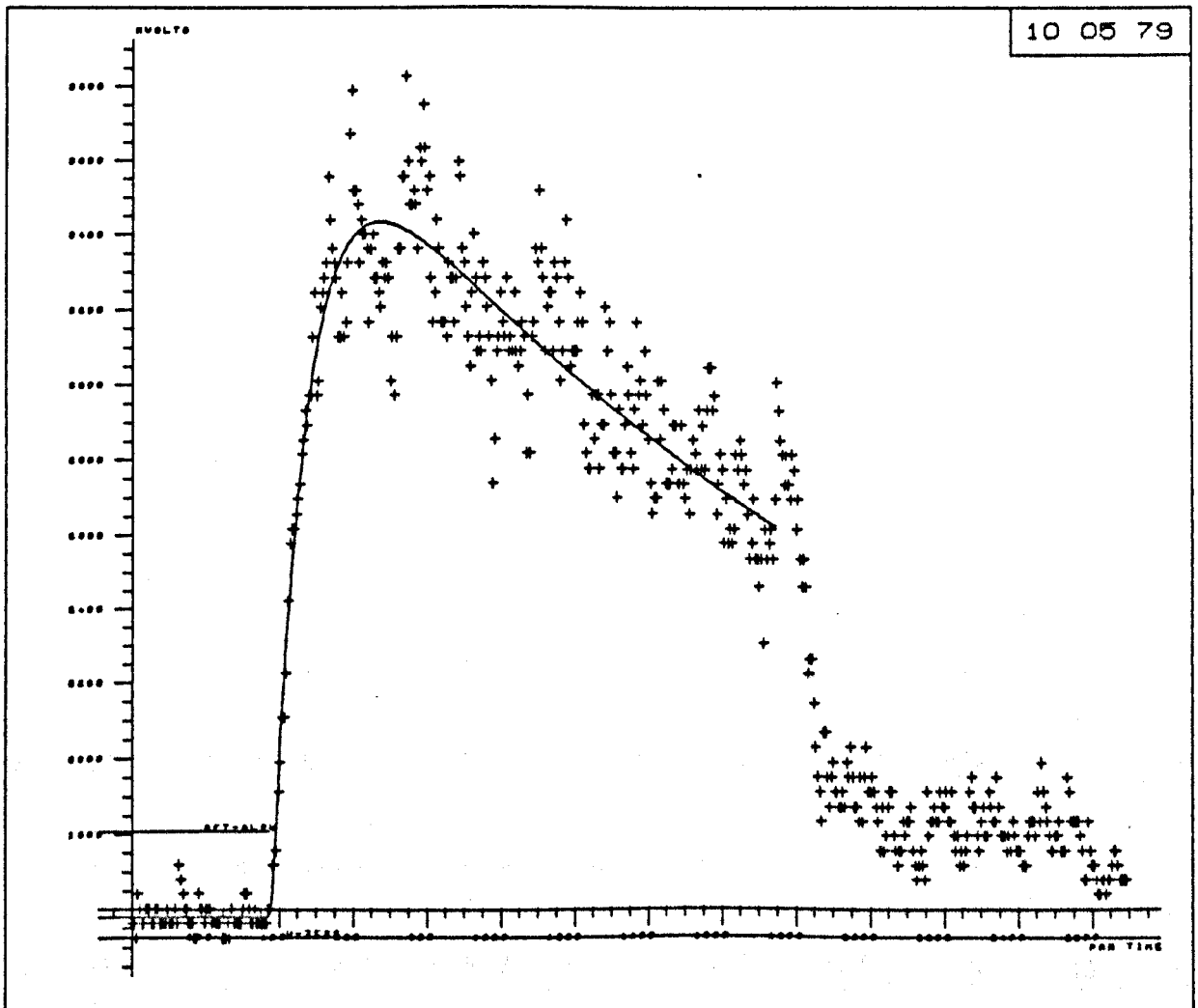

RUN NO 993 SIGMA FITTED BY KEN RELAXATION NOT INCLUDED					
QUENCHING CONST	:	.0096965	ERR	.0004945	FITTED
RATIO (K)	:	8.386935	ERR	.0610444	FITTED
DECAY CONSTANT	:	-.000569			
INTEGRATION TIME	:	29.28318	ERR	5.310581	FITTED

Table 8.6.

Results of the Analysis of Shocks at 762 nm into 45% Oxygen/45% Nitrogen/10% Argon.

Run No.	Pre Shock Measurements P_1 /torr	Glow /mV	Decay /m^{-1}	Speed /km s^{-1}	ρ_2/ρ_1	K	Rate Constants /l mol^{-1} s^{-1} $k_q/10^6$	$k_p/10^5$	T_2/K
A991	6.31	34.0	0.467	1.655	5.286	9.77	8.45	14.6	1620
992	6.80	40.4	0.524	1.635	5.260	9.52	5.51	9.31	1589
A992	6.80	34.6	0.524	1.635	5.260	10.85	4.42	8.51	1589
993	5.82	53.8	0.430	1.631	5.257	8.39	5.79	8.40	1586
A993	5.82	48.6	0.430	1.631	5.257	8.66	8.06	12.3	1586
994	6.10	87.8	0.464	0.879	3.483	2.44	1.21	0.51	667
A994	6.10	81.1	0.464	0.879	3.483	2.42	1.51	0.49	667
995	6.59	78.9	0.478	0.964	3.748	2.38	1.82	0.77	755
A995	6.59	87.0	0.478	0.964	3.748	2.54	1.89	0.85	755
996	7.05	101	0.515	0.953	3.715	2.71	1.42	0.69	743
A996	7.05	98.7	0.515	0.953	3.715	2.55	1.96	0.89	743

Table 8.6.(continued)

Results of the Analysis of Shocks at 762 nm into 45% Oxygen/45% Nitrogen/10% Argon.

Run No.	Pre Shock Measurements P_1 /torr	Glow /mV	Decay $/m^{-1}$	Speed /km s^{-1}	ρ_2/ρ_1	K	Rate Constants /l mol^{-1} s^{-1} $k_q/10^6$	$k_p/10^5$	T_2/K
C121A	6.55	37.2	0.496	1.379	4.663	6.08	3.32	3.56	1258
C123A	6.39	37.6	0.463	1.404	4.702	6.47	3.43	3.92	1293
C124	6.51	66.6	0.487	1.437	4.752	6.63	4.39	5.14	1341
C124A	6.51	106	0.487	1.437	4.752	6.14	4.67	5.06	1341
C125	6.47	104	0.495	1.411	4.713	6.43	4.02	4.54	1303
C125A	6.47	108	0.497	1.411	4.713	6.45	3.82	4.37	1303
C126	6.92	89.6	0.535	1.380	4.664	6.02	3.33	3.57	1259
C126A	6.92	86.1	0.535	1.380	4.664	5.94	3.45	3.64	1259

Figure 8.21. Temperature Dependence of Quenching Rate Constant for Mixture 45% Oxygen/45% Nitrogen/10% Argon.

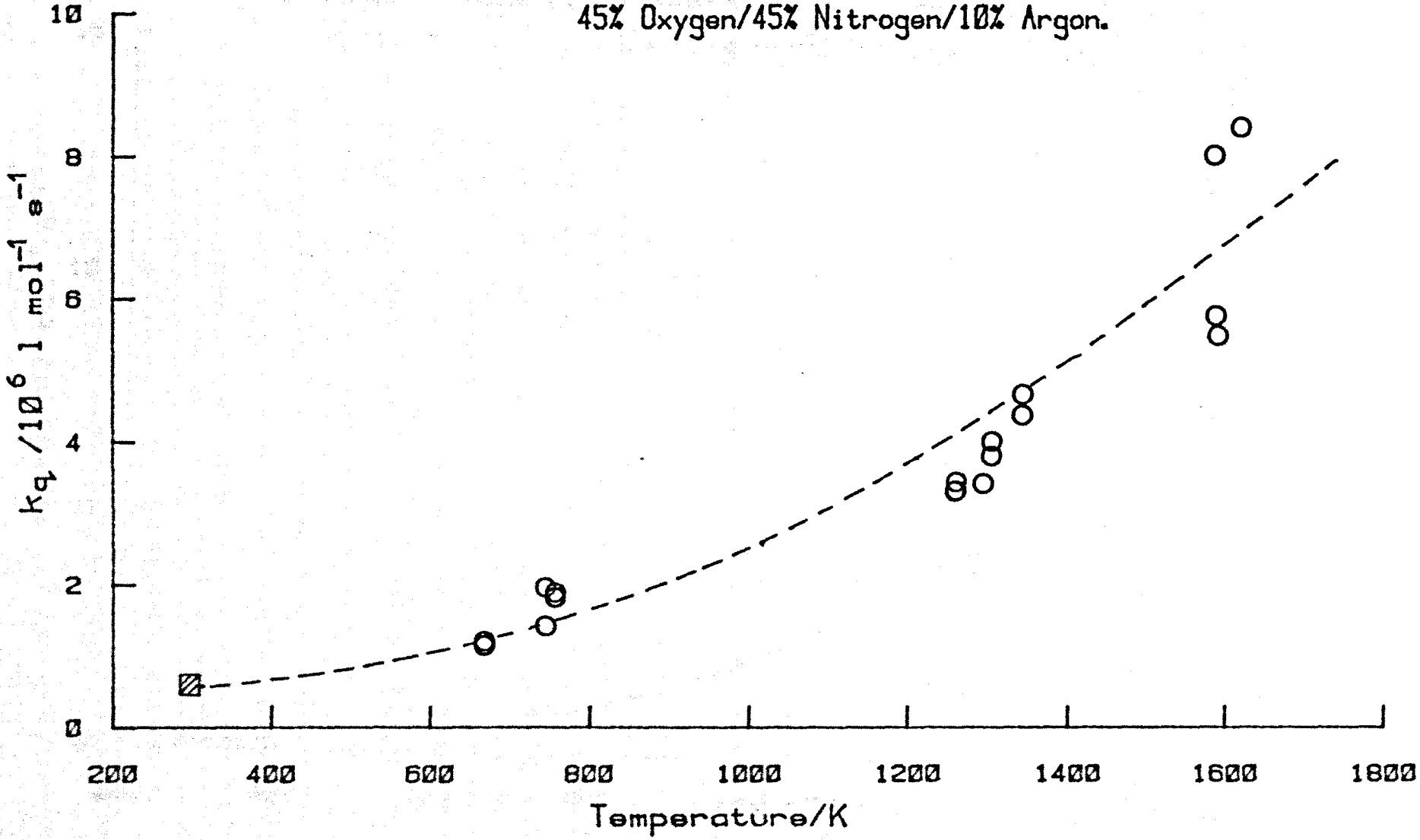

Figure 8.22. Temperature Dependence of Energy Pooling Rate Constant.
45% Oxygen/45% Nitrogen/10% Argon.

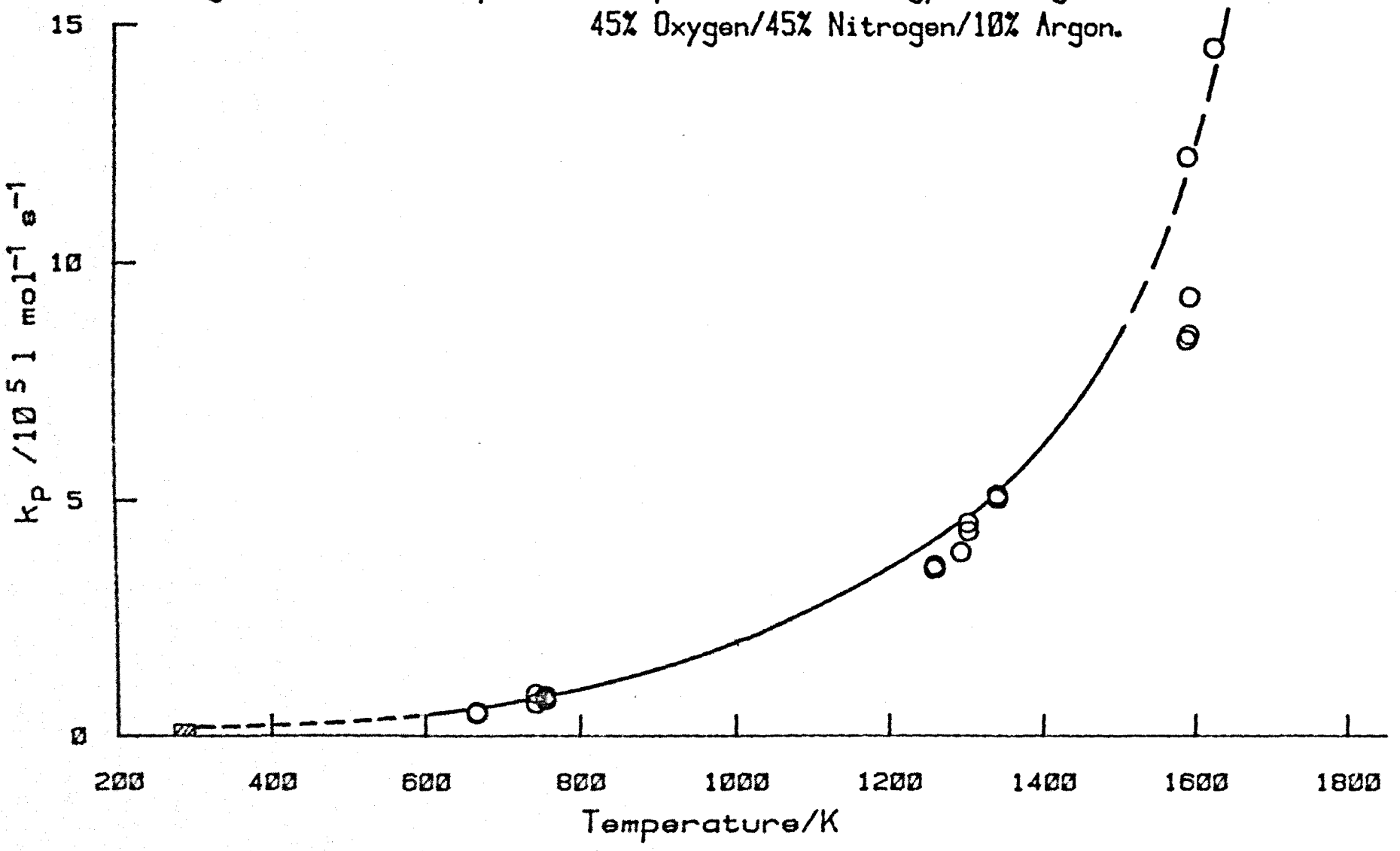

8.4.8. 30% Oxygen/30% Nitrogen/40% Argon

A trace of the shock output can be seen in figure 8.19b, and a computer plot of the analysis in figure 8.23. The postulated model and the experimental points fit well.

The results are listed in table 8.7 and plots of the quenching rate constant for the mixture, and the energy pooling rate constant against temperature are shown in figures 8.24 and 8.25.

Figure 8.23

A Computer Plot of the Analysis.

30% Oxygen/30% Nitrogen/40% Argon

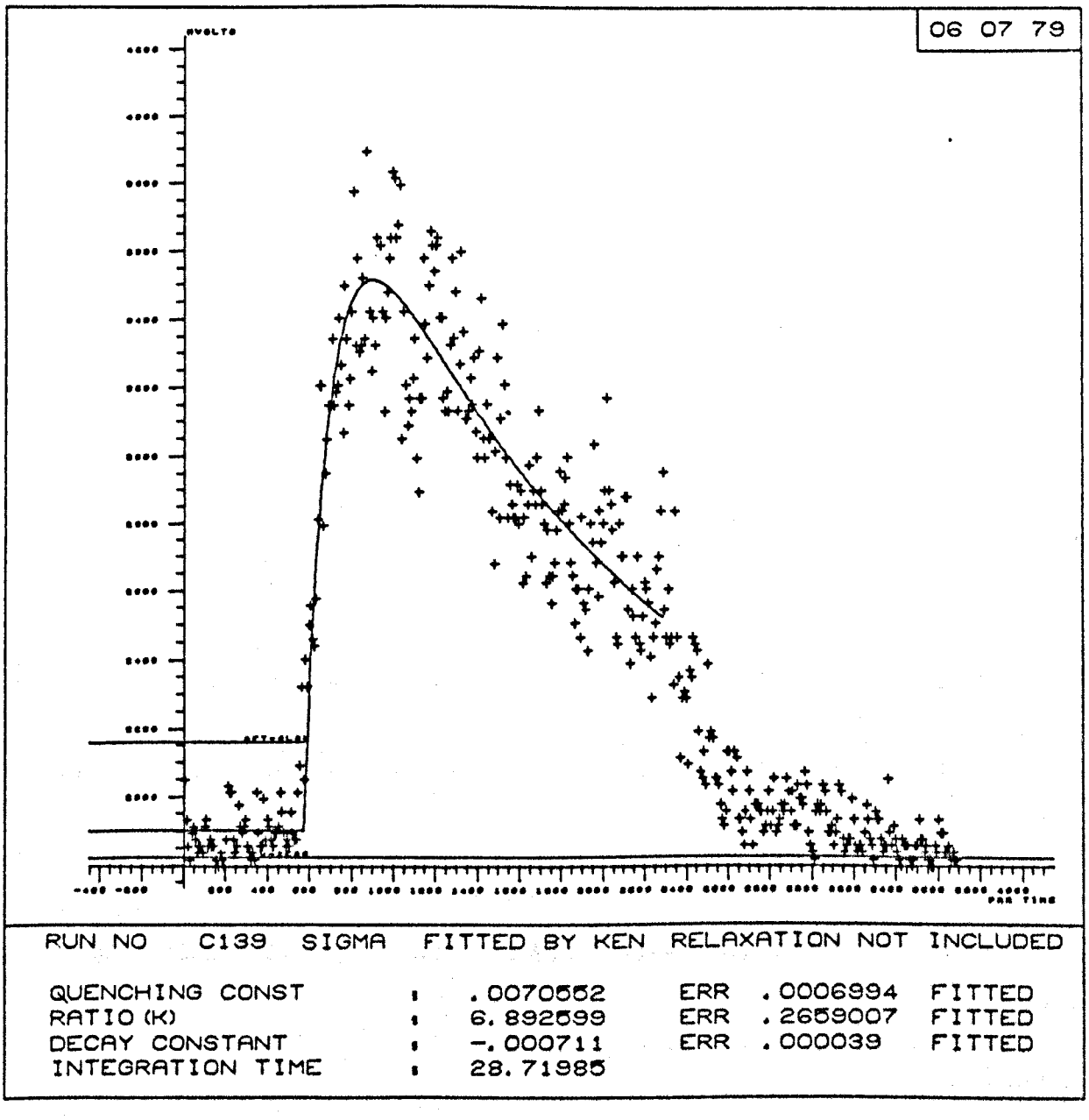

RUN NO C139 SIGMA FITTED BY KEN RELAXATION NOT INCLUDED

QUENCHING CONST	: .0070552	ERR .0006994	FITTED
RATIO (K)	: 6.892599	ERR .2659007	FITTED
DECAY CONSTANT	: -.000711	ERR .000039	FITTED
INTEGRATION TIME	: 28.71985		

Table 8.7.

Results of the Analysis of Shocks at 762 nm into 30% Oxygen/30% Nitrogen/40% Argon.

Run No.	Pre Shock Measurements P_1 /torr	Glow /mV	Decay /m^{-1}	Speed /km s^{-1}	ρ_2/ρ_1	K	Rate Constants /l mol^{-1} s^{-1} $k_q/10^6$	$k_\rho/10^5$	T_2/K
C138	6.96	57.0	0.602	1.393	4.494	8.73	2.37	5.30	1438
C139	6.31	78.7	0.606	1.401	4.506	6.89	4.82	8.30	1451
C140	6.47	80.2	0.588	1.393	4.494	8.64	3.39	7.38	1438
C141	6.72	60.1	0.600	1.581	4.727	12.01	5.84	17.76	1767
C142	6.84	53.8	0.592	1.608	4.756	14.95	5.38	20.43	1817
C142A	6.84	53.4	0.592	1.608	4.756	10.36	6.59	17.34	1817
C143	6.76	46.6	0.584	1.616	4.764	13.53	5.60	19.25	1832
C143A	6.76	51.6	0.584	1.616	4.764	10.66	6.78	18.36	1832
C144	6.64	50.1	0.583	1.479	4.607	8.11	4.65	9.54	1583
C144A	6.64	47.7	0.583	1.479	4.607	7.29	4.53	8.36	1583
C145	7.08	42.6	0.598	1.470	4.596	9.99	4.67	11.96	1568
C145A	7.08	44.2	0.598	1.470	4.596	7.77	3.49	6.94	1568

Table 8.7.(continued)

Results of the Analysis of Shocks at 762 nm into 30% Oxygen/30% Nitrogen/40% Argon.

Run No.	Pre Shock Measurements P_1 /torr	Glow /mV	Decay /m^{-1}	Speed /km s^{-1}	ρ_2/ρ_1	K	Rate Constants /l mol^{-1} s^{-1} $k_q/10^6$	$k_p/10^5$	T_2/K
C146	6.80	34.3	0.567	1.200	4.180	4.55	3.47	4.01	1177
C146A	6.80	41.5	0.583	1.200	4.180	4.16	1.81	1.91	1177
C147	6.68	57.2	0.578	1.201	4.182	7.44	1.41	2.65	1178
C147A	6.68	54.4	0.578	1.201	4.182	7.15	1.17	2.11	1178
C148	6.76	53.4	0.583	1.212	4.201	6.48	1.57	2.59	1195
C148A	6.76	53.4	0.583	1.212	4.201	4.75	2.62	3.17	1195
C149	6.60	68.1	0.574	0.869	3.396	2.55	1.53	0.85	759
C149A	6.60	69.4	0.574	0.869	3.396	2.02	1.69	1.01	759
C150	6.60	109.	0.563	0.881	3.432	2.08	1.18	0.62	773
C150A	6.60	110.	0.563	0.881	3.432	3.61	0.79	0.72	773
C151	6.92	120.	0.600	0.873	3.408	2.68	1.45	0.88	764
C151A	6.92	113.	0.600	0.873	3.408	2.17	1.43	0.79	764

Figure 8.24. Temperature Dependence of Quenching Rate Constant for Mixture 30% Oxygen/30% Nitrogen/40% Argon.

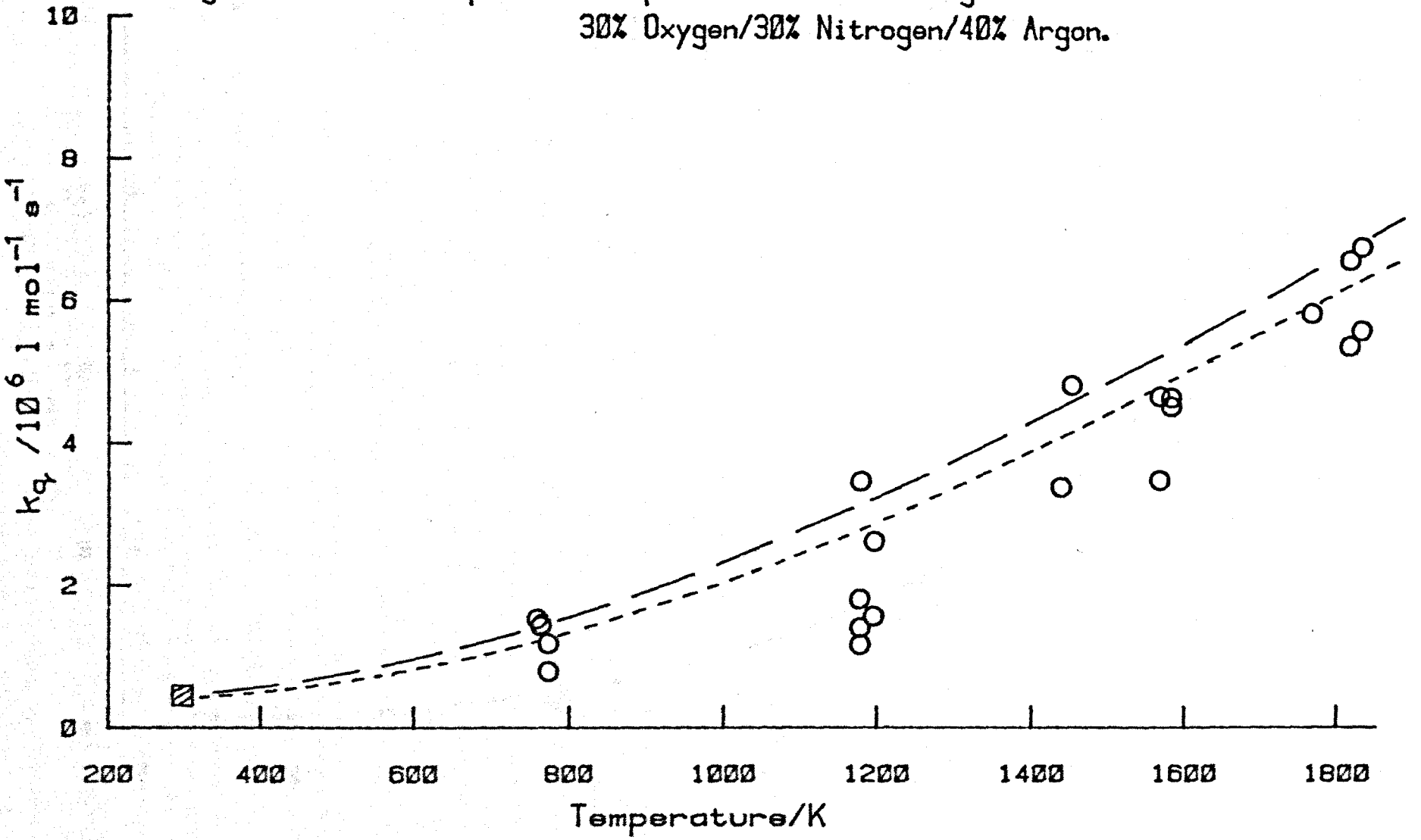

Figure 8.25. Temperature Dependence of Energy Pooling Rate Constant.
30% Oxygen/30% Nitrogen/40% Argon.

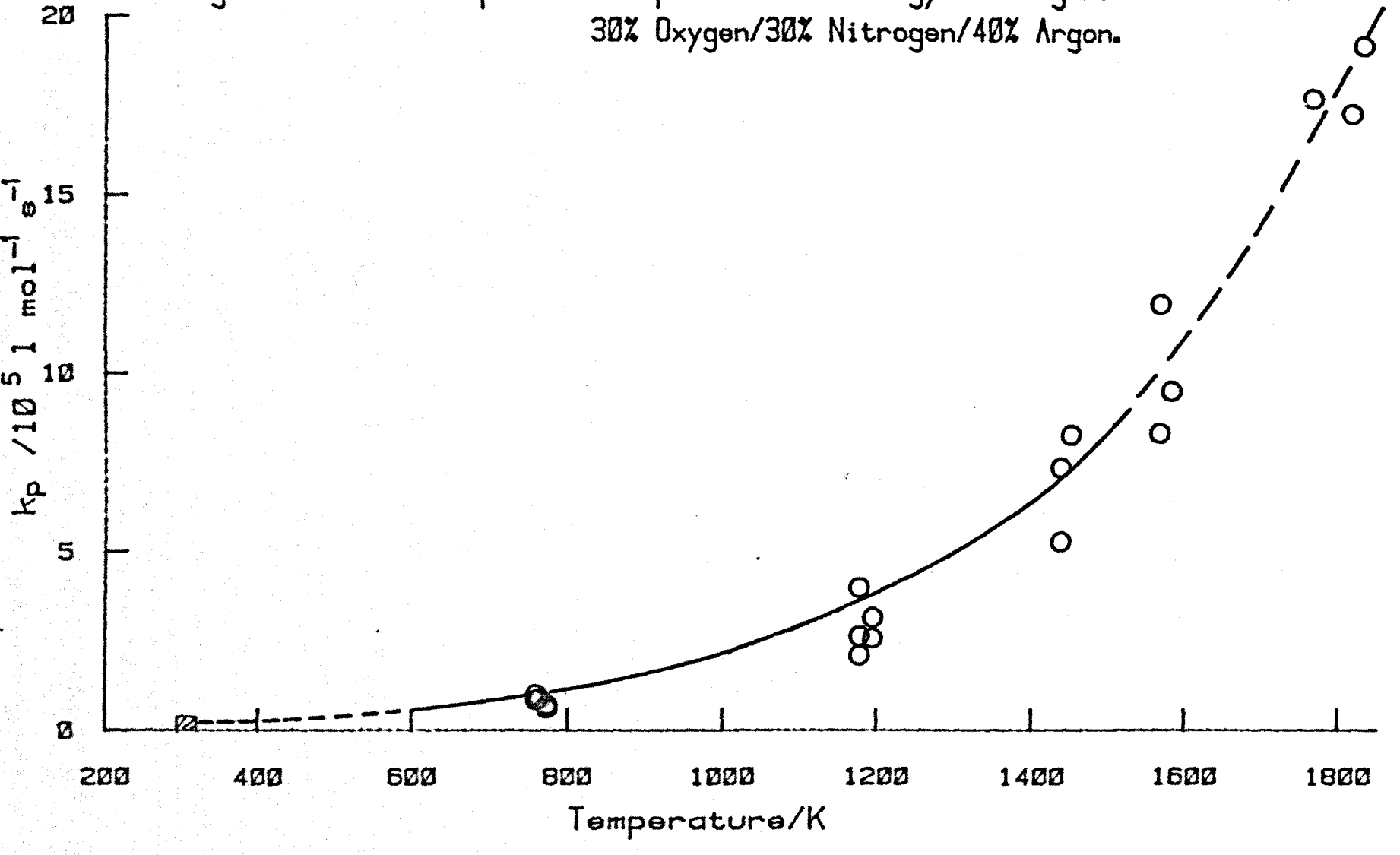

8.5. Discussion

Young and Black[20] suggested that the emission from $O_2(^1\Sigma_g^+)$ at 762 nm is collisionally enhanced. Using their rate constant for the emission (7.8×10^3 ℓ mol^{-1} s^{-1}) and assuming that it is not temperature dependent, the increase in emission at the shock front would be 5.7 ρ_2/ρ_1 at 1600 K. The results in this chapter show that at the shock front the intensity of emission varies simply as the density ratio, for shocks into pure oxygen and all mixtures with nitrogen and argon. There is no evidence for any collisional enhancement of the 762 nm emission.

8.5.1. Oxygen/Nitrogen Mixtures

The addition of nitrogen to the oxygen flow after the discharge decreases the pre-shock glow, but increases the shock emission. The shock enhancement gives a clearly defined relaxation zone leading to a better precision for the rate constants. A comparison of the K values for each mixture at the same shock temperature shows that the equilibrium emission enhancement can be up to ten times higher than expected from the shock compression at 1400 K.

% Oxygen	Run No.	T/K	K value
At T = 850 K			
100	856	(943)	1.03
90	A913	852	1.54
72	886	847	2.16
46	893	865	3.81
25	A900	856	4.09
At T = 1170 K			
100	882	1181	1.08
90	M202	1172	1.99
72	M188	1179	2.84
46	M166	1175	4.57
25	A899	1173	7.13

% Oxygen	Run No.	T/K	K value
At T = 1430 K			
100	884	1449	1.41
90	M206	1424	2.80
72	M185	(1347)	4.27
46	M168	1434	6.25
25	M196	1439	11.52

Vibrational relaxation is included in the analysis of all oxygen and oxygen/nitrogen shocks. It has most effect on the pure oxygen shocks where the value of K is near one, and if it is not included, the value of k_q will be underestimated. At higher concentrations of nitrogen where the relaxation rate of the mixture is slower than for pure oxygen and the K value high, the effect of vibrational relaxation on the quenching rate constant is small. A comparison of figures 6.5 and 8.13 for the analysis of run number A891 shows that when vibrational relaxation is not included, the pseudo first order quenching constant, k_q' can be underestimated by up to 20%.

8.5.2. The Collisional Quenching of $O_2(^1\Sigma_g^+)$ by Oxygen and Nitrogen

The quenching rate constants for the various oxygen/nitrogen mixtures, plotted against shock temperature all give curved plots (figures 8.7, 8.10, 8.14 and 8.17); the curvature is different for each mixture. If values are taken at various temperatures from the "best line" for each mixture, a normal kinetic plot of k_q against mole fraction of oxygen can be made at each temperature; values from the 100% oxygen graph (figure 8.4) are not included in this plot, lines at 100 K intervals are shown in figure 8.26; they obey, within experimental error, equation 8.17 :

$$k_q^M = k_q^{O_2} x_{O_2} + k_q^{N_2} x_{N_2} \qquad 8.17$$

where $x_{N_2} = 1 - x_{O_2}$

Extrapolation of these plots gives values of the quenching rate constants of $O_2(^1\Sigma_g^+)$ by pure oxygen, $k_q^{O_2}$, and pure nitrogen, $k_q^{N_2}$, at each temperature.

The values are listed in table 8.8 and plotted against temperature in figure 8.27.

At room temperature, nitrogen is a more efficient quencher of $O_2(^1\Sigma_g^+)$ than oxygen, but above 1000 K where the lines cross, oxygen becomes more efficient than nitrogen.

The measured values of $k_q^{O_2}$ obtained from shocks into 100% oxygen lie below the extrapolated values from the kinetic plot (figure 8.26). Considering the difficulty in defining the relaxation zone for shocks with K values near one, the extrapolated values are preferred.

Arrhenius plots for the quenching rate constants are curved over the temperature range 295 to 1600 K (figure 8.28). A Landau-Teller plot of the quenching of $O_2(^1\Sigma_g^+)$ by oxygen possibly gives a straight

line in the temperature range 700 to 1200 K, but at the extremes of this range, the linearity is lost (figure 8.29). It is obvious that there is no simple temperature dependence for these quenching reactions.

Figure 8.26. Variation of Quenching Rate Constant with Mole Fraction of Oxygen at various Temperatures.

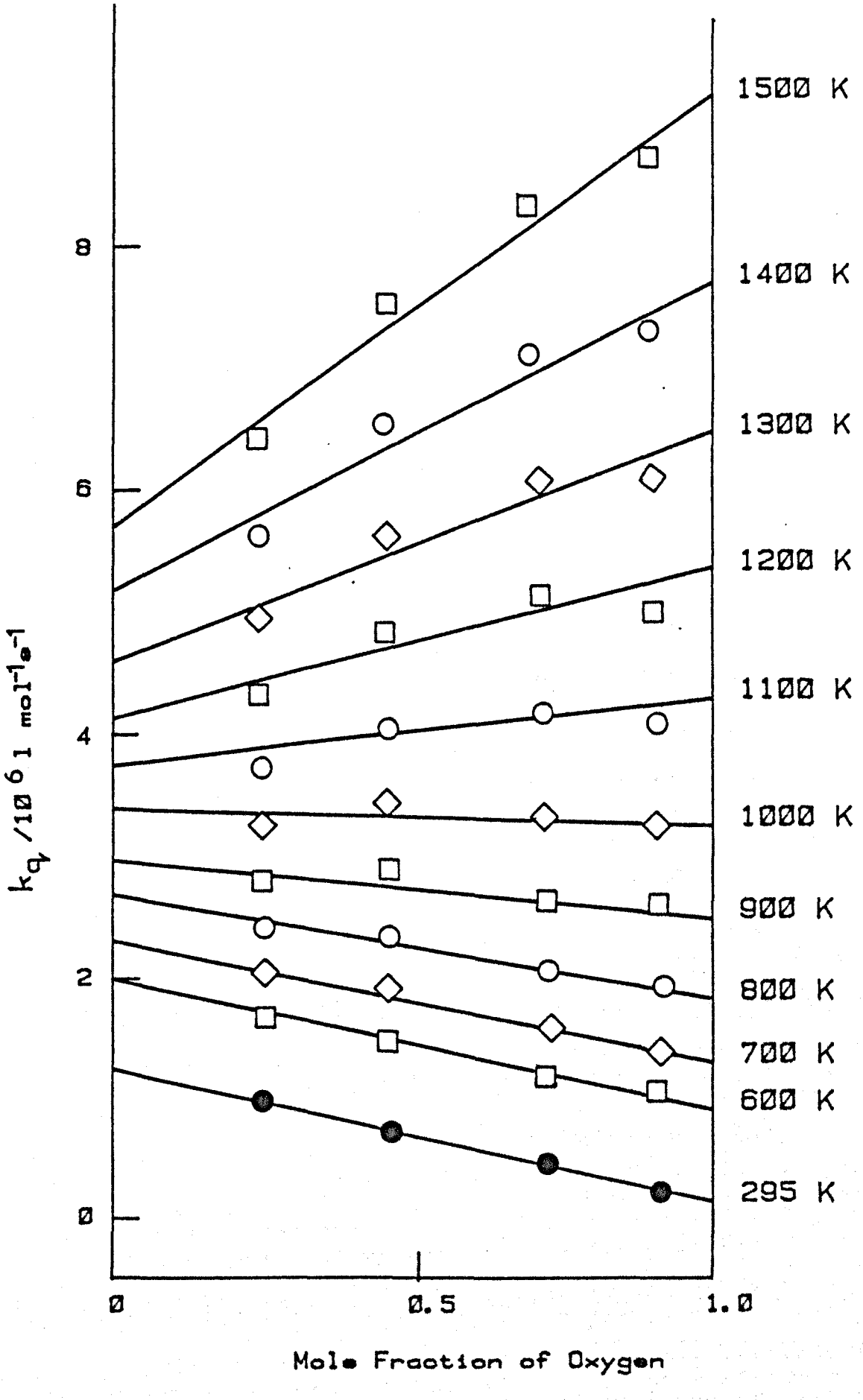

Table 8.8.

Quenching and Energy Pooling Rate Constants at various Temperatures.

Temperature/K	Rate Constants /l mol^{-1} s^{-1}		
	$k_q^{O_2}/10^6$	$k_q^{N_2}/10^6$	$k_\rho/10^5$
295	0.10	1.27	0.12
600	0.86	2.02	0.51
700	1.29	2.32	0.75
800	1.77	2.68	1.06
900	2.45	2.98	1.46
1000	3.23	3.38	2.15
1100	4.21	3.72	2.84
1200	5.30	4.14	3.75
1300	6.39	4.62	4.95
1400	7.70	5.20	6.42
1500	9.24	5.70	8.41
1600	-	-	11.05
1700	-	-	14.43
1800	-	-	18.07

Figure 8.27. Temperature Dependence of Quenching Rate Constant of $O_2(^1\Sigma_g^+)$ by Oxygen and Nitrogen.

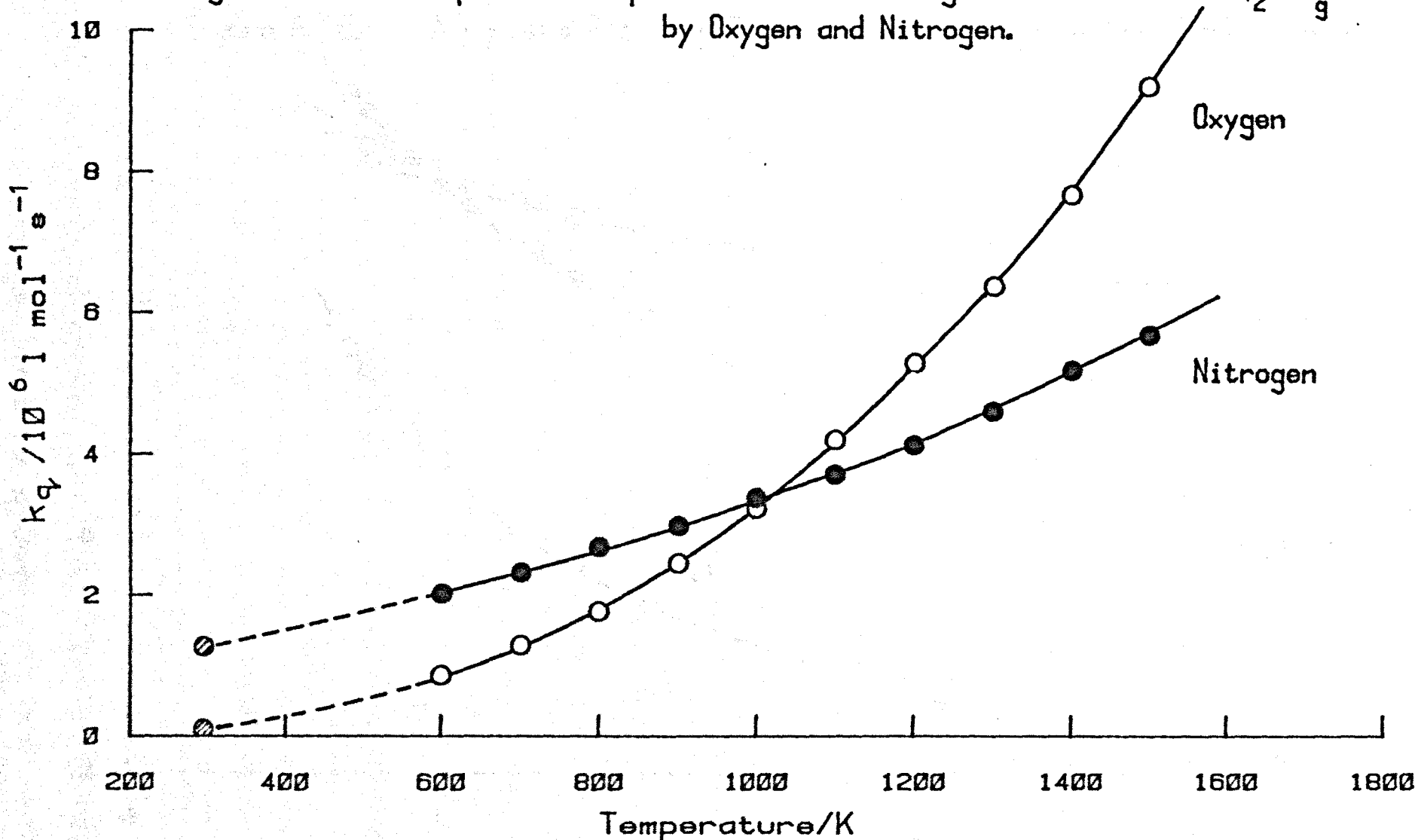

Figure 8.28. Arrhenius Plot for Quenching and Energy Pooling Rate Constants.

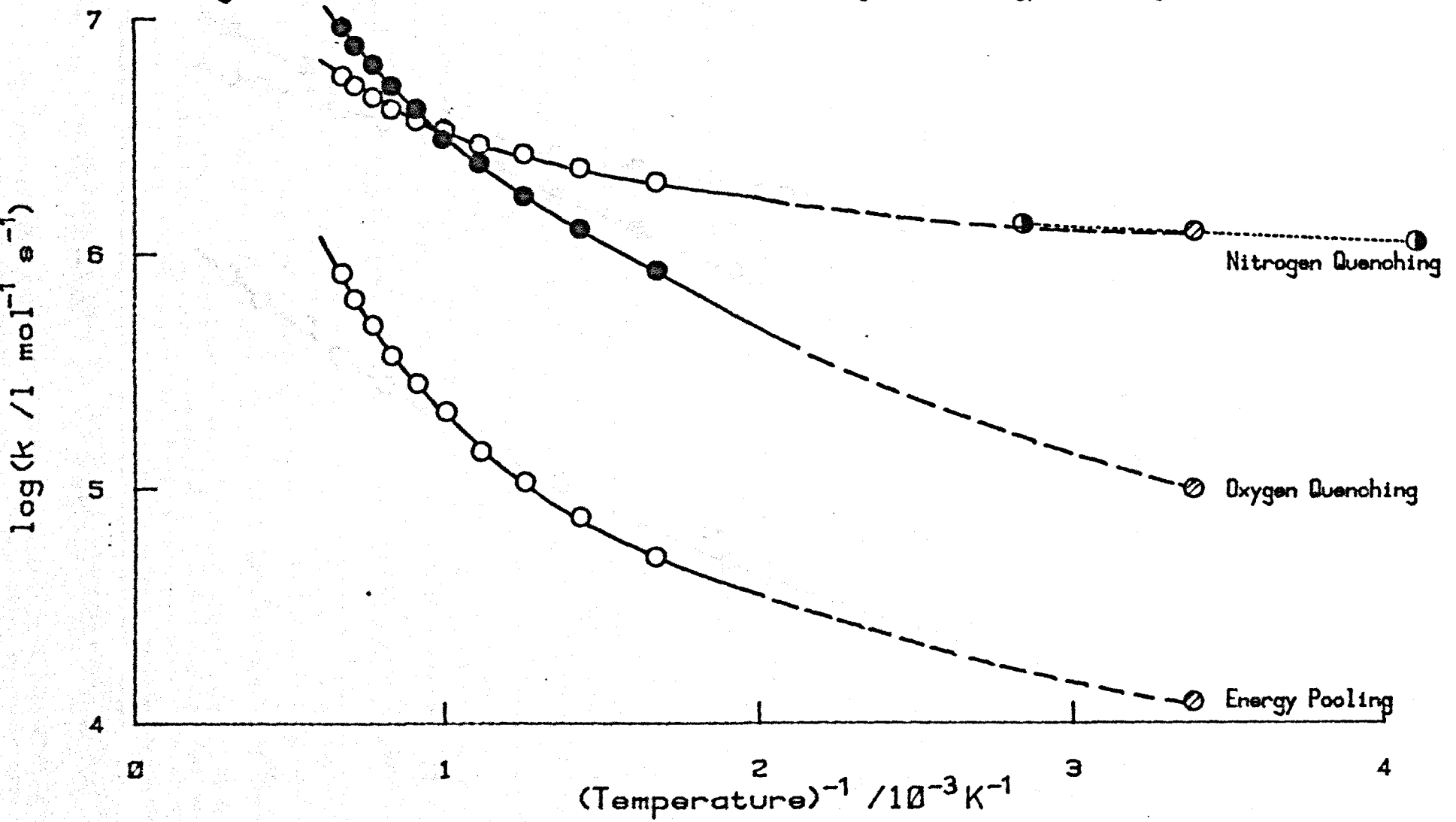

Figure 8.29. Landau-Teller Plot for Quenching and Energy Pooling Rate Constants.

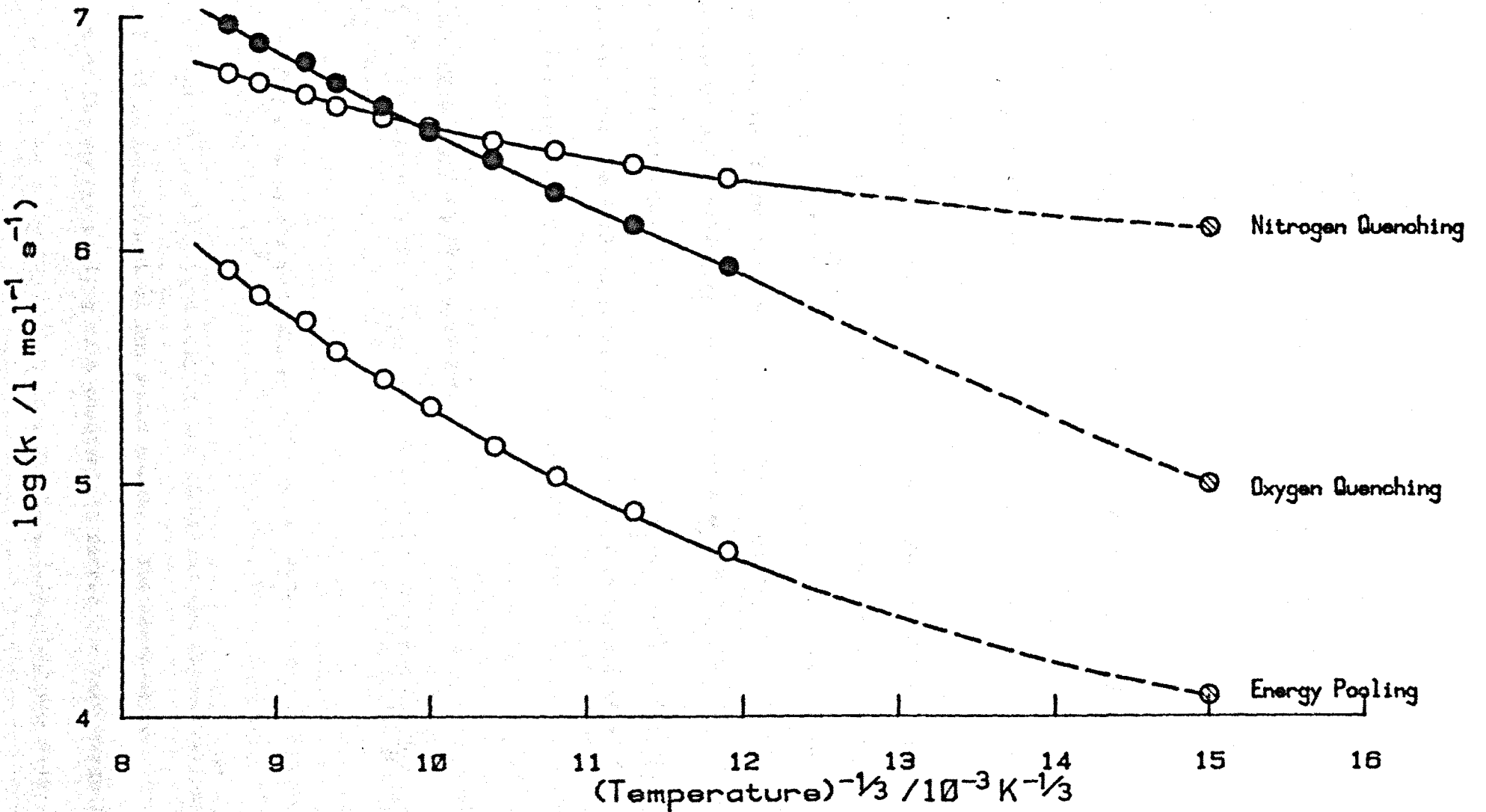

8.5.3. The Collisional Quenching of $O_2(^1\Sigma_g^+)$ by Argon

The temperature dependence of the quenching constant for the mixture for both sets of results with argon show a similar shape to the 50% oxygen/50% nitrogen results. The added nitrogen, although complicating the analysis, gives the high K values wanted for accurate results.

The room temperature quenching constant for $O_2(^1\Sigma_g^+)$ by argon is slow (9×10^3 ℓ mol^{-1} s^{-1}). The results in figures 8.21 and 8.24 show that this value is little changed at the higher shock temperature, and only an upper limit can be given.

The dotted lines in figure 8.21 and 8.24 are calculated from the values of $k_q^{N_2}$ (at T_2) and $k_q^{O_2}$ (at T_2) from table 8.8 and the unchanged room temperature value of k_q^{Ar}, and give quite a good fit to the points. The dashed line in figure 8.24 defines an upper limit for the quenching rate constant of $O_2(^1\Sigma_g^+)$ by argon at 1500 K of 9×10^5 ℓ mol^{-1} s^{-1}. The results from the argon mixtures above 1500 K cannot yield quenching rate constants for the individual gases as there are no values of $k_q^{O_2}$ and $k_q^{N_2}$ above 1500 K.

8.5.4. The Energy Pooling Rate Constant

$O_2(^1\Sigma_g^+)$ is formed in the energy pooling reaction from two $O_2(^1\Delta_g)$ molecules.

$$O_2(^1\Delta_g) + O_2(^1\Delta_g) \xrightarrow{k_p} O_2(^1\Sigma_g^+) + O_2(^3\Sigma_g^-) \qquad 8.2$$

This reaction should depend only on the square of the concentration of $O_2(^1\Delta_g)$ and be independent of any added gases. The temperature dependence of the energy pooling rate constant is curved for each oxygen/nitrogen mixture, as each graph shows (figures 8.8, 8.11, 8.15 and 8.18).

Figure 8.30. *Temperature Dependence of Energy Pooling Rate Constant for all Oxygen/Nitrogen Mixtures.*

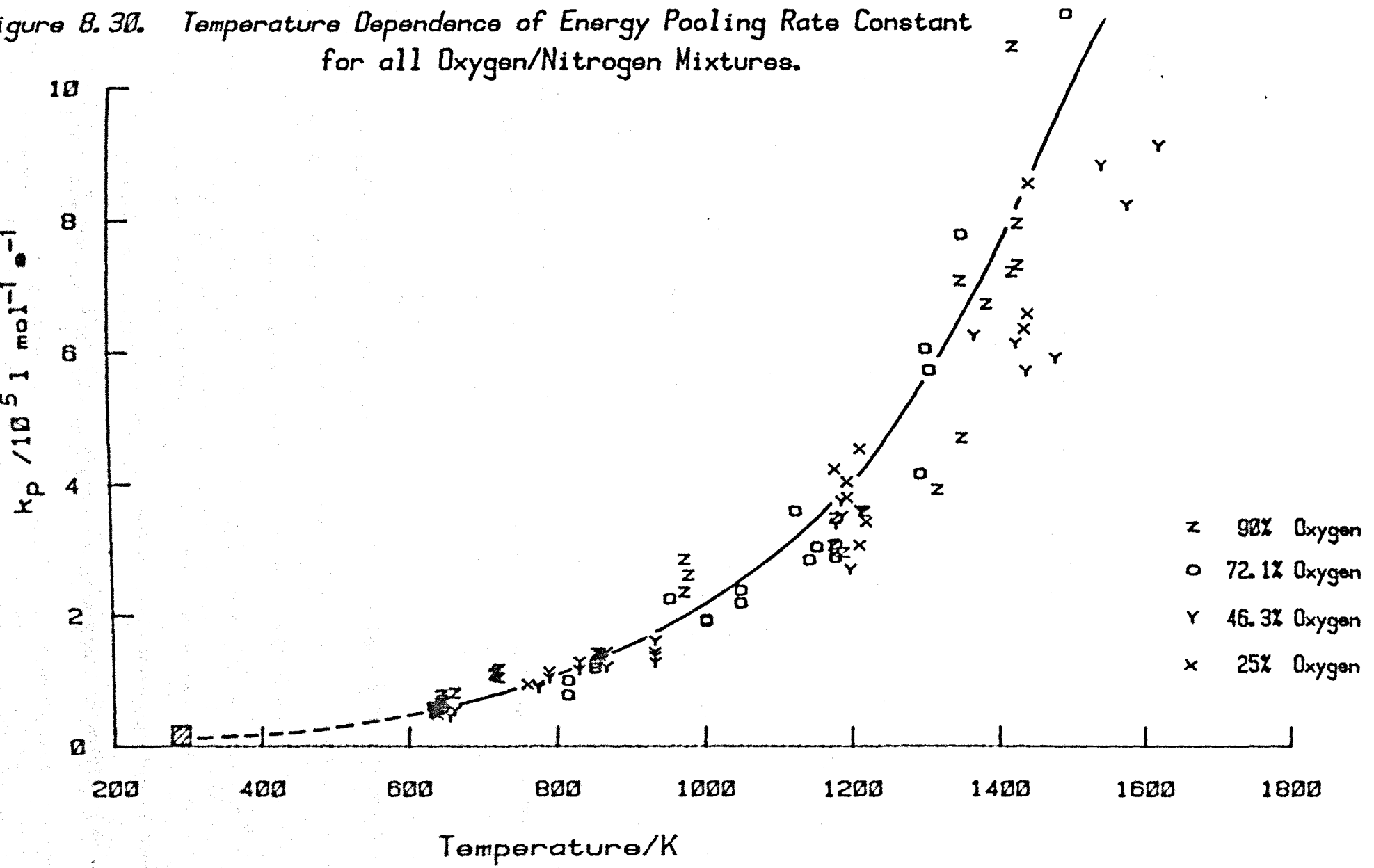

All the results are plotted on one graph in figure 8.30 where it can be seen that there is no composition dependence. This provides confirmation that the energy pooling rate constant is independent of added gases, and additional proof of the correctness of the model. Results of the energy pooling rate constant are listed with temperature in table 8.8.

The energy pooling rate constant plots for the argon mixtures (figures 8.22 and 8.25) give the same values and show the same temperature dependence; the lines drawn in the figures come from the oxygen/nitrogen mixtures. The points fit the lines well and provide striking confirmation that the energy pooling rate constant is independent of added gases. Additional values of k_p at temperatures above 1500 K from the argon mixtures are listed in table 8.8.

An Arrhenius plot for the energy pooling rate constant does not give a straight line (figure 8.28), and a Landau-Teller plot is also curved (figure 8.29).

8.5.5. Revised 100% Oxygen Results

The 100% oxygen values for the energy pooling rate constant listed in table 8.1. fall systematically below the line in figure 8.30 (see the dashed line in figure 8.4).

The value of k_p obtained from figure 8.30 at each shock temperature, together with the measured K value, is used to calculate a new $k_q^{O_2}$ (at T_2) from equation 8.11 for each run listed in table 8.1. The revised values are listed in table 8.9 and plotted against temperature in figure 8.31. The revised values still fall below the line calculated from the results of the oxygen/nitrogen mixtures, especially at temperatures above 1000 K; at higher temperatures the scatter is considerable.

Table 8.9.

Revised Rate Constants for 100% Oxygen.

Run No.	Rate Constants /l mol^{-1} s^{-1} $k_q/10^6$ measured	$k_p/10^5$ from Fig 8.30	$k_q/10^6$ revised	T_2/K
770	3.48	7.75	6.24	1475
777	4.25	7.45	7.57	1460
797	4.13	7.82	7.19	1480
801	3.13	3.60	4.20	1185
803	-	0.58	0.83	650
835	-	0.82	1.12	739
839	3.38	4.19	5.58	1238
853	-	1.91	2.57	961
854	2.38	1.76	2.51	935
855	2.24	1.77	2.18	937
856	2.19	1.81	2.45	943
870	-	2.50	2.81	1054
A881	3.67	3.72	4.63	1197
882	2.72	3.57	4.39	1181
A884	4.79	7.29	6.81	1449
910	3.91	7.71	4.79	1473
A910	4.39	7.71	4.85	1473
M110	2.73	3.16	3.37	1140
M124	6.84	8.21	8.42	1497
M125	-	0.61	0.91	673
M127	1.05	0.65	0.83	681
M129	-	0.46	0.89	611
M146	-	3.96	4.90	1220
M147	5.37	11.85	8.20	1647
M150	8.13	11.91	6.97	1655
M151	3.37	10.78	4.66	1608

Figure 8.31. Temperature Dependence of Quenching Rate Constant for 100% Oxygen (revised).

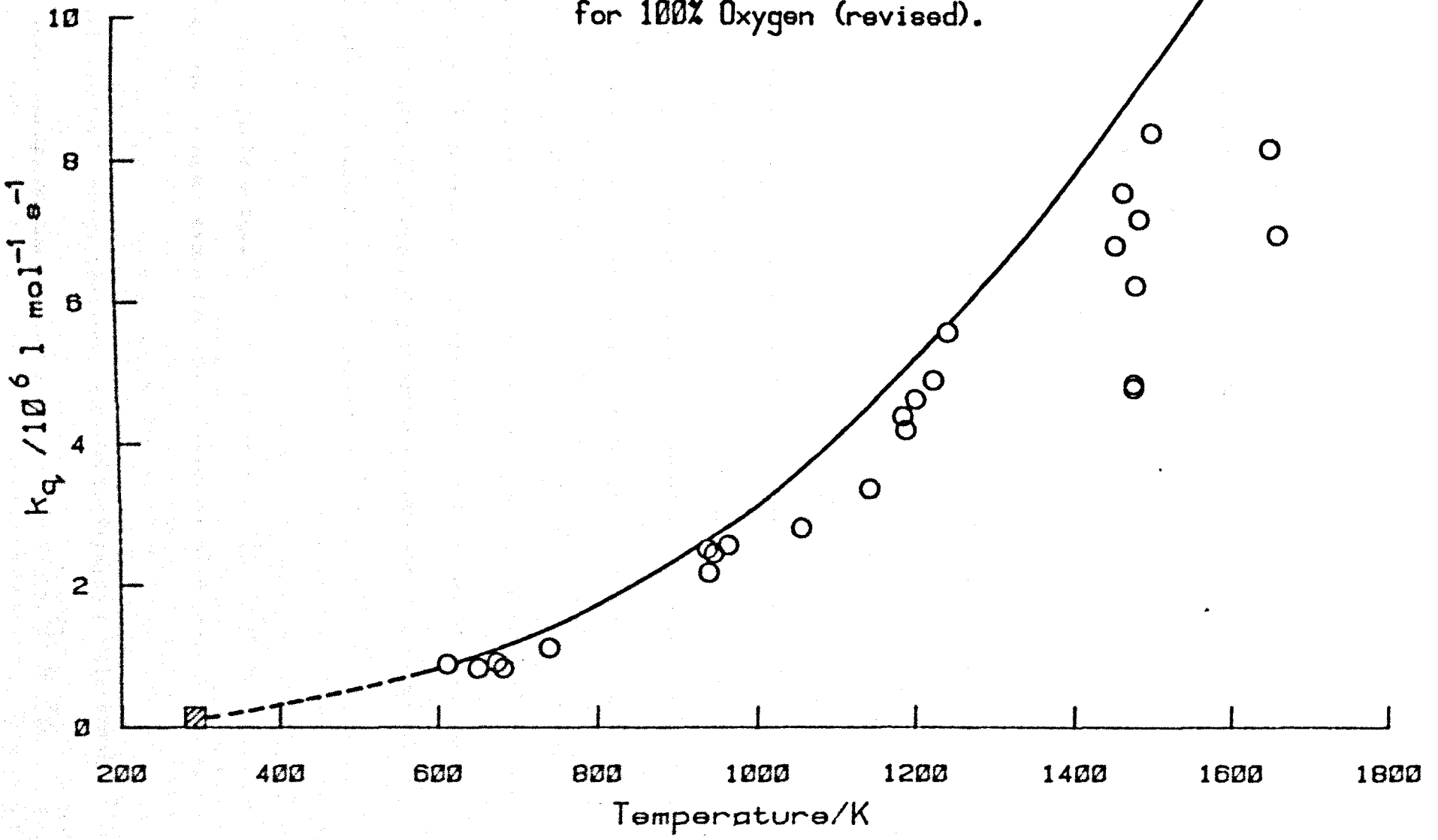

We are unable to get better values when K is near one and the 100% oxygen results are not used in the kinetic plots (figure 8.26) or listed in table 8.8.

8.5.6. Concluding Remarks

The curved plots in figures 8.28 and 8.29 suggest that there is no simple temperature dependence for collisional quenching of $O_2(^1\Sigma_g^+)$ or for the energy pooling reaction.

Recent work by Kohse-Höinghaus and Stuhl[129] on the temperature dependence of quenching of $O_2(^1\Sigma_g^+)$ in the range 200 to 350 K by H_2, N_2, HCl, CH_4, NH_3 and the corresponding deuterated compounds showed linear Arrhenius plots. Their values for nitrogen are included as the dotted line in figure 8.28 at the low temperature end. The slope of their line fits our points well, but over the wider temperature range in this study the Arrhenius plot curves above 600 K.

For these quenching reaction rates, it may be useful to remove the small $T^{\frac{1}{2}}$ dependence of the rate constant which is always present for bimolecular reactions (from collision theory - chapter 1) and usually masked by any stronger temperature dependence. The logarithm of the probability of a collision leading to quenching of $O_2(^1\Sigma_g^+)$ is plotted against temperature in figure 8.32, where it can be seen that while the probability of quenching by oxygen increases with temperature, that for nitrogen remains nearly constant, increasing only slightly between 600 and 1500 K.

The curved plots suggest that two processes with different dependences may be responsible for the collisional quenching of $O_2(^1\Sigma_g^+)$ by oxygen and nitrogen. At high temperatures, short range repulsive forces could control energy transfer, and the conversion of electronic to vibrational energy on the repulsive part of the potential energy

Figure 8.32. Temperature Dependence of the Probability of Quenching of $O_2(^1\Sigma_g^+)$ by Oxygen and Nitrogen.

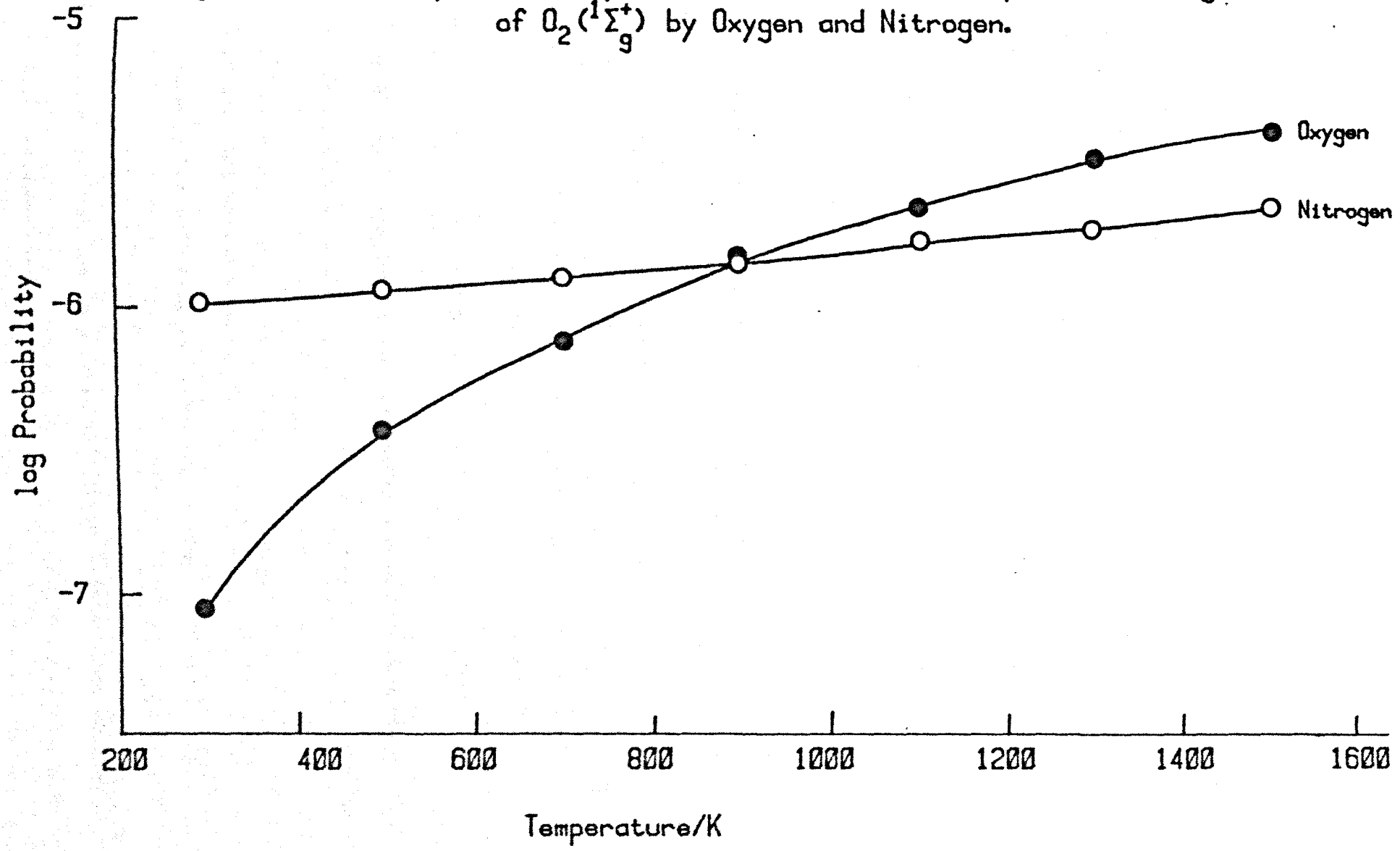

curve could show a $(\text{temperature})^{-1/3}$ dependence, as vibrational energy transfer does. The Landau-Teller plots are curved (figure 8.29), so clearly this is not a complete solution to the route for energy transfer, although it may dominate at high temperatures. At the lower temperatures the rate may be enhanced by long range multipolar interactions which might well have a negative temperature dependence.[130]

The collisional quenching of $O_2(^1\Sigma_g^+)$ is treated theoretically by Kear and Abrahamson[69] in their paper on short range repulsive interactions, and by Braithwaite, Davidson and Ogryzlo[70] considering long range interactions. The theoretical results agree quite well with experiments for diatomic quenchers other than oxygen, at room temperature. The values for oxygen and nitrogen are listed below.

Rate Constants for the Quenching of $O_2(^1\Sigma_g^+)$ at 300 K
/ℓ mol^{-1} s^{-1}

Quencher	Experimental	Calculated	
		Kear and Abrahamson	Braithwaite, Davidson and Ogryzlo
O_2	2.8×10^4	3.4×10^1	~ 10
N_2	1.3×10^6	9.7×10^3	9.12×10^5

For nitrogen, the long range interactions calculation gives a value more in line with the experimental value, but for oxygen, neither model describes the experimental findings.

Braithwaite, Davidson, Ogryzlo and Schiff[71,72] have calculated rate constants for both long range and short range interactions for a temperature range 170 to 400 K for hydrogen and hydrogen bromide, and suggest that although the long range multipolar interactions account for most of the quenching, the short range repulsive interactions may

also be important. Here the sum of the two calculated values best fits the experimental results.

The study of Thomas and Thrush[73] finding a common suprisal plot for the quenching of both $O_2(^1\Sigma_g^+)$ and $O_2(^1\Delta_g)$ apparently indicates a non-specific quenching process, though their work did not include oxygen as a quencher, and was only carried out at room temperature.

The similarity in temperature dependence for the rate constants for collisional quenching and energy pooling suggest that both may proceed by common parallel mechanisms.

The argon results show that for a gas with a slow deactivation rate constant at room temperature, any change with temperature would have to be very large to be observed within the hot flow time available for measurements in a discharge flow shock tube.

More definite conclusions for these temperature dependences might be made when results are obtained from gases which have a higher quenching rate constant at room temperature. Experiments are in progress with carbon dioxide and nitrous oxide, and preliminary results indicate an interesting negative temperature dependence.

Chapter 9.

The Dimol Emissions of $O_2(^1\Delta_g)$.

9.1. Introduction

The three dimol emissions of $O_2(^1\Delta_g)$ were first identified by Gray and Ogryzlo[16]

$$O_2(^1\Delta_g) + O_2(^1\Delta_g) \rightarrow O_2(^3\Sigma_g^-) + O_2(^3\Sigma_g^-) + h\nu(\lambda = 634\ nm) \qquad 9.1$$

$$O_2(^1\Delta_g)_{v=0} + O_2(^1\Delta_g)_{v=0} \rightarrow O_2(^3\Sigma_g^-)_{v=1} + O_2(^3\Sigma_g^-)_{v=0} + h\nu(\lambda = 703\ nm) \qquad 9.2$$

$$O_2(^1\Delta_g)_{v=1} + O_2(^1\Delta_g)_{v=0} \rightarrow O_2(^3\Sigma_g^-)_{v=0} + O_2(^3\Sigma_g^-)_{v=0} + h\nu(\lambda = 579\ nm) \qquad 9.3$$

These three emissions have been studied both at room temperature and at the high temperature attained when a shock is run into the flowing discharged gas. We have been able to check the assignment kinetically, determine the relative emissivities and estimate rate constants for the emissions between 1150 and 1500 K.

9.2. Experimental Proceedure

The two photomultipliers were clamped in position at the observation station throughout the series of experiments. For the high temperature studies, three shocks at nominally the same temperature, gave one result for the 634 nm emission, one result for the 703 nm emission and one result for the 579 nm emission from one detector. The second detector observed the 634 nm emission for all shocks and was used as a reference to correct for variations in shock speed and pre-shock glow for the three results. For all shocks the downstream pressure was adjusted to $\sim$ 6.5 torr (0.87 kPa) and the oxygen flow was maintained at 1.62 m s^{-1} (28 ml s^{-1} at 1 atmosphere pressure).

At room temperature, comparative readings were taken at each wavelength from the same detector as for the shock results, the reference detector was kept with a 634 nm filter, and the emissions were corrected for any long term changes.

The pre-shock decay rate along the tube was not measured, but the value of the post shock decay rate showed that the system was behaving normally.

The filters used peaked at 630 nm (for the 634 nm emission), 706 nm (for the 703 nm emission) at 579 nm; all had measured half-height peak widths of 10 $\pm$ 1 nm. For each dimol band, the published spectrum[83,18] was matched with the filter transmittance. The area under the band was measured by summing the height at 1 nm intervals. The fraction seen by the filter was calculated by summing the product of the filter transmittance and the band height at 1 nm intervals, and compared with the value for the whole band. The actual shape of the band is important in these calculations, but the height cancels out. Figure 7.7 shows the band and filter for the 634 nm emission. For each filter we are observing 24 $\pm$ 3% of the incident intensity.

For the emission ratios, no corrections were made for the filters and as the measurements were made with one detector clamped in position, the geometry of the system was unimportant. The emissions were corrected for the variation in quantum efficiency with wavelength of the photomultipliers, which was plotted out from the manufacturers published curves (figure 3.12). Schurath[116] found these to correspond, within experimental accuracy, to his calibration curve for the similar 9659 QB photomultiplier (EMI).

9.3. Treatment of Results

9.3.1. The 634 nm Emission

The analysis of results at 634 nm has been discussed already (Chapter 7).

The emission rate constants for the 634 nm emission can be calculated from the room temperature rate constant of 0.016 ℓ mol^{-1} s^{-1} measured by Derwent and Thrush[49], using the equation:

$$^{634}k_{T_2} = {}^{634}k_{T_1} \; K \left(\frac{T_2}{T_1}\right)^{\frac{1}{2}} \qquad 9.4$$

where k_T is the rate constant at temperature T, and K is the enhancement factor measured from the shock trace. The rate constant varies with $T^{\frac{1}{2}}$ as expected for a simple collisional process[46], and the extra emission observed at higher temperatures is taken into account by the inclusion of K in equation 9.4.

9.3.2. The 703 nm Emission

The emission at 703 nm should follow the same pattern at high temperatures as the 634 nm emission if the assignment of Gray and Ogryzlo is correct, as it comes from the same pair of molecules.

$$O_2(^1\Delta_g)_{v=0} + O_2(^1\Delta_g)_{v=0} \rightarrow O_2(^3\Sigma_g^-)_{v=1} + O_2(^3\Sigma_g^-)_{v=0} + h\nu(\lambda = 703 \text{ nm}) \qquad 9.2$$

The emission, then, can be fitted to a similar equation: (Equation 7.4):

$$^{703}I_2 = {}^{703}I_1 \; K\left(\frac{\rho_2}{\rho_1}\right)^2 \left(\frac{T_2}{T_1}\right)^{\frac{1}{2}} e^{At} \qquad 9.5$$

The trace is analysed as described in Chapter 6.

The emission rate constants for the 703 nm emission can be calculated from the measured emission intensity ratios and the values already found for the rate constants at 634 nm, at each temperature:

$$\frac{703_I}{634_I} = \frac{703_k \ [O_2(^1\Delta_g)]^2}{634_k \ [O_2(^1\Delta_g)]^2} = \frac{703_k}{634_k} \qquad 9.6$$

provided the respective K values are shown to be the same, and cancel out.

9.3.3. The 579 nm Emission

The analysis of results at 579 nm will be discussed in Chapter 10.

The emission rate constants can be calculated from the measured emission intensity ratios at the shock temperature and the values already found for the 634 nm emission, using:

$$\frac{579_I}{634_I} = \frac{579_k \ [O_2(^1\Delta_g)_{v=0}][O_2(^1\Delta_g)_{v=1}]}{634_k \ [O_2(^1\Delta_g)_{v=0}]^2} \qquad 9.7$$

The relative concentrations of the zeroth and first vibrational level of $O_2(^1\Delta_g)$ can be calculated from the Boltzmann distribution function for a harmonic oscillator:

$$\frac{[O_2(^1\Delta_g)_{v=1}]}{[O_2(^1\Delta_g)_{v=0}]_{Total}} = e^{-\varepsilon/RT}[1-e^{-\varepsilon/RT}] \qquad 9.8$$

where ε is in J mol^{-1} and ε/R is 2131K for $O_2(^1\Delta_g)$ (see Appendix II). The results show that at room temperature the rate constant cannot be obtained using equation 9.7, as the number of vibrationally excited molecules in the flowing discharged gas is greater than would be expected from the Boltzmann distribution at that temperature, since the gas is not

in thermal equilibrium.

The emission at 579 nm is assigned to the transition from two $O_2(^1\Delta_g)$ molecules, where one is in the first vibrational level, (reaction 9.3) and this assignment can be checked from a study of the K values found for shocks at 579 nm.

At the post shock temperature when the adjustment to equilibrium is complete, the emission will be related to the calculated concentration at that temperature:

$$^{579}I_2^{Eq} = K'^{579}k' \; T^{\frac{1}{2}} \; [O_2(^1\Delta_g)_{v=0}{}^{Eq}] \, [O_2(^1\Delta_g)_{v=1}{}^{Eq}] \qquad 9.9$$

where $^{579}k'$ is the temperature independent term in the rate constant for the 579 nm emission. The measured K' enhancement value includes both the extra emission seen because of the greater concentration of vibrationally excited molecules at the shock temperature, and the increase in emission at higher temperatures as seen with the 634 nm emission. The equilibrium emission, $^{579}I_2^{Eq}$, is extrapolated back to zero time and can be seen in the diagram in section 10.3.1. The relative emission at 579 nm to that at 634 nm is obtained from the extrapolated equilibrium emission at the shock front i.e. at zero time.

$$\frac{^{579}I_2^{Eq}}{^{634}I_2^{Eq}} = \frac{K' \; ^{579}I_1}{K \; ^{634}I_1} \qquad 9.10$$

where K is the enhancement factor for the 634 nm emission.

$$\frac{K' \; ^{579}I_1}{K \; ^{634}I_1} = \frac{^{579}k'}{^{634}k'} \; \frac{[O_2(^1\Delta_g)_{v=0}{}^{Eq}] \, [O_2(^1\Delta_g)_{v=1}{}^{Eq}]}{[O_2(^1\Delta_g)_{v=0}{}^{O}]^2} \qquad 9.11$$

At the shock front, the vibrational distribution of $O_2(^1\Delta_g)$ molecules is the same as at room temperature where nearly all the $O_2(^1\Delta_g)$ molecules are in the zeroth vibrational level, and $[O_2(^1\Delta_g)_{v=0}{}^0]$ is equal to the total concentration of $O_2(^1\Delta_g)$. So, using the partition functions for a harmonic oscillator:

$$\frac{[O_2(^1\Delta_g)_{v=0}{}^{Eq}]}{[O_2(^1\Delta_g)_{v=0}{}^0]} = 1-e^{-\epsilon/RT} \qquad 9.12$$

and

$$\frac{[O_2(^1\Delta_g)_{v=1}{}^{Eq}]}{[O_2(^1\Delta_g)_{v=0}{}^0]} = e^{-\epsilon/RT}(1-e^{-\epsilon/RT}) \qquad 9.13$$

So equation 9.11 becomes:

$$\frac{K'\,{}^{579}I_1}{K\,{}^{634}I_1} = \frac{{}^{579}k'}{{}^{634}k'}\, e^{-\epsilon/RT}(1-e^{-\epsilon/RT})^2 \qquad 9.14$$

The measured terms on the left hand side of equation 9.14 can be compared with the calculated terms on the right hand side to give a value of the ratio of emission rate constants.

9.4. Results

Shocks, in groups of three giving one result each at 634, 703 and 579 nm, are listed in table 9.1. Also listed are the pre and post shock flows, corrected for different emission levels from the standard photomultiplier at 634 nm.

9.4.1. The 634 nm Emission

The K values for the 634 nm emission (chapter 7) are listed at various temperatures in table 9.2. The emission rate constants at these temperatures calculated from equation 9.4 are listed together with the room temperature value of Derwent and Thrush[49].

9.4.2. The 703 nm Emission

An oscillograph of the emission at 703 nm is shown in figure 9.1. together with the corresponding trace of the 634 nm emission for the same shock. The two shapes are identical, as expected for emissions from the same pair of molecules (reactions 9.1 and 9.2) A computer plot of a 703 nm emission result (figure 9.2) shows that the postulated model fits the experimented points well. The K values give the same results as for the 634 nm emission, and show the same increase with temperature. The same post shock decay rate is found for the 703 nm and 634 nm emissions. The ratios of emission inetnsity at 703 nm to that at 634 nm, corrected for the variation in quantum efficiency of the photomultiplier at the two wavelengths, are listed in table 9.2 at various temperatures. The emission at 703 nm is more intense than that at 634 nm at all temperatures, by a factor of 1.81 ± 0.45. The emission rate constants at 703 nm from equation 9.6 are also listed.

9.4.3. The 579 nm Emission

A precise value of the ratio of emission intensity at 579 nm to that at 634 nm, corrected for the photomultiplier quantum efficiency, is listed in table 9.2 from the shocks in table 9.1 at 1400K.

Table 9.1.

Results of the Analysis of Groups of Three Shocks.

Run No.	P_1 /torr	Filter /nm	Pre-Shock Glow /mV	corr.	K	Post-Shock Glow /mV	corr.	T_2/K
4	6.10	634	30.0		1.23	3805		1454
		579	14.2	13.0	4.94	5323	5055	
5	6.59	634	27.5		1.24	2584		1449
		703	99.2	99.2	1.11	8322	8580	
6	6.39	634	27.5		1.32	2664		1410
		634	81.8	81.8	1.09	6558	6558	
C132	6.51	634	44.7		1.05	2112		1146
		579	7.3	6.76	3.17	1151	1082	
C134	6.51	634	41.4		1.08	1986		1132
		634	40.2	40.2	1.03	1830	1830	
C135	6.51	634	39.3		1.02	1991		1146
		703	49.7	52.4	0.94	2073	2068	
C133	6.55	634	42.7		1.18	3687		1408
		579	6.9	6.69	4.25	2146	2146	
C136	6.55	634	38.6		1.06	2929		1382
		703	49.3	52.9	1.06	3741	4709	
12	6.27	634	45.5		1.21	4038		1416
		634	44.1	40.1	1.16	3762	3435	

Figure 9.1.

A Trace of the Shock Emission.
Run No. C14

a. 634 nm

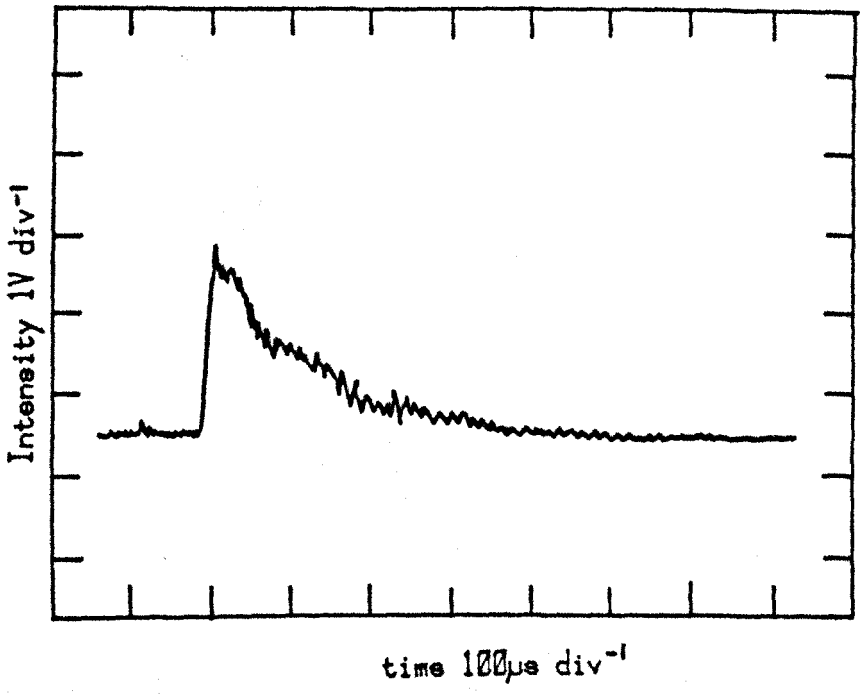

b. 703 nm

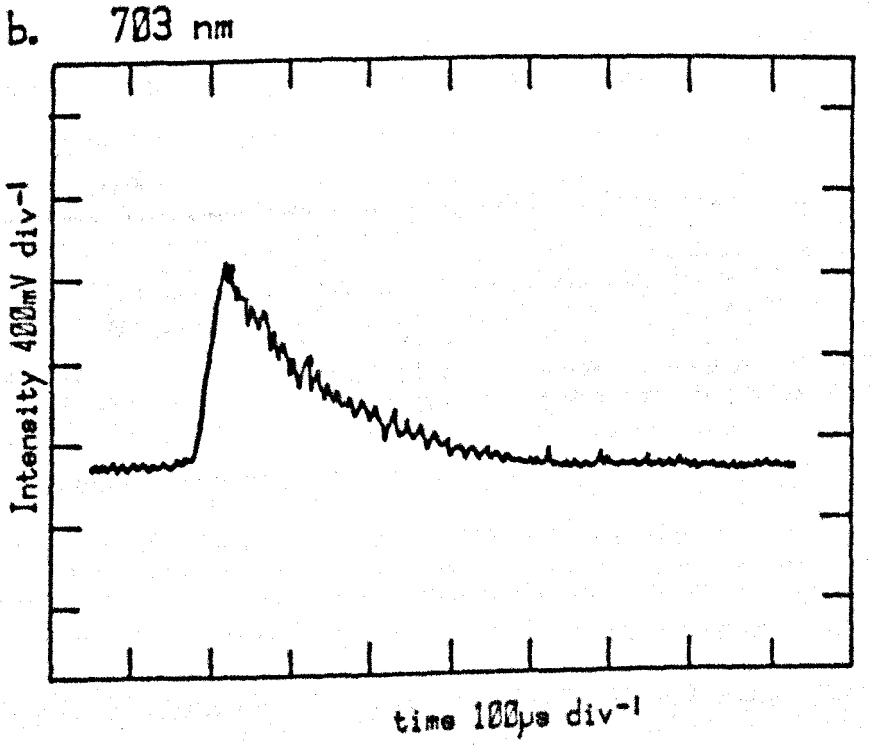

Figure 9.2.

A Computer Plot of the Analysis of a Shock at 703 nm.

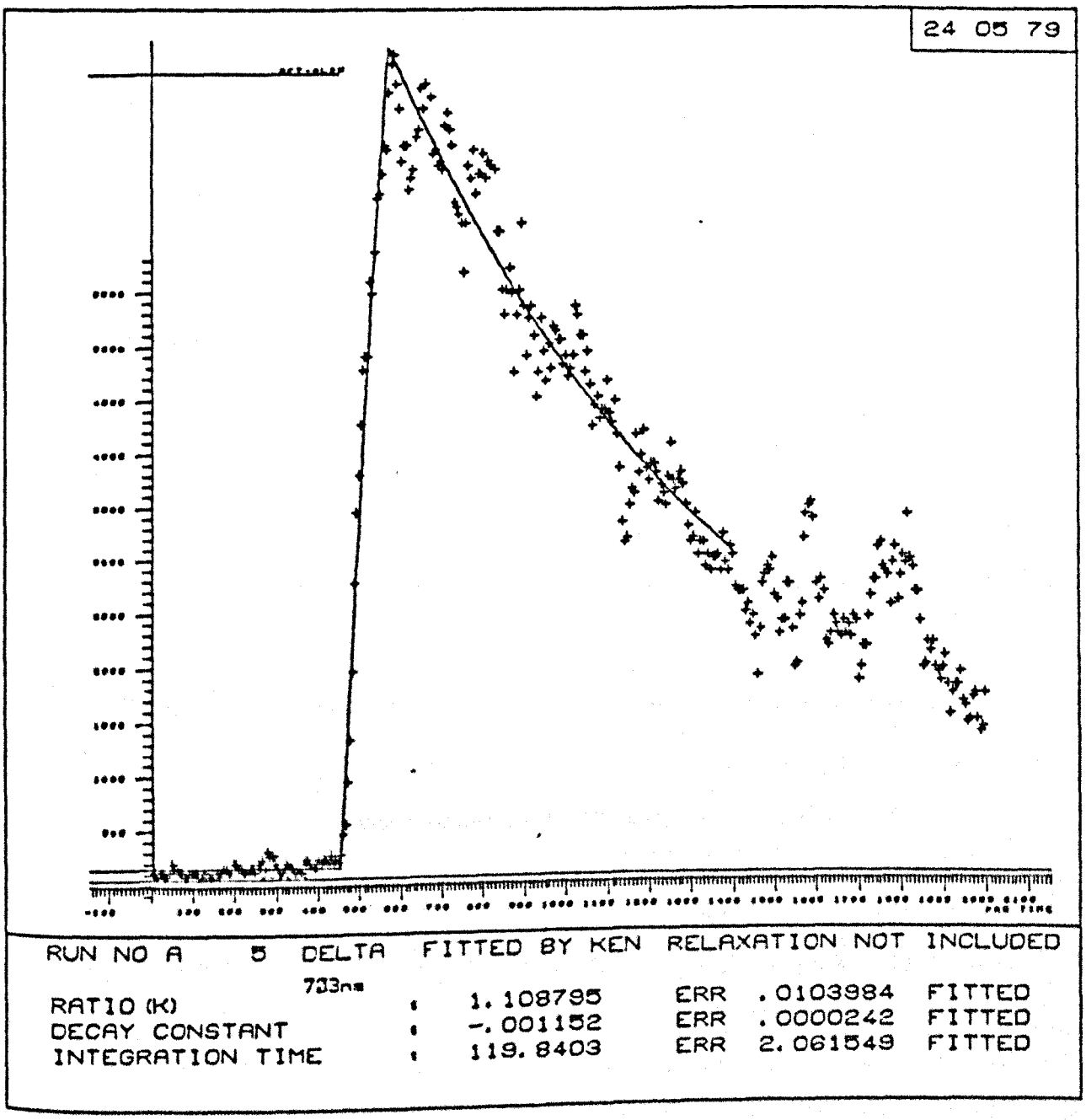

Table 9.2.

Intensity Ratios and Emission Rate Constants at Several Temperatures.

Temperature/K	295	1150	1400	1500
^{634}K	1.0	1.10	1.24	1.30
^{634}k /l $mol^{-1}s^{-1}$	0.016*	0.035	0.043	0.047
$^{703}I/^{634}I$	1.87	1.63	1.97	1.78
^{703}k /l $mol^{-1}s^{-1}$	0.030	0.057	0.085	0.083
$^{579}I/^{634}I$	-	-	0.48	-
^{579}k /l $mol^{-1}s^{-1}$	(0.045)	(0.098)	0.122	(0.132)

* from Derwent and Thrush

Figure 9.3. A Plot of Equation 9.14 for the 579 nm Emission.

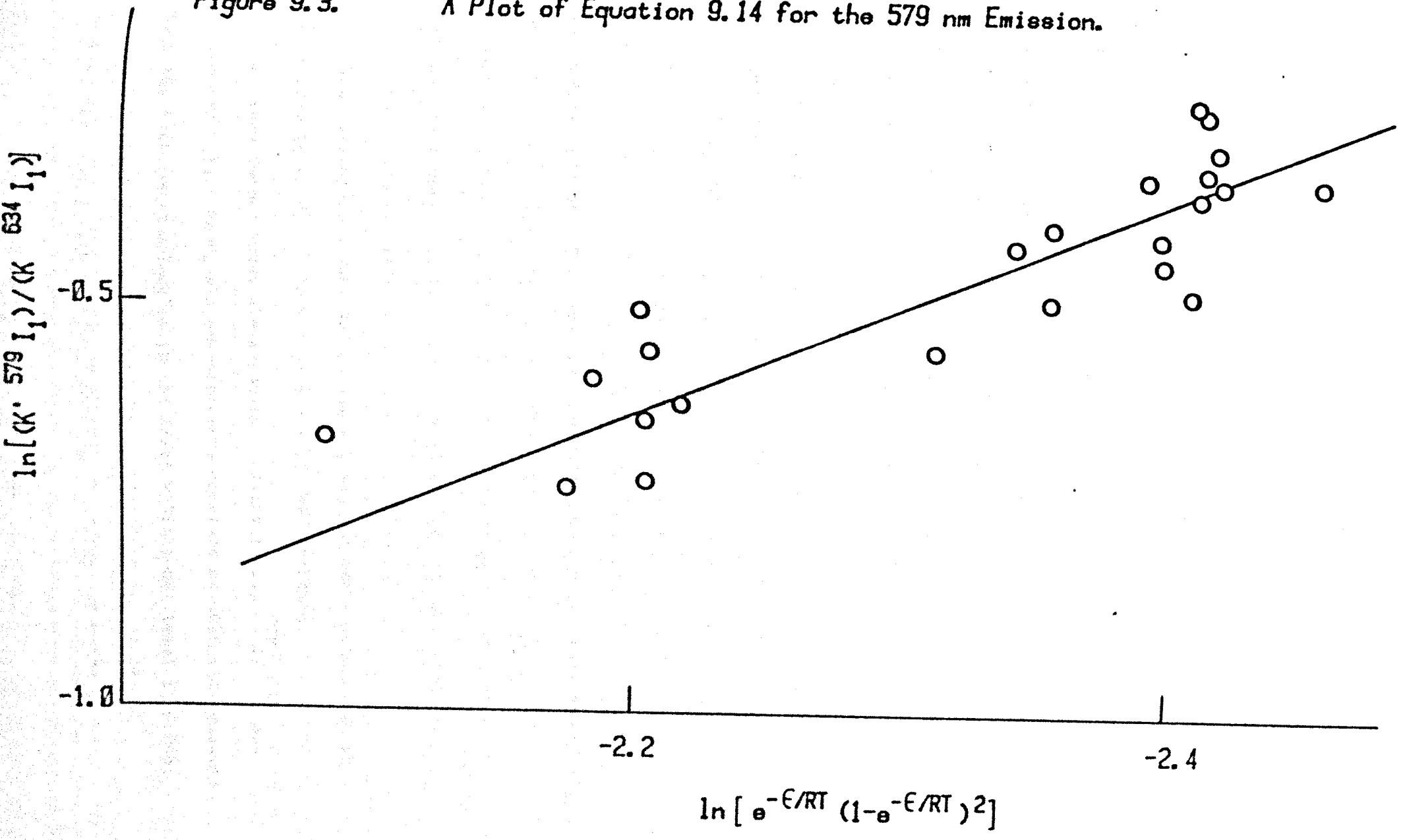

The emission rate constant is calculated from equation 9.7, where the extra emission at higher temperatures is assumed to follow the same pattern as the 634 nm and 703 nm emissions.

The shocks listed in table 10.1 for the studies of vibrational relaxation of $O_2(^1\Delta_g)$ (chapter 10).may be treated with equation 9.14. Figure 9.3 shows a plot of $\ln \frac{K' \, {}^{579}I_1}{K \, {}^{634}I_1}$ against $\ln[e^{-\epsilon/RT}(1-e^{-\epsilon/RT})^2]$, essentially a log v^{1}/T plot, for all shocks in table 10.1, which is linear. The linearity verifies the assignment of Gray and Ogryzlo[16] for the 579 nm emission (reaction 9.3), and shows that the enhancement of the 579 nm emission over that shown for the 634 nm emission is in fact due to the greater population of vibrationally excited $O_2(^1\Delta_g)$ molecules at the higher shock temperature. The relaxation zone observed is then characteristic of the vibrational relaxation of $O_2(^1\Delta_g)$ (chapter 10).

The slope of the line in figure 9.3.does not yield a value of ${}^{579}k'/{}^{634}k'$ directly, as the two emissions in these cases are from different detectors; so the geometry of the system would need to be taken into account. The straight line does however show that the 579 nm emission rate constant follows the $T^{\frac{1}{2}}$ temperature dependence, when the different relative populations are taken into account, and so the emission rate constants at other temperatures can be estimated from the value at 1400K. They too are listed in table 9.2.

The scatter in figure 9.3 is quite small for shock results which are extremely sensitive to the position of the detectors.

At room temperature, the measured emission ratio, ${}^{579}I/{}^{634}I$ has a value of 0.13. Using the emission rate constant at 295K and equation 9.7, the fraction of molecules in the first vibrational level is 0.046. This ratio corresponds to a vibrational temperature in the gas of $\sim$700K at the observation station. Knowing the decay of $O_2(^1\Delta_g)$

concentration along the tube, and assuming the room temperature vibrational relaxation of $O_2(^1\Delta_g)$ to be the same as ground state oxygen (0.042 s atm), oxygen issuing from the discharge has a vibrational temperature of 750 ± 50K.

Discussion

The intensity ratios for unit population of the three dimol emissions are listed in table 9.3 together with previous results. These ratios are expressed on the basis of number of quantum emitted and not total energy.

The errors were minimised by taking comparative measurements at the same point along the tube with the same detector. The largest source of error remaining is probably the variation in quantum efficiency with wavelength of the photomultiplier. The manufacturers published curves should be a good guide, and indeed Schurath[116] found them so, though individual tubes may differ. It was not possible to measure the quantum efficiency of the photomultipliers directly, and so it is suggested that the ratios listed in table 9.3 are accurate to ± 25%.

The result for the 703/634 ratio agrees well with that of Seliger[131] when his result is corrected for the spectral sensitivity of his system, but is almost double that of Whitlow and Findlay[112] who found the emission at 703 nm comparable with that at 634 nm. Their measurements were made with small concentrations of $O_2(^1\Delta_g)$ at room temperature.

The value for the 579/634 ratio is higher than that of Kahn and Kasha[18] who measured integrated intensities of very weak absorption bands. For both ratios we have been able to work at much higher concentrations of $O_2(^1\Delta_g)$ attained in the shock compression than other workers, and these values are preferred.

Dianov-Klokov[133], working on liquid oxygen found an enhanced dimol emission intensity over the single molecule transition, and suggested that a loss of centre of symmetry with vibrational excitation of one member of the molecular pair could account for the observed enhancement.

Robinson[134] and Krishna[135] treated the problem of intensity enhancement for the dimol emissions theoretically, and successfully

Table 9.3.

Intensity Ratios for Unit Populations measured as Number of Quantum Emitted

$^{703nm}/_{634nm}$	$^{579nm}/_{634nm}$	References
1.81 ± 0.45	2.8 ± 0.7	This work
2.0	-	131
1.05	-	112
-	1.44	18

- - - - - - - - - -

Franck Condon factors for Single Molecule Transitions

6.8×10^{-3}	2.2×10^{-2}	132

explained some of the aspects of transitions in oxygen pairs. Robinson suggested that the dimol transition probability for the oxygen pair might be enhanced from that for the forbidden transition in the single molecule, by borrowing intensity from the allowed Schuman-Runge transition in the ultra-violet, under the influence of intermolecular interactions.

$$O_2(^3\Sigma_u^-) \rightarrow O_2(^3\Sigma_g^-) + h\nu \qquad 9.15$$

Tsai and Robinson[136] calculated the intensity of the double transitions from both $O_2(^1\Delta_g)$ and $O_2(^1\Sigma_g^+)$ using a model based on a pair of molecules at a fixed distance, 3.81Å, apart, and found satisfactory agreement between theory and experiment. They also calculated Franck-Condon factors for the (0,0), (1,0) and (2.0) dimol transitions from $O_2(^1\Delta_g)$ and found them close in value to those for the single molecule transitions.

Einstein A factors calculated from the Franck-Condon factors for the single molecule transitions are listed in table 9.3. These are clearly a poor guide to the intensities of the dimol emissions.

In solid oxygen, Landau, Allin and Welsh[137] found the (1,0) dimol transition at 579 nm to be more intense than the (0,0) transition at 634 nm. Tsai and Robinson, in trying to explain the enhanced intensity of the (1,0) transition, suggested that a change in the intermolecular overlap of the electronic wavefunction due to nuclear vibrational motion might be responsible for the stronger observed intensity. Clearly the calculations do not fit the observed intensity distributions.

The low rates predicted by Franck Condon factors result from the similarity in bond length for the $O_2(^1\Delta_g)$ and $O_2(^3\Sigma_g^-)$ molecules. If,

in the emitting pair of $O_2(^1\Delta_g)$ molecules a complex is formed and the bond lengths change, then different Franck Condon factors may make emissions to and from vibrational excited molecules more favourable. In the gas phase, however, there is no thermodynamic evidence for complex formation. The dimol emission at 634 nm has been shown in Chapter 7 to be essentially a simple collisional process, and Arnold, Ogryzlo et al[14,15] concluded from their experiments that the emitting complex is not bound. Falick and Mahon[55] suggested that the only binding energy is Van der Waals attractive forces. The spectroscopic evidence for binary cluster formation at room temperature is negligible[138] although Blickensderfer and Ewing[139] believe that bound O_4 molecules exist at low temperatures. However, spectra from the O_4 dimer have been observed[140] in solid neon host at 4.2K, and from the α, β and γ forms of solid oxygen[137].

Chapter 10

Vibrational Relaxation of $O_2(^1\Delta_g)$

10.1 Introduction

The vibrational relaxation of $O_2(^1\Delta_g)$ may be studied by observing the dimol emission at 579 nm where one of the colliding $O_2(^1\Delta_g)$ molecules is in the first vibrational level[16]:

$$O_2(^1\Delta_g)_{v=1} + O_2(^1\Delta_g)_{v=0} \rightarrow 2\,O_2(^3\Sigma_g^-)_{v=0} + h\nu(\lambda = 579\ nm) \qquad 10.1$$

We studied the 579 nm emission at the high temperature attained when a shock is run into the flowing discharged gas, and obtained relaxation times for the temperature range 1000 to 1700 K. The results are compared with previous results for the ground state molecule.

The change in concentration of the vibrationally excited $O_2(^1\Delta_g)$ as the gas flows along the shock tube was studied at room temperature by measuring the decay in emission at 579 nm. Although this study yielded some information on the reactions involved, it was not possible to obtain a vibrational relaxation time for $O_2(^1\Delta_g)$ at this temperature.

This chapter is divided into two parts, the room temperature studies first, followed by the results at the shock temperature. A general discussion of the whole temperature range completes the chapter.

10.2. Room Temperature Studies of the 579 nm Emission.

10.2.1. Treatment of Results.

As we have seen before (Chapter 5) the rate of decay of $O_2(^1\Delta_g)_{v=0}$ is:

$$\frac{-d[O_2(^1\Delta_g)_{v=0}]}{dt} = k_q[O_2][O_2(^1\Delta_g)_{v=0}] + k_w[O_2(^1\Delta_g)_{v=0}] \qquad 10.2$$

$$= k_\Delta[O_2(^1\Delta_g)_{v=0}] \qquad 10.3$$

so that at any time, t;

$$\frac{[O_2(^1\Delta_g)_{v=0}]}{[O_2(^1\Delta_g)_{v=0}]_0} = e^{-k_\Delta t} = \left[\frac{634_I}{634_{I_0}}\right]^{\frac{1}{2}} \qquad 10.4$$

where $[O_2(^1\Delta_g)_{v=0}]_0$ is the concentration of $O_2(^1\Delta_g)_{v=0}$ at time, t = 0. The rate of decay along the tube is measured as a function of length and converted to the time scale by the linear flow velocity of the gas (Chapter 5).

If $O_2(^1\Delta_g)_{v=1}$ molecules are formed in or just after the discharge, there will be a greater population of the vibrationally excited molecules in the gas flow than would be predicted by the Boltzmann distribution function at that temperature. These vibrationally excited molecules lose their excess energy as the flowing gas attains vibrational equilibrium at room temperature.

So, by adding a term to the equation for the decay of the unvibrationally excited $O_2(^1\Delta_g)$, the rate of decay of $O_2(^1\Delta_g)_{v=1}$

should be given by:

$$\frac{-d[O_2(^1\Delta_g)_{v=1}]}{dt} = k_q[O_2(^1\Delta_g)_{v=1}][O_2] + k_w[O_2(^1\Delta_g)_{v=1}]$$

$$+ k^*_{rel}[O_2(^1\Delta_g)_{v=1}][O_2] \qquad 10.5$$

$$= k^*_\Delta[O_2(^1\Delta_g)_{v=1}] \qquad 10.6$$

where k^*_{rel} is the vibrational relaxation constant; in this case:

$$O_2(^1\Delta_g)_{v=1} + O_2 \xrightarrow{k^*_{rel}} O_2(^1\Delta_g)_{v=0} + O_2 \qquad 10.7$$

The reverse reaction will be very slow at room temperature and is ignored.

Similarly, at the same time, t,

$$\frac{[O_2(^1\Delta_g)_{v=1}]}{[O_2(^1\Delta_g)_{v=1}]_0} = e^{-k^*_\Delta t} \qquad 10.8$$

where $[O_2(^1\Delta_g)_{v=1}]_0$ is the concentration at time t = 0.

Now for the intensity of emission:

$$\frac{^{579}I}{^{579}I_0} = \frac{[O_2(^1\Delta_g)_{v=0}][O_2(^1\Delta_g)_{v=1}]}{[O_2(^1\Delta_g)_{v=0}]_0[O_2(^1\Delta_g)_{v=1}]_0} \qquad 10.9$$

and from equations 10.4, 10.8 and 10.9:

$$\frac{579_I}{579_{I_0}} = e^{-(k_\Delta^* + k_\Delta)t} \qquad 10.10$$

Plots of ln I/I_0 against distance, then converted to time, for both the 634 nm and 579 nm emissions, give values for the pseudo first order rate constants k_Δ and k_Δ^*. If it is assumed that the quenching by oxygen, and the wall deactivation is the same for both the v=0 and v=1 states of $O_2(^1\Delta_g)$, then:

$$579_\alpha - 634_\alpha = k_{rel}^*[O_2] \qquad 10.11$$

where α is the measured decay rate. So the vibrational relaxation rate constant can be calculated from the difference in measured decay rates between the two dimol emissions.

10.2.2. Experimental Procedure.

Measurements were made with one detector for both 634 nm and 579 nm emissions, at two positions along the tube, 900 mm apart. The complete room temperature decay line was not measured, as it was impractical to change the filter on the photomultiplier at each station, and it was felt that the long time taken to do a complete line at one wavelength, followed by the second wavelength, would mean that any long term changes in emission would lead to errors.

For the 579 nm emission, the recorded voltage levels were very small, varying between 20 mV and 2 mV. The background light level was of the order of 4 mV, and the procedure for measuring this was checked.

Normally the background light level was the voltmeter reading when the photomultiplier was isolated from the shock tube by black cloth. If the discharge was switched off, a smaller value was

obtained, but as the discharge is the major producer of stray light, this value was discarded. Switching off the oxygen flow produced a bright purple discharge in the resulting vacuum, but the higher background light obviously gave an erroneous reading and it too was discarded. Finally, a modification was made to the apparatus, so that the flowing discharged oxygen could be pumped away without flowing along the shock tube and past the detector. The zero correction so obtained was the same as for the "black cloth" method and this value was adopted, and checked with each emission reading.

10.2.3. Results.

The decay rate of the dimol emission at 634 nm as measured at two positions along the tube gave the value as the complete decay line previously measured (Chapter 5) for the same downstream pressure and flow rate.

Contrary to expectations, the rate of decay of the vibrationally excited $O_2(^1\Delta_g)$ molecules was almost the same as that measured at 634 nm, and in most cases, fractionally slower. For a series of nineteen experiments at pressures ranging from 4 to 12 torr (533 - 1600 Pa) and flow rates of 14 and 28 ml s^{-1} at one atmosphere pressure:

$$579_\alpha/634_\alpha = 0.94 \pm 0.22 \qquad 10.12$$

where the error is twice the standard deviation.

10.3 High Temperature Studies of the 579 nm Emission.

10.3.1 Treatment of Results.

The emission trace from a shock at 579 nm has the form shown below.

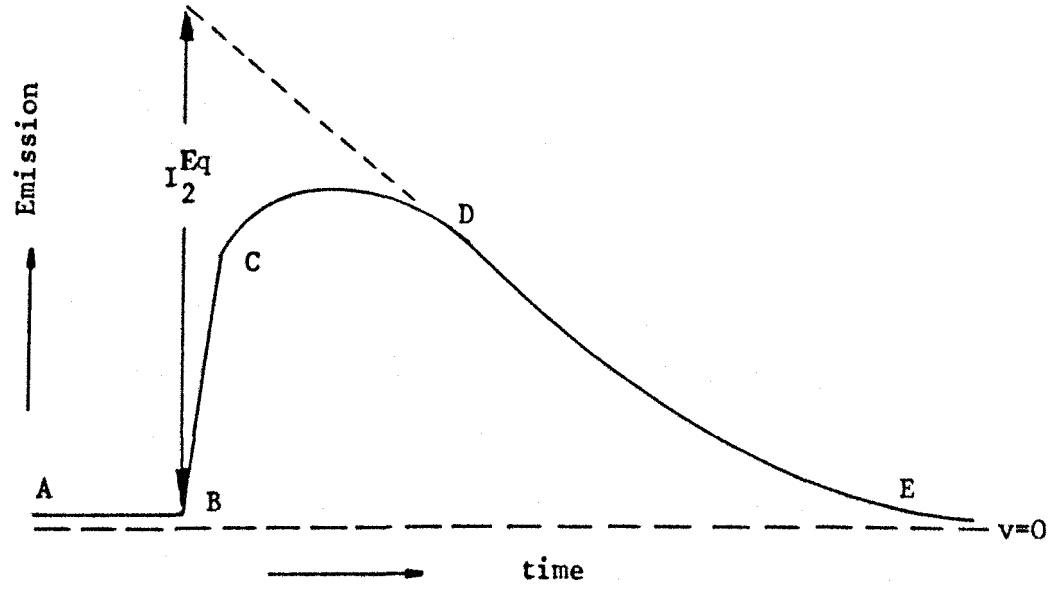

The height of AB above the zero line is a measure of the pre-shock glow and BC is the initial rise at the shock front due to the shock compression. The decay DE reflects the pre-shock decay of excited species as the gas flows along the tube. It is preceded by a relaxation zone, CD, where the concentration of vibrationally excited $O_2(^1\Delta_g)$ is adjusting to the higher shock temperature. The vibrational relaxation time is obtained from the analysis of this region.

The trace has a similar shape to that from the 762 nm emission (Chapter 8) but the relative heights are different, as can be seen from the position of the zero intensity line. The relaxation zone, although similar in shape, is a result of different processes.

For the 579 nm emission, the emission is dependent on two

electronically excited molecules colliding:

$$O_2(^1\Delta_g)_{v=1} + O_2(^1\Delta_g)_{v=0} \rightarrow 2\,O_2(^3\Delta_g^-)_{v=0} + h\nu(\lambda = 579\ nm) \qquad 10.1$$

and, as for the 634 nm emission, the rise at the shock front can be described by:

$$^{579}I_2^o = {}^{579}I_1 \left\{\frac{\rho_2}{\rho_1}\right\}^2 \left\{\frac{T_2}{T_1}\right\}^{\frac{1}{2}} \qquad 10.13$$

for a simple collisional process.

The enhancement in emission in the relaxation zone is due to the increase in vibrationally excited $O_2(^1\Delta_g)$ molecules as the gas relaxes to equilibrium at the higher shock temperature. The equilibrium emission, $^{579}I_2^{Eq}$, at T_2 is shown on the diagram above, and is the emission extrapolated back to zero time, i.e. at the shock front. It is defined as:

$$^{579}I_2^{Eq} = {}^{579}I_1\ K'\left\{\frac{\rho_2}{\rho_1}\right\}^2 \left\{\frac{T_2}{T_1}\right\}^{\frac{1}{2}} \qquad 10.14$$

where the enhancement factor, K', also includes any extra emission at temperatures above 1100 K, as seen in the 634 nm emission.

For vibrational relaxation, two processes are occurring:

$$O_2(^1\Delta_g)_{v=0} + O_2 \xrightarrow{k_+} O_2(^1\Delta_g)_{v=1} + O_2 \qquad 10.15$$

and

$$O_2(^1\Delta_g)_{v=1} + O_2 \xrightarrow{k_-} O_2(^1\Delta_g)_{v=0} + O_2 \qquad 10.16$$

Then the rate of formation of the vibrationally excited level is:

$$\frac{d[O_2(^1\Delta_g)_{v=1}]}{dt} = k_+[O_2][O_2(^1\Delta_g)_{v=0}] - k_-[O_2][O_2(^1\Delta_g)_{v=1}] \quad 10.17$$

and

$$[O_2(^1\Delta_g)_{v=0}] = [O_2(^1\Delta_g)_{v=0}]_0 - [O_2(^1\Delta_g)_{v=1}] \quad 10.18$$

where $[O_2(^1\Delta_g)_{v=0}]_0$ is the concentration of $O_2(^1\Delta_g)_{v=0}$ at zero time. Integrating equation 10.17 between time = 0 and time = t:

$$\frac{[O_2(^1\Delta_g)_{v=1}]}{[O_2(^1\Delta_g)_{v=1}]_0} = \frac{k_+[O_2][O_2(^1\Delta_g)_{v=0}]_0}{(k_- + k_+)[O_2][O_2(^1\Delta_g)_{v=1}]_0}$$

$$+ e^{-(k_- + k_+)[O_2]t}\left[1 - \frac{k_+[O_2][O_2(^1\Delta_g)_{v=0}]_0}{(k_- + k_+)[O_2][O_2(^1\Delta_g)_{v=1}]_0}\right] \quad 10.19$$

$[O_2(^1\Delta_g)_{v=1}]_0$ can be identified with the initial rise at the shock front, $^{579}I_2^0$, and the vibrational relaxation time, τ, is $1/(k_+ + k_-)[O_2]$ for the two level process described here.

Taking the overall decay along the tube, A, into account, equation 10.19 can be written as:

$$^{579}I_2 = {}^{579}I_1\left\{\frac{\rho_2}{\rho_1}\right\}^2\left\{\frac{T_2}{T_1}\right\}^{\frac{1}{2}}\{K' + e^{-t/\tau}(1 - K')\}e^{At} \quad 10.20$$

where $K' = \dfrac{k_+[O_2(^1\Delta_g)_{v=0}]_0}{(k_+ + k_-)[O_2(^1\Delta_g)_{v=1}]_0}$ and also takes into account

the extra enhancement of emission at higher temperatures as seen at 634 nm. Equation 10.20 must be integrated as before (Chapters 7 and 8) to allow for the finite rise time of the system,

$$\frac{1}{\Delta t}\int_{t-\Delta t}^{t} {}^{579}I_2\, dt, \text{ where } \Delta t \text{ is the integration time; giving:}$$

$$^{579}I_2 = \frac{^{579}I_1}{\Delta t}\left\{\frac{\rho_2}{\rho_1}\right\}^2\left\{\frac{T_2}{T_1}\right\}^{\frac{1}{2}}\left[\frac{1-K'}{A-{}^1/\tau}\left(1-e^{-\Delta t/\tau}\right)e^{(At-t/\tau)} + \frac{K'}{A}e^{At}\left(1-e^{A\Delta t}\right)\right] \qquad 10.21$$

and it is this equation to which the experimental points are fitted using the routine described in Chapter 6. This equation is similar in form to that for the 762 nm emission (equation 8.14) but the initial rise at the shock front is different, and K' and τ have other meanings.

Optimum values of K', τ, A and Δt are found on itera-tion for each shock. The value of the relaxation time, τ, is corrected for the shock pressure in torr and expressed as a Napier time in μs atmospheres.

$$\text{tau}/\mu\text{s. atm.} = \tau \cdot \frac{P_2}{760} \qquad 10.22$$

10.3.2. Results

The two detectors are clamped in position at the observation station during these experiments, so that a comparison of the two emissions can be made (Chapter 9), and so no pre-shock decay rates are measured. However, the pre-shock decay rate for the 634 nm emission is identical to the post-shock decay rate (Chapter 7)

which is constant, within experimental error, throughout these experiments.

The shape of the 579 nm emission trace can be seen in figure 10.1; the 634 nm emission trace has the form described in Chapter 7, the 579 nm emission trace has the form described here. A computer plot for the 579 nm emission is shown in figure 10.2, the computed line fits the points well, showing that the suggested model is correct. Analysis of the K' values shows that the higher population of vibrationally excited molecules at the shock temperature results in increased emission, and that the relaxation zone is characteristic of the vibrational relaxation time (Chapter 9).

The results are listed in table 10.1 and give the parameters for both 634 nm and 579 nm emissions from the two detectors for each shock. The flow rate of oxygen was 28 ml s^{-1} at 1 atmosphere pressure, and all runs were performed with the discharge power at 100 watts.

The results listed in table 10.2 had the microtron power at 80 watts, which effectively reduced the production of excited molecules. The small pre-shock glow for the 579 nm emission made these shocks difficult to analyse. The last three shocks listed in table 10.2 had only 75% of the oxygen flowing through the discharge. A measurable pre-shock glow was obtained by opening the slits on the detectors.

A Landau-Teller plot of the Napier times for $O_2(^1\Delta_g)$ relaxation against frozen temperature at the shock front (ln tau against $T^{-1/3}$) is shown in figure 10.3. The full line is the averaged results from previous work on ground state oxygen,[102] the dashed line is the least squares fit to the points.

The points plotted in figure 10.4 are from the results listed in table 10.2 where the concentration of $O_2(^1\Delta_g)$ was reduced. Apart

from two anomalously high Napier times, these results are in reasonable agreement with the previous runs. The scatter is too great to discern any effect of the lower concentration of $O_2(^1\Delta_g)$ on the relaxation time, and further reductions in microtron power or discharged oxygen, produced results which were too noisy for analysis.

The experimental results for the vibrational relaxation of discharged oxygen in the temperature range 1000 to 1700 K fit the equation:

$$\ln(\tau/\mu s.\ atm.) = 126.7\ T^{-1/3} - 8.47 \qquad 10.23$$

Figure 10.1.

Traces of the Shock Emission.
Run No. 941

a. 634 nm

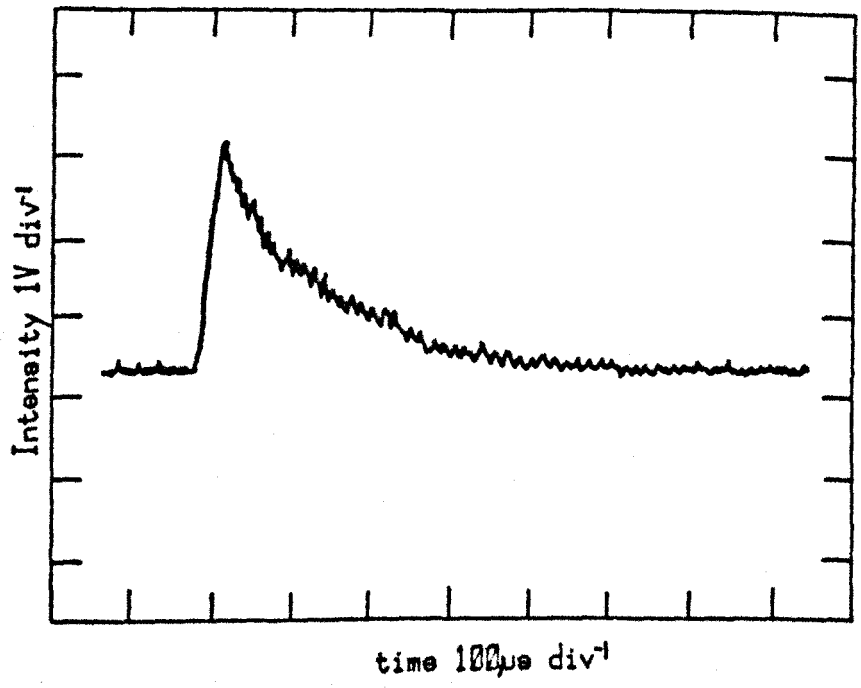

b. 579 nm

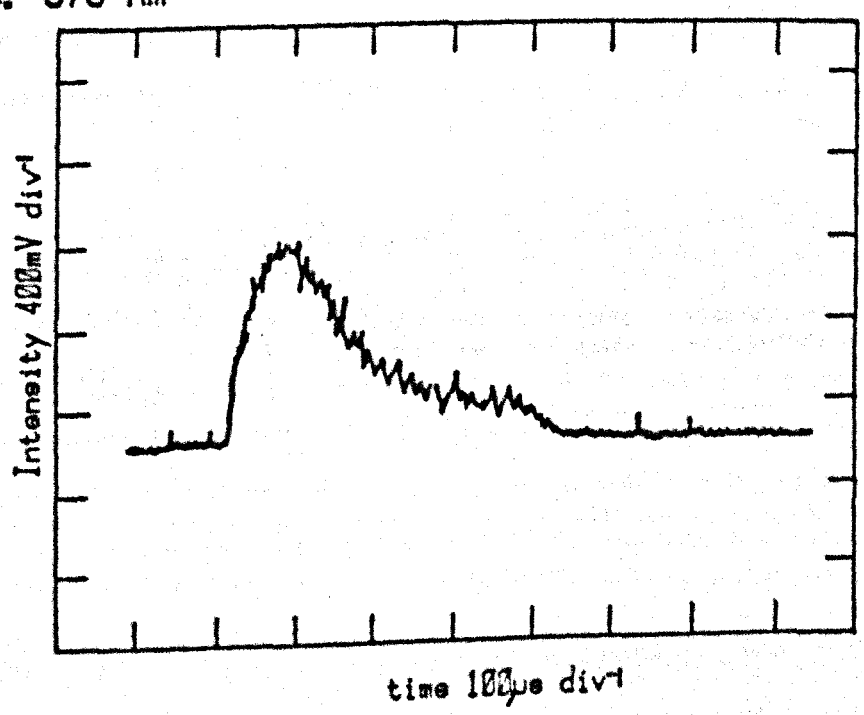

Figure 10.2.

A Computer Plot of the Analysis of a Shock at 579 nm.

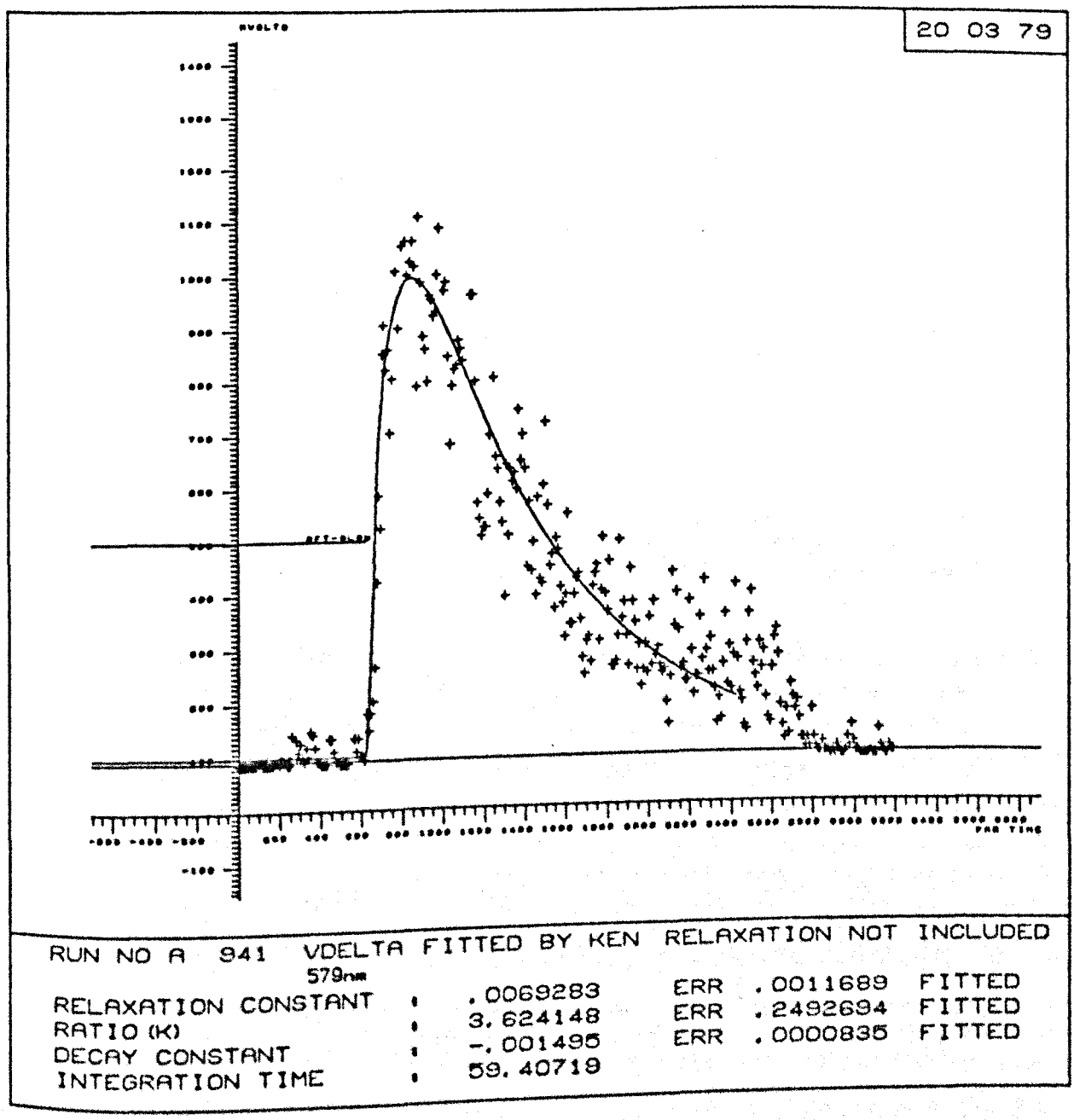

Table 10.1.

Results of the Analysis of Shocks at 579 nm and 634 nm into 100% Oxygen.

Run No.	P_1 /torr	Pre-Shock Glow/mV 634	579	Speed /km s^{-1}	Shock Temperature T_A/K	T_2/K	Enhancement ^{634}K	^{579}K	Post-Shock Decay/m^{-1} 634	579	tau /us atm
930	6.68	28.3	5.0	1.371	1279	1147	1.24	4.43	1.12	1.41	28.5
931	6.51	35.9	6.0	1.586	1620	1426	1.29	4.85	1.08	1.24	10.5
933	6.35	37.9	6.6	1.500	1478	1310	1.29	3.74	1.04	0.96	8.5
934	6.31	34.0	6.0	1.372	1281	1148	1.11	3.08	1.10	1.10	28.6
935	6.39	28.8	5.0	1.372	1281	1148	1.20	3.64	1.01	1.13	21.7
936	6.68	29.1	5.1	1.610	1661	1459	1.28	5.37	1.12	1.22	13.6
938	6.84	36.8	6.6	1.350	1249	1122	1.26	3.41	1.21	1.31	21.4
939	6.76	40.1	7.1	1.287	1160	1049	1.15	3.36	1.09	1.51	36.3
940	6.64	45.0	7.9	1.225	1078	978	1.08	3.73	1.09	1.50	64.5
941	6.59	44.4	7.9	1.383	1297	1162	1.15	3.45	1.12	1.32	22.1

Table 10.1.(continued)

Results of the Analysis of Shocks at 579 nm and 634 nm into 100% Oxygen.

Run No.	P_1 /torr	Pre-Shock Glow/mV 634	579	Speed /km s^{-1}	Shock Temperature T_A/K	T_2/K	Enhancement ^{634}K	^{579}K	Post-Shock Decay/m^{-1} 634	579	tau /us atm
C54	6.72	34.6	6.1	1.624	1685	1479	1.39	5.64	1.23	1.39	18.5
C57	6.39	29.8	5.3	1.607	1656	1455	1.51	6.00	1.15	1.27	13.1
C58	6.47	27.9	4.5	1.589	1625	1430	0.71	4.68	0.97	1.04	11 4
C59	6.47	27.8	5.0	1.602	1647	1448	1.36	4.78	1.16	1.21	13.3
C60	6.55	30.6	6.0	1.373	1282	1149	1.25	3.67	1.13	1.48	28.7
C61	6.88	35.4	6.6	1.582	1613	1420	1.26	4.90	1.18	1.20	10.8
C62	6.88	35.0	6.1	1.565	1585	1397	1.27	5.23	1.25	1.34	10.6
C63	6.64	42.7	7.6	1.523	1515	1341	1.23	4.63	1.08	1.25	15.5
C64	6.72	41.8	7.4	1.473	1435	1275	1.41	4.64	1.32	1.33	12.4
C65	6.72	41.9	7.6	1.523	1515	1341	1.06	3.72	1.01	1.18	10.4

Table 10.1.(continued)

Results of the Analysis of Shocks at 579 nm and 634 nm into 100% Oxygen.

Run No.	P_1 /torr	Pre-Shock Glow/mV 634	579	Speed /km s^{-1}	Shock Temperature T_A/K	T_2/K	Enhancement 634_K	579_K	Post-Shock Decay/m^{-1} 634	579	tau /us atm
C67	6.84	40.5	7.4	1.506	1488	1318	1.13	4.06	1.07	1.27	13.5
C68	6.76	41.0	6.7	1.529	1525	1349	1.12	5.26	1.13	1.30	14.1
C69	6.40	39.2	6.8	1.630	1696	1487	1.29	5.76	0.87	1.32	6.3
C70	6.68	42.6	7.1	1.604	1651	1451	1.16	5.47	0.79	1.36	11.0
C72	6.76	43.6	7.6	1.714	1846	1606	1.42	5.80	1.07	1.16	6.0
C73	6.59	42.2	7.2	1.620	1678	1473	1.26	5.51	0.94	1.28	9.9
C94	6.72	33.8	5.9	1.358	1260	1131	1.12	3.57	1.10	1.58	19.4
C95	6.72	38.7	6.8	1.376	1287	1153	1.23	5.03	0.90	1.37	39.5
C96	6.72	42.9	7.7	1.363	1268	1137	1.17	3.00	1.01	1.12	15.3
C97	6.72	45.1	8.1	1.360	1263	1134	1.29	3.14	1.04	1.06	11.4

Table 10.2.

Results of the Analysis of Shocks at 579 nm and 634 nm into 100% Oxygen.(Power 80 watts) (Final 3 Shocks - 75% Oxygen through Discharge)

Run No.	P_1 /torr	Pre-Shock Glow/mV 634	579	Speed /km s^{-1}	Shock Temperature T_A/K	T_2/K	Enhancement ^{634}K	^{579}K	Post-Shock Decay/m^{-1} 634	579	tau /us atm
942	6.43	20.6	4.05	1.586	1620	1426	1.26	7.07	0.80	1.15	44.6
943	6.84	21.1	4.0	1.571	1595	1405	1.24	4.36	1.10	1.24	19.4
944	6.31	22.1	4.3	1.488	1459	1295	1.32	7.56	1.24	1.97	47.1
945	6.35	16.6	3.3	1.465	1422	1265	1.14	3.28	1.24	1.31	10.0
C74	6.55	40.2	7.0	1.390	1308	1165	0.85	1.85	0.98	1.18	15.2
C75	6.64	21.3	4.3	1.378	1290	1156	1.37	2.82	1.25	1.24	18.0
C76	6.51	26.5	5.3	1.386	1302	1165	1.11	3.09	1.02	1.21	15.7
C78	6.84	24.0	4.8	1.592	1630	1434	1.16	3.70	1.06	1.12	7.1
956	6.23	43.1	7.7	1.386	1302	1165	1.19	3.48	0.98	1.14	13.0
958	6.39	44.5	7.9	1.597	1639	1441	1.27	5.17	0.97	1.14	10.6
959	6.96	41.0	6.9	1.573	1598	1408	1.18	4.90	0.96	1.14	11.5

Figure 10.3.

Landau-Teller Plot for Vibrational Relaxation of Discharged Oxygen.

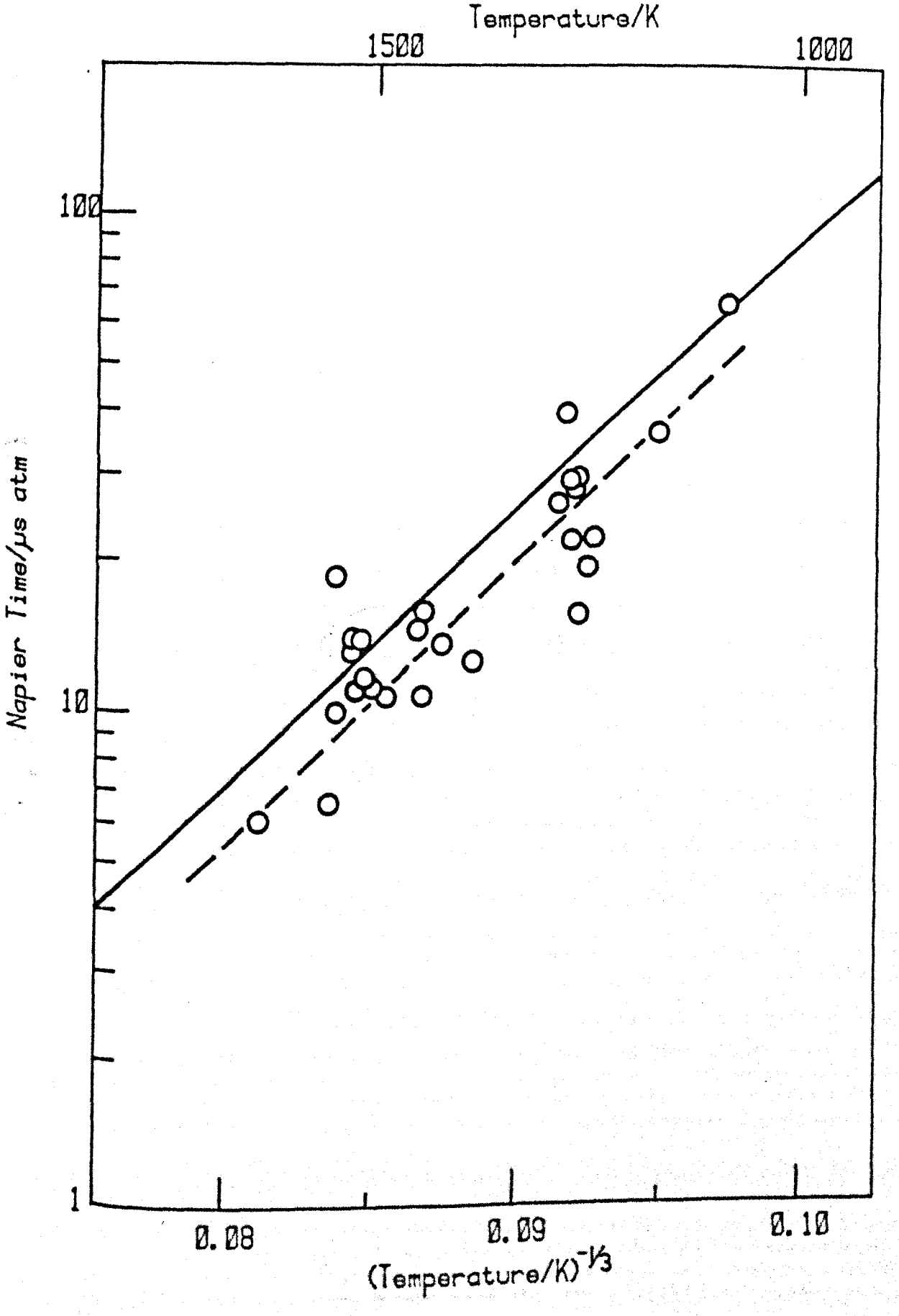

Figure 10.4.

Landau-Teller Plot for Vibrational Relaxation of Discharged Oxygen.

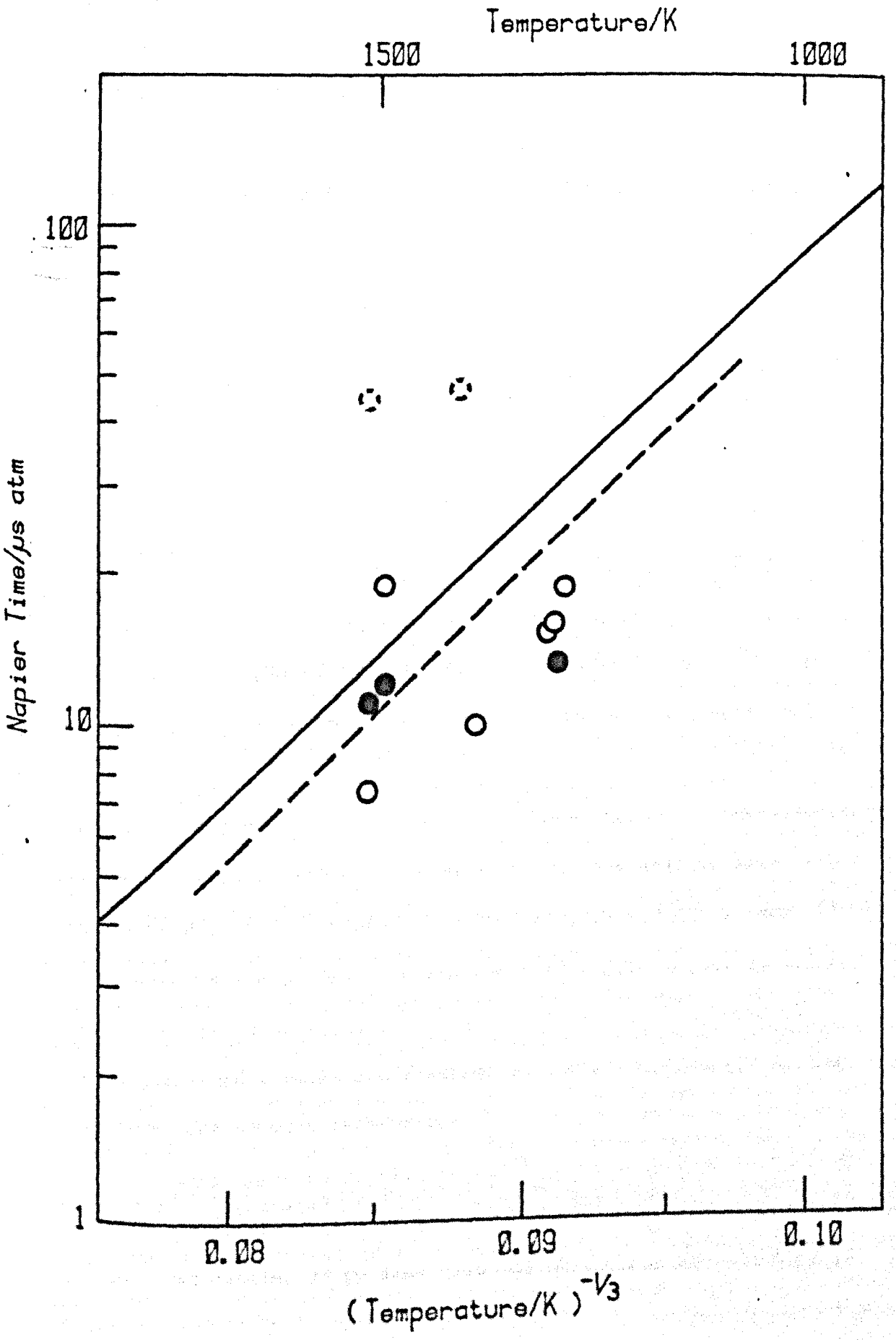

10.4. Discussion

Vibrational relaxation in ground state oxygen has been studied extensively by many workers, both at room temperature, and in shock tubes to temperatures up to 7000 K.

The results of Generalov and Losev[141] who measured the change in ultra-violet absorption spectra between 1200 and 7000 K, White and Millikan[142] from interferometry at 600 to 2600 K, and Lutz and Kiefer[143] using a laser schlieren technique at 1000 to 3000 K, all fit well the equation for vibrational relaxation of ground state oxygen[102].

$$\log_{10}(\tau/\mu s.\ atm) = 54.7\ T^{-1/3} - 9.535$$

or

$$\ln(\tau/\mu s.\ atm) = 126.0\ T^{-1/3} - 8.14 \qquad 10.24$$

At room temperature, the Landau-Teller plot has a definite curvature, as found for many non-polar diatomic molecules, where the transition probability is increased by attractive forces[2]. Extrapolation of equation 10.24 gives τ_{O_2} = 0.042 s. atm. at 295 K, but measurements using an acoustic resonance tube at 296 K by Parker[144] gave τ_{O_2} = 0.018 ± 0.010 s. atm. from extrapolation of oxygen/hydrogen mixtures. Holmes, Smith and Tempest[145] using a similar resonance tube method at 303 K obtained a value of 0.016 ± 0.024 s. atm. These experiments are subject to considerable errors as oxygen is not an easy molecule to study, with a high characteristic vibrational temperature and a small contribution of vibrational energy to the specific heat at room temperature.

The vibrational relaxation of $O_2(^1\Delta_g)$ has only been studied by Collins and Husain[146] and Parker and Ritke[147], both at room temperature. Collins and Husain, using time resolved absorption spectroscopy in

the vacuum ultra violet gave rate data for the vibrational relaxation of $O_2(^1\Delta_g)$ and ground state oxygen on collision with helium, argon, nitrogen, SF_6 and CF_4. They concluded that vibrational equilibrium was maintained between $O_2(^1\Delta_g)_{v=1}$ and $O_2(^3\Sigma_g^-)_{v=1}$ over a wide pressure range, in the presence of helium and CF_4.

$$O_2(^1\Delta_g)_{v=1} + O_2(^3\Sigma_g^-)_{v=0} \rightleftharpoons O_2(^1\Delta_g)_{v=0} + O_2(^3\Sigma_g^-)_{v=1} \qquad 10.25$$

Parker and Ritke working at a pressure of 35 atmospheres of oxygen in a high pressure gas cell equipped with an acoustic detector concluded that vibration-vibration energy transfer was not a significant step in the deactivation of $O_2(^1\Delta_g)_{v=1}$.

The results of these experiments in figure 10.3 show a significant deviation from the experimental results for $O_2(^3\Sigma_g^-)$. This might be expected if $O_2(^1\Delta_g)$ relaxes faster than $O_2(^3\Sigma_g^-)$. Calculations using the semi empirical Millikan and White correlation[148] (Appendix IIIa) give values reasonably in agreement with experiment for ground state oxygen, and up to a factor of two faster for $O_2(^1\Delta_g)$.

The faster relaxation rate from that of ground state oxygen found in this work, could be the result of impurities in the system. Polyatomic molecules increase the relaxation rate due to the availability of several vibrational levels. In our system water is the only likely impurity and it is present at concentrations less than 30 ppm in the flowing gas. Calculations of the effect of this amount of water on the relaxation time of ground state oxygen, using

a value of 80 for Z_{AB}, the collision number for inter molecular vibrational energy transfer between oxygen and water[149], suggests that the difference in vibrational relaxation time will be negligible. The effect of impurities will not be considered further.

In our system, the relaxation processes occurring are:

$$O_2(^1\Delta_g)_{v=1} + O_2 \rightleftarrows O_2(^1\Delta_g)_{v=0} + O_2 \qquad 10.26$$

$$O_2(^3\Sigma_g^-)_{v=1} + O_2 \rightleftarrows O_2(^3\Sigma_g^-)_{v=0} + O_2 \qquad 10.27$$

and the vibration-vibration exchange reaction:

$$O_2(^1\Delta_g)_{v=1} + O_2(^3\Sigma_g^-)_{v=0} \rightleftarrows O_2(^1\Delta_g)_{v=0} + O_2(^3\Sigma_g^-)_{v=1} \qquad 10.25$$

It is assumed that collisions with either $O_2(^3\Sigma_g^-)$ or $O_2(^1\Delta_g)$ have the same efficiency for vibrational relaxation. The emission at 579 nm is a measure of the vibrational relaxation of $O_2(^1\Delta_g)$, but if V-V exchange is rapid (equation 10.25) the vibrational populations will keep in step, and the value of the Napier time obtained will be the vibrational relaxation time of the mixture of about 10% $O_2(^1\Delta_g)$ in ground state oxygen. If the relaxation of $O_2(^1\Delta_g)$ is fast, then this will be the preferred route to equilibrium.

It is possible to calculate vibration relaxation times for V-V exchange reactions near resonance from an equation developed by Rapp[150] (Appendix IIIb), giving values for τ_{VV} of 0.026 μs. atm. at 1000 K and 0.013 μs. atm. at 1500 K, a factor of 10^3 - 10^4 times faster than the vibrational relaxation of ground state oxygen.

Vibrational relaxation times for a two component system where V-V exchange is important can be calculated from equations developed by Schotter and Bauer[151, 152] (Appendix IIIc). Using values of the vibrational relaxation of $O_2(^3\Sigma_g^-)$ and $O_2(^1\Delta_g)$ calculated from the Millikan and White correlation, and the above values for the V-V exchange reaction, gives τ for the mixture of 10% $O_2(^1\Delta_g)$ in 90% $O_2(^3\Sigma_g^-)$ of 117 μs. atm. at 1000 K and 22.2 μs. atm. at 1500 K which when standardized to the experimental values for $O_2(^3\Sigma_g^-)$ give 78.1 and 16.5 μs. atm. respectively. These values are shown in figure 10.5, together with the experimental results. This small deviation from the ground state results would be difficult to observe, and we believe that our values deviate more than this.

The experiments to reduce the concentration of $O_2(^1\Delta_g)$ in the flow gave inconclusive results because of the difficulty in analysing shocks with weak emissions, and it was not possible to discern if the results in figure 10.4 lie on or above the dashed line in figure 10.3, the results for 10% $O_2(^1\Delta_g)$.

A similar calculation using the Schotter and Bauer equations takes the experimental results for ground state oxygen and the results in this chapter for 10% $O_2(^1\Delta_g)$ in $O_2(^3\Sigma_g^-)$ and calculates the vibrational relaxation of pure $O_2(^1\Delta_g)$. The values for $O_2(^1\Delta_g)$ are 24.2 μs. atm. at 1000 K and 4.8 μs. atm. at 1500 K and are also indicated in figure 10.5, they are a factor of 5 faster than for ground state oxygen. These values are faster than would be expected for a molecule whose vibrational temperature and vibrational levels do not differ much from that of ground state oxygen, but are not unreasonably fast, indicating that the results in this study may be described as the vibrational relaxation of a mixture of 10% $O_2(^1\Delta_g)$ in $O_2(^3\Sigma_g^-)$ where V-V exchange is fast compared to the

Figure 10.5.

Landau-Teller Plot for Vibrational Relaxation in Oxygen.

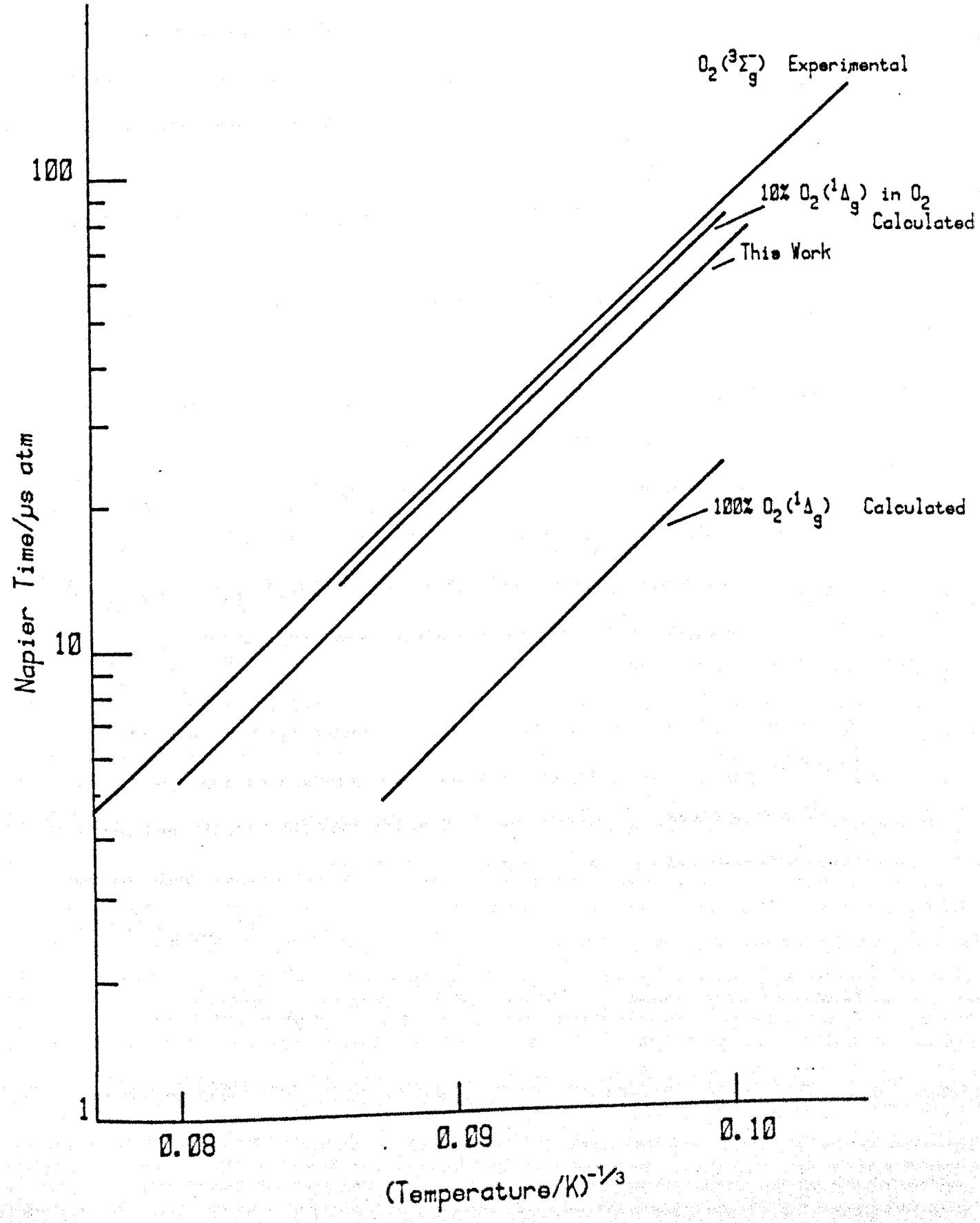

rates for vibrational relaxation.

If, however, V-V exchange is slow, the observed relaxation will be from the two electronic states relaxing independently. This would give relaxation times comparable with those found in this study.

The calculated relaxation time for equation 10.25 is fast, and it seems reasonable to suggest that V-V exchange would be important for the two molecules near resonance. So although it is not possible to distinguish between the two possibilities from these results, the fast V-V exchange is more favoured in agreement with the findings of Collins and Husain at room temperature.

A complete solution to the problem will only be found when the relaxation of both species can be monitored simultaneously.

At room temperature, the similarity of the decay rates for the 579 and 634 nm emissions ($^{579}\alpha/^{634}\alpha = 0.94 \pm 0.22$) fits with the conclusions of Parker and Ritke who find that the significant deactivation paths for $O_2(^1\Delta_g)_{v=1}$ are to $O_2(^3\Sigma_g^-)_{v=1}$ followed by vibrational deactivation, and, vibrational deactivation to $O_2(^1\Delta_g)_{v=0}$ followed by electronic deactivation. The V-V exchange reaction 10.25 does not play a significant part.

The assumptions made for the room temperature kinetics in section 10.2.1 may not be correct, and the analysis would need to be modified where the electronic deactivation of the $O_2(^1\Delta_g)_{v=1}$ state may not be the same as for the $O_2(^1\Delta_g)_{v=0}$ state; $k_q^* \neq k_q$. So, deactivation of $O_2(^1\Delta_g)_{v=1}$ is

$$O_2(^1\Delta_g)_{v=1} + O_2 \xrightarrow{k_q^*} O_2(^3\Sigma_g^-)_{v=1} + O_2 \qquad 10.28$$

followed by

$$O_2(^3\Sigma_g^-)_{v=1} + O_2 \xrightarrow{k_{rel}} O_2(^3\Sigma_g^-)_{v=0} + O_2 \qquad 10.29$$

and $$O_2(^1\Delta_g)_{v=1} + O_2 \xrightarrow{k^*_{rel}} O_2(^1\Sigma_g)_{v=0} + O_2 \qquad 10.7$$

followed by

$$O_2(^1\Delta_g)_{v=0} + O_2 \xrightarrow{k_q} O_2(^3\Sigma_g^-)_{v=0} + O_2 \qquad 10.30$$

So, as before:

$$^{634}\alpha/2 = k_q[O_2] + k_w \qquad 10.31$$

but now:

$$^{579}\alpha = k^*_q[O_2] + k_w + k^*_{rel}[O_2] + k_q[O_2] + k_w \qquad 10.32$$

Assuming the wall deactivation is the same for both states:

$$\frac{^{579}\alpha}{^{634}\alpha} = 0.94 = \frac{k^*_q + k^*_{rel} + k_q}{2k_q} \qquad 10.33$$

Parker and Ritke's value for the vibrational relaxation time for $O_2(^1\Delta_g)$ at 35 atmospheres is 1.002×10^{-3} s which converts to $k^*_{rel} = 7.0 \times 10^2$ ℓ mol^{-1} s^{-1}. From chapter 5, $k_q = 9.4 \times 10^2$ ℓ mol^{-1} s^{-1}, and k^*_q from equation 10.33 is 1.3×10^2 ℓ mol^{-1} s^{-1}, a much slower collisional quenching rate for the vibrationally excited state.

Parker and Ritke give a value for k^*_q/k_q of 0.093, the result here for the same ratio is 0.135, in fair agreement.

These calculations are only valid if V-V exchange is slow compared with the collisional quenching rate. If V-V exchange (reaction 10.25) is fast in comparison, the vibrational populations will keep in step, and the electronic deactivation will be through $O_2(^1\Delta_g)_{v=0}$, the faster rate. The assumptions in section 10.2.1 would be correct and $^{579}\alpha$ would be expected to be greater than $^{634}\alpha$, the difference being due to the relaxation of $O_2(^1\Delta_g)$.

At room temperature it appears that V-V exchange is not important in the quenching of $O_2(^1\Delta_g)_{v=1}$, in agreement with the findings of Parker and Ritke; at the high temperature V-V exchange is fast and vibrational equilibrium is maintained between $O_2(^1\Delta_g)_{v=1}$ and $O_2(^3\Sigma_g^-)_{v=1}$, in agreement with Collins and Husain.

Chapter 11

Conclusions, and Suggestions for Further Work

11.1. Singlet Molecular Oxygen

The discharge flow shock tube has been used in this work to obtain accurate kinetic data for the singlet states of molecular oxygen over a wide temperature range.

$O_2(^1\Delta_g)$ is formed in or just after the discharge and then flows into the shock tube. Its reactions are studied by observing the change in concentration along the shock tube before the shock, and comparing this with the rate of decay observed in the emission behind the shock front. Although the deactivation of $O_2(^1\Delta_g)$ is slow enough at room temperature for there to be an appreciable concentration of $O_2(^1\Delta_g)$ along the tube, at the high shock temperature the increase in collisional quenching rate of $O_2(^1\Delta_g)$ is not large enough to measure within the hot flow time available for shock tube measurements.

However, it may be possible to measure the temperature dependence of collisional quenching of $O_2(^1\Delta_g)$ by some organic compounds, if the pre-shock emission is strong enough to measure accurately a room temperature decay rate along the shock tube before the shock. The increase in quenching rate constant at the high shock temperature would have to be large enough to produce a change in the decay rate of at least 15% of the pre-shock decay rate for measurements to be made. This would correspond to an activation energy of about 5 kJ mol^{-1} for a reaction with a normal Arrhenius temperature dependence.

$O_2(^1\Sigma_g^+)$ is formed in the flowing gas by the energy pooling reaction from two $O_2(^1\Delta_g)$ molecules. The addition of nitrogen to the system showed that rate constants can be obtained in this case where the steady state concentration of $O_2(^1\Sigma_g^+)$ at any point in the tube adjusts to a new steady state at the high shock temperature. The oxygen and nitrogen

results have been published.[153]

The work on the collisional quenching of $O_2(^1\Sigma_g^+)$ by oxygen and nitrogen yielded interesting curved temperature dependences, possibly indicating two contributory mechanisms. Since the completion of the experimental work for this thesis, the quenching studies have continued. Experiments are presently being performed with carbon dioxide and nitrous oxide, and are proposed for hydrogen chloride and nitric oxide. The preliminary results for carbon dioxide[154] and nitrous oxide suggest quenching rate constants with negative temperature dependences in the region 700 to 1300 K, where the quenching is possibly dominated by long range multipolar interactions with these polyatomic molecules. It is hoped to correlate the experimental results with calculated values,[155,156,157] over a wider temperature range then Braithwaite, Davidson, Ogryzlo and Schiff[71,72] used for hydrogen bromide and hydrogen.

The studies of the relative intensities of the unusual dimol emissions of $O_2(^1\Delta_g)$ gave interesting results in accord with other workers, but not in agreement with Franck-Condon factors for the single molecule transitions, illustrating the unique nature of these emissions.[158]

The dimol emission at 634 nm has been shown to be essentially a simple collisional process at temperatures between 650 and 1600 K, although the enhanced emission observed above 1100 K is difficult to explain. Two tentative suggestions are put forward in chapter 5, but we are now considering whether the extra emission is a result of reactions between vibrationally excited $O_2(^1\Delta_g)$ molecules which will be present in increasing numbers at the higher shock temperatures. Further shocks would need to be performed with a slightly different filter to test this idea.

Spectra of discharged oxygen at shock temperatures would show if this theory is correct, but such experiments are not possible at the moment.

The studies at 579 nm gave results on the vibrational relaxation of $O_2(^1\Delta_g)$; the increased vibrational relaxation rate of $O_2(^1\Delta_g)$ is illustrated, and it is suggested that vibration-vibration exchange is important. This work is being published[159]. The 579 nm emission studies also confirmed the validity of discharge flow shock tube results where a good straight line is obtained between measured equilibrium emissions and calculated values from spectroscopic data (figure 9.3) over the temperature range 1000 to 1700 K.

However, relaxation studies are limited to pure oxygen, the addition of nitrogen lengthens the relaxation time and the relaxation zone becomes difficult to define. Polyatomic molecules increase the rate of relaxation giving vibrational relaxation times comparable with the integration time and impossible to measure.

11.2. Different Systems for Future Study

The compounds isoelectronic with oxygen possess low-lying $(^1\Delta_g)$ and $(^1\Sigma_g^+)$ electronically excited states which might be expected to behave in a similar way to oxygen and could make an interesting comparison with the oxygen work. Barnes, Becker and Fink[160,161] have studied the chemiluminescence from SO and S_2 and more recently Se_2, SeS and SeO.[162] Unfortunately, apart from the disagreeable nature of some of these compounds, sulphur and selenium would be deposited on the walls of the apparatus and would interfere with emission studies in a large apparatus difficult to clean easily.

The addition of iodine to singlet oxygen produces an interesting chemiluminescence,[163] but here too solid iodine in the system could give problems.

Studies with oxygen atoms seem the most promising to yield interesting results. Although the weak emission from oxygen atom recombination[164] would be difficult to detect, their reactions with other molecules could

be studied, where the concentrations of oxygen atoms could be monitored with the emission from their reaction with nitric oxide. Reactions with oxygen atoms are important in combustion studies; in the discharge flow shock tube the oxygen atoms are generated into a clean system and combustion can be studied at lower temperatures than previously used. The oxygen atom reactions are likely to have a sufficiently high activation energy for the increased reaction rates at the high shock temperature to be measurable in the discharge flow shock tube apparatus.

References

1. J. Nicholas, "Chemical Kinetics", (1976), Harper and Row, London.
2. J.D. Lambert, "Vibrational and Rotational Relaxation in Gases", (1977), Oxford.
3. R.N. Schwartz, Z.I. Slawsky and K.F. Herzfeld, J. Chem. Phys., 20, (1952) 1591.
4. G. Herzberg, "Spectra of Diatomic Molecules", (1961) Van Nostran, New York.
5. R. McWeeny, "Coulson's Valence", (1979) Oxford.
6. R.P. Wayne, Advan. Photochem., 7, (1969) 311.
7. D.H. Katayama, S. Ogawa, M. Ogawa and Y. Tanaka, J. Chem. Phys., 67, (1977) 2132.
8. K.K. Rohatgi-Mukherjee, Proc. Symposium on Singlet Molecular Oxygen, (1976) 35, Bombay.
9. R.M. Badger, A.C. Wright and R.F. Whitlock, J. Chem. Phys., 43, (1965) 4345.
10. W.H.J. Childs and R. Mecke, Z. Physik., 68, (1931) 344.
11. L. Wallace and D.M. Hunten, J. Geophys. Res., 73, (1968) 4813.
12. H.H. Seliger, Anal. Biochem. 1 (1960) 60.
13. A.U. Khan and M. Kasha, J. Chem. Phys., 39, (1963) 2105.
14. S.J. Arnold, E.A. Ogryzlo and H. Witzke, J. Chem. Phys., 40 (1964) 1769.
15. S.J. Arnold, R.J. Browne and E.A. Ogryzlo, Photochem. and Photobiol., 4, (1965) 963.
16. E.W. Gray and E.A. Ogryzlo, Chem. Phys. Letters, 3 (1969) 658.
17. A.U. Khan and M. Kasha, J. Amer. Chem. Soc., 88 (1966) 1576.
18. A.U. Khan and M. Kasha, J. Amer. Chem. Soc., 92 (1970) 3293.

19. R.A. Young and G. Black, J. Chem. Phys., 42, (1965) 3740.

20. R.A. Young and G. Black, J. Chem. Phys., 47, (1967) 2311.

21. H.P. Broida and A.G. Gaydon, Proc. R. Soc., A222, (1954) 181.

22. R.D. Kenner, E.A. Ogryzlo and S. Turley, J. Photochem, 10, (1979) 199.

23. S.J. Arnold and E.A. Ogryzlo, Canad. J. Phys., 45, (1967) 2053.

24. S.J. Arnold, M. Kubo and E.A. Ogryzlo, Advan. Chem., 77, (1968) 133.

25. M.A.A. Clyne, B.A. Thrush and R.P. Wayne, Photochem and Photobiol, 4, (1965) 957.

26. R.E. March, S.G. Furnival and H.I. Schiff, Photochem and Photobiol, 4, (1965) 971.

27. R.L. Brown, J. Phys. Chem., 71, (1967) 2492.

28. K.H. Becker, W. Groth and U. Schurath, Chem. Phys. Letters, 14, (1972) 489.

29. M. Yaron and A. von Engel, Chem. Phys. Letters, 33, (1975) 316.

30. M. Yaron, A. von Engel and P.H. Vidaud, Chem. Phys. Letters, 37, (1976) 159.

31. P.H. Vidaud, R.P. Wayne and M. Yaron, Chem. Phys. Letters, 38, (1976) 306.

32. K. Furukawa and E.A. Ogryzlo, Chem. Phys. Letters, 12, (1971) 370.

33. D.R. Snelling, Chem. Phys. Letters, 2,(1968) 346.

34. F.D. Findlay, C.J. Fortin and D.R. Snelling, Chem. Phys. Letters, 3, (1969) 204.

35. F.D. Findlay and D.R. Snelling, J. Chem. Phys., 55,(1971) 545.

36. D.R. Kearns, Chem. Rev., 71, (1971) 395.

37. K. Gollink, Advan. Photochem., 6, (1968) 1.

38. T.C. Frankiewicz and R.S. Berry, J. Chem. Phys., 58, (1973) 1787.

39. I.T.N. Jones and K.D. Bayes, J. Chem. Phys., 59, (1973) 3119.

40. S.V. Filseth, A. Zia and K.H. Welge, J. Chem. Phys., 52, (1970) 5502.

41. F. Stuhl and H. Niki, Chem. Phys. Letters, 5, (1970) 573.

42. J.A. Davidson, K.E. Kear and E.W. Abrahamson, J. Photochem., 1, (1972) 307.

43. L.R. Martin, R.B. Cohen and J.F. Schatz, Chem. Phys. Letters, 41, (1976) 394.

44. S.A. Lawton and A.V. Phelps, J. Chem. Phys., 69, (1978) 1055.

45. R.J. Browne and E.A. Ogryzlo, Proc. Chem. Soc., (1964) 117.

46. D.L. Heustis, G. Black, S.A. Edelstein and R.L. Sharpless, J. Chem. Phys., 60, (1974) 4471.

47. L. Elias, E.A. Ogryzlo and H.I. Schiff, Canad. J. Chem., 37, (1959) 1680.

48. D.J. Giachardi, G.W. Harris and R.P. Wayne, J. Chem. Soc. Faraday II, 72, (1976) 619.

49. R.G. Derwent and B.A. Thrush, Trans. Faraday Soc., 67, (1971) 2036.

50. J-L. Dumas and B. Garnier, J. Chim. Phys., 72, (1975) 44.

51. T.P.J. Izod and R.P. Wayne, Proc. R. Soc., A308, (1968) 8.

52. A. Fontijn, C.B. Meyer and H.I. Schiff, J. Chem. Phys., 40, (1964) 64.

53. I.D. Clark and R.P. Wayne, Proc. R. Soc., A314, (1969) 111.

54. I.D. Clark and R.P. Wayne, Proc. R. Soc., A316, (1970) 539.

55. A.M. Falick and B.H. Mahan, J. Chem. Phys., 47, (1967) 4778.

56. C.K. Duncan and D.R. Kearns, J. Chem. Phys., 55 (1971) 5822.

57. A.T. Pritt, R.D. Coombe, I.B. Goldberg, D. Pilipovich and R.I. Wagner, Rockwell Science Centre Report AFWL-TR-77-265 (1978).

58. A.M. Falick, B.H. Mahan and R. J. Myers, J. Chem. Phys., 42, (1965) 1837.

59. M. Gauthier and D.R. Snelling, Chem. Phys. Letters, 5, (1970) 93.

60. M. Gauthier and D.R. Snelling, J. Chem. Phys., 54, (1971) 4317.

61. I.T.N. Jones and R.P. Wayne, Proc. R. Soc., A319, (1970) 273.

62. M.J. Gauthier and D.R. Snelling, J. Photochem., 4, (1975) 27.

63. A.M. Winer and K.D. Bayes, J. Phys. Chem., 70, (1966) 302.

64. P.D. Bartlett and G.D. Mendenhall, J. Amer. Chem. Soc., 92, (1970) 210.

65. P.D. Bartlett, G.D. Mendenhall and A.P. Schaap, Ann. N.Y. Acad. Sci., 171, (1970) 79.

66. P.B. Merkel and D.R. Kearns, J. Amer. Chem. Soc., 94 (1972) 1029.

67. E.A. Ogryzlo, Photophysiology, 5, (1970) 35.

68. J.A. Davidson and E.A. Ogryzlo, "Chemiluminescence and Bioluminscene", Ed. M.J. Cormier, D.M. Hercules and J. Lee, (1973) Plenum Press N.Y.

69. K. Kear and E.W. Abrahamson, J. Photochem., 3, (1975) 409.

70. M. Braithwaite, J.A. Davison and E.A. Ogryzlo, J. Chem. Phys., 65, (1976) 771.

71. M. Braithwaite, E.A. Ogryzlo, J.A. Davidson and H.I. Schiff, J. Chem. Soc. Faraday II, 72, (1976) 2075.

72. M. Braithwaite, E.A. Ogryzlo, J.A. Davison and H.I. Schiff, Chem. Phys. Letters, 42, (1976) 158.

73. R.G.O. Thomas and B.A. Thrush, Proc. R. Soc., A356, (1977) 307.

74. R.G.O. Thomas and B.A. Thrush, Proc. R. Soc., A356, (1977) 295.

75. P.B. Merkel and D.R. Kearns, J. Amer. Chem. Soc., 94, (1972) 7244.

76. C.A. Long and D.R. Kearns, J. Amer. Chem. Soc., 97, (1975) 2018.

77. R.D. Ashford and E.A. Ogryzlo, J. Amer. Chem. Soc., 97, (1975) 3604.

78. B.L. Monroe, J. Phys. Chem., 82, (1978) 15.

79. G.A. Hollinden and R.B. Timmons, J. Amer. Chem. Soc., 92, (1970) 4181.

80. "Singlet Oxygen - Reactions with Organic Compounds and Polymers", Ed. B. Ranby and J.F. Rabek, (1978) Wiley.

81. "Singlet Oxygen", Ed. H.H. Wasserman and R.W. Murray, (1979) Academic Press N.Y.

82. D. Belluš, Advan. Photochem, 11, (1979) 105.

83. L.W. Bader and E.A. Ogryzlo, Disc. Faraday Soc., 37, (1964) 46.

84. H.P. Gush and H.L. Buijs, Canad. J. Phys., 42, (1964) 1037.

85. M.N. Vlasov, J. Atmos. and Terres. Phys., 38, (1976) 807.

86. J. Houghton, Proc. R. Soc., A288, (1965) 545.

87. J.N. Pitts, Symp. Proc. "Chemical Reactions in Urban Atmospheres", (1969) Elsevier.

88. R.A. Hartunian, W.P. Thompson and E.W. Hewitt, J. Chem. Phys., 44, (1966) 1765.

89. P. Borell, P.M. Borrell and A. Brittain, (1969), U.S. Clearing House Ed. Sci. Tech. Inform., AD 702808.

90. R.W.F. Gross, J. Chem. Phys., 48, (1968), 1302.

91. R.W.F. Gross and N. Cohen, J. Chem. Phys., 48, (1968) 2582.

92. N. Cohen and R.W.F. Gross, J. Chem. Phys., 50, (1969) 3119.

93. J.E. Breen, R.B. Quy and G.P. GLass, J. Chem. Phys., 59, (1973) 556.

94. J.E. Breen, R.B. Quy and G.P. Glass, "Recent Developments in Shock Tube Research", Ed. D. Bershader and W. Griffiths (1973) Stanford University Press.

95. A.D. MacDonald and S.J. Tetenbaum, Gaseous Electronics 1, (1978) 173.

96. W.F. Meggers, J. Opt. Sci. A, 38, (1948) 7.

97. P.W. Atkins, "Physical Chemistry", (1978) Oxford.

98. G.M. Barrow, "Physical Chemistry", (1966) McGraw-Hill.

99. J.R. Partington, "An Advanced Treatise in Physical Chemistry", Vol. I, (1949) Longmans.

100. J.N. Bradley, "Shock Waves in Chemistry and Physics", (1962) Methuen, London.

101. M. Camac, J. Chem. Phys., 34, (1961) 448.

102. P. Borrell, "Transfer and Storage of Energy by Molecules", Ed. G.M. Burnett and A.M. North, (1969) Wiley, N.Y.

103. R.C. Millikan, General Electric Research Laboratory Report (1964) No. 64 - RL 3700C.

104. JANAF (1965) Thermochemical Tables. The Dow Chemical Company, Michigan.

105. A.G. Gaydon and I.R. Hurle, "The Shock Tube in High Temperature Chemical Physics", (1963) Chapman and Hall, London.

106. R.W. Lutz and J.H. Kiefer, J. Chem. Phys., 44, (1966) 658.

107. G.E. Millward, Ph.D. Thesis (1970) University of Keele.

108. R.L. Belford and R. Strehlow, Ann. Rev. Phys, Chem., 20, (1969) 247.

109. H. Mirels, Phys. Fluids, 6, (1963) 1201.

110. M.D. Pedley, Ph.D. Thesis (1978) University of Keele.

111. C.T. Bowman and R.K. Hanson, J. Phys. Chem., 83, (1979) 757.

112. S.H. Whitlow and F.D. Findlay, Canad. J. Chem., 45, (1967) 2087.

113. T.P.J. Izod and R.P. Wayne, Nature, 217, (1968) 947.

114. D.J. Giachardi, G.W. Harris and R.P. Wayne, Chem. Phys. Letters, 32, (1975) 586.

115. A. Leiss, U. Schurath, K.H. Becker and E.H. Fink, J. Photochem, 8, (1978) 211.

116. U. Schurath, J. Photochem, 47, (1975) 215.

117. I.D. Clark and R.P. Wayne, Chem. Phys. Letters, 3, (1969) 93.

118. P. Borrell, P.M. Borrell and M.D. Pedley, Chem. Phys. Letters, 51, (1977) 300.

119. R.P. Steer, R.A. Ackerman and J.N. Pitts Jr., J. Chem. Phys., 51, (1969) 843.

120. K.G. Vohra, J.P.S. Chatha, P.K. Arova and N. Raja, Proc. Symposium on Singlet Molecular Oxygen, (1976) 35, Bombay.

121. K.H. Becker, W. Groth and U. Schurath, Chem. Phys. Letters, 8, (1971) 259.

122. P. Moore, J. Chem. Soc. Faraday I, 68, (1972) 1890.

123. Nottingham Algorithms Group, N.A.G. Library routine, E04GAF, Nottingham, 1972.

124. P. Borrell, Computers in Chemistry, (accepted for publication)(1980).

125. R.J. Collins, D. Husain and R.J. Donovan, J. Chem. Soc. Faraday II, 69, (1973) 145.

126. J.H. Miller, R.W. Boese and L.P. Giver, J. Quant. Spect. Radiative Transfer, 9, (1969) 1507.

127. D.R. White, J. Chem. Phys., 49, (1968) 5472.

128. R.G.O. Thomas and B.A. Thrush, J. Chem. Soc. Faraday II, 71, (1975) 664.

129. K. Kohse-Höinghaus and F. Stuhl, J. Chem. Phys., 72, (1980) 3720.

130. C.S. Parmenter and M. Seaver, Chem. Phys. Letters, 67, (1979) 279.

131. H.H. Seliger, J. Chem. Phys., 40, (1964) 3133.

132. P.H. Krupenie, J. Phys. and Chem. Ref. Data, 1, (1972) 423.

133. V.I. Dianov-Klokov, Opt. Spectros, 6, (1959) 290.

134. G.W. Robinson, J. Chem. Phys., 46, (1967) 572.

135. V.G. Krishna, J. Chem. Phys., 50, (1969) 792.

136. S.C. Tsai and G.W. Robinson, J. Chem. Phys., 51, (1969) 3559.

137. A. Landau, E.J. Allin and H.L. Welsh, Spectrochim. Acta, 18, (1962) 1.

138. R.P. Blickensderfer and G.E. Ewing, J. Chem. Phys., 47, (1967) 331.

139. R.P. Blickensderfer and G.E. Ewing, J. Chem. Phys., 51, (1969) 873, 5284.

140. J. Goodman and L.E. Brus, J. Chem. Phys., 67, (1977) 4398 and 4408.

141. N.A. Generalov and S.A. Losev, J. Quant. Spect. Radiative Transfer, 6, (1966) 101.

142. D.R. White and R.C. Millikan, J. Chem. Phys., 39, (1963) 1803 and 1807.

143. R.W. Lutz and J.H. Kiefer, Phys. Fluids, 9, (1966) 1638.

144. J.G. Parker, J. Chem. Phys., 34, (1961) 1763.

145. R. Holmes, F.A. Smith and W. Tempest, Proc. Phys. Soc., 81, (1963) 311.

146. R.J. Collins and D. Husain, J. Photochem., 1, (1972) 481.

147. J.G. Parker and D.N. Ritke, J. Chem. Phys., 61, (1974) 3408.

148. R.C. Millikan and D.R. White, J. Chem. Phys., 39, (1963) 3209.

149. D.G. Jones, J.D. Lambert and J.L. Stretton, Proc. Phys. Soc., 86, (1965) 857.

150. D. Rapp, J. Chem. Phys., 43, (1965) 316.

151. H.J Bauer and R. Schotter, J. Chem. Phys., 51, (1969) 3261.

152. H.J Bauer, "Physical Acoustics", Vol. II Pt. A, Ed. W.P. Mason (1965), Academic Press, N.Y.

153. P. Borrell, P.M. Borrell, M.D. Pedley and K.R. Grant, Proc. R. Soc. Lond., A367, (1979) 395.

154. P. Borrell, P.M. Borrell and K.R. Grant, Nuovo Cimento (1980) accepted for publication.

155. C. Fotakis, Private Communication.

156. H.-M. Lin, M. Seaver, K.Y. Tang, A.E.W. Knight and C.S. Parmenter, J. Chem. Phys., 70 (1979) 5442.

157. C.S. Parmenter and M. Seaver, J. Chem. Phys., 70, (1979) 5458.

158. P. Borrell, P.M. Borrell and K.R. Grant, J. Chem. Soc. Faraday II (1980) in press.

159. P. Borrell, P.M. Borrell and K.R. Grant, J. Chem. Soc. Faraday II (1980) in press.

160. I. Barnes, K.H. Becker and E.H. Fink, Chem. Phys. Letters, 67, (1979) 310.

161. I. Barnes, K.H. Becker and E.H. Fink, Chem. Phys. Letters, 67, (1979) 314.

162. I. Barnes, E.H. Fink, J. Wildt, R. Winter and F. Zabel, 6th Int. Conf. Gas Kinetics, Southampton. (1980).

163. R.G. Derwent and B.A. Thrush, J. Chem. Soc. Faraday II, 68, (1972) 720.

164. T.G. Slanger, J. Chem. Phys., 69, (1978) 4779.

Appendix I

Calculation of length of Shock Tube

It is possible to calculate the length of the test section of the shock tube, from the diaphragm to the observation section, x, for any given Mach number and the required observation, or hot flow time, Δt. The equations used are from Gaydon and Hurle[105] :

$$x = t_c \left\{ \frac{2a_1(M^2-1)}{(\gamma_1+1)M} \right\} \qquad \text{I.1}$$

$$t = t_c \left\{ 1 - \frac{2(M^2-1)}{(\gamma_1+1)M} \right\} \qquad \text{I.2}$$

where t_c is the time of arrival of the contact surface at the observation station.

The minimum length of the driver section, x_d, can also be calculated :

$$t_c = \frac{2x_d}{a_4} \left\{ 1 - \left[\frac{\gamma_4-1}{\gamma_1+1}\right] \frac{a_1}{a_4} \left[\frac{M^2-1}{M^2}\right] \right\}^{-[(\gamma_4+1)/2(\gamma_4-1)]} \qquad \text{I.3}$$

where the suffix 1 refers to the test gas and 4 to the driver gas.

These equations apply to "perfect" shocks into ideal gas.

Appendix II

Calculation of Energy Levels for Oxygen

$$E = T_e + (v+\tfrac{1}{2})\omega_e - (v+\tfrac{1}{2})^2\omega_e x_e$$

where T_e is the electronic energy in cm^{-1} above the potential energy zero, v is the vibrational quantum number, ω_e is the vibrational constant, and $\omega_e x_e$ is the anharmonicity factor.[4]

For ground state oxygen $O_2(^3\Sigma_g^-)$

$T_e = 0$

$\omega_e = 1580.4 \ cm^{-1}$

$\omega_e x_e = 12.07 \ cm^{-1}$

For the zeroth vibrational level : $E_0 = 787.2 \ cm^{-1}$

For the first vibrational level : $E_1 = 2343.4 \ cm^{-1}$

For $O_2(^1\Delta_g)$

$T_e = 7918 \ cm^{-1}$

$\omega_e = 1509 \ cm^{-1}$

$\omega_e x_e = 12.9 \ cm^{-1}$

For the zeroth vibrational level : $E_{\Delta_0} = 8669.3 \ cm^{-1}$

For the first vibrational level : $E_{\Delta_1} = 10152 \ cm^{-1}$

For $O_2(^1\Sigma_g^+)$

$T_e = 13195 \ cm^{-1}$

$\omega_e = 1432.7 \ cm^{-1}$

$\omega_e x_e = 13.95 \ cm^{-1}$

For the zeroth vibrational level : $E_{\Sigma_0} = 13907.9 \ cm^{-1}$

$E_{\Sigma_1} = 15375 \ cm^{-1}$

Electronic Energy Spacing

Spacing between $O_2(^1\Delta_g)$ and $O_2(^3\Sigma_g^-)$

$\Delta E_\Delta = E_{\Delta_o} - E_o = 7882.1\ cm^{-1}$

and $\Delta E/R = 11309.6\ K$

Spacing between $O_2(^1\Sigma_g^+)$ and $O_2(^3\Sigma_g^-)$

$\Delta E_\Sigma = E_\Sigma - E_o = 13120.7\ cm^{-1}$

and $\Delta E_\Sigma/R = 18826\ K$

Partition functions for Electronic States

$$pf_e = g_o\, e^{-E_o/RT} + g_\Delta\, e^{-E_\Delta/RT} + g_\Sigma\, e^{-E_\Sigma/RT}$$

where g is the degeneracy

For $O_2(^3\Sigma_g^-)$ $g_o = 3$

For $O_2(^1\Delta_g)$ $g_\Delta = 2$

For $O_2(^1\Sigma_g^+)$ $g_\Sigma = 1$

At Thermal Equilibrium :

Fraction of molecules in $O_2(^1\Delta_g)$ state $\frac{n_\Delta}{N} = \frac{2}{3}\, e^{-\Delta E_o/RT}$

At 295 K $n_\Delta/N = 1.49 \times 10^{-7}$

At 1500 K $n_\Delta/N = 3.54 \times 10^{-4}$

Fraction of molecules in $O_2(^1\Sigma_g^+)$ state $\frac{n_\Sigma}{N} = \frac{1}{3}\, e^{-\Delta E_\Sigma/RT}$

At 295 K $n_\Sigma/N = 4.15 \times 10^{-29}$

At 1500 K $n_\Sigma/N = 1.18 \times 10^{-6}$

Vibrational Energy Spacing

Vibrational spacing :

$$\Delta'_{\omega} = \omega_e[(v' + \tfrac{1}{2}) - (v + \tfrac{1}{2})] - \omega_e x_e[(v' + \tfrac{1}{2})^2 - (v + \tfrac{1}{2})^2]$$

For ground state oxygen, $O_2(^3\Sigma_g^-)$

Spacing between zeroth and first vibrational level (v=0 and v'-v=1);

$$\Delta_{\omega} = 1556.2 \text{ cm}^{-1}$$

$$\Delta E/R = \Delta H/k = hc\Delta_{\omega}/k$$

$$\Delta E/R = 2232 \text{ K}$$

[Reference 101 gives 2228 K and reference 148 gives 2239 K]

For $O_2(^1\Delta_g)$

$$\Delta_{\omega} = 1485 \text{ cm}^{-1}$$

and $\Delta E/R = 2131$ K

Vibrational Partition Function

$$pf_v = 1/(1 - e^{-E/RT})$$

Relative population of n^{th} vibrational level

$$\frac{n_n}{N_{total}} = e^{-nE/RT}(1 - e^{-E/RT})$$

At thermal equilibrium :

For ground state oxygen, $O_2(^3\Sigma_g^-)$, fraction of molecules in first vibrational level :

at 295 K $n_1/N = 5.17 \times 10^{-4}$

at 1500 K $n_1/N = 0.175$

For $O_2(^1\Delta_g)$, fraction of molecules in first vibrational level :

at 295 K : $n_1/N = 7.35 \times 10^{-4}$

at 1500 K : $n_1/N = 0.183$

Appendix IIIa

Millikan and White Correlation

Millikan and White[148] plotted experimental vibrational relaxation times for many simple systems, and found that for Landau-Teller plots, the straight lines intersect at a single point at high temperature. This lead to the formation of an empirical equation correlating vibrational relaxation times with the characteristic temperature, θ, of the oscillator.

$$\log_{10}(p\tau_v) = (5.0 \times 10^{-4})\mu^{\frac{1}{2}}\,\theta^{4/3}(T^{-1/3} - 0.015\mu^{1/4}) - 8.0$$

For ground state oxygen $O_2(^3\Sigma_g^-)$ θ = 2232 K

Temperature /K	$T^{-1/3}$	$p\tau_v$/μs. atm. calculated	$p\tau_v$/μs. atm. Experimental value from equation 10.24
295	0.1502	1.17×10^5	4.83×10^4
600	0.1186	1.61×10^3	9.01×10^2
1000	0.1000	1.30×10^2	8.65×10
1500	0.0874	2.36×10	1.77×10

For $O_2(^1\Delta_g)$ θ = 2131 K

Temperature /K	$T^{-1/3}$	$p\tau_v$/μs. atm. calculated	$p\tau_v$/μs. atm. Experimental value from figure 10.3
295	0.1502	4.4×10^4	-
600	0.1186	7.84×10^2	-
1000	0.1000	7.39×10	67
1500	0.0874	1.48×10	13.5

Appendix IIIb.

Calculation of Probability of Vibration-Vibration Exchange at near Resonance (from D. Rapp[150])

$$P_{10 \rightarrow 01} = 3.7 \times 10^{-6}\ T\ \mathrm{sech}^2\ \frac{0.174\ \Delta E}{T^{\frac{1}{3}}}$$

where ΔE is difference in vibrational energy of colliding molecules in cm^{-1}.

$$O_2(^1\Delta_g)_{v=1} + O_2(^3\Sigma_g^-)_{v=0} \rightleftarrows O_2(^1\Delta_g)_{v=0} + O_2(^3\Sigma_g^-)_{v=1}$$

Vibrational Energy Spacing for $O_2(^3\Sigma_g^-) = 1556\ cm^{-1}$, Vibration Energy Spacing for $O_2(^1\Delta_g) = 1483\ cm^{-1}$

$$\text{Difference } \Delta E = 73\ cm^{-1}$$

To calculate vibrational relaxation time: (Chapter 1)

$$P_{10 \rightarrow 01} = k_{10}/Z$$

and

$$\tau = 1/k_{10}$$

Temperature /K	$P_{10 \rightarrow 01}$	Z /μs^{-1} atm^{-1}	τ /μs atm
295	6.60×10^{-4}	6.62×10^{3}	2.3×10^{-1}
1000	3.16×10^{-3}	1.215×10^{4}	2.6×10^{-2}
1500	4.99×10^{-3}	1.488×10^{4}	1.3×10^{-2}

Appendix IIIc

Calculation of Vibrational Relaxation Time for a Two Component System, A, and B, where both are Diatomic Molecules and Vibration-Vibration Energy Transfer is taken into account,[151, 152]

The processes occurring are: Relaxation Times

1. $A_1 + A \underset{k_{-1}}{\overset{k_1}{\rightleftarrows}} A_0 + A$ τ_{AA}

2. $A_1 + B \underset{k_{-2}}{\overset{k_2}{\rightleftarrows}} A_0 + B$ τ_{AB}

3. $B_1 + B \underset{k_{-3}}{\overset{k_3}{\rightleftarrows}} B_0 + B$ τ_{BB}

4. $B_1 + A \underset{k_{-4}}{\overset{k_4}{\rightleftarrows}} B_0 + A$ τ_{BA}

5. $A_1 + B_0 \underset{k_{-5}}{\overset{k_5}{\rightleftarrows}} A_0 + B_1$

For relaxation of all processes:

$$\left[\frac{1}{\tau_V} - \frac{x_A}{\tau_{AA}} - \frac{x_B}{\tau_{AB}}\right]\left[\frac{1}{\tau_V} - \frac{x_B}{\tau_{BB}} - \frac{x_A}{\tau_{BA}}\right] - k_5\, k_{-5}\, x_A\, x_B = 0$$

where $$\frac{1}{\tau_{AA}} = \left[1 + \frac{C_{A_1}}{C_{A_0}}\right] k_{-1}$$

$$\frac{1}{\tau_{AB}} = \left[1 + \frac{C_{A_1}}{C_{A_0}}\right] k_{-2} + k_{-5} \Big/ \left[1 + \frac{C_{B_1}}{C_{B_0}}\right]$$

Appendix IIIc continued

$$\frac{1}{\tau_{BB}} = \left[1 + \frac{C_{B_1}}{C_{B_0}}\right] k_{-3}$$

and $$\frac{1}{\tau_{BA}} = \left[1 + \frac{C_{B_1}}{C_{B_0}}\right] k_{-4} + k_5 \Big/ \left[1 + \frac{C_{A_1}}{C_{A_0}}\right]$$

In this case A = $O_2(^3\Sigma_g^-)$ and B = $O_2(^1\Delta_g)$ and the relaxation of $O_2(^3\Sigma_g^-)$ [or $O_2(^1\Delta_g)$] is the same if the collision partner is either $O_2(^3\Sigma_g^-)$ or $O_2(^1\Delta_g)$, so $k_1 = k_2$, $k_{-1} = k_{-2}$, $k_3 = k_4$ and $k_{-3} = k_{-4}$.

Then $$\frac{1}{\tau_{AB}} = \frac{1}{\tau_{AA}} + \frac{k_{-5}(1 + C_{A_1}/C_{A_0})}{(1 + C_{B_1}/C_{B_0})}$$

and $$\frac{1}{\tau_{BA}} = \frac{1}{\tau_{BB}} + \frac{k_5(1 + C_{B_1}/C_{B_0})}{(1 + C_{A_1}/C_{A_0})}$$

The relative concentrations are calculated from the Boltzmann distribution function

$$C_{A_1}/C_{A_0} = e^{-2232/T}$$

$$C_{B_1}/C_{B_0} = e^{-2131/T}$$

k_5 the rate constant for vibrational exchange has been calculated previously (Appendix IIIb)

and $$k_5 = k_{-5}\, e^{-101/T}$$

Appendix IIIc continued

If it is assumed that 10% of the oxygen flow is $O_2(^1\Delta_g)$ then $x_B = 0.1 + x_A = 0.9$.

Taking the calculated vibrational relaxation times from the Millikan and White correlation (Appendix IIIa) for τ_{O_2} (τ_{AA}) and τ_Δ (τ_{BB}), it is possible to calculate τ_V, the expected relaxation time for the mixture, at several temperatures.

A similar calculation uses the experimental values for ground state oxygen and τ_V found in this work, and calculates τ_Δ, (τ_{BB}), the vibrational relaxation of pure $O_2(^1\Delta_g)$.

Results.

Temperature /K	τ_{O_2} (Experimental values)	τ_V (Calculated, and corrected for experimental values τ_{O_2})	τ_{Expt} (This work)	τ_Δ (Calculated from values in columns 2 and 4)
1000	86.5	78.1	67.	24.2
1500	17.7	16.5	13.5	4.8

These results are displayed in figure 10.5.